New Potential Waveforms for Cyclic and Linear-Sweep Voltammetry



Yuki Uchida

Keble College

University of Oxford

A thesis submitted for the degree of

Doctor of Philosophy

Trinity Term 2019

Acknowledgements

First and foremost I would like to thank Professor Richard Compton for welcoming me into his group, supervising and encouraging me throughout the three years of my DPhil. Thank you for always taking the time to discuss projects and being available for support.

I would also like to deeply thank Dr. Enno Kältelhön and Dr. Chuhong Lin for guiding me during my first year and working closely with me on all of my projects and Dr. Hatem Amin for running experiments. Thank you also to the rest of the Compton Group, especially Henry Chan for helping me settle into the group and Hannah Hodson for taking me out for cycling.

Immeasurable thanks must go to my parents for funding my DPhil for three years and for their constant support. I would also like to give a special thanks to my grandfather, who is dearly missed, for always loving me and caring for me. I would like to thank my brother and grandmother as well who have been encouraging me throughout the three years.

I cannot thank Tabish Rashid enough for his continous support. I could not have made it this far without his help. Thank you for everything you do and continue to do. Thank you to all of my friends who have made this incredible journey possible. Liz Parish and Avraham Sherman - I appreciated all the cat memes you sent me which a lot of the times gave me the energy I needed to get through the day. Tabish Rashid, Alun Vaughan-Jackson, and Luis Porangaba - I really enjoyed our movie group and the ramen afterwards. Yum! Thank you to my friends back in Japan, who always give me a warm welcome-home everytime and anytime I travel back.

My experience at Oxford has been wonderful and fruitful because of the people I met, and I am extremely grateful that I was surrounded by so many extraordinary people. Leaving a place I lived for a while is always bitter-sweet but I am excited for the next journey and am happy I have made lifelong friends here. Thank you to everyone who was there for me throughout the three years of my DPhil. You will always have a special place in my heart.

Abstract

This thesis is concerned with the simulation of electrochemical systems in general and of voltammetry using various potential waveforms in particular. Chapter 1 introduces the fundamental principles of electrochemistry essential to the understanding of this thesis, and Chapter 2 outlines the methodology used in the numerical simulation of the systems of interest.

Chapters 3 and 4 discuss the application and benefit of a non-triangular/non-linear potential waveform to run cyclic voltammetry/potential-sweep voltammetry. In both chapters, a one-dimensional macroelectrode system is modelled for a one-electron electrochemically reversible reaction. Chapter 3 investigates the effect of cosine-based potential waves on the capacitive and Faradaic currents and proposes new opportunities to determine the formal potential of a redox couple based on the peak-to-peak separation in measured voltammograms. Chapter 4 extends the concept of a non-linear potential wave and studies the effect of a semi-circular potential wave on the current response for increased sensitivity of detection in electroanalysis. In both chapters, an experimental verification of the method are provided.

Chapters 5 and 6 extend the semi-circular potential wave method to a two-dimensional microelectrode system. Chapter 5 illustrates that the semi-circular potential wave method produces similar trends at a microelectrode as it does at a macroelectrode and shows the increased applicability of the method. Chapter 6 proposes a new method for determining the standard electrochemical rate constant through the application of a semi-circular potential wave at a microelectrode based on the voltammetric features.

Chapter 7 applies the semi-circular potential waveform to stripping voltammetry for a one-electron electrochemically reversible reaction and shows how the unique voltammetric curves resulting from the semi-circular potential wave markedly increase the sensitivity.

Contents

List of Figures **xi**

1 Introduction **1**

1.1 Electrochemical Equilibrium 1

1.1.1 The Nernst Equation 2

1.1.2 Electrochemical Cell 4

1.2 Electrode Kinetics 6

1.3 Electrical Double Layer 8

1.4 Effect of Supporting Electrolyte 9

1.5 Mass Transport 10

1.5.1 Fick's First Law 10

1.5.2 Fick's Second Law 12

1.6 Faradaic and Non-Faradaic Processes 13

1.7 Electrode Size 13

1.8 Electrochemical Techniques 14

1.8.1 Cyclic and Linear-Sweep Voltammetry 15

1.8.2 Stripping Voltammetry 19

2 Electrochemical Simulations **25**

2.1 Dimensionless Coordinates 25

2.2 Finite Difference Method 26

2.3 Time Evolution: Discretizing Fick's Second Law 29

2.3.1 Explicit Method 29

2.3.2 Implicit Method 30

2.3.3 Thomas Algorithm 30

2.4 One-dimensional Simulation 32

2.5 Two-dimensional Simulation 34

2.6 Convergence 37

3 Cosine-based Potential Waves **41**
3.1 Introduction 42
3.2 Theory 43
3.2.1 Theoretical Model 43
3.2.2 Proposed Method 45
3.2.3 Dimensionless Coordinates 45
3.2.4 Simulation via Finite Differences 46
3.3 Results and Discussion 48
3.3.1 Capacitive Currents 48
3.3.2 Voltammetry Obtained Using a Cosine Potential Wave When $n = 1$ 52
3.3.3 Voltammetric Effects of Cosine Potential Wave When $n > 1$ 55
3.4 Conclusions 60
3.5 Experimental Verification 61
3.5.1 Chemicals 61
3.5.2 Instrumental 61
3.5.3 Results and Discussion 62
3.5.4 Conclusions 69

4 Semi-circular Potential Waves in Voltammetry: Theory and Experiment **73**
4.1 Introduction 74
4.2 Theory 75
4.2.1 Theoretical Model 75
4.2.2 Dimensionless Coordinates 77
4.2.3 Semi-circular Potential Sweep 78
4.2.4 Simulation via Finite Differences 81
4.3 Results and Discussion 82
4.3.1 Single Electrochemically Reversible Species: Linear versus Semi-circular Potential Waves 82
4.3.2 Two Species Linear versus Semi-circular Potential Sweeps . . 85
4.4 Conclusions 94
4.5 Experimental Verification 95
4.5.1 Chemicals 95
4.5.2 Instrumental 96
4.5.3 Results and Discussion 96
4.6 Conclusions 103

5 Semi-circular Potential Waves: Microelectrode 107
5.1 Introduction . . . 108
5.2 Theory . . . 109
5.2.1 Theoretical Model . . . 109
5.2.2 Boundary Conditions . . . 110
5.2.3 Dimensionless Coordinates . . . 112
5.2.4 Semi-circular Potential Wave . . . 113
5.2.5 Simulation via Finite Differences . . . 114
5.3 Results and Discussion . . . 115
5.3.1 Linear versus Semi-circular Potential Sweeps: 3 Different Scan Rates . . . 115
5.3.2 Semi-circular Potential Sweeps: Different θ_{shift} Values . . . 121
5.4 Conclusions . . . 128

6 Determining Kinetic Parameters Through Semi-circular Potential Wave Voltammetry at Microelectrodes 131
6.1 Introduction . . . 132
6.2 Theory . . . 133
6.2.1 Theoretical Model . . . 133
6.2.2 Boundary Conditions . . . 134
6.2.3 Dimensionless Coordinates . . . 135
6.2.4 Semi-circular Potential Wave . . . 136
6.2.5 Simulation via Finite Differences . . . 138
6.3 Results and Discussion . . . 138
6.3.1 Linear versus Semi-circular Potential Sweeps: 1.0 V s^{-1} Scan Rate . . . 138
6.3.2 Determining k_0 . . . 141
6.3.3 Linear versus Semi-circular Potential Sweeps: 100.0 mV s^{-1} Scan Rate . . . 146
6.4 Conclusions . . . 147

7 Cathodic Stripping Voltammetry using Semi-circular Potential Waves for Increased Sensitivity of Detection 151
7.1 Introduction . . . 152
7.2 Theory . . . 153
7.2.1 Theoretical Model . . . 153
7.2.2 Dimensionless Coordinates . . . 155
7.2.3 Semi-circular Potential Wave . . . 156
7.2.4 Simulation via Finite Difference . . . 157
7.3 Results and Discussion . . . 157

7.3.1 Effect of Potential Window Shift . . . 158
7.3.2 Features of Semi-circular Potential Wave Voltammetry . . . 161
7.3.3 Experimental Applications . . . 167
7.4 Conclusions . . . 168

8 Conclusions **171**

Appendices

A Appendix **177**
A.1 Butler-Volmer Derivation . . . 177
A.2 Chapter 3 Additional Figures . . . 181
A.3 Chapter 4 Additional Figures . . . 184
A.3.1 $\Delta\theta$ Convergence . . . 184
A.3.2 Full-Scale Voltammograms . . . 187
A.4 Chapter 5 Additional Figures . . . 191
A.4.1 Determination of the appropriate K_0 . . . 191
A.5 Chapter 6 Additional Figures . . . 193
A.5.1 Convergence Tests . . . 193

List of Figures

1.1 Schematic representation of a two electrode setup. The electrodes are labelled 1 and 2 to represent the working and reference electrodes, respectively. 5

1.2 Schematic representation of the Stern-Grahame model depicting the double layer and the potential drop ($\phi_M - \phi_S$) as a function of distance from the electrode. The green, pink, and blue circles represent the anions, cations, and solvent molecules, respectively. 9

1.3 Schematic representation of the molecular basis of Fick's First Law. 11

1.4 Schematic representation of (a) linear diffusion at a macroelectrode and (b) convergent diffusion at a microelectrode. 14

1.5 Schematic representation of a triangular potential wave. 15

1.6 Schematic representation of voltammetric response at (a) a macrodisc electrode and (b) a microdisc electrode. In (b), the steady-state response is shown. 16

1.7 Schematic representation of voltammetric responses at (a) a macrodisc electrode and (b) a microdisc electrode. In both figures, (i) corresponds to reversible, (ii) corresponds to quasi-reversible, and (iii) corresponds to irreversible systems. 16

1.8 Schematic representation of a steady-state voltammograms with quartile potentials. 18

1.9 Schematic representation of voltammetric response of an electrochemically reversible one-electron transfer reaction at (a) a macrodisc electrode and (b) a microdisc electrode. In both figures, (i) corresponds to slow scan rate, (ii) corresponds to relatively fast scan rate, and (iii) corresponds to fast scan rate. 19

1.10 Schematic representation of CSV for an electrochemically reversible one-electron transfer process. 21

2.1 Schematic representation of the forward (red line), backward (green line), and central (blue line) approximations. 27

2.2 34

3.1 A schematic representation of the three potential waves centrered at $\theta = 0$ with an amplitude of 1. The blue line corresponds to the triangular wave, the green line corresponds to the cosine wave when $n = 1$, and the magenta line corresponds to the cosine wave when $n = 2$. 47

3.2 A schematic representation of the capacitive current of the three potential waves shown in Figure 3.1 with the same color scheme. A jump in the capacitive current is seen at $\tau_{1/2}$, the point of reversal, for the triangular method whereas both cosine-based methods show a continuous curve at said point. Here, the double-layer capacitance is assumed to be potential independent. 49

3.3 Dimensionless voltammograms obtained by applying the triangular, cosine, and cosine square potential waves at $\sigma = 10^4$ and $\theta_{shift} = 0$. The same color scheme is used as in Figure 3.1. 50

3.4 A comparison between voltammograms with and without capacitive perturbations at $\sigma = 10^4$ and $\theta_{shift} = 0$ for $C_{dl} = 20$ µF cm^{-2}. Each figure is labeled with the corresponding potential wave: A is for triangular, B is for cosine when $n = 1$, and C is when $n = 2$. The solid curves represent the dimensionless Faradaic current and the dashed curves represent the total current (Faradaic + capacitive). . 51

3.5 Voltammograms obtained from a triangular and cosine potential wave for $\sigma = 10^4$ and $\theta_{shift} = 0$ with the same color scheme as in Figure 3.1. The light blue dash-dot line corresponds to the dimensionless peak current value of a conventional triangular cyclic voltammetry predicted by the dimensionless Randles-Ševčík equation (3.20) and the yellow dash-dot line is the dimensionless peak current observed for the cosine voltammogram. 53

3.6 Dimensionless peak currents plotted against the square root of dimensionless scan rate for triangular and cosine potential wave methods at $\theta_{shift} = 0$. The blue dots correspond to the peak currents of the triangular method and the green dots correspond to the peak currents of the cosine method. The light blue line is the predicted peak current values at each scan rate given by Equation (3.20) and the yellow line was obtained by performing a linear fit on the green dots. 54

3.7 The two figures show the solution concentration of A for the cosine square potential wave voltammogram in Figure 3.3. $\sigma = 10^4$ and $\theta_{shift} = 0$. 56

3.8 Voltammograms using a cosine square potential wave with different θ_{shift} values. A corresponds to $\theta_{shift} = -5$, B corresponds to $\theta_{shift} = -2$, C corresponds to $\theta_{shift} = -1$, D corresponds to $\theta_{shift} = 0$, E corresponds to $\theta_{shift} = 1$, and F corresponds to $\theta_{shift} = 2$. 57

3.9 Dimensionless peak currents of individual voltammograms plotted against the corresponding θ_{shift} values for triangular, cosine, and cosine square potential waveforms. The blue dotted line is obtained from the triangular method, the green dotted line is from the cosine method, and the magenta and pink dotted lines correspond to the first and second peak of the cosine square voltammogram, respectively. 58

3.10 Dimensionless peak-to-peak separation plotted against corresponding θ_{shift} values for triangular, cosine, and cosine square potential waveforms. The same color scheme is used as in Figure 3.1. 60

3.11 Voltammograms of (a) triangular, (b) cosine, and (c) cosine square potential waves obtained at GC electrode in blank 0.10 M KCl solution (red solid curve, capacitive current) and in 0.96 mM $[Ru(NH_3)_6]Cl_3$/0.10 M KCl solution (black solid curve, Faradiac + capacitive currents) at a scan rate of 0.05 V s^{-1}. The E_{centre} for this figure is -0.2 V. The green solid curve is the experimental Faradaic-only current obtained via subtraction of the red curve from the black curve, and the green dashed line is the simulated Faradaic current. 63

3.12 Plot of capacitive current-corrected cathodic peak currents against the square root of the scan rate using triangular, cosine, and cosine square potential waves ranging from 0.025 to 2 V s^{-1} in $[Ru(NH_3)_6]Cl_3$/0.10 M KCl solution at 298 K. The linear regressions are shown. 65

3.13 Capacitive current-corrected voltammograms obtained at GC electrode with cosine square potential waveform at different E_{centre} values in 0.96 mM $[Ru(NH_3)_6]Cl_3$/0.10 M KCl solution at an average scan rate of 0.05 V s^{-1}. 66

3.14 Plot of the cathodic peak currents (capacitive current-corrected) obtained from the corresponding voltammograms with the triangular, cosine, and cosine square waves using different E_{centre} values. 67

3.15 Plot of the peak-to-peak separation obtained from the corresponding capacitive current-corrected voltammograms using the triangular, cosine, and cosine square waves at different E_{centre} values. 69

4.1 A schematic representation of the two potential waves centrered at $\theta = 0$ with an amplitude of 1. The blue line corresponds to the linear wave and the orange line corresponds to the semi-circular wave. . . 79

4.2 Voltammetric scan of species A obtained using linear and semi-circular potential waves at different θ_{shift} values where $\theta_f^0 = 0$ and $d_A = 1$. A is when $\theta_{shift} = -10$, B is when $\theta_{shift} = -8$, C is when $\theta_{shift} = -4$, D is when $\theta_{shift} = 0$, E is when $\theta_{shift} = 2$, and F is when $\theta_{shift} = 4$. The blue solid line represents the results from the linear potential wave and the solid orange line represents results from the semi-circular potential wave. The dotted line shows the peak current predicted by Equation (4.22). 84

4.3 Voltammograms using linear and semi-circular potential waves at different θ_{shift} values for species A and B with a formal potential difference of -8 dimensionless units (-0.21 V). $\theta^0_{f,A/C} = 0$, and $d_A = 1.0$ while $d_B = 0.5$. A is when $\theta_{shift} = -10$, B is when $\theta_{shift} = -8$, C is when $\theta_{shift} = -4$, D is when $\theta_{shift} = 0$, E is when $\theta_{shift} = 2$, and F is when $\theta_{shift} = 4$. The blue solid lines correspond to results from the linear potential wave: light blue represents A, bright blue represents B, and dark blue represents the total dimensionless current $(A + B)$. The orange/red solid lines correspond to results from the semi-circular potential wave: light orange represents A, bright red represents B, and dark red represents the total dimensionless current $(A + B)$. The light green dash line and dark green dash-dotted line show the peak currents predicted by Equation (4.22) for species A and B, respectively. 86

4.4 Peak flux plotted against the corresponding θ_{shift} value at which it was recorded for species A, B, and their total currents obtained through the semi-circular potential wave. The formal potential difference between the two species is -8 dimensionless units, and $d_A = 1.0$ and $d_B = 0.5$. The light orange dotted line represents peak currents for species A, the bright red dotted line represents peak currents for species B, and the dark red dotted line represents peak currents for the total current. 88

4.5 Voltammograms using linear and semi-circular potential waves at different θ_{shift} values for species A and B with a formal potential difference of -4 dimensionless units (-0.1 V). Formal potential of species $A = 0$, $d_A = 1.0$, and $d_B = 0.5$. A is when $\theta_{shift} = -6$, B is when $\theta_{shift} = -4$, C is when $\theta_{shift} = -2$, D is when $\theta_{shift} = 0$, E is when $\theta_{shift} = 2$, and F is when $\theta_{shift} = 4$. The same color scheme is used as in Figure 4.3. 90

4.6 Peak flux plotted against the corresponding θ_{shift} value at which it was recorded for species A, B, and their total dimensionless currents obtained through the semi-circular potential wave. The formal potential difference between the two species is -4 dimensionless units, $d_A = 1.0$, and $d_B = 0.5$. The same color scheme is used as in Figure 4.4. 91

4.7 Voltammograms using linear and semi-circular potential waves at different θ_{shift} values for species A and B with a formal potential difference of -2 dimensionless units (-0.05 V). Formal potential of species $A = 0$, $d_A = 1.0$, and $d_B = 0.5$. A is when $\theta_{shift} = -4$, B is when $\theta_{shift} = -2$, C is when $\theta_{shift} = -1$, D is when $\theta_{shift} = 0$, E is when $\theta_{shift} = 2$, and F is when $\theta_{shift} = 4$. The same color scheme is used as in Figures 4.3 and 4.5. 92

4.8 Peak flux plotted against the corresponding θ_{shift} value at which it was recorded for species A, B, and their total currents obtained through the semi-circular potential wave. The formal potential difference between the two species is -2 dimensionless units, $d_A = 1.0$, and $d_B = 0.5$. The same color scheme is used as in Figures 4.4 and 4.6. 93

4.9 Voltammograms obtained using (a) linear and (b) semi-circular potential waveforms at a GC electrode in blank 0.5 M KCl solution (blue curves, capacitive currents) and in 0.265 mM $[Ru(NH_3)_6]Cl_3$/0.5 M KCl solution (green curves, Faradaic + capacitive currents) at an average scan rate of 0.025 V s^{-1}. The experimental Faradaic-only currents (red curves) were obtained by subtraction of the blue curve from the green curve and base line correction. The Faradaic currents obtained from the simulations are displayed as black dashed lines. The arrows show the direction of the potential sweep. 97

4.10 Capacitive current-corrected voltammograms obtained at a GC electrode with the triangular potential waveform 99

4.11 Capacitive current- and base line-corrected voltammograms obtained from experiment (solid red curves) and simulation (dashed black curves) at a GC electrode using the semi-circular potential waveform at different E_{centre} values in 0.265 mM $[Ru(NH_3)_6]Cl_3$/0.5 M KCl solution at an average scan rate of 0.025 V s^{-1}. 100

4.12 Plot of the maximum peak currents for different E_{centre} values using the semi-circular potential wave. Data were obtained for 0.265 mM $[Ru(NH_3)_6]Cl_3$/0.5 M KCl solution at 0.025 V s^{-1} from the corresponding experimental (correted for the capacitive current and the baseline, red speheres) and simulated (black diamonds) voltammograms. The formal potential estimated from the prior triangular voltammetry is indicated by the dashed blue line while the simulated potential of the maximum peak current calculated using the E_f^0 from the triangular wave voltammetry is indicated by the dash-dotted black line and the maximum peak current from the semi-circular experiment is indicated by the dotted red line. 102

5.1 A schematic representation of the two potential waves centrered at $\theta = 0$ with an amplitude of 1. The blue line corresponds to the linear wave and the orange line corresponds to the semi-circular wave. . . 114

5.2 Voltammetric response using linear and semi-circular potential waves at $\sigma = 10^3$ and $\theta_{shift} = 0$. The blue solid line represents the linear potential wave result and the orange solid line represents the semi-circular potential wave result. The blue-green solid horizontal line, the dark blue dash-dotted horizontal line, and the light blue dashed horizontal line represent the theoretical peak current of a reversible system at a microelectrode using a linear potential wave predicted by Equation (5.23), (5.24), and (5.25), respectively. The arrow indicates the direction of the sweep. 116

5.3 Voltammetric response using linear and semi-circular potential waves at $\sigma = 10^1$ and $\theta_{shift} = 0$. Further detail is provided in the caption of Figure 5.2. 117

5.4 Voltammetric response using linear and semi-circular potential waves at $\sigma = 10^{-1}$ and $\theta_{shift} = 0$. Further detail is provided in the caption of Figure 5.2. 118

5.5 Voltammetric response using linear and semi-circular potential waves at $\sigma = 10^8$ and $\theta_{shift} = 0$. Further detail is provided in the caption of Figure 5.2. 119

5.6 Voltammetric response using linear and semi-circular potential waves at $\sigma = 10^{-4}$ and $\theta_{shift} = 0$. Further detail is provided in the caption of Figure 5.2. 120

5.7 Voltammetric response using the semi-circular potential wave at $\sigma = 10^3$ with varying θ_{shift} values. A corresponds to $\theta_{shift} = -4$, B corresponds to $\theta_{shift} = -2$, C corresponds to $\theta_{shift} = -1$, D corresponds to $\theta_{shift} = 0$, E corresponds to $\theta_{shift} = 2$, and F corresponds to $\theta_{shift} = 4$. The arrows indicate the direction of the sweep. 122

5.8 Voltammetric response using the semi-circular potential wave at $\sigma = 10^1$ with varying θ_{shift} values. Further detail is provided in the caption of Figure 5.7. 124
5.9 Voltammetric response using the semi-circular potential wave at $\sigma = 10^{-1}$ with varying θ_{shift} values. Further detail is provided in the caption of Figure 5.7. 125
5.10 127

6.1 A schematic representation of the two potential waves centrered at $\theta = 0$ with an amplitude of 1. The blue line corresponds to the linear wave and the orange line corresponds to the semi-circular wave. . . 137
6.2 Dimensionless current responses using (a)linear potential waves and (b)semi-circular potential waves with various K_0 values and $\sigma = 3.89$ evaluated for $\theta_{shift} = 0$ and $\alpha = 0.5$. Each voltammogram is color-coded and the corresponding K_0 values are listed in the label and the arrow indicates the direction of the sweep. The graphs approach the irreversible limit (low K_0) towards the left and reversible limit (high K_0) towards the right. 139
6.3 Dimensionless current responses using (a) linear potential wave and (b) semi-circular potential wave with various K_0 values and $\sigma = 10^{-4}$. The pink dashed line represents the steady-state limiting flux predicted by Equation (6.22). Further detail is provided in the caption of Figure 6.2. 143
6.4 144
6.5 145
6.6 Dimensionless current responses using (a)linear potential wave and (b)semi-circular potential wave with various K_0 values and $\sigma = 0.389$. Further detail is provided in the caption of Figure 6.2. 147

7.1 A schematic representation of linear and semi-circular potential wave graphs centered at 0 with an amplitude of 20. The blue line corresponds to the linear wave and the green line corresponds to the semi-circular wave. Similar schematic representations are provided in Chapters 5 and 6. 157
7.2 Voltammograms plotted for various θ_{shift} values. A corresponds to $\theta_{shift} = 0$, B corresponds to $\theta_{shift} = 5$, C corresponds to $\theta_{shift} = 10$, and D corresponds to $\theta_{shift} = 15$. 158

7.3 Peak flux values plotted against varying θ_{shift} values at (a) $\sigma = 10^{-4}$ and (b) $\sigma = 10^{-5}$. The solid blue circular line represents the peak flux from the linear method, the solid light green triangular line represents the peak flux of the sharp peak from the semi-circular method, and the dashed orange triangular line represents the peak flux of the broad peak from said method. 160

7.4 Dimensionless current response using linear and semi-circular potential waves at $\theta_{shift} = 0$. The blue line represents the result from the linear wave while the green line represents the result from the semi-circular wave. The pink horizontal and vertical dashed lines are the peak current and peak potential values predicted from Equations (7.18) and (7.19). 162

7.5 (a) shows the change in dimensionless surface volume concentration of A and the ratio of A (7.20) with respect to potential. The blue solid line represents the surface volume concentration of A when a linear wave is applied and the green solid line represents the surface volume concentration of A when a semi-circular potential wave is applied. The light blue and light green dashed lines show the ratio of the surface volume concentration of A to the surface volume concentration of $A + B$ for the linear and semi-circular method, respectively, which perfectly overlap in (a). The arrow represents the direction of the sweep. (b) shows the change in dimensionless surface volume concentration of A and the ratio of A with respect to time. Note that for direct comparability, the time axis points to the left. The same color schemes are employed as in (a). 164

7.6 The two figures show the solution concentrations when (a) a linear potential wave is applied, and (b) a semi-circular potential wave is applied. The colorbar on the right hand side of the figure represents the dimensionless concentration. 166

A.1 Schematic representation of the effect of potential change on the standard Gibbs' energy of activation for a one-electron transfer process. 178

A.2 A comparison between voltammograms with and without capacitive perturbations at $\sigma = 10^6$ and $\theta_{shift} = 0$ for $C_{dl} = 20$ µF cm^{-2}. Each figure is labeled with the corresponding potential wave: A is for triangular, B is for cosine when $n = 1$, and C is when $n = 2$. The solid curves represent the dimensionless Faradaic current and the dashed curves represent the total current (Faradaic + capacitive). . 181

A.3 Capacitive current-corrected voltammograms obtained at GC electrode using (a) triangular, (b) cosine, (c) cosine square potential waves at scan rates from 0.025 to 2 V s^{-1} in 0.96 mM $[Ru(NH_3)_6]Cl_3$/0.10 M KCl solution at 298 K. 182
A.4 Capacitive current-corrected voltammograms obtained at GC electrode with (a) triangular, (b) cosine, and (c) cosine square potential waves at different E_{centre} values in 0.96 mM $[Ru(NH_3)_6]Cl_3$/0.10 M KCl solution at an average scan rate of 0.05 V s^{-1} at 298 K. 183
A.5 Steady-state voltammogram of an apoxy-coated carbon fibre (9 µm diameter, GoodFellow, U.K.) microelectrode in 1 mM $[Ru(NH_3)_6]Cl_3$/0.10 M KCl solution. 183
A.6 Peak flux of linear and semi-circular results plotted against $\log_{10}$ of the corresponding $\Delta\theta$ values at $\sigma = 10^4$. The blue dots represent results obtained using the linear potential wave and the orange diamonds represent results obtained using the semi-circular potential wave. 185
A.7 Figure (a) shows the voltammograms obtained using the semi-circular potential waves with vayring $\Delta\theta$ values and (b) shows the zoomed-up version of (a) to give a closer look near the singularity. 186
A.8 Full-scale figure of the voltammograms shown in Figure 4.2. 187
A.9 Full-scale figure of the voltammograms shown in Figure 4.3. 188
A.10 Full-scale figure of the voltammograms shown in Figure 4.5. 189
A.11 Full-scale figure of the voltammograms shown in Figure 4.7. 190
A.12 Peak flux plotted against $\log_{10}$ of the corresponding K_0 values used. 191
A.13 Voltammograms obtained using the semi-circular potential wave with varying K_0 values. 192
A.14 Peak flux of linear and semi-circular results plotted against $\log_{10}$ of the corresponding $\Delta\theta$ values with $\sigma = 3.89$ and $K_0 = 10^2$. The blue dots represent results obtained using the linear potential wave and the green diamond shapes represent results obtained using the semi-circular potential wave. 194
A.15 Peak flux of linear and semi-circular results plotted against $\log_{10}$ of corresponding h values with $\sigma = 3.89$ and $K_0 = 10^2$. The same color scheme as in Figure A.14 is used. 195
A.16 Peak flux of linear and semi-circular results plotted against corresponding ω values with $\sigma = 3.89$ and $K_0 = 10^2$. The same color scheme as in Figures A.14 and A.15 is used. 196

1 Introduction

This chapter reviews the fundamental concepts of electrochemistry and the electrochemical techniques essential to the understanding of this thesis.

Contents

1.1 Electrochemical Equilibrium 1
1.1.1 The Nernst Equation 2
1.1.2 Electrochemical Cell 4
1.2 Electrode Kinetics 6
1.3 Electrical Double Layer 8
1.4 Effect of Supporting Electrolyte 9
1.5 Mass Transport 10
1.5.1 Fick's First Law 10
1.5.2 Fick's Second Law 12
1.6 Faradaic and Non-Faradaic Processes 13
1.7 Electrode Size 13
1.8 Electrochemical Techniques 14
1.8.1 Cyclic and Linear-Sweep Voltammetry 15
1.8.2 Stripping Voltammetry 19

1.1 Electrochemical Equilibrium

Electrochemistry is the study of charge transfer across the solution/electrode interface involving electrons and/or ions. Consider a general one-electron reduction reaction of A to B:

$$A^{z_A}(aq) + e^- \rightleftharpoons B^{z_B}(aq) \tag{1.1}$$

where A is the oxidized species in solution denoted as (aq), e is the electron transferred from the electrode, B is the reduced species in solution, and the superscripts denote the corresponding charges of each species involved in the reaction. When an electrode is inserted into a solution containing both A and B, an electron transfer may occur between the electrode and the solution until an equilibrium is established at the electrode surface. At that point there will be a charge separation between the metal and solution phase resulting in a potential difference, which is denoted as $\phi_M - \phi_S$.

1.1.1 The Nernst Equation

In addition to having a charge separation, at equilibrium, the chemical potential and electrical energies - henceforth called the electrochemical potential with the symbol $\bar{\mu}$ ([J mol^{-1}]) - must be balanced between the reactant and product. The electrochemical potential of species j is:

$$\bar{\mu_j} = \mu_j + z_j F \phi_j \tag{1.2}$$

where μ and z are the chemical potential ([J mol^{-1}]) and the charge of species j, respectively, F is the Faraday constant ([96487 C mol^{-1}]) corresponding to the charge of one mole of electrons, and ϕ is the potential ([V]) of the phase in which the species is found, i.e. electrode or solution. The chemical potential is related to the standard chemical potential, μ_j^0, measured at unit activity and standard temperature:

$$\mu_j = \mu_j^0 + RTln(a_j) \tag{1.3}$$

where R is the universal gas constant ([8.3145 J K^{-1} mol^{-1}]), T is the temperature ([K]), and a is the activity of species j. At equilibrium the sum of the electrochemical potentials of the species on each side of an equilibrium must be equal:

$$\bar{\mu_A} + \bar{\mu_{e^-}} = \bar{\mu_B} \tag{1.4}$$

and substituting Equation (1.2) in (1.4) yields:

$$(\mu_A + z_A F\phi_S) + (\mu_{e^-} - F\phi_M) = (\mu_B + z_B F\phi_S) \tag{1.5}$$

From conservation of charge and from Equation (1.3), Equation (1.5) can be rewritten in terms of the potential difference between the metal and solution phase with respect to the standard chemical potential:

$$\phi_M - \phi_S = \frac{1}{F}(\mu_A^0 + \mu_{e^-} - \mu_B^0) + \frac{RT}{F} ln\left(\frac{a_A}{a_B}\right) \tag{1.6}$$

The left hand side of the equation is the potential drop at a single electrode/solution interface. If the interfacial potential drop, $\phi_M - \phi_S$, at the electrode of interest is measured relative to a reference electrode (1.1.2) then Equation (1.6) becomes Equation (1.7):

$$E = E^0 + \frac{RT}{F} ln\left(\frac{a_A}{a_B}\right) \tag{1.7}$$

where E is the potential of the interface measured relative to the reference potential and E^0 is the standard potential of the redox couple A/B measured against the same reference electrode. In practice, however, it is more convenient to consider the concentrations of the analyte rather than their activities and hence the following term is used to relate the activity of species to its concentration in solution phase:

$$a_j = \gamma_j c_j \tag{1.8}$$

in which γ is the activity coefficient of species j. From Equation (1.8), Equation (1.7) can now be expressed in terms of the formal potential of the A/B redox couple and their concentrations (now written in the form, $[j]$), known as the Nernst equation [1]:

$$E = E_f^0 + \frac{RT}{F} ln\left(\frac{[A]}{[B]}\right) \tag{1.9}$$

where

$$E_f^0 = E^0 + \frac{RT}{F} ln \left(\frac{\gamma_A}{\gamma_B} \right) \tag{1.10}$$

which shows that the formal potential incorporates the standard electrode potential and the activity coefficients.

1.1.2 Electrochemical Cell

As discussed in Section 1.1.1, the value of $(\phi_M - \phi_S)$ must be measured relative to a secondary electrode known as the reference electrode. The reason for this is that the measurement of such quantities require a closed circuit and thus at least two electrodes are necessary as shown in Figure 1.1. The measured value is therefore the difference:

$$\text{Potential difference} = (\phi_M - \phi_S)_{electrode1} + IR - (\phi_M - \phi_S)_{electrode2} \tag{1.11}$$

Electrode 1 is where the redox reaction of interest is observed and is called the working electrode (WE). Electrode 2 is the reference electrode which is at equilibrium and has a a well-defined and stable potential. Commonly used reference electrodes (RE) are the *SHE* (standard hydrogen electrode), the *SCE* (saturated calomel electrode), and the *silver/silver chloride* electrode. Their respective potential determining equilibrium are given in Equations (1.12), (1.13), and (1.14).

$$H^+(aq) + e^-(m) \rightleftharpoons \frac{1}{2} H_2(g) \tag{1.12}$$

$$\frac{1}{2} Hg_2Cl_2(s) + e^-(m) \rightleftharpoons Hg(l) + Cl^-(aq) \tag{1.13}$$

$$AgCl(s) + e^-(m) \rightleftharpoons Ag(s) + Cl^-(aq) \tag{1.14}$$

The key feature of a reference electrode is that it possesses a constant makeup in order to ensure a fixed potential, $(\phi_M - \phi_S)_{ref}$, is provided throughout the measurement. The IR term is known as the Ohmic drop, which is the electrical resistance

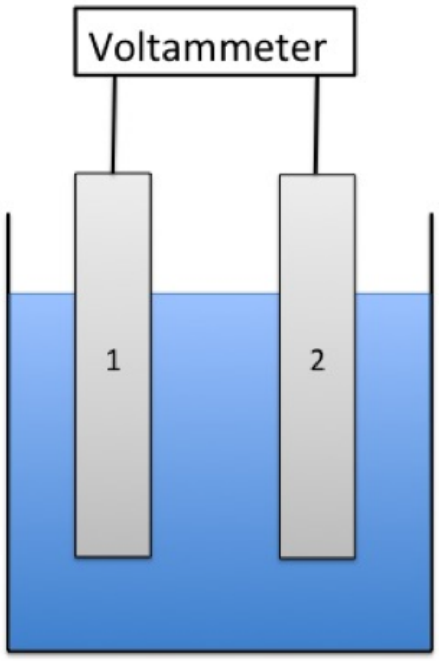


Figure 1.1: Schematic representation of a two electrode setup. The electrodes are labelled 1 and 2 to represent the working and reference electrodes, respectively.

of the bulk solution between the working and reference electrode. When the passing current at the reference electrode is negligible [2], the IR term can be discarded.

The setup presented in Figure 1.1 is for measuring the electrode potential when the system is at electrochemical equilibrium and thus no external potential is applied to the working electrode and no steady current flows. When performing electrochemical analysis, however, the potential of the working electrode is altered through an external power supply and inevitably requires an appreciable amount of current to pass. Therefore a third electrode called the counter (or auxiliary) electrode (CE) is required. In an electrochemical experiment, a potentiostat is used to apply a fixed potential E between the working and reference electrodes which induces a current flow through the former whilst ensuring no current flows through the latter. The role of a CE is to pass the same amount of current as the WE to ensure the RE produces a stable and reliable potential and to avoid Ohmic drop. Without a CE, current may flow through RE causing a shift in the equilibrium

in accordance with the Nernst equation, which in turn would change the value of $(\phi_M - \phi_S)_{RE}$. Additionally, the IR changes with respect to the applied potential E in an unknown fashion as does the $(\phi_M - \phi_S)_{WE}$ and hence $(\phi_M - \phi_S)_{WE}$ would no longer be controlled. Inert materials such as a platinum wire or disk are commonly used as a counter electrode with a sufficiently large surface area in order to ensure the reaction at CE does not interfere with those occurring at WE [3].

1.2 Electrode Kinetics

So far the focus of the discussion has been on a system in electrochemical equilibrium. The Nernst equation relates the electrode potential to the concentration of analytes at the electrode surface and is only applicable when the rate of electron transfer is fast to establish a thermodynamic equilibrium. Therefore the effect of electrode kinetics on the electrochemical reaction at the interface must further be considered. Referring back to the one-electron reduction reaction in Equation (1.1), the forward and backward rate constants are k_{red} and k_{ox} respectively. According to the rate law, the forward and backward rate of reaction is:

$$j_{red} = k_{red}[A]_0 \tag{1.15}$$

$$j_{ox} = k_{ox}[B]_0 \tag{1.16}$$

where $[A]_0$ and $[B]_0$ represent the surface concentrations of A and B, respectively, which differ from the bulk concentration due to the redox reaction occuring at the electrode surface. The net rate (flux) of the reaction is given as:

$$j_{net} = j_{red} - j_{ox} \tag{1.17}$$

which gives the net rate of the heterogeneous electrochemical reaction at the interface. Given that current is proportional to the rate of charge passed, it can be related to j_{net} ([mol cm^{-2} s^{-1}]) via the following expression:

$$I_{net} = -FA_{ele}j_{net} \tag{1.18}$$

where F is again, the Faraday constant and A_{ele} is the area of the electrode. Based on the Butler-Volmer model given in Equation (1.19), the rate constants can be rewritten as a function of the applied potential, E, as shown in Equations (1.20) and (1.21). A full discussion on the derivation of the Butler-Volmer expression is provided in *Appendix*: A.1.

$$j_{net} = k_0 exp\left[\frac{-\alpha F}{RT}(E - E_f^0)\right][A]_0 - k_0 exp\left[\frac{\beta F}{RT}(E - E_f^0)\right][B]_0 \tag{1.19}$$

$$k_{red} = k_0 exp\left[\frac{-\alpha F}{RT}(E - E_f^0)\right] \tag{1.20}$$

$$k_{ox} = k_0 exp\left[\frac{\beta F}{RT}(E - E_f^0)\right] \tag{1.21}$$

k_0 is the standard electrochemical rate constant ([cm s^{-1}]) and α and β are the electrochemical transfer coefficients such that $\alpha + \beta = 1$ for a one-electron transfer reaction. The transfer coefficients indicate the transition state between reactants and products [4, 5] such that if α is close to zero, the transition state resembles the reactant whereas if α is close to one, the transition state resembles the product. $(E - E_f^0)$ is called the overpotential (often represented by the Greek letter η) and is the driving force for the redox reaction where a negative overpotential favors a reduction and a positive overpotential favors an oxidation reaction. k_0 provides information on the kinetics of the reaction. High k_0 results in fast reaction while low k_0 results in slow reaction requiring a larger overpotential to drive the reaction. Combining Equations from (1.15) to (1.21) produces the expression for the net current as a function of the applied potential:

$$I_{net} = -FA_{ele}k_0\left(exp\left[\frac{-\alpha F}{RT}(E - E_f^0)\right][A]_0 - exp\left[\frac{\beta F}{RT}(E - E_f^0)\right][B]_0\right) \tag{1.22}$$

An important feature to note from Equation (1.22) is the fact that at high k_0 values, the expression collapses to the Nernst equation. A system with fast kinetics establishes a dynamic equilibrium which yields a zero net current.

1.3 Electrical Double Layer

This section discusses the concept of the electrical double layer, which describes the capacitor-like behavior at the electrode/solution interface. When a positive voltage is applied at the working electrode, the electrode experiences a deficit of electrons and vice versa with a negative voltage. This charge build-up forces the nearby electrolyte ions to reorient themselves in order to maintain electroneutrality.

The idea of an electrical double layer was first introduced by Helmholtz in the 1850's [6] and the 1870's [7], who proposed that oppositely charged ions build up on the electrode surface as a monolayer. In the Helmholtz model, the layer immediately adjacent to the electrode is the solvation layer comprised of water molecules. Next to the solvation layer is the solvated ions with charges opposite to that of the electrode, and the distance between the electrode surface and the inner radius of the solvated ions is known as the "Outer Helmholtz Plane" (OHP). In this model the potential between the electrode surface and the OHP drops linearly with distance.

The Helmholtz model was later revised by Gouy [8] and Chapman [9] independently in the 1910's. While the Helmholtz model predicts that the ions behave as a sheet on the electrode surface, the Gouy-Chapman model postulates that the ions are distributed near the electrode within the "diffuse double layer", and that the potential difference between the electrode and the edge of the diffuse layer falls off approximately exponentially.

The most widely accepted model is the Stern-Grahame model [10, 11] that combines the Helmholtz and Gouy-Chapman model in which the OHP and diffuse layer coexist. Depending on the chemical identity of the ions, they can replace the solvent molecules and adsorb to the electrode surface. The distance between the electrode and the centre of the adsorbed ion is termed the "Inner Helmholtz Layer" (IHP). In this model, the potential drops linearly between the electrode surface and

OHP, and then decreases approximately exponentially throughout the diffuse layer. A schematic representation of the Stern-Grahame model is given in Figure 1.2.

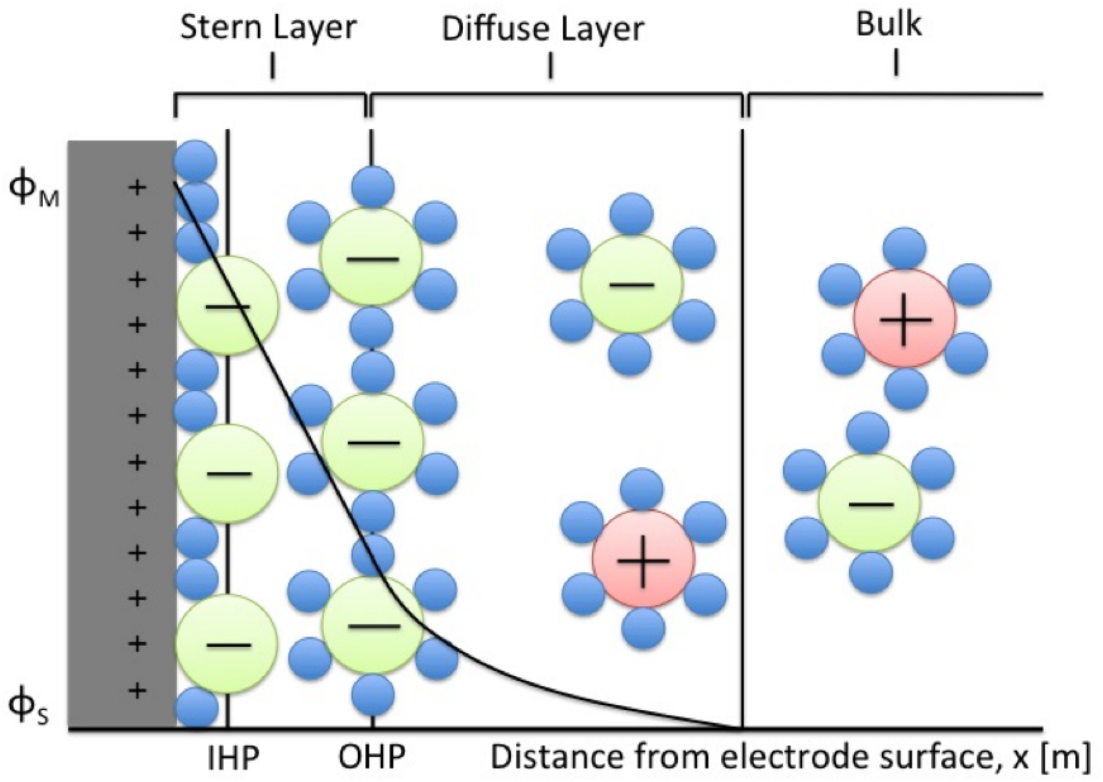


Figure 1.2: Schematic representation of the Stern-Grahame model depicting the double layer and the potential drop ($\phi_M - \phi_S$) as a function of distance from the electrode. The green, pink, and blue circles represent the anions, cations, and solvent molecules, respectively.

1.4 Effect of Supporting Electrolyte

From the discussion above, the importance of supporting electolyte can be understood. Electron transfer between the electrode and species in solution occurs via quantum mechanical tunnelling which takes place over a distance of *ca.* 10-20 Å from the electrode surface and thus the potential drop between ϕ_M and ϕ_S must be confined within this distance if the electron transfer is to be "fully driven". For this purpose, it is common practice to use high concentrations of supporting electrolyte and all the models discussed in this thesis are reported under the assumption that excess supporting electrolyte is present in the solution. Furthermore, excess

supporting electrolyte ensures high solution conductivity which reduces the Ohmic drop effect [3] and minimizes migration [12–16].

1.5 Mass Transport

This section explores the modes of mass transport, which describes the movement of molecules. There are three modes of mass transport: diffusion, migration, and convection. Migration refers to the movement of charged particles through an interaction with an external electric field and convection refers to the movement of molecules caused by an external force such as stirring. In this thesis, all models are reported under the assumption that diffusion is the only means of mass transport and so the discussion will focus solely on the mathematics of diffusion. Further discussion of migration and convection can be found in literature [2, 16–18].

Diffusion is caused by the difference in concentration between the electrode surface and the bulk solution where molecules move from a zone with higher concentration to a zone with lower concentration. The model of diffusion is described by Fick's First and Second Laws in which the former relates the change in concentration with respect to space, and the latter predicts the change in concentration with respect to time.

1.5.1 Fick's First Law

When a potential is applied to a working electrode and an electrochemical reaction takes place, the concentration of analyte changes with respect to space to produce a concentration gradient. Due to this gradient, a diffusive flux will be observed at every spatial point, x, as given by Fick's First Law:

$$j = -D\frac{\partial c}{\partial x} \tag{1.23}$$

where j is the number of moles of analyte passing through a unit area at a given time with units ([mol m^{-2} s^{-1}]) - henceforth referred to as the flux. D is the diffusion coefficient of the species passing with units ([cm^2 s^{-1}]) and $\frac{\partial c}{\partial x}$ is the local concentration gradient at point x. The nature of Fick's First Law can be understood

from a molecular basis by considering Figure 1.3 where a box is divided into two parts at an arbituary spatial point x, each with a width δx and a cross sectional area A_{cs}.

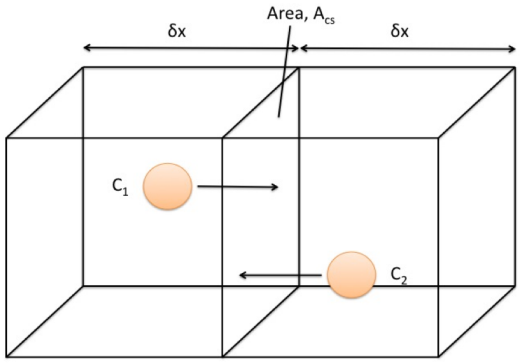


Figure 1.3: Schematic representation of the molecular basis of Fick's First Law.

Assuming that the molecules in either of the parts are equally likely to move into either direction and that each molecule moves δx per δt on average, the number of moles moving from left to right and right to left can be expressed as $\frac{1}{2}c_1 A_{cs}\delta x$ and $\frac{1}{2}c_2 A_{cs}\delta x$, respectively. The net rate of the movement of molecules within the box is thus:

$$Rate_{net} = \frac{(c_1 - c_2)A_{cs}\delta x}{2\delta t} \tag{1.24}$$

$\frac{\partial c}{\partial x}$ can be approximated as $-\frac{(c_1-c_2)}{\delta x}$, which gives $(c_1 - c_2) \approx -\delta x \frac{\partial c}{\partial x}$. Equation (1.24) can hence be rewritten in the form:

$$Rate_{net} \approx -\frac{A_{cs}(\delta x)^2}{2\delta t}\left(\frac{\partial c}{\partial x}\right) \tag{1.25}$$

Dividing Equation (1.25) by the area gives the rate density, which is equal to the flux:

$$j = -\frac{(\delta x)^2}{2\delta t}\left(\frac{\partial c}{\partial x}\right) \tag{1.26}$$

and assuming $D = \frac{(\delta x)^2}{2\delta t}$ Fick's First Law of diffusion is obtained. It is clear that the diffusion coefficient provides the distance the molecule travels within a given time. The root mean square displacement, x ([m]), in time, t ([s]), is expressed as [2]:

$$\sqrt{\langle x^2 \rangle} = \sqrt{2Dt} \tag{1.27}$$

From Equation (1.27), the thickness of the diffusion layer - the region in which analytes are depleted - can be estimated. The diffusion layer grows with time for example from 31.6 to 100 µm between $t = 1$ s and $t = 10$ s if $D = 5 \cdot 10^{-10}$ m^2 s^{-1} and this requires materials to diffuse from a further distance to reach the tunnelling distance (10-20 Å) so as to react at the electrode. It is important to recognize that the diffusion layer ranges approximately between 10-100 µm for typical voltammetric timescales whilst the diffuse layer ranges roughly between 10-100 Å depending on the electrolyte concentration [2]. As explained in Section 1.4, this must be confined to within 10-20 Å so that the full driving force $(\phi_M - \phi_S)$ is available for the electrode reaction.

1.5.2 Fick's Second Law

Given Fick's First Law of diffusion, Fick's Second Law can be derived, which predicts the rate of change in concentration with respect to time at a specific spatial point x. Consider a slab with thickness δx and cross sectional area A_{cs}. Assuming that flux enters through x and leaves from $x + \delta x$ over some time δt, the change in number of molecules, δn in one-dimension is:

$$\delta n = [j(x) - j(x + \delta x)]A_{cs}\delta t \tag{1.28}$$

Based on the conservation of mass, the change in concentration within the volume of the box over time must equal the change in the number of molecules in the slab giving:

$$[c(t + \delta t) - c(t)]A_{cs}\delta x = [j(x) - j(x + \delta x)]A_{cs}\delta t \tag{1.29}$$

which can be rearranged to give the form:

$$\frac{\partial c}{\partial t} = -\frac{\partial j}{\partial x} \tag{1.30}$$

Substituting Equation (1.23) provides Fick's Second Law, which shows that the change in concentration over time is proportional to the derivative of the flux:

$$\frac{\partial c}{\partial t} = D\frac{\partial^2 c}{\partial x^2} \tag{1.31}$$

1.6 Faradaic and Non-Faradaic Processes

The current produced as a result of applied potential is comprised of two types of processes: Faradaic and non-Faradaic. Faradaic processes involve the transfer of electrons across the metal/solution interface and are thus the result of redox processes. In a Faradaic process, current is related to the flux of the species undergoing electrolysis:

$$I_{net} = FAj \tag{1.32}$$

In Section 1.2, the current was expressed in terms of the net rate of the forward and backward reaction. Equations (1.18) and (1.32) thus yield the relationship:

$$j = -j_{net} \tag{1.33}$$

A non-Faradaic process arises when charge accumulates at the interface and hence does not involve any electron transfer between the metal and solution. As discussed in Section 1.3, upon application of potential, a charge separation is created between the electrode and the solution (double layer) that acts like a capacitor and produces what is known as a capacitive current. The capacitive current is proportional to the scan rate:

$$I_c = A_{ele} C_{dl} \frac{dE}{dt} = A_{ele} C_{dl} \nu \tag{1.34}$$

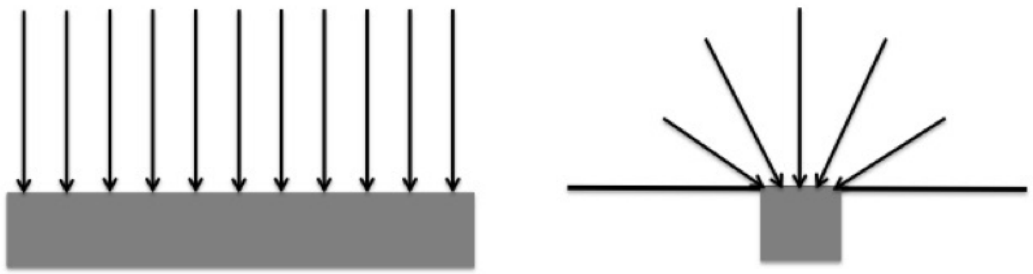
where I_c is the capacitive current ([A]), C_{dl} is the double layer capacitance typically between the ranges of 10 - 40 µF cm^{-2} [19], and $\frac{dE}{dt} = \nu$ which is the scan rate ([V s^{-1}]). From Equation (1.34), it is clear that the capacitive current increases with increasing scan rate.

1.7 Electrode Size

The size of the working electrode used in electrochemical experiments are categorized into two types according to their sizes: macroelectrodes and microelectrodes.

Depending on the size, different mass transport behaviors are observed at the electrode surface. Macroelectrodes, which typcially have dimensions of a millimeter in radius, are much larger than the diffusion layer thickness. As a result, the flux approches the electrode perpendicularly and uniformly across the entire surface and are said to be "uniformly accessible".

Microelectrodes refer to electrodes on the scale of a micrometer and are described as "non-uniformly accessible". Since the electrode size is comparable to the diffusion layer thickness, the flux is no longer uniform across the surface. At the edge of the electrode, convergent mass transport is observed and, at steady-state, produces a hemispherical diffusion layer. Some of the key features of a microelectrode include enhanced mass transport, reduced ohmic drop, and reduced capacitance. When voltammograms are recorded at sufficiently slow scan rates, the mass transport becomes efficient and establishes a steady-state. Throughout this thesis, planar macro and micro electrodes are considered, and Figure 1.4 shows the two modes of diffusion.



(a) Linear diffusion. **(b)** Convergent diffusion.

Figure 1.4: Schematic representation of (a) linear diffusion at a macroelectrode and (b) convergent diffusion at a microelectrode.

1.8 Electrochemical Techniques

This section introduces the major methodologies used for electrochemical analysis which are used throughout this thesis. In particular, cyclic and linear voltammetry at macro- and microdisc electrodes are discussed followed by stripping voltammetry.

1.8.1 Cyclic and Linear-Sweep Voltammetry

Cyclic voltammetry (CV) and linear-sweep voltammetry (LSV) are the most widely used electroanalytical techniques to study redox processes. In conventional cyclic voltammetry, a triangular potential wave is applied at the working electrode from an initial potential, E_1 to a reverse potential, E_2, and back to E_1 as in Figure 1.5. The slope of the wave gives the scan rate, ν ([V s^{-1}]), which is the rate at which the potential changes.

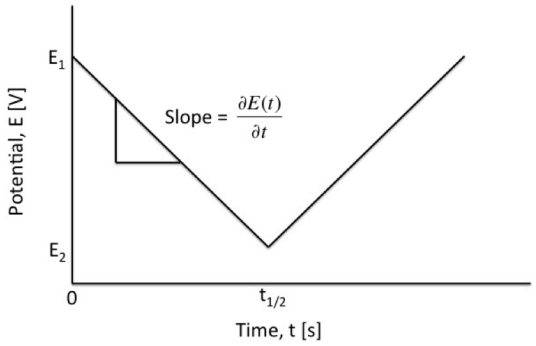
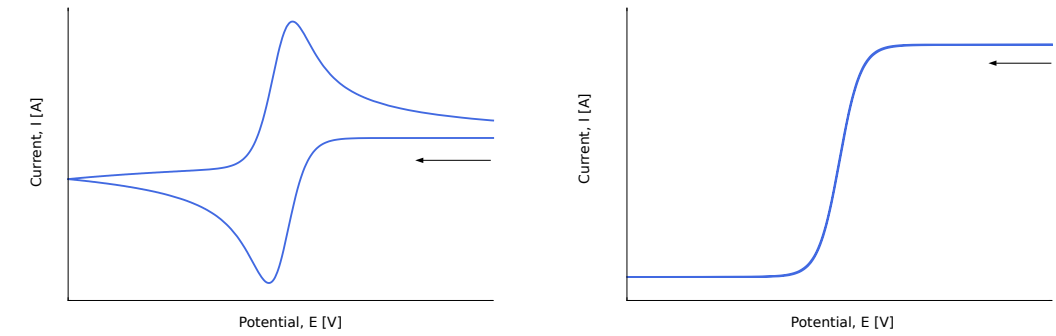


Figure 1.5: Schematic representation of a triangular potential wave.

Mathematically, the triangular wave is given as:

$$E(t) = \begin{cases} \pm\nu t + E(t=0) & \text{for} \quad t < t_{1/2} \\ \mp\nu(t - t_{1/2}) + E(t = t_{1/2}) & \text{for} \quad t \geq t_{1/2} \end{cases} \tag{1.35}$$

where the $\pm$ and $\mp$ signs indicate oxidation or reduction. In LSV, only the forward sweep is considered. The window is chosen in a manner such that the desired redox process occurs between E_1 and E_2 and the resulting current is measured against the applied potential to produce a voltammogram. Typical voltammograms obtained from a macro and a microdisc electrode are shown in Figure 1.6(a) and Figure 1.6(b), respectively, for a simple one-electron transfer process such as in Equation (1.1). Figure 1.6(b) shows a voltammogram obtained at a microelectrode using a slow scan rate to produce a steady-state current.

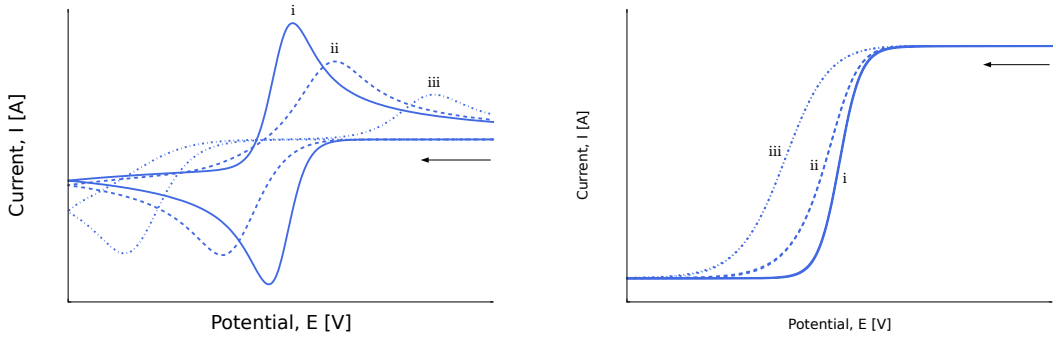


(a) **(b)**

Figure 1.6: Schematic representation of voltammetric response at (a) a macrodisc electrode and (b) a microdisc electrode. In (b), the steady-state response is shown.

Reversible vs Irreversible Kinetics

In Section 1.2, the concept of "fast electron transfer" was introduced. In order to understand voltammograms in more depth, the relative term "fast" must be defined in relation to reaction rates, which lead to the concept of "reversible" and "irreversible" processes. Figures 1.7(a) and 1.7(b) show a schematic representation of voltammograms obtained at three different k_0 values at a macro and microdisc electrode, respectively, for a one-electron transfer process. In both figures, (i) corresponds to reversible, (ii) corresponds to quasi-reversible, and (iii) corresponds to irreversible kinetics.



(a) **(b)**

Figure 1.7: Schematic representation of voltammetric responses at (a) a macrodisc electrode and (b) a microdisc electrode. In both figures, (i) corresponds to reversible, (ii) corresponds to quasi-reversible, and (iii) corresponds to irreversible systems.

The reversibility of a system is measured by the rate constant, k_0, relative to

the mass transport coefficient given as:

$$m_T = \frac{D}{\delta} \tag{1.36}$$

where δ is the diffusion layer thickness, which is dependent on time as shown through Equation (1.27). The scan time, t ([s]), is defined as:

$$t \sim \frac{RT}{F\nu} \tag{1.37}$$

and hence the mass transport coefficient for a cyclic voltammetric experiment at a macroelectrode is:

$$m_T \sim \sqrt{\frac{FD}{RT}\nu} \tag{1.38}$$

From the above relations, "fast" and "slow" electrode kinetics is expressed as:

$$k_0 >> m_T \text{ (reversible)} \tag{1.39}$$

$$k_0 << m_T \text{ (irreversible)} \tag{1.40}$$

In 1955, Matsuda and Ayabe [20] introduced a parameter, Λ, to differentiate between reversible, quasi-reversible, and irreversible processes at a macroelectrode based on the ratio of the rate constant to the mass transport coefficient:

$$\Lambda = \frac{k_0}{\sqrt{\frac{FD}{RT}\nu}} \tag{1.41}$$

in which the following classifications are available for stationary macroelectrodes:

Reversible: $\Lambda \geq 15, \quad \Lambda \geq 0.3\sqrt{\nu} \quad \text{cm s}^{-1}$ (1.42)

Quasi-reversible: $15 > \Lambda > 10^{-3}, \quad 0.3\sqrt{\nu} > k_0 > 2 \times 10^{-5}\sqrt{\nu} \quad \text{cm s}^{-1}$ (1.43)

Irreversible: $\Lambda \leq 10^{-3}, \quad k_0 \leq 2 \times 10^{-5}\sqrt{\nu} \quad \text{cm s}^{-1}$ (1.44)

Apart from the Matuda-Ayabe classification, the reversibility of a macroelectrode system can be determined through the voltammogram via the peak-to-peak separation. Each voltammogram in Figure 1.7(a) shows a peak in the forward and reverse direction and the potential difference between these two peaks, ΔE_{pp}, gives an indication of the reaction kinetics. For a reversible process, a ΔE_{pp} of approximately 57 mV (at 298 K) is recorded and becomes increasingly larger with decreasing k_0 as the system approaches the irreversible limit.

For steady-state voltammograms recorded using a microelectrode such as those in Figure 1.7(b), the slope and position of the curve changes with respect to k_0. The quartile potentials, $E_{1/4}$ and $E_{3/4}$ (indicated in Figure 1.8) provide means to determine the kinetic parameters through tables reported by Mirkin and Bard [21].

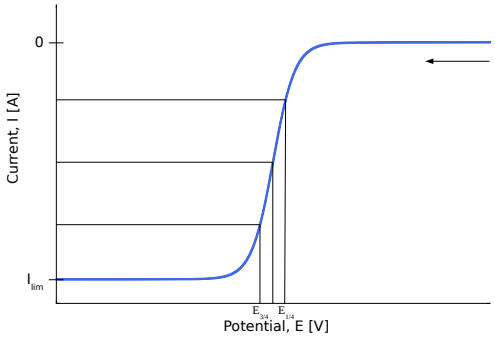


Figure 1.8: Schematic representation of a steady-state voltammograms with quartile potentials.

Effect of Scan Rate

The voltammetric responses recorded at both, macro and microelectrodes show scan rate dependencies. For a one-electron transfer reaction recorded at a macroelectrode, the forward peak is proportional to the square root of the scan rate and is expressed through the Randles-Ševčík equation [22, 23]:

$$I_p = -0.446FA_{ele}c_A^*\sqrt{\frac{FD_A\nu}{RT}} \tag{1.45}$$

$$I_p = -0.496\sqrt{\alpha}FA_{ele}c_A^*\sqrt{\frac{FD_A\nu}{RT}} \tag{1.46}$$

where Equations (1.45) and (1.46) correspond to the reversible and irreversible one electron transfer processes, respectively. An important feature to note is that for a reversible process, the scan rate does not affect the potential at which the peak currents occur such as shown in Figure 1.9(a) whereas in quasi-reversible and irreversible processes, increasing the scan rate increases the peak-to-peak separation according to the following expression [2]:

$$\Delta E_{pp} = \frac{RT}{\alpha F} ln(\nu) + C \quad \text{mV} \tag{1.47}$$

where C is a constant.

Meanwhile voltammograms recorded at a microelectrode behave more and more like that recorded at a macroelectrode with increasing scan rate such as shown in Figure 1.9(b) where a forward and reverse peak are observed at high scan rates. When the scan duration time is short, the diffusion layer is essentially planar and thus the system acts diffusionally as a macroelectrode.

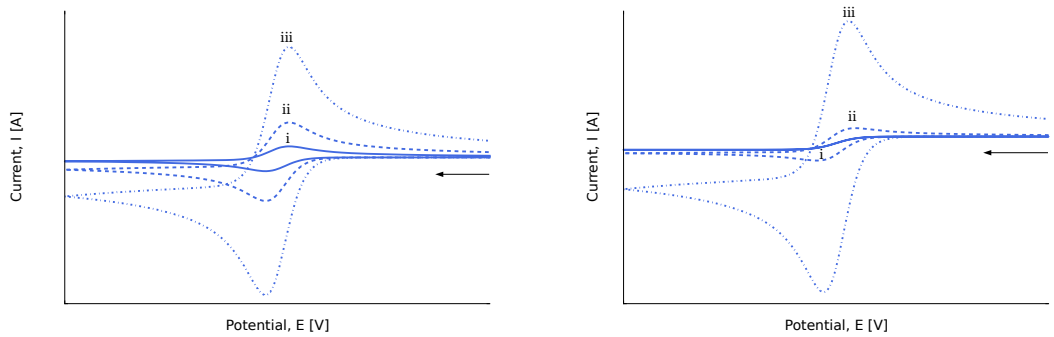


Figure 1.9: Schematic representation of voltammetric response of an electrochemically reversible one-electron transfer reaction at (a) a macrodisc electrode and (b) a microdisc electrode. In both figures, (i) corresponds to slow scan rate, (ii) corresponds to relatively fast scan rate, and (iii) corresponds to fast scan rate.

1.8.2 Stripping Voltammetry

An important technique widely employed in electroanalysis, which is used for the detection of metals, metal complexes [24, 25] and organic substances [26, 27] at low concentrations [2, 28], is stripping voltammetry and can be categorized into

three main techniques: anodic stripping voltammetry (ASV), cathodic stripping voltammetry (CSV), and adsorptive stripping voltammetry (AdSV). All three methodologies involve a "pre-concentration step" in which the analyte is accumulated on the electrode surface followed by the stripping step in which the measurement is recorded. In ASV, the target species is electrodeposited via an application of a negative potential to produce an amalgam or a metallic layer [29, 30] while in CSV, the metal ion analytes are oxidized to form a layer of metal oxides on the electrode surface [31]. In contrast, in AdSV, the pre-concentration step occurs via a non-electrolytic process [32] through the adsorption of molecules on the surface of the electrode. Examples of the pre-concentration reactions of the three methods are the following [2]:

$$\text{ASV:} \quad M^{n+}(aq) + ne^- \rightarrow M(electrode) \tag{1.48}$$

$$\text{CSV:} \quad 2M^{2+}(aq) + mH_2O \rightarrow M_2O_m(electrode) + 2mH^+ + 2(m-n)e^- \tag{1.49}$$

$$\text{AdSV:} \quad A(aq) \rightarrow A(ads) \tag{1.50}$$

After the pre-concentration step, the potential is swept so as to reverse the accumulation process causing the materials to be "stripped" from the electrode and produces a current response where the stripping charge is directly proportional to the amount of species pre-concentrated on the electrode which in turn is related to the amount of analyte in solution. A schematic representation of a CSV for an electrochemically reversible one electron transfer reaction is shown in Figure 1.10 for the following reaction:

$$A\,(ads) + e \rightleftharpoons B\,(sol) \tag{1.51}$$

The peak current [33–36] and peak position [35] are given by the following equations, respectively:

$$I_p = 0.2975nFA_{ele}\sigma' dc_A^* \tag{1.52}$$

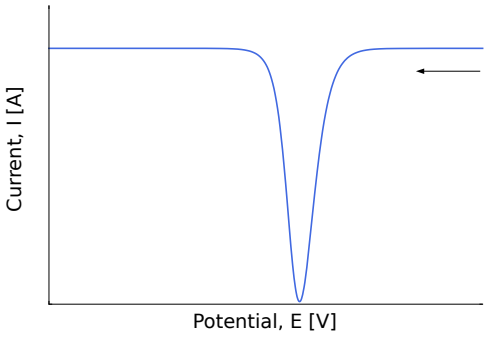


Figure 1.10: Schematic representation of CSV for an electrochemically reversible one-electron transfer process.

$$n(E_p - E_f^0) = -1.43 + 12.85ln\left(\frac{d^2\sigma'}{D_B}\right) \tag{1.53}$$

where n is the number of electrons involved in reaction (here, $n = 1$), $\sigma' = \frac{nF}{RT}\nu$, d is the thickness of the film, c_A^* is the initial volume concentration of species A in the film, and D_B is the diffusion coefficient of species B. The current response of a stripping voltammetry differs from that of LSV (where the reactant and product are both diffusive) in that the current starts from zero and following the reduction/oxidation peak, the current returns to zero. This is due to the fact that the reactants are adsorbed to the electrode and thus all species react during electrolysis causing the concentration gradient at the interface to fall off to zero after a certain time. In contrast, in LSV, more reactants can continuously diffuse from the bulk and hence a concentration gradient always exists at the electrode surface.

The analysis of a stripping voltammetry curve focuses on the area under the curve which gives the amount of charge, Q ([C]), passed, and from that information the initial surface concentration, c_A^s ([mol m^{-2}]), deposited on the electrode can be determined via Faraday's Law:

$$c_A^s = \frac{Q}{nFA_{ele}} = \frac{\int_0^{t_{max}} Idt}{nFA_{ele}} \tag{1.54}$$

where $n = 1$ in this particular example. Calibration plots are often used to relate c_A^s to the concentration of analyte in solution.

References

[1] C. G. Zoski, *Handbook of Electrochemistry*, Elsevier, **2007**.

[2] R. G. Compton, C. E. Banks, *Understanding Voltammetry*, Imperial College Press, **2010**.

[3] N. Elgrishi, K. J. Rountree, B. D. McCarthy, E. S. Rountree, T. T. Eisenhart, J. L. Dempsey, *Journal of Chemical Education* **2018**, *95*, 197–206.

[4] R. Guidelli, R. G. Compton, J. M. Feliu, E. Gileadi, J. Lipkowski, W. Schmickler, S. Trasatti, **2014**, *86*, 259–262.

[5] R. Guidelli, R. G. Compton, J. M. Feliu, E. Gileadi, J. Lipkowski, W. Schmickler, S. Trasatti, **2014**, *86*, 245–258.

[6] H. Helmholtz, *Ann. Phys.* **1853**, *165*, 211–233.

[7] H. Helmholtz, *Ann. Phys.* **1879**, *243*, 337–382.

[8] G. Gouy, *J. Phys. Theor. Appl.* **1910**, *9*, 457–468.

[9] D. L. Chapman, *Philos. Mag.* **1913**, *25*, 475–481.

[10] O. Stern, *Elektrochem.* **1924**, *30*, 508–516.

[11] D. C. Grahame, *Chem. Rev.* **1947**, *41*, PMID: 18895519, 441–501.

[12] D. H. Evans, K. M. O'Connell, R. A. Petersen, M. J. Kelly, *Journal of Chemical Education* **1983**, *60*, 290.

[13] C. Amatore, A. Oleinick, I. Svir, *Analytical Chemistry* **2008**, *80*, 7947–7956.

[14] S. Ching, R. Dudek, E. Tabet, *Journal of Chemical Education* **1994**, *71*, 602.

[15] J. Heinze, *Angewandte Chemie International Edition in English* **1984**, *23*, 831–847.

[16] A. J. Bard, L. R. Faulkner, *Electrochemical Methods: Fundamentals and Applications*, John Wiley & Sons Inc, **2000**.

[17] C. M. A. Brett, A. M. O. Brett, *Electrochemistry : Principles, Methods, and Applications*, Oxford University Press, **1993**.

[18] F. Scholz, *Electroanalytical Methods*, Springer-Verlag Berlin Heidelberg, **2010**.

[19] J. Wang, *Analytical Electrochemistry*, John Wiley & Sons Inc., **2001**.

[20] H. Matsuda, Y. Ayabe, *Zeitschrift für Elektrochemie Berichte der Bunsengesellschaft für physikalische Chemie* **1955**, *59*, 494–503.

[21] M. V. Mirkin, A. J. Bard, *Analytical Chemistry* **1992**, *64*, 2293–2302.

[22] J. E. B. Randles, *Trans. Faraday Soc.* **1948**, *44*, 327–338.

[23] A. Ševčík, *Collect. Czech. Chem. Commun.* **1948**, *13*, 349–377.

[24] J. Barón-Jaimez, M. R. Joya, J. Barba-Ortega, *Journal of Physics: Conference Series* **2013**, *466*, 012023.

[25] T. A. O'Shea, K. H. Mancy, *Analytical Chemistry* **1976**, *48*, 1603–1607.

[26] M. Iwamoto, R. Osteryoung, *Journal of Electroanalytical Chemistry and Interfacial Electrochemistry* **1984**, *169*, 181–194.

[27] T. Florence, *Journal of Electroanalytical Chemistry and Interfacial Electrochemistry* **1979**, *97*, 219–236.

[28] S. Otles, *Handbook of Food Analysis Instruments*, CRC Press, **2009**.

[29] G. Herzog, D. W. M. Arrigan, *TrAC Trends in Analytical Chemistry* **2005**, *24*, Trace-metal analysis, 208–217.

[30] G. Herzog, V. Beni, *Analytica Chimica Acta* **2013**, *769*, 10–21.

[31] S. E. W. Jones, F. G. Chevallier, C. A. Paddon, R. G. Compton, *Analytical Chemistry* **2007**, *79*, 4110–4119.

[32] D. W. M. Arrigan, *Analyst* **1994**, *119*, 1953–1966.

[33] Z. Stojek, Z. Kublik, *Journal of Electroanalytical Chemistry and Interfacial Electrochemistry* **1979**, *105*, 247–259.

[34] W. D. Vries, E. van Dalen, *Journal of Electroanalytical Chemistry and Interfacial Electrochemistry* **1967**, *14*, 315–327.

[35] C. M. A. Brett, A. M. C. F. O. Brett, *Journal of Electroanalytical Chemistry and Interfacial Electrochemistry* **1989**, *262*, 83–95.

[36] J. C. Ball, R. G. Compton, *Electroanalysis* **1997**, *9*, 765–769.

2

Electrochemical Simulations

This thesis is concerned with the simulation of electrochemical systems and therefore this chapter outlines the basis of the simulations and discusses the numerical techniques used throughout this thesis. All results are reported for a system using a planar disc electrode of either macro or micro dimensions and thus the discussion will focus on the development of models appropriate for such systems.

Contents

2.1 Dimensionless Coordinates 25
2.2 Finite Difference Method 26
2.3 Time Evolution: Discretizing Fick's Second Law 29
2.3.1 Explicit Method 29
2.3.2 Implicit Method 30
2.3.3 Thomas Algorithm 30
2.4 One-dimensional Simulation 32
2.5 Two-dimensional Simulation 34
2.6 Convergence 37

2.1 Dimensionless Coordinates

In Chapter 1 it was shown that the voltammetric response is dependent on variables such as the bulk concentration c^*, radius ϵ, and time t, which vary from experiment to experiment. It is thus common to employ dimensionless coordinates when running

electrochemical simulations in which the dimensional parameters are normalized with respect to a reference variable with the same units for convenience. The benefit is that the output is described in terms of the minimum number of parameters and ensures the generality of the results. A couple of coordinate transformations are shown in Equations (2.1) to (2.4) for a one electron transfer process of A to B:

$$C_j = \frac{c_j}{c_A^*} \tag{2.1}$$

$$d_j = \frac{D_j}{D_A} \tag{2.2}$$

$$X = \frac{x}{\epsilon} \tag{2.3}$$

$$\tau = \frac{D_A t}{\epsilon^2} \tag{2.4}$$

where C is the dimensionless concentration of species j in which the concentration c_j is normalized against the bulk concentration of species A (c_A^*), d is the dimensionless diffusion coefficient of species j in which the diffusion coefficient D_j is normalized against the diffusion coefficient of species A (D_A), X is the dimensionless space normalized against the electrode radius (ϵ), τ is the dimensionless time, and j is the species of interest (A or B).

A detailed dimensional to dimensionless coordinate transformation for each project is provided in the corresponding chapters. Given the transformations, the dimensionless Fick's Second Law is then:

$$\frac{\partial C}{\partial \tau} = \frac{\partial^2 C}{\partial X^2} \tag{2.5}$$

for a one-dimensional macroelectrode system.

2.2 Finite Difference Method

The Finite Difference method is one of the most widely used numerical methods to solve partial differential equations such as the Fick's Second Law. The method works in such a way that a continuous function is discretized over finite steps and its derivative is approximated by taking the linear slope of discrete points. Given a

function $C(X)$ where C is the dimensionless concentration over dimensionless space, X, the first derivative of $C(X)$ at some point X_i can be approximated in three different ways via the forward, backward, and central difference approximation as shown in Equations (2.6), (2.7), and (2.8), respectively:

$$\left(\frac{dC}{dX}\right)_{X_i}^{forward} = \frac{C_{i+1} - C_i}{X_{i+1} - X_i} \tag{2.6}$$

$$\left(\frac{dC}{dX}\right)_{X_i}^{backward} = \frac{C_i - C_{i-1}}{X_i - X_{i-1}} \tag{2.7}$$

$$\left(\frac{dC}{dX}\right)_{X_i}^{central} = \frac{C_{i+1} - C_{i-1}}{X_{i+1} - X_{i-1}} \tag{2.8}$$

and a schematic representation of the three approximations are shown in Figure 2.1.

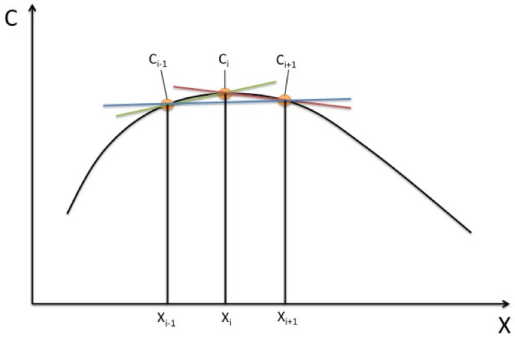


Figure 2.1: Schematic representation of the forward (red line), backward (green line), and central (blue line) approximations.

For simplicity, $X_i - X_{i-1} = X_{i+1} - X_i = \Delta X$ and the approximation approaches the true value with decreasing ΔX. The dependency of the error on ΔX can be understood by examining the truncation error defined as:

$$\Gamma = \left(\frac{dC}{dX}\right)_{X_i} - \frac{C_{i+1} - C_i}{\Delta X} \tag{2.9}$$

Equation (2.9) shows the forward difference method as an example.

Based on the forward and backward approximations, two Taylor Series expansions can be written:

$$C_{i+1} = C_i + \Delta X \left(\frac{dC}{dX}\right)_{X_i} + \frac{(\Delta X)^2}{2!}\left(\frac{d^2C}{dX^2}\right)_{X_i} + \frac{(\Delta X)^3}{3!}\left(\frac{d^3C}{dX^3}\right)_{X_i} + ... \quad (2.10)$$

$$C_{i-1} = C_i - \Delta X \left(\frac{dC}{dX}\right)_{X_i} + \frac{(\Delta X)^2}{2!}\left(\frac{d^2C}{dX^2}\right)_{X_1} - \frac{(\Delta X)^3}{3!}\left(\frac{d^3C}{dX^3}\right)_{X_i} + ... \quad (2.11)$$

Rearranging and solving Equations (2.10) and (2.11) give the following:

$$\left(\frac{dC}{dX}\right)_{X_i} - \frac{C_{i+1} - C_i}{\Delta X} = -\frac{\Delta X}{2!}\left(\frac{d^2C}{dX^2}\right)_{X_i} - \frac{(\Delta X)^2}{3!}\left(\frac{d^3C}{dX^3}\right)_{X_i} - ... \quad (2.12)$$

$$\left(\frac{dC}{dX}\right)_{X_i} - \frac{C_i - C_{i-1}}{\Delta X} = \frac{\Delta X}{2!}\left(\frac{d^2C}{dX^2}\right)_{X_i} - \frac{(\Delta X)^2}{3!}\left(\frac{d^3C}{dX^3}\right)_{X_i} + ... \quad (2.13)$$

from which the forward and backward truncation errors, $\Gamma_{forward}$ and $\Gamma_{backward}$, can be established:

$$\Gamma_{forward} = -\frac{\Delta X}{2!}\left(\frac{d^2C}{dX^2}\right)_{X_i} - \frac{(\Delta X)^2}{3!}\left(\frac{d^3C}{dX^3}\right)_{X_i} - ... \quad (2.14)$$

$$\Gamma_{backward} = \frac{\Delta X}{2!}\left(\frac{d^2C}{dX^2}\right)_{X_i} - \frac{(\Delta X)^2}{3!}\left(\frac{d^3C}{dX^3}\right)_{X_i} + ... \quad (2.15)$$

The truncation error of the central differencing is given by the average of the forward and backward truncation errors:

$$\Gamma_{central} = -\frac{(\Delta X)^2}{3!}\left(\frac{d^3C}{dX^3}\right)_{X_i} - \frac{(\Delta X)^4}{5!}\left(\frac{d^5C}{dX^5}\right)_{X_i} - ... \quad (2.16)$$

In all three methods, the first term is the largest source of error and thus the error of the forward and backward differencing are proportional to ΔX whereas in the central differencing the error is proportional to $(\Delta X)^2$. Therefore the central difference approximation is more accurate compared to the other two and thus will be used throughout this thesis.

Using the central difference approximation, the second derivative becomes:

$$\left(\frac{d^2C}{dX^2}\right)_{X_i} = \frac{C_{i+1} - 2C_i + C_{i-1}}{(\Delta X)^2} \quad (2.17)$$

2.3 Time Evolution: Discretizing Fick's Second Law

Up until this point the change in concentration across the simulation space, X, was considered. However, Equation (2.5) shows that the concentration evolves over time as well and thus time must also be discretized. k is used to denote the discretized timestep. Since the concentration at a timestep beyond the current one is unknown, a backward difference method must be used in which the concentration at τ^k and τ^{k-1} is considered. The left hand side of the Fick's Second Law is thus approximated as:

$$\frac{\partial C_i}{\partial \tau} \approx \frac{C_i^k - C_i^{k-1}}{\Delta \tau} \tag{2.18}$$

where the subscript i denotes the spatial point. The discretized Fick's Second Law is then:

$$\frac{C_i^k - C_i^{k-1}}{\Delta \tau} = \frac{C_{i+1} - 2C_i + C_{i-1}}{(\Delta X)^2} \tag{2.19}$$

Given Equation (2.19), it is clear that the right-hand side of the equation must also be discretized with respect to the timestep at either τ^{k-1} or τ^k.

2.3.1 Explicit Method

In the explicit method, the concentration on the right-hand side of Equation (2.19) is evaluated at τ^{k-1} giving:

$$\frac{C_i^k - C_i^{k-1}}{\Delta \tau} = \frac{C_{i+1}^{k-1} - 2C_i^{k-1} + C_{i-1}^{k-1}}{(\Delta X)^2} \tag{2.20}$$

Rearranging Equation (2.20) provides an expression for which only one-term is unknown:

$$C_i^k = C_i^{k-1} + \lambda(C_{i-1}^{k-1} - 2C_i^{k-1} + C_{i+1}^{k-1}) \tag{2.21}$$

where

$$\lambda = \frac{\Delta\tau}{(\Delta X)^2} \tag{2.22}$$

Equation (2.21) is easy to solve but is only conditionally stable for when $\lambda < 0.5$ [1–5] and naturally requires $\Delta\tau$ to be significantly small compared to ΔX, which becomes computationally more expensive with decreasing ΔX.

2.3.2 Implicit Method

The implicit method solves the right-hand side of Equation (2.19) at τ^k:

$$\frac{C_i^k - C_i^{k-1}}{\Delta\tau} = \frac{C_{i+1}^k - 2C_i^k + C_{i-1}^k}{(\Delta X)^2} \tag{2.23}$$

which rearranges to:

$$C_i^{k-1} = C_i^k + \lambda(C_{i-1}^k - 2C_i^k + C_{i+1}^k) \tag{2.24}$$

Unlike in the explicit method, only one term is known (C_i^{k-1}), and contains three unknown variables: C_{i-1}^k, C_i^k, and C_i^{k+1}. At every timestep k, the system is expressed in the form of Equation (2.24) over all n spatial points, which can more conveniently be expressed in the form:

$$\alpha_i C_{i-1}^k + \beta_i C_i^k + \gamma_i C_{i+1}^k = \delta_i \tag{2.25}$$

and must be solved simultaneously for all i. Despite the added complexity, the implicit method is unconditionally stable [6–8] and is thus used for all simulations in this thesis.

2.3.3 Thomas Algorithm

A set of simultaneous equations is commonly expressed in the form of a matrix:

$$\mathbf{A}x = b \tag{2.26}$$

which for Equation (2.25) is:

$$\begin{pmatrix} \beta_0 & \gamma_0 & 0 & 0 & 0 & 0 & 0 & \dots \\ \alpha_1 & \beta_1 & \gamma_1 & 0 & 0 & 0 & 0 & \dots \\ 0 & \alpha_2 & \beta_2 & \gamma_2 & 0 & 0 & 0 & \dots \\ & & \ddots & \ddots & \ddots & & & \\ & & & \ddots & \ddots & \ddots & & \\ \dots & 0 & 0 & 0 & \alpha_{n-3} & \beta_{n-3} & \gamma_{n-3} & 0 \\ \dots & 0 & 0 & 0 & 0 & \alpha_{n-2} & \beta_{n-2} & \gamma_{n-2} \\ \dots & 0 & 0 & 0 & 0 & 0 & \alpha_{n-1} & \beta_{n-1} \end{pmatrix} \begin{pmatrix} C_0^k \\ C_1^k \\ C_2^k \\ \vdots \\ \vdots \\ C_{n-3}^k \\ C_{n-2}^k \\ C_{n-1}^k \end{pmatrix} = \begin{pmatrix} f(\theta) \\ C_1^{k-1} \\ C_2^{k-1} \\ \vdots \\ \vdots \\ C_{n-3}^{k-1} \\ C_{n-2}^{k-1} \\ C_{n-1}^{k-1} \end{pmatrix} \tag{2.27}$$

where $f(\theta)$ is a function with respect to the applied dimensionless potential θ at the electrode surface where $i = 0$. Matrix of this type is called a tridiagonal matrix and can be solved using the Thomas Algorithm [9–11]. In the Thomas algorithm, the matrix $\mathbf{A}$ is represented as a product of a lower and upper triangular matrix such that $\mathbf{A} = \mathbf{LU}$ where $\mathbf{L}$ and $\mathbf{U}$ are shown in Equations (2.28) and (2.29), respectively:

$$\mathbf{L} = \begin{pmatrix} \beta_0' & & & & & \\ \alpha_1 & \beta_1' & & & & \\ & \ddots & \ddots & & & \\ & & \ddots & \ddots & & \\ & & & \alpha_{n-2} & \beta_{n-2}' & \\ & & & & \alpha_{n-1} & \beta_{n-1}' \end{pmatrix} \tag{2.28}$$

$$\mathbf{U} = \begin{pmatrix} 1 & \gamma_0' & & & & \\ & 1 & \gamma_1' & & & \\ & & \ddots & \ddots & & \\ & & & \ddots & \ddots & \\ & & & & 1 & \gamma_{n-2}' \\ & & & & & 1 & \gamma_{n-1}' \end{pmatrix} \tag{2.29}$$

where β' and γ' differ from β and γ. The decomposed $n \times n$ matrix A is written in the format:

$$\mathbf{A}x = \mathbf{LU}x = \mathbf{L}d = b, \qquad d = \mathbf{U}x \tag{2.30}$$

and $\mathbf{U}x = d$ can be written out as:

$$\begin{pmatrix} 1 & \gamma'_0 & & & & & \\ & 1 & \gamma'_1 & & & & \\ & & \ddots & \ddots & & & \\ & & & \ddots & \ddots & & \\ & & & & 1 & \gamma'_{n-2} & \\ & & & & & 1 & \gamma'_{n-1} \end{pmatrix} \begin{pmatrix} C_0^k \\ C_1^k \\ \vdots \\ \vdots \\ C_{n-2}^k \\ C_{n-1}^k \end{pmatrix} = \begin{pmatrix} \delta'_0 \\ \delta'_1 \\ \vdots \\ \vdots \\ \delta'_{n-2} \\ \delta'_{n-1} \end{pmatrix} \tag{2.31}$$

In order to solve for x, first the coefficients γ'_i and δ'_i must be calculated using the following expressions:

$$\gamma'_i = \begin{cases} \frac{\gamma_i}{\beta_i} & \text{for } i = 0 \\ \frac{\gamma_i}{(\beta_i - \gamma'_{i-1}\alpha_i)} & \text{for } i = 1, 2, ..., n-2 \end{cases} \tag{2.32}$$

$$\delta'_i = \begin{cases} \frac{\delta_i}{\beta_i} & \text{for } i = 0 \\ \frac{(\delta_i - \delta'_{i-1}\alpha_i)}{(\beta_i - \gamma'_{i-1}\alpha_i)} & \text{for } i = 1, 2, ..., n-1 \end{cases} \tag{2.33}$$

Once γ'_i and δ'_i are known, x can be solved via the back substitution.

$$x = C_i^k = \begin{cases} \delta'_{n-1} & \text{for } i = n-1 \\ \delta'_i - \gamma'_i C_{i+1}^k & \text{for } i = n-2, n-3, ...0 \end{cases} \tag{2.34}$$

2.4 One-dimensional Simulation

So far the discretized spatial grid has been assumed to be even in which $X_{i+1} - X_i = X_i - X_{i-1} = \Delta X$. However, since the concentration varies significantly at and near the electrode surface while smaller changes are observed towards the outer boundary, an exponentially expanding grid [12, 13] is commonly employed in the electrochemical simulations in order to concentrate grid points in the region of interest [14]. The spatial grid expands according to the following expression:

$$X_0 = 0 \tag{2.35}$$

$$X_1 = h \tag{2.36}$$

$$X_i = X_{i-1} + h\omega^{i-1} \tag{2.37}$$

where h is the first spatial increment and ω is the expanding factor such that $\omega > 1$.

When using the expanding grid, the discretized Fick's Second Law must be adjusted accordingly. Given $X_{i+1} - X_i = \Delta X_+$ and $X_i - X_{i-1} = \Delta X_-$:

$$\frac{C_i^k - C_i^{k-1}}{\Delta\tau} = \frac{\frac{C_{i+1}^k - C_i^k}{\Delta X_+} - \frac{C_i^k - C_{i-1}^k}{\Delta X_i}}{\frac{1}{2}[\Delta X_+ + \Delta X_-]} \tag{2.38}$$

and the Thomas Algorithm coefficients are:

$$\alpha = -\frac{2\Delta\tau}{\Delta X_-^2 + \Delta X_+ \Delta X_-} \tag{2.39}$$

$$\beta = \frac{2\Delta\tau}{\Delta X_+^2 + \Delta X_+ \Delta X_-} + \frac{2\Delta\tau}{\Delta X_-^2 + \Delta X_+ \Delta X_-} + 1 \tag{2.40}$$

$$\gamma = -\frac{2\Delta\tau}{\Delta X_+^2 + \Delta X_+ \Delta X_-} \tag{2.41}$$

In order to ensure that all concentration changes are included within the simulated space, the maximum spatial point X_{max} is defined as:

$$X_{max} = 6\sqrt{\tau_{max}} \tag{2.42}$$

and

$$\tau_{max} = \frac{2(\theta_f - \theta_i)}{\sigma} \tag{2.43}$$

θ_i and θ_f are the dimensionless initial and final potential values and σ is the dimensionless scan rate of the linear/triangular potential wave. A more detailed conversion between the dimensional and dimensionless coordinates are provided in each chapters corresponding to the appropriate models used. The total number of timesteps, m, is defined as:

$$m = \frac{\tau_{max}}{\Delta\tau} = \frac{2(\theta_f - \theta_i)}{\sigma\Delta\tau} \tag{2.44}$$

for which $\Delta\tau = \frac{\Delta\theta}{\sigma}$ where $\Delta\theta$ is the change in potential per timestep when a triangular or linear potential wave is employed. The results of the simulation are reported in dimensionless terms and thus the recorded current is also dimensionless, which is the concentration gradient at the electrode surface:

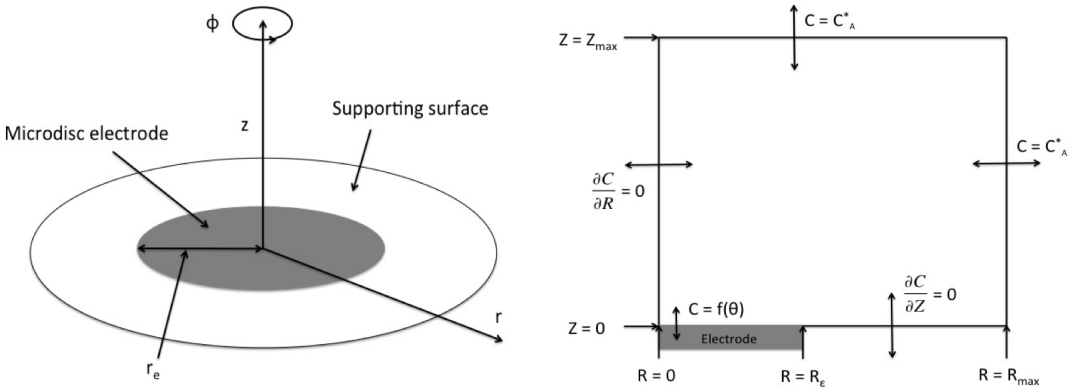
$$J = -\left(\frac{C_1^k - C_0^k}{X_1 - X_0}\right) \tag{2.45}$$

2.5 Two-dimensional Simulation

A one-dimensional model is employed when simulating systems at a macroelectrode since the diffusion is linear and thus the diffusion in the X direction normal to the electrode is only considered. On the other hand, a microelectrode introduces convergent diffusion as discussed in Chapter 1 and therefore diffusion in the direction of the radius of the conducting surface must be taken into account. This adds another dimension to the diffusion equation and is commonly expressed in cylindrical polar coordinates (r, z):

$$\frac{\partial c}{\partial t} = D_j\left(\frac{\partial^2 c}{\partial r^2} + \frac{1}{r}\frac{\partial c}{\partial r} + \frac{\partial^2 c}{\partial z^2}\right) \tag{2.46}$$

A graphical representation of the coordinate system is shown in Figure 2.2(a).



(a) Graphical representation of the coordinate system of a microdisc electrode.

(b) Schematic representation of the rectangular simulation space.

Figure 2.2

In the figure, the angle around the vertical axis z is shown denoted as ϕ but since the system is cylindrically symmetric, the change in concentration with respect to ϕ does not appear in Equation (2.46). The r and z coordinates are again normalized against the electrode radius, ϵ:

$$R = \frac{r}{\epsilon} \tag{2.47}$$

$$Z = \frac{z}{\epsilon} \tag{2.48}$$

Given the above transformations, Equation (2.46) can be expressed in dimensionless coordinates:

$$\frac{\partial C}{\partial \tau} = \left(\frac{\partial^2 C}{\partial R^2} + \frac{1}{R}\frac{\partial C}{\partial R} + \frac{\partial^2 C}{\partial Z^2} \right) \tag{2.49}$$

Based on Figure 2.2(a), it is clear that the microdisc electrode has a mirror symmetry about the perpendicular axis z at $(r, z) = (0, 0)$ and thus only half of the plane needs to be considered, creating a rectangular simulation space (r, z) as shown in Figure 2.2(b).

Since the simulation plane is rotationally symmetric about the Z axis at $R = 0$, the concentration on either side of the Z axis is equal and hence the flux must be zero at this boundary:

$$\left(\frac{\partial C}{\partial R} \right)_{R=0} = 0 \tag{2.50}$$

while the concentration change at the conducting surface of the electrode is described by the function:

$$C = f(\theta) \tag{2.51}$$

On the other hand, at the remote outer boundaries where $R = R_{max}$ and $Z = Z_{max}$ the concentration does not change and is thus equal to the initial bulk concentration:

$$C = C_A^* \tag{2.52}$$

Furthermore, beyond $R = R_\epsilon$ is the insulating supporting surface and there can therefore be no flux normal to the surface:

$$\left(\frac{\partial C}{\partial Z} \right)_{Z=0} = 0 \tag{2.53}$$

The grid expands exponentially in the R and Z direction but when creating the grid in the R direction, the grids are mirrored between $R = 0$ and $R = 0.5$, and $R = 0.5$ and $R = 1$. Beyond $R = 1$ (dimensionless radius of the conducting surface), a regular expanding grid such as in Section 2.4 is used. This is to ensure that the edges of the electrode has high density of points and low densities everywhere else. Mathematically, the expanding grids in the R and Z directions are:

$$0 < R \leq 0.5 \qquad R_i = R_{i-1} + h\omega^{i-1} \tag{2.54}$$

$$0.5 < R < 1 \qquad R_i = R_{i-1} + h\omega^{n_\epsilon - i} \tag{2.55}$$

$$1 \leq R \leq R_{max} \qquad R_i = 1 + h\omega^{i-n_\epsilon - 1} \tag{2.56}$$

and

$$Z_0 = 0 \tag{2.57}$$

$$Z_1 = h \tag{2.58}$$

$$Z_j = Z_{j-1} + h\omega^{j-1} \tag{2.59}$$

where i and j are the discretized spatial points in the R and Z direction, respectively, and n_ϵ is the spatial point at which $R_{n_\epsilon} = 1$. The simulation space in the R and Z directions are defined in Equations (2.60) and (2.61).

$$R_{max} = R_\epsilon + 6\sqrt{\tau_{max}} \tag{2.60}$$

$$Z_{max} = 6\sqrt{\tau_{max}} \tag{2.61}$$

The implicity discretized form of Equation (2.49) is:

$$\begin{aligned}\frac{C_i^k - C_i^{k-1}}{\Delta\tau} = &\left(\frac{C_{i+1,j}^k - C_{i,j}^k}{\Delta R+} - \frac{C_{i,j}^k - C_{i-1,j}^k}{\Delta R_-}\right)\frac{2}{\Delta R_+ + \Delta R_-} \\ &+ \left(\frac{C_{i,j+1}^k - C_{i,j}^k}{\Delta Z_+} - \frac{C_{i,j}^k - C_{i,j-1}^k}{\Delta Z_-}\right)\frac{2}{\Delta Z_+ + \Delta Z_-} \\ &+ \frac{1}{R_i}\left(\frac{C_{i+1,j}^k - C_{i-1,j}^k}{\Delta R_+ + \Delta R_-}\right)\end{aligned} \tag{2.62}$$

which contains five unknowns. In order to solve Equation (2.62), the ADI (alternating direction implicit) method [15, 16] must be used. In the ADI method, the finite difference equation is split in the Z-direction and R-direction which are implicitly solved over two half-timesteps, $k-0.5$ and k. Doing so reduces the unknown variables to three and can be solved using the Thomas Algorithm. The Z-sweep discretization is:

$$\begin{aligned}\frac{C_i^{k-0.5}-C_i^{k-1}}{\Delta\tau} = &\left(\frac{C_{i+1,j}^{k-1}-C_{i,j}^{k-1}}{\Delta R+}-\frac{C_{i,j}^{k-1}-C_{i-1,j}^{k-1}}{\Delta R_-}\right)\frac{2}{\Delta R_+ + \Delta R_-}\\ &+\left(\frac{C_{i,j+1}^{k-0.5}-C_{i,j}^{k-0.5}}{\Delta Z_+}-\frac{C_{i,j}^{k-0.5}-C_{i,j-1}^{k-0.5}}{\Delta Z_-}\right)\frac{2}{\Delta Z_+ + \Delta Z_-}\\ &+\frac{1}{R_i}\left(\frac{C_{i+1,j}^{k-1}-C_{i-1,j}^{k-1}}{\Delta R_+ + \Delta R_-}\right)\end{aligned} \quad (2.63)$$

and the R-sweep discretization is:

$$\begin{aligned}\frac{C_i^{k}-C_i^{k-0.5}}{\Delta\tau} = &\left(\frac{C_{i+1,j}^{k}-C_{i,j}^{k}}{\Delta R+}-\frac{C_{i,j}^{k}-C_{i-1,j}^{k}}{\Delta R_-}\right)\frac{2}{\Delta R_+ + \Delta R_-}\\ &+\left(\frac{C_{i,j+1}^{k-0.5}-C_{i,j}^{k-0.5}}{\Delta Z_+}-\frac{C_{i,j}^{k-0.5}-C_{i,j-1}^{k-0.5}}{\Delta Z_-}\right)\frac{2}{\Delta Z_+ + \Delta Z_-}\\ &+\frac{1}{R_i}\left(\frac{C_{i+1,j}^{k}-C_{i-1,j}^{k}}{\Delta R_+ + \Delta R_-}\right)\end{aligned} \quad (2.64)$$

Since the flux to the electrode surface is uneven in a microelectrode system, it must be integrated over the entire surface:

$$J = -0.5\sum_{i=1}^{n-1}\left[\frac{(C_{i,1}-C_{i,0})R_i + (C_{i-1,1}-C_{i-1,0})R_{i-1}}{Z_1 - Z_0}\right](R_i - R_{i-1}) \quad (2.65)$$

2.6 Convergence

As briefly mentioned in Section 2.2, the truncation error inherent in these numerical approximations inevitably causes the simulation results to deviate from the true value. However, the accuracy of the numerical solution can be improved by decreasing the space and time intervals, ΔX and $\Delta\tau$, at which the system is

said to be "convergent". A convergence test is carried out by changing these two values while keeping all other parameters fixed to find the appropriate set of ΔX and $\Delta\tau$ which produce results that agree closely with the known expressions such as the peak current and peak-to-peak separation in a one-dimensional simulation and steady-state current in a two-dimensional simulation [17]. When such analytical solutions are not available, a conservation of mass test is used to check the validity of the simulation. As the accuracy of the result increases so does the runtime and thus a compromise must be made between the two, known as the accuracy tolerance. In this thesis the accuracy tolerance for a one-dimensional and two-dimensional system are set to 0.5 % and 1 % [18], respectively.

References

[1] K. W. Morton, *Numerical Solution of Partial Differential Equations: An Introduction*, Cambridge University Press, **2005**.

[2] G. D. Smith, *Numerical Solution of Partial Differential Equations: Finite Difference Methods*, Oxford University Press, **1985**.

[3] A. W. Bott, *Curr. Seps.* **2000**, *19*, 45–48.

[4] F. Magno, G. Bontempelli, M. Andreuzzi-Sedea, *Analytica Chimica Acta* **1982**, *140*, 65–76.

[5] R. Seeber, S. Stefani, *Analytical Chemistry* **1981**, *53*, 1011–1016.

[6] R. G. Compton, E. Laborda, K. R. Ward, *Understanding Voltammetry: Simulation of Electrode Processes*, Imperial College Press, **2013**.

[7] M. Rudolph, *Journal of Electroanalytical Chemistry and Interfacial Electrochemistry* **1991**, *314*, 13–22.

[8] L. K. Bieniasz, O. Østerby, D. Britz, *Computers & Chemistry* **1995**, *19*, 121–136.

[9] D. Zhou, F. Gao, E. Breaz, A. Ravey, A. Miraoui, *IEEE Transactions on Industrial Electronics* **2018**, *65*, 7106–7118.

[10] A. Jameson, E. Turkel, *Math. Comp.* **1981**, *37*, 385–397.

[11] W. Press, S. A. Teukolsky, W. T. Vetterling, B. P. Flannery, *Numerical Recipes: The Art of Scientific Computing*, Cambridge University Press, **2007**.

[12] D. J. Gavaghan, *Journal of Electroanalytical Chemistry* **1998**, *456*, 1–12.

[13] S. W. Feldberg, *Journal of Electroanalytical Chemistry and Interfacial Electrochemistry* **1981**, *127*, 1–10.

[14] T. Joslin, D. Pletcher, *Journal of Electroanalytical Chemistry* **1974**, *49*, 171–186.

[15] D. Peaceman, H. H. Rachford, *Journal of the Society for Industrial and Applied Mathematics* **1955**, *3*, 28–41.

[16] J. Heinze, *Journal of Electroanalytical Chemistry and Interfacial Electrochemistry* **1981**, *124*, 73–86.

[17] E. Kätelhön, R. G. Compton, *Analyst* **2015**, *140*, 2592–2598.

[18] D. J. Gavaghan, *Journal of Electroanalytical Chemistry* **1997**, *420*, 147–158.

3

Cosine-based Potential Waves in Cyclic Voltammetry: Theory and Experiment

This chapter investigates the use of a cosine-based potential waveform in voltammetry. The results reported in this chapter are based on published work in the '*Journal of Electroanalytical Chemistry* 2017, 801, 381-387' [1] and the '*Journal of Electroanalytical Chemistry* 2018, 815, 24-29' [2].

Contents

3.1 Introduction 42
3.2 Theory 43
3.2.1 Theoretical Model 43
3.2.2 Proposed Method 45
3.2.3 Dimensionless Coordinates 45
3.2.4 Simulation via Finite Differences 46
3.3 Results and Discussion 48
3.3.1 Capacitive Currents 48
3.3.2 Voltammetry Obtained Using a Cosine Potential Wave When $n = 1$ 52
3.3.3 Voltammetric Effects of Cosine Potential Wave When $n > 1$ 55
3.4 Conclusions 60
3.5 Experimental Verification 61
3.5.1 Chemicals 61
3.5.2 Instrumental 61
3.5.3 Results and Discussion 62
3.5.4 Conclusions 69

3.1 Introduction

For decades, cyclic voltammetry [3–6] has been the key technique in electrochemistry and still today remains an integral part of most electrochemical and electro-analytical studies published. As explained in Chapter 1, in a typical cyclic voltammetry experiment, an electrode is set in contact with an electrolyte solution containing an analyte of interest. The surface is then biased with respect to the solution, while a triangular potential wave $E(t)$ is applied to the electrode relative to a reference electrode:

$$E(t) = \begin{cases} \pm\nu t + E(t=0) & \text{for} \quad t < t_{1/2} \\ \mp\nu(t - t_{1/2}) + E(t = t_{1/2}) & \text{for} \quad t \geq t_{1/2} \end{cases} \tag{3.1}$$

where ν is the scan rate and $t_{1/2}$ is half of the duration of one cycle. During the potential scan, the electrode current - the current through the solid-liquid interface - is monitored and enables diverse insights into the nature of the reaction at the electrode surface. As a vast amount of accessible and easy-to-use theory exists [7], numerous physical quantities can be readily extracted from voltammetric data including analyte concentrations, diffusion constants, and rate constants.

Aside from the great opportunities offered by cyclic voltammetry using the triangular wave (3.1), experimental challenges inevitably result from the discontinuity of the potential's first derivative with respect to time. As capacitive contributions, I_c, to the measured current ($I = I_c + I_F$) are proportional to the first derivative of the applied electrode potential, $E(t)$, with respect to time:

$$I_c \propto \frac{dE(t)}{dt} \tag{3.2}$$

I_c is discontinuous, which entails perturbed voltammetric data following the turning point at $t = t_{1/2}$. The perturbations are mostly due to parasitic capacitances present in the measurement set-up, which may in a complex fashion depend on parameters such as the scan rate, potential, and current magnitude, and hence can typically not be distinguished from actual voltammetric data. A more detailed discussion on capacitive effects can be found in recent literature [8]. While such perturbations

are of course present at any time of the experiment and generally affect all data, their influence may however be much larger at discontinuities in the current where they pose a much greater change to the acquisition and quantitative analysis of experimental results and which should therefore desirably be avoided.

This chapter presents an alternative approach to cyclic voltammetry using a slightly different waveform to the above triangular wave to prevent discontinuities in the measured electrode current. Related voltammetry is investigated in much detail and an expression for the value of the first peak is established akin to the well-known Randles-Ševčík equation [9, 10]. The analysis further reveals that the proposed method gives rise to unique voltammetric features that can be exploited to determine the formal potential of a reaction at ease and clarity beyond means offered by triangular wave cyclic voltammetry.

3.2 Theory

In the following sections, a theoretical model is introduced and the proposed method of an alternative non-triangular waveform is explained. Furthermore, practical dimensionless coordinates employed in the simulation are introduced.

3.2.1 Theoretical Model

A simple one-electron electrochemically-reversible reduction reaction of A to B was investigated at a planar macrodisc electrode under diffusion-only conditions, where both species have equal diffusion coefficients:

$$A(aq) + e^- \rightleftharpoons B(aq) \tag{3.3}$$

The system was assumed to be fully-reversible in which the electrode kinetics are much faster in comparison to the mass transport resulting in a Nernstian equilibrium at the electrode surface [4, 11]:

$$E = E_f^0 + \frac{RT}{F} ln \frac{[A]_0}{[B]_0} \tag{3.4}$$

In this system, only diffusion was considered as means of mass transport of the analytes to the electrode surface [12–14] with no convection and the presence of a sufficiently high concentration of supporting electrolyte is assumed so that migration can be neglected [5, 15–19]. It is, however, important to note that with sufficiently long scan duration times, convection may affect experimental results [4, 5, 20–22]. The transport of analyte is hence described via the one-dimensional diffusion equation given by Fick's Second Law, which relates the change in concentration, c, over space x, with time, t [23, 24]:

$$\frac{\partial c_j}{\partial t} = D_j \frac{\partial^2 c_j}{\partial x^2} \tag{3.5}$$

where j is the species of interest and D is the diffusion coefficient of said species. In order to solve the diffusion equation, boundary conditions are established for the case where initally only species A is present in the bulk solution [4, 23], and the concentrations of both A and B are uniform in space:

$$t \leq 0,\ \text{all}\, x,\ c_A = c_A^*,\ c_B = 0 \tag{3.6}$$

As t increases, both c_A and c_B change, however, at a distance significantly far from the electrode, no reaction is observed and the solution concentration remains the same as the initial condition:

$$t > 0,\ x \to \infty,\ c_A = c_A^*,\ c_B = 0 \tag{3.7}$$

Since both species have the same diffusion coefficient and by conservation of mass, the amount of A consumed at the electrode equals the amount of B gained:

$$t > 0,\ x = 0,\ -\frac{\partial c_A}{\partial x} = \frac{\partial c_B}{\partial x} \tag{3.8}$$

and, due to the symmetry of all boundary conditions with respect to the exchange of A and B, the following condition holds at any point in space:

$$c_A(x,t) + c_B(x,t) - c_A^* = 0 \tag{3.9}$$

3.2.2 Proposed Method

In contrast to a triangular wave, the here-introduced method uses a cosine-based potential wave with varying powers, while the scanned potential window is shifted between different experiments. The cosine potential wave equation is given as:

$$E(t) = A_0 \cdot \left| cos\left(2\pi \frac{t}{t_{max}}\right) \right|^n \cdot \frac{cos\left(2\pi \frac{t}{t_{max}}\right)}{\left| cos\left(2\pi \frac{t}{t_{max}}\right) \right|} + E_{avg} \tag{3.10}$$

where A_0 is the amplitude of the wave in volts, n is the power of the function greater than or equal to 1, and E_{avg} is the offset of the wave defined as:

$$E_{avg} = \frac{E_i + E_f}{2} \tag{3.11}$$

and hence E_{avg} provides the midpoint of the potential window.

3.2.3 Dimensionless Coordinates

For simplicity and both an easier and a more general application of the results to various experimental conditions, dimensionless parameters [23] were used for simulations, and the conversion factors are shown in Table 3.1.

Table 3.1: Dimensionless parameters. [23]

Parameter	Normalization
concentration	$C_j = \frac{c_j}{c_A^*}$
diffusion coefficient	$d_j = \frac{D_j}{D_A}$
spatial coordinate	$X = \frac{x}{\epsilon}$
time	$\tau = \frac{D_A t}{\epsilon^2}$
potential	$\theta = \left(\frac{F}{RT}\right)(E - E_f^0)$
scan rate	$\sigma = \left(\frac{\epsilon^2}{D_A}\right)\left(\frac{F}{RT}\right)\nu$
current	$J = \frac{I}{\pi \epsilon F D_A c_A^*}$

Given these expressions, the diffusion equation transforms to:

$$\frac{\partial C_j}{\partial \tau} = d_j \frac{\partial^2 C_j}{\partial X^2} \tag{3.12}$$

where $d_j = 1$ for species A.

3.2.4 Simulation via Finite Differences

The above theoretical model was simulated via a finite difference approach. To this end, the dimensionless Fick's Second Law (3.12) was discretized using the backward implicit method as explained in detail in Chapter 2. Given the transformations in Table 3.1 and the finite difference method introduced earlier, Equation (3.10) can be rewritten in its discretized dimensionless form:

$$\theta(\tau_k) = \theta_{A_0} \cdot |cos(2\pi \cdot a \cdot k\Delta\tau)|^n \cdot \frac{cos(2\pi \cdot a \cdot k\Delta\tau)}{|cos(2\pi \cdot a \cdot k\Delta\tau)|} + \theta_{shift} \tag{3.13}$$

where θ_{A_0} is the dimensionless amplitude of the wave, a is an auxiliary coefficient defined as $\frac{\sigma}{4\theta_{A_0}}$ in which σ is the dimensionless average scan rate obtained from the slope of the triangular potential wave, k is the time step, $\Delta\tau$ is the difference between each dimensionless time step, and θ_{shift} is the dimensionless potential shift defined as $\theta_{shift} = \theta_{avg} - \theta_f^0$. Since by definition $\theta_f^0 = 0$, $\theta_{shift} = \theta_{avg}$. The auxiliary coefficient is necessary in order to maintain the same duration time between the triangular and non-triangular potential waves. The justification of adding the auxiliary term is given below. The cosine wave given in Equation (3.13), regardless of the power, has the following special traits when $\theta_{shift} = 0$:

$$\begin{aligned} \text{at } k = 0 \text{ and } k = m,\ \theta(\tau_k) &= \theta_{A_0} \\ \text{at } k = \frac{m}{4} \text{ and } k = \frac{3m}{4},\ \theta(\tau_k) &= 0 \\ \text{at } k = \frac{m}{2},\ \theta(\tau_k) &= -\theta_{A_0} \end{aligned} \tag{3.14}$$

Given that $\Delta\tau = \frac{\tau_{max}}{m}$ where m is the number of timesteps, and $\tau_{max} = \frac{4\theta_{A_0}}{\sigma}$ from Chapter 2, Equation (3.13) can be simplified to give the following:

$$\theta(\tau_k) = \theta_{A_0} \cdot \left|cos(2\pi \cdot \frac{k}{m})\right|^n \cdot \frac{cos(2\pi \cdot \frac{k}{m})}{\left|cos(2\pi \cdot \frac{k}{m})\right|} + \theta_{shift} \tag{3.15}$$

which fulfills the conditions given in (3.14) when $\theta_{shift} = 0$.

Figure (3.1) shows the three waveforms employed in this project in dimensionless coordinates where the blue line corresponds to the triangular wave, the green line

corresponds to the cosine wave when $n = 1$, and the magenta line corresponds to the cosine wave when $n = 2$. All three waves are centred at $\theta = 0$ ($\theta_{shift} = 0$ since $\theta_f^0 = 0$ by definition) with an amplitude of 1.

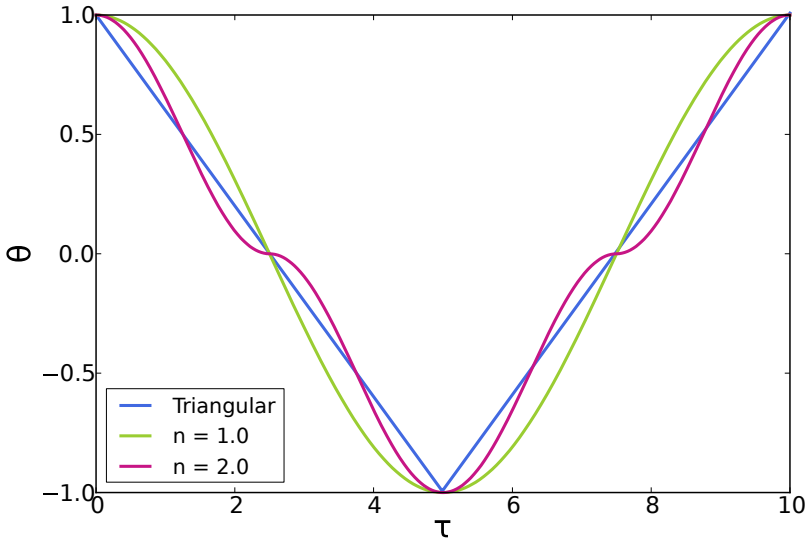


Figure 3.1: A schematic representation of the three potential waves centrered at $\theta = 0$ with an amplitude of 1. The blue line corresponds to the triangular wave, the green line corresponds to the cosine wave when $n = 1$, and the magenta line corresponds to the cosine wave when $n = 2$.

As can be seen, the duration time is kept the same for all three methods but the instantaneous scan rate at any potential differs depending on the applied potential for the non-triangular waveforms. In addition, the figure reveals that there are no discontinuities in the first temporal derivative of the cosine-based potential waves and so the above-bespoken perturbations arising from parasitic capacitances will not be observed in experimental data. It is further noted that a plateau is observed for the cosine square wave at the midpoint of the applied potential range, which moves up or down depending on the potential window shift, θ_{shift}, and results in unique voltammetric behavior as discussed in later sections.

All numerical procedures were implemented in *C++* and data processing and visualization were performed in *Python* via the software packages *NumPy* and *matplotlib*. As part of the convergence test, peak-to-peak separations and peak currents were compared with the theoretical predictions where applicable.

3.3 Results and Discussion

The following sections discuss the opportunities arising from the proposed voltammetric method. The discussion first focuses on the implications of the altered potential wave on the capacitive current before addressing the voltammetric response to the above cosine-based wave with an exponent of 1. Finally, the study is concerned with the voltammetry observed for greater exponents and outlines an entirely novel but highly practical approach to the determination of the formal potential of a redox couple. Simulations were run using several scan rates ranging from $\sigma = 10^2$ to 10^7 while the results shown below were obtained for $\sigma = 10^4$ unless stated otherwise. Other parameters used for simulations were: $\Delta\theta = 10^{-4}$, $\omega = 1.05$, and $h = 10^{-7}$ (definition given in Chapter 2). All simulation results are reported in dimensionless coordinates.

3.3.1 Capacitive Currents

As explained in Chapter 1, whenever a potential is applied to an electrode in an experimental system, a double layer forms at the interface between the electrode and the electrolyte solution [25] as electrostatic effects compensate for the charge difference and effectively screen the electrode potential in solution [5]. The double layer acts as a capacitor and thereby generates a capacitive current contribution to the electrode current if the electrode potential is varied: see Equation (3.2). Figure 3.2 shows the dimensionless capacitive currents for triangular, cosine, and cosine square potential waves plotted against dimensionless time using the same color scheme as in Figure 3.1.

For the linear sweep, a discontinuous capacitive current is observed at the point where the potential sweep is reversed, which is intuitive from Figure 3.1 since the slope changes signs in equal magnitude at said point. In reality, a distinct step is not seen because of the time constant of the electrochemical cell, however, as discussed in the previous section, the discontinuity in the capacitive current disrupts the voltammogram obtained in experiments and often results in an unwanted complication of the measured data. In contrast, cosine and cosine square waves are

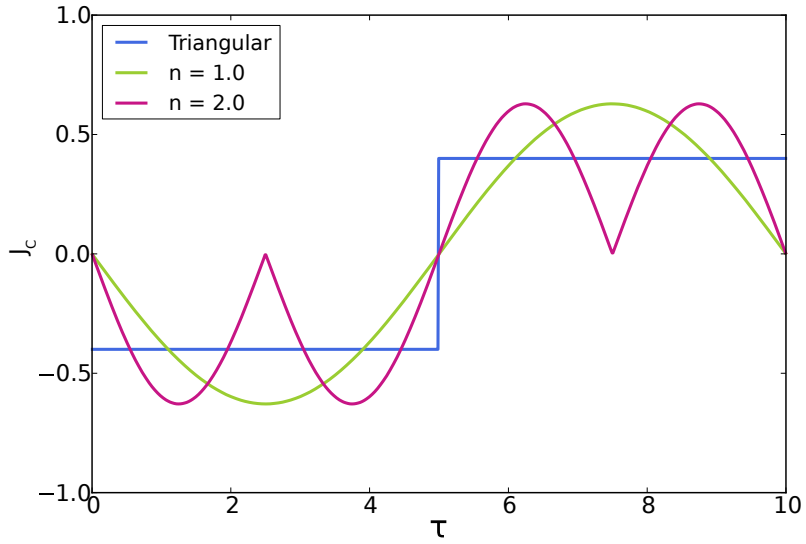


Figure 3.2: A schematic representation of the capacitive current of the three potential waves shown in Figure 3.1 with the same color scheme. A jump in the capacitive current is seen at $\tau_{1/2}$, the point of reversal, for the triangular method whereas both cosine-based methods show a continuous curve at said point. Here, the double-layer capacitance is assumed to be potential independent.

both continuous at the point of reversal as well as at all other points throughout the entire sweep, minimizing the effect of capacitive current drop and the perturbation of the voltammogram. In this particular example, the double-layer capacitance is assumed to be potential independent, and thus the figure is plotted from the temporal derivative of the three potential waves in Figure 3.1.

Before discussing the capacitive effect, first the voltammetric curves with exclusively the Faradaic current are considered. Figure 3.3 shows the dimensionless voltammograms obtained by applying the three potential waves introduced earlier at $\sigma = 10^4$ and $\theta_{shift} = 0$. Again, the same color scheme is used as in Figure 3.1. The notable difference is the larger current of the cosine result when $n = 1$ compared to the triangular method, and the presence of a double peak when $n = 2$. These two behaviors are discussed in detail in later sections.

Next the capacitive current effect on the individual voltammograms was investigated. Figure 3.4 shows the theoretical behavior of voltammograms when a capacitive current is considered in the modelling of triangular, cosine, and cosine

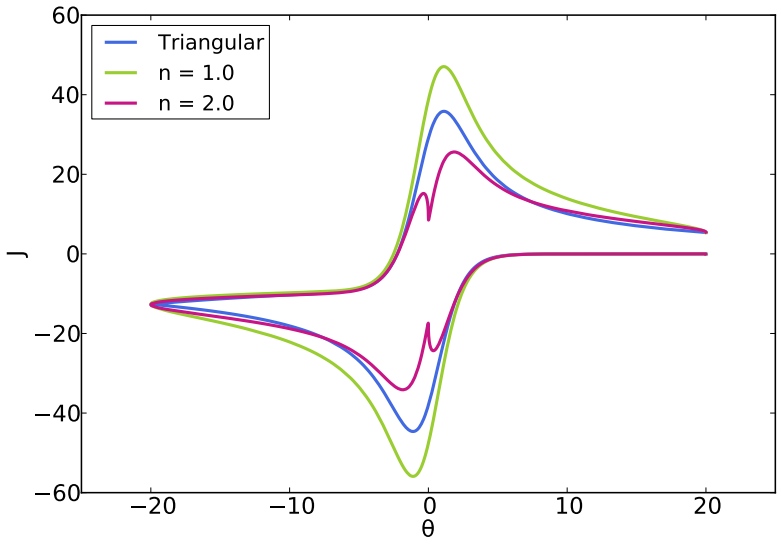


Figure 3.3: Dimensionless voltammograms obtained by applying the triangular, cosine, and cosine square potential waves at $\sigma = 10^4$ and $\theta_{shift} = 0$. The same color scheme is used as in Figure 3.1.

square potential waves. Each figure is labeled for the corresponding potential wave employed: 3.4A is for triangular, 3.4B is for cosine when $n = 1$, and 3.4C is when $n = 2$. In all three figures, the solid curve represents the dimensionless Faradaic current and the dashed curve represents the total current (Faradaic + capacitive). As expected, the voltammogram with triangular waveform shows a step caused by the capacitive current at the point of reversal whereas voltammograms with cosine and cosine square waves show minimal perturbation at said point.

The capacitive current was calculated using the following equation:

$$I_c = A_{ele} C_{dl} \nu \tag{3.16}$$

where C_{dl} is the double layer capacitance per surface area. The equation was transformed into dimensionless coordinates using the conversion factors listed in Table 3.1 in order to obtain a dimensionless expression for the capacitance, K_{dl}:

$$K_{dl} = \frac{C_{dl} RT}{\epsilon F^2 c_A^*} \tag{3.17}$$

and the dimensionless capacitive current expression is:

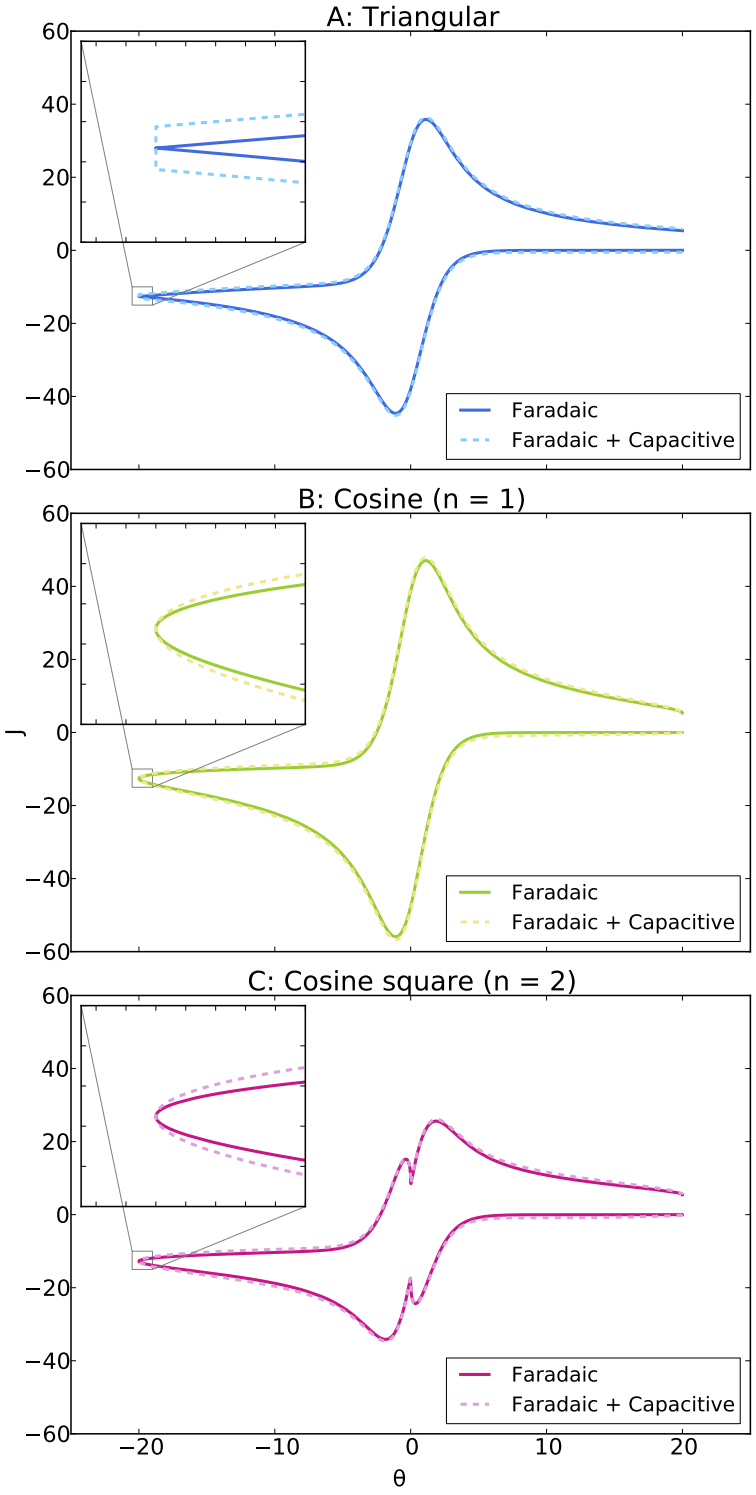


Figure 3.4: A comparison between voltammograms with and without capacitive perturbations at $\sigma = 10^4$ and $\theta_{shift} = 0$ for $C_{dl} = 20$ µF cm^{-2}. Each figure is labeled with the corresponding potential wave: A is for triangular, B is for cosine when $n = 1$, and C is when $n = 2$. The solid curves represent the dimensionless Faradaic current and the dashed curves represent the total current (Faradaic + capacitive).

$$J_c = K_{dl}\sigma \tag{3.18}$$

It is intuitive from Equation (3.18) that the capacitive flux increases with increasing scan rate, and thus the effect on the voltammogram would become more prominent with increasing scan rate as shown in *Appendix*: A.2. The total currents in Figure 3.4 were plotted by adding the dimensionless Faradaic current and the dimensionless capacitive current which was calculated for dimensional parameters of C_{dl} = 20 µF cm^{-2}, $\epsilon = 10^{-3}$ m, $c_A^* = 1.0$ mol m^{-3}, and $T = 298$ K.

3.3.2 Voltammetry Obtained Using a Cosine Potential Wave When $n = 1$

Figure 3.5 shows the voltammograms simulated for the conventional triangular wave and a cosine pulse wave ($n = 1$), both of which are symmetric with respect to the formal potential of the redox couple under investigation ($\theta_{shift} = 0$) at a scan rate of $\sigma = 10^4$. The voltammograms follow the same color scheme as in Figure 3.1. The light blue dash-dot line corresponds to the dimensionless peak current value of a conventional triangular cyclic voltammetry obtained from the Randles-Ševčík equation [9, 10, 23, 26] which in dimensional form is:

$$I_p = -0.446FA_{ele}c_A^*\sqrt{\frac{FD_A\nu}{RT}} \tag{3.19}$$

and shows a square root dependence on the scan rate, ν [27]. Using the aforementioned conversion factors between dimensional and dimensionless coordinates, Equation (3.19) was converted into its dimensionless form:

$$J_p = -0.446\sqrt{\sigma} \tag{3.20}$$

The value indicated by the yellow dash-dot line is the dimensionless peak current observed in the simulated cosine voltammogram. In the figure, it can clearly be seen that the cosine peak current exceeds the triangular peak current. This can be understood by comparing the temporal scan rates in the region of the formal potential; although the duration time of the sweep of both, the triangular and

the cosine wave methods, are equal, their temporal scan rates differ with the cosine wave featuring a higher transient scan rate in the region of the formal potential. The observed current response is hence elevated as higher scan rates lead to increased rates of material reacting.

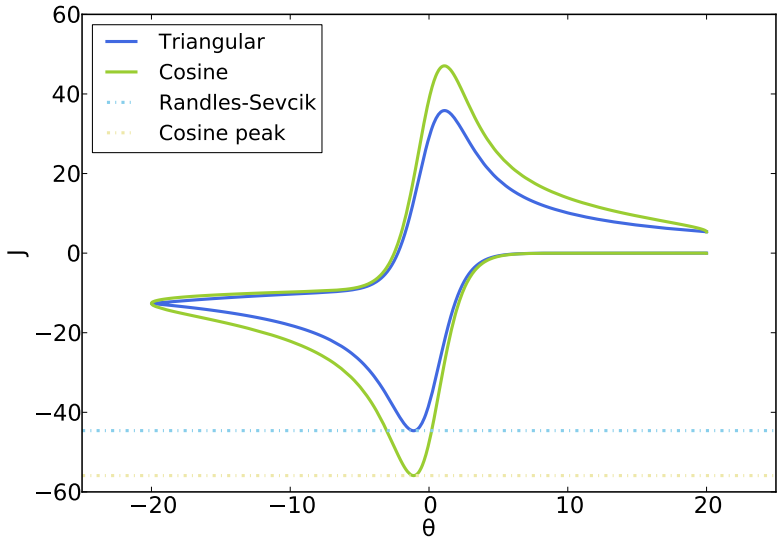


Figure 3.5: Voltammograms obtained from a triangular and cosine potential wave for $\sigma = 10^4$ and $\theta_{shift} = 0$ with the same color scheme as in Figure 3.1. The light blue dash-dot line corresponds to the dimensionless peak current value of a conventional triangular cyclic voltammetry predicted by the dimensionless Randles-Ševčík equation (3.20) and the yellow dash-dot line is the dimensionless peak current observed for the cosine voltammogram.

The peak currents of the cosine model were further investigated in analogy with the Randles-Ševčík equation by fitting a linear function to the graph obtained by plotting the peak currents at various scan rates against the square root of the respective scan rate as shown in Figure 3.6 in which all data were obtained for $\theta_{shift} = 0$.

In the figure, the blue and green dots correspond to the dimensionless peak currents of the voltammograms simulated with triangular and cosine waves, respectively, at varying dimensionless scan rates ranging between 10^2 and 10^7. The theoretical peak currents for the triangular potential wave were calculated by the dimensionless Randles-Ševčík equation (3.20) to produce the light blue line. The line passes through the centres of the dots demonstrating that the simulated results

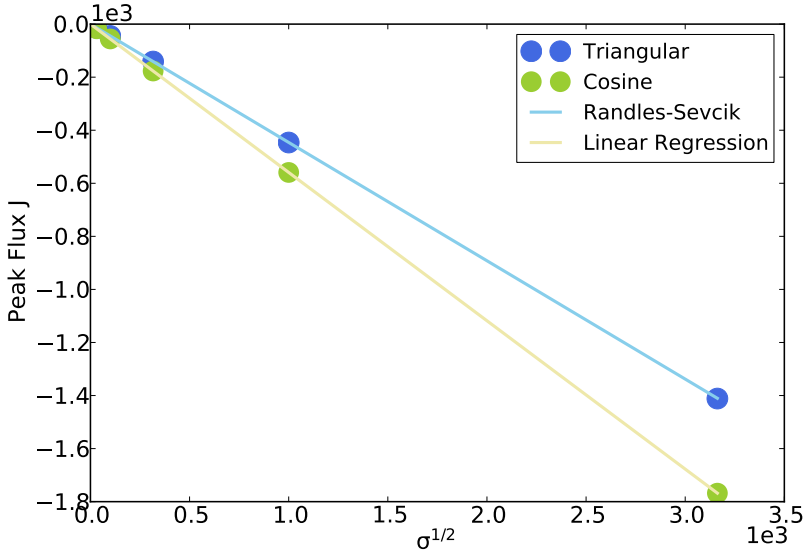


Figure 3.6: Dimensionless peak currents plotted against the square root of dimensionless scan rate for triangular and cosine potential wave methods at $\theta_{shift} = 0$. The blue dots correspond to the peak currents of the triangular method and the green dots correspond to the peak currents of the cosine method. The light blue line is the predicted peak current values at each scan rate given by Equation (3.20) and the yellow line was obtained by performing a linear fit on the green dots.

coincide with the theoretical value. The yellow line was generated by performing a linear regression on the green dots, whose slope was then used to determine the coefficient of the peak current equation for the cosine potential wave akin to the Randles-Ševčík expression:

$$J_p = -0.559\sqrt{\sigma} \tag{3.21}$$

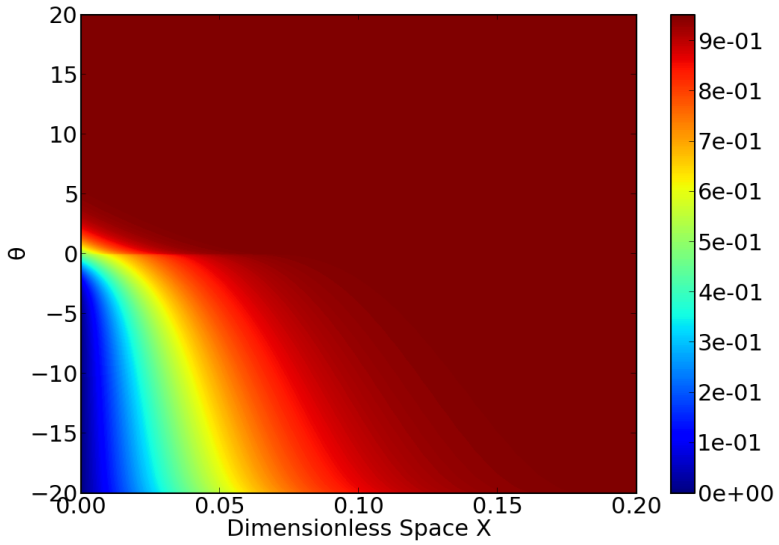
Similar to the triangular potential wave voltammogram, the peak current of the cosine potential wave voltammogram shows a square root dependence on the scan rate. The simulations were run using dimensionless parameters and hence the mathematical expression for the linear regression shown in Figure 3.6 was obtained in dimensionless coordinates. This can be converted to a dimensional expression using the conversion factors listed in Table 3.1:

$$I_p = -0.559FA_{ele}c_A^*\sqrt{\frac{FD_A\nu}{RT}} \tag{3.22}$$

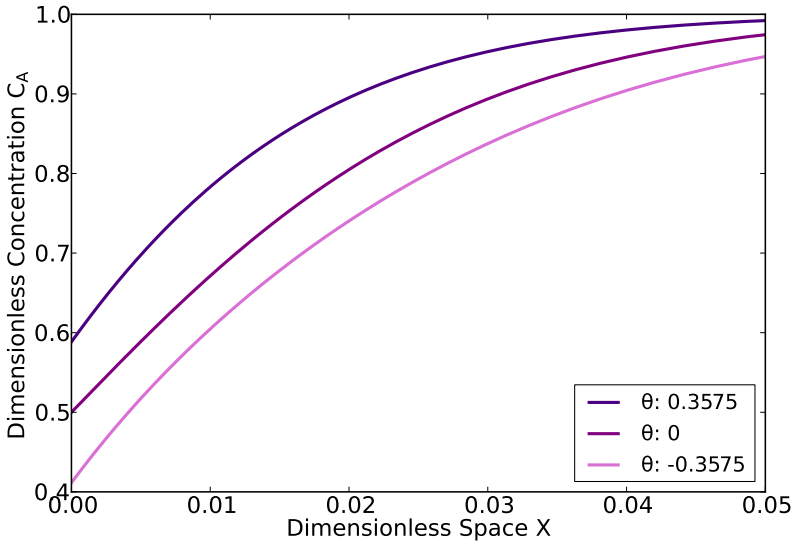
Equation (3.22) shows approximately a 25 % increase in the peak current compared to that obtained from the Randles-Ševčík equation. The reasoning behind this can again be attributed to the steeper slope of the applied potential waveform around the formal potential where the electron transfer occurs most significantly. It is important, however, to note that Equation (3.21) was calculated from results using $\theta_{shift} = 0$ and thus should not be applied when the potential window is shifted.

3.3.3 Voltammetric Effects of Cosine Potential Wave When $n > 1$

When the value of n in Equation (3.13) is larger than 1, a plateau is found in the applied potential as shown in Figure 3.1, which becomes more pronounced with increasing n. The plateau, which signifies a temporary halt in the potential sweep, causes a double peak in the voltammogram such as in Figure 3.3. As the potential approaches the plateau during the sweep, the scan rate slows down leading to slower rate of material consumption while giving enough time for more A to diffuse from the bulk towards the interface. The slower reaction rate and the build up of A reduces the concentration gradient at the electrode surface which leads to a reduced current in the voltammogram. Once past the plateau, the scan rate and hence the reaction rate increase again resulting in a steeper concentration gradient, which manifests in the second peak. These two observations can be verified by examining the concentration profiles of the cosine square potential wave voltammogram. Figures 3.7(a) and 3.7(b) are both concentration profiles of the cosine square voltammogram shown in Figure 3.3. Figure 3.7(a) is the solution concentration of A during the forward sweep plotted with respect to the dimensionless potential and dimensionless space, and Figure 3.7(b) is the solution concentration of A at specific θ values plotted against the dimensionless space. The θ values chosen for Figure 3.7(b) were 0.3575, 0, and -0.3575 where $\theta = 0.3575$ is the potential at which the first peak is observed and $\theta = 0$ is the potential at which the plateau occurs. $\theta = -0.3575$ was chosen to illustrate the evolution of the concentration profile after the plateau.



(a) Solution concentration of A for the cosine square potential wave voltammogram plotted with respect to dimensionless potential and dimensionless space.



(b) Solution concentration of A for the cosine square potential wave voltammogram at specific θ plotted against dimensionless space.

Figure 3.7: The two figures show the solution concentration of A for the cosine square potential wave voltammogram in Figure 3.3. $\sigma = 10^4$ and $\theta_{shift} = 0$.

Looking at Figure 3.7(a), it is noticeable that the diffusion is distorted at $\theta = 0$, and Figure 3.7(b) shows the concentration at and near this potential. At $\theta = 0.3575$, the gradient at the interface is steep but decreases at $\theta = 0$ and increases again at $\theta = -0.3575$ which explains the double peak.

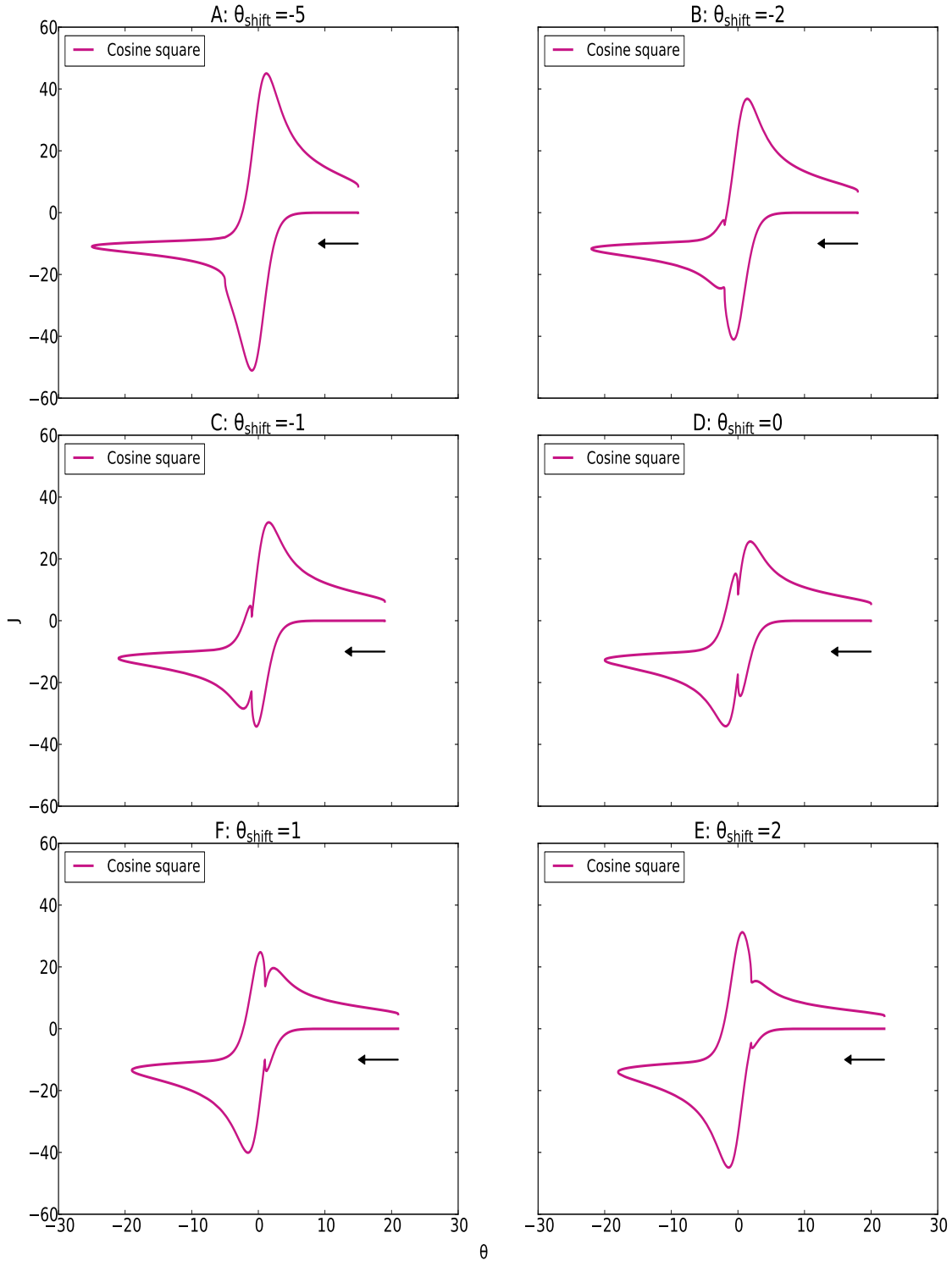


Figure 3.8: Voltammograms using a cosine square potential wave with different θ_{shift} values. A corresponds to $\theta_{shift} = -5$, B corresponds to $\theta_{shift} = -2$, C corresponds to $\theta_{shift} = -1$, D corresponds to $\theta_{shift} = 0$, E corresponds to $\theta_{shift} = 1$, and F corresponds to $\theta_{shift} = 2$.

The double peak is most apparent for potential waves that are approximately symmetric with respect to the formal potential but become less prominent at other potential shifts. Figure 3.8 shows voltammograms obtained using a cosine square pulse wave with different potential shifts in dimensionless coordinates. 3.8A corresponds to $\theta_{shift} = -5$, 3.8B corresponds to $\theta_{shift} = -2$, 3.8C corresponds to $\theta_{shift} = -1$, 3.8D corresponds to $\theta_{shift} = 0$, 3.8E corresponds to $\theta_{shift} = 1$, and 3.8F corresponds to $\theta_{shift} = 2$.

When $\theta_{shift} = 0$ such as in 3.8D and other θ_{shift} values close to 0, two distinct peaks are observed. However, from Figure 3.8 it is evident that when the potential shift is significantly negative, only one peak is observed whereas when the potential shift is significantly positive, one of the peaks diminishes. This behavior is clearer when the dimensionless peak current of each voltammogram is plotted against the corresponding potential shift. Figure 3.9 shows the dimensionless peak currents of the voltammograms plotted against their corresponding dimensionless potential shifts for all three potential waveforms: triangular, cosine ($n = 1$), and cosine square ($n = 2$).

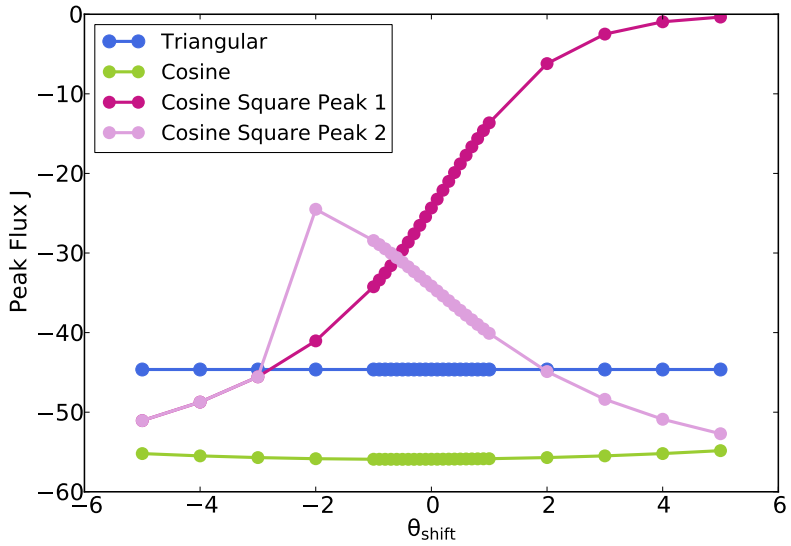


Figure 3.9: Dimensionless peak currents of individual voltammograms plotted against the corresponding θ_{shift} values for triangular, cosine, and cosine square potential waveforms. The blue dotted line is obtained from the triangular method, the green dotted line is from the cosine method, and the magenta and pink dotted lines correspond to the first and second peak of the cosine square voltammogram, respectively.

The blue dotted line represents the triangular results, the green dotted line represents the cosine results, and the magenta and pink dotted lines represent the first and second peak of the cosine square results, respectively. The triangular results show no variation in the peak current with respect to varing θ_{shift} values, which is to be expected since the triangular wave has a constant scan rate throughout the sweep. The cosine results show a slight change in peak current with respect to θ_{shift} as can be predicted from the change in temporal scan rates. This is the reason Equation (3.21) can only be applied to results obtained for $\theta_{shift} = 0$. In contrast to the triangular and cosine results, the cosine square peak currents exhibit considerable difference with respect to θ_{shift}. At $\theta_{shift} = -2$, two peaks emerge as represented by the magenta and pink dotted lines. The absolute value of the first peak current approaches 0 as the potential shift becomes increasingly positive while both peaks merge with decreasing potential shift. A sudden change in the second peak current is observed at $\theta_{shift} = -2$, which is the threshold at which two peaks are seen. Below $\theta_{shift} = -2$, only one peak is visible, but at the said potential shift, the second peak emerges and the first peak diminishes as evident from Figure 3.8. Beyond the point of intersection of the magenta and pink dotted lines, the two peaks swap dominance and the second peak becomes prominent while the first gradually diminishes.

The double peak caused by the cosine square wave results in a characteristic peak-to-peak separation as shown in Figure 3.10, which shows the changes in peak-to-peak separation of the voltammograms with varying θ_{shift} values. The results are again reported for the three potential waveforms using the same color scheme as in Figure 3.1.

For the triangular and cosine potential waves, the peak-to-peak separation shows very little to no variation and remain at a value of approximately 2.2 dimensionless units, which in dimensional term corresponds to approximately 57 mV (the standard peak-to-peak separation of a reversible system at 298 K when a triangular potential wave is employed). On the other hand, the peak-to-peak separation changes markedly depending on the θ_{shift} for the cosine square potential wave. As the potential shift approaches 0, the peak-to-peak separation decreases but at $\theta_{shift} = 0$

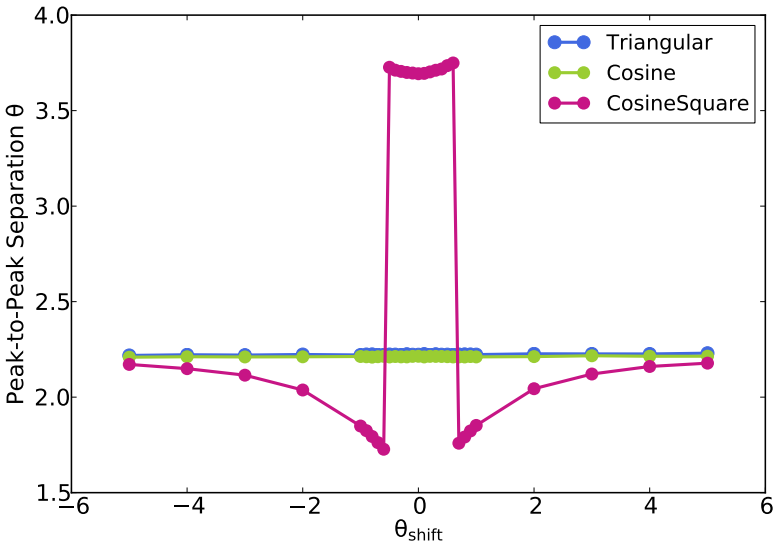


Figure 3.10: Dimensionless peak-to-peak separation plotted against corresponding θ_{shift} values for triangular, cosine, and cosine square potential waveforms. The same color scheme is used as in Figure 3.1.

and in its immediate vicinity, the peak-to-peak separation shows a sharp increase. The fact that double peaks appear and drastic changes in peak-to-peak separation are observed with varying potential shifts suggest that cosine waves with $n > 1$ can be used to determine the formal potential of a species of interest. From the figure, it is clear that the minimum of the potential jump occurs at $\theta_{shift} = 0$.

In practice, this would be performed by applying the cosine wave given by Equation (3.10) to an electrode and measuring the peak-to-peak separation of the voltammogram obtained. The same process would be repeated with different E_{avg} values and based on the plot of the experimental peak-to-peak separation against E_{avg}, the formal potential can be determined by obtaining the E_{avg} at which the minimum in the potential jump is observed.

3.4 Conclusions

This chapter proposed a novel approach to cyclic voltammetry, where a non-triangular waveform is repeatedly applied while the wave's average potential, E_{avg}, is shifted with respect to the reference potential. By this means, two challenges

were addressed. First, in triangular wave cyclic voltammetry, an instantaneous change in capacitive current is observed at the point of reversal where it causes a perturbation of the voltammogram. In contrast, the here-proposed waveform features a continuous slope across the entire potential range, minimizing the disruption of the voltammogram at the said point. Secondly, the proposed waveform yields double peaks in the voltammogram when n > 1, which separately vary in intensity depending on the difference between E_{avg} and E_f^0, and result in a sharp increase in the peak-to-peak separation at and near $E_{avg} - E_f^0 = 0$. It was shown that this effect can in principle be exploited as a tool to determine the formal potential of a reaction.

3.5 Experimental Verification

This section discusses the experimental verification of the aforementioned cosine-based potential wave method for electroanalysis. The characteristic voltammetric shapes when $n = 1$ and $n = 2$ were investigated and compared against the conventional triangular method. In particular, the capacitive current effect of the three methods were looked at closely and the formal potential of the $[Ru(NH_3)_6]^{3+}/[Ru(NH_3)_6]^{+2}$ couple was determined using the cosine-square potential wave. All experiments were performed by Dr. Hatem M. A. Amin.

3.5.1 Chemicals

Hexaammineruthenium(III) chloride ($[Ru(NH_3)_6]Cl_3$, 98 %, Aldrich) and potassium chloride (Aldrich, > 99 %) were used as received without further purification. All solutions were prepared with Milli-Q water with of resisitivity 18.2 MΩ cm at 298 K (Millipore Water Systems, U.K.) and degassed for 30 min with N_2 (99.998 %, BOC, U.K.) prior to each experiment and over solution during the measurement.

3.5.2 Instrumental

All experiments were conducted using a three-electrode setup with a glassy carbon disc (GC, 3.0 mm diameter, ALS Co. Ltd., Japan) as the working electrode, a

saturated calomel electrode (SCE, ALS Co. Ltd., Japan) for the reference electrode, and a Pt wire (GoodFellow, Cambridge, U.K.) as the counter electrode. The temperature was maintained constant at 298 K using a water bath connected to a temperature controller (SCT1, Stuart, U.K.) in a Faraday cage. A more detailed discussion on the experimental setup is given in the published work [2].

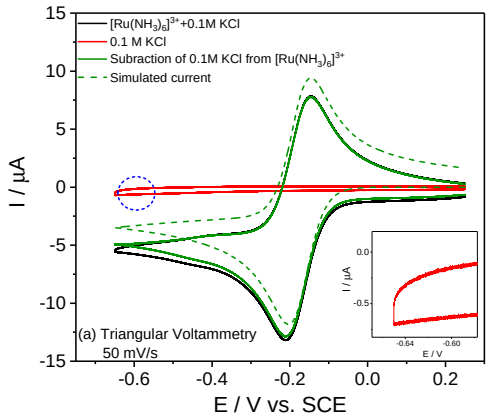
3.5.3 Results and Discussion

This section is divided into four parts; the first part discusses the capacitive effect of the three methods, the second part discusses the scan rate dependency of the voltammograms, the third part analyzes the voltammetric behavior when $n = 2$, and the fourth part focuses on the formal potential determination.

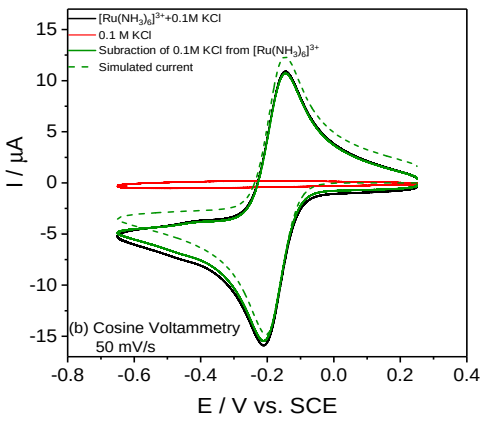
Cyclic Voltammetry with Triangular, Cosine, and Cosine Square Potential Waveforms

First, the influence of the aforementioned waveforms on the capacitive current is addressed in blank solutions, and then the voltammetric behavior of $[Ru(NH_3)_6]Cl_3$ is discussed when the three waveforms are applied. Figure 3.11 compares the experimental voltammograms obtained in both, blank solution (0.10 M KCl) and in 0.96 mM $[Ru(NH_3)_6]Cl_3$/0.10 M KCl solution using the three different waveforms at a scan rate of 0.05 V s^{-1}: (a) triangular, (b) cosine, and (c) cosine square. All three figures were plotted for an E_{avg} (denoted in the following sections as E_{centre}) of -0.2 V. The black solid curve shows the raw data including both Faradaic and capacitive current, the red solid curve shows the capacitive current, the green solid curve shows the experimental Faradaic-only current obtained by subtracting the red curve from the black curve, and the green dashed line is the simulated Faradaic current.

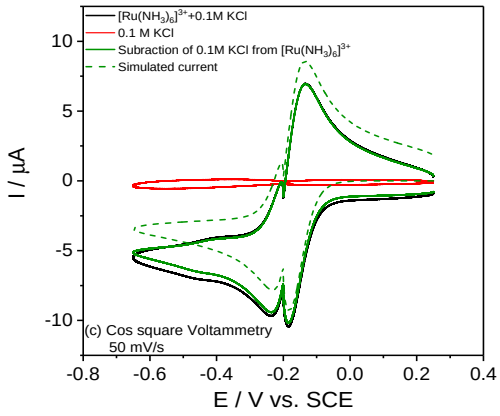
Looking at the triangular result in Figure 3.11(a), the capacitive current shows a curved-corner rectangle at the point of reversal. At this point, a sharp change in the capacitive current is observed becasuse the current instantly drops upon switching the sweep from forward to backward direction, causing a discontinuity. On the other hand, the capacitive currents obtained using the cosine and cosine square potential waves are continuous at all points as these waves are based on continuous



(a) Triangular voltammogram.



(b) Cosine voltammogram.



(c) Cosine square voltammogram

Figure 3.11: Voltammograms of (a) triangular, (b) cosine, and (c) cosine square potential waves obtained at GC electrode in blank 0.10 M KCl solution (red solid curve, capacitive current) and in 0.96 mM $[Ru(NH_3)_6]Cl_3$/0.10 M KCl solution (black solid curve, Faradiac + capacitive currents) at a scan rate of 0.05 V s^{-1}. The E_{centre} for this figure is -0.2 V. The green solid curve is the experimental Faradaic-only current obtained via subtraction of the red curve from the black curve, and the green dashed line is the simulated Faradaic current.

functions, avoiding the current cut at the reversal potential and thus eliminate any consecutive influence of the discontinuity on the voltammetric behavior. The results shown here agree with the theoretical behavior shown in Figure 3.4. The difference between the experimental and simulated curves was most likely due to the history of the electrode in which some materials may have been adsorbed or desorbed, causing a shift in the recorded voltammogram.

As mentioned in Section 3.3.3, the voltammetric response of $[Ru(NH_3)_6]Cl_3$ to the applied cosine square potential wave is markedly different from the response

to the conventional triangular sweep voltammetry. In contrast to the single redox peak observed in standard cyclic voltammetry, two distinct peaks were observed at certain values of E_{centre}. However, the cosine potential wave shows a similar voltammetric behavior to the triangular method.

Scan Rate Dependency of the Voltammograms

This section discusses the voltammetric response to variable scan rates, which were varied from 0.025 to 2 V s^{-1} using the same GC electrode in 0.96 mM $[Ru(NH_3)_6]Cl_3$/0.10 M KCl solution. For the cosine-based waves the duration of a single cycle was adjusted such that the average scan rate was the same as that in the corresponding triangular cyclic voltammogram. Independent of the applied potential waveform, the measured Faradaic current was shown to be directly proportional to the square root of the scan rate as shown in Figure 3.12, which plots the absolute peak currents of the voltammograms recorded at $E_{centre} = -0.18$ V against the square root of the scan rates. For the reversible one-electron reduction of $[Ru(NH_3)_6]^{3+}$, a square root dependency of peak current on scan rate is seen according to the Randles-Ševčík equation. Since the figure was plotted using the absolute peak currents, the equation was also modified to be expressed in absolute values:

$$I_p = 0.446 F A_{ele} c_A^* \sqrt{\frac{F D_A \nu}{RT}} \tag{3.23}$$

where $D_A = 8.43 \cdot 10^{-10}$ m^2 s^{-1} [28], and $c_A^* = 0.96$ mol m^{-3}. From these values, the linear regression of the peak currents obtained from triangular cyclic voltammetry revealed a pre-factor of 0.434 ± 0.001, which is in good agreement with the theoretical value of 0.446; the error bars of the pre-factors are based on the standard error of the slope. However, for the voltammograms with cosine waveform, the peak currents and consequently the pre-factor in the Randles-Ševčík equation were 24 % higher than that obtained from the triangular wave, as explained earlier. For the cosine wave, the modified Randles-Ševčík equation pre-factor was determined to be 0.539 ± 0.001, which is close to the simulated value of 0.559. Although for the cosine square potential wave the peak is split into two peaks with lower currents,

the peak currents are both directly proportional to the square root of the scan rate and gave pre-factors of 0.346 ± 0.0025 for the first peak and 0.215 ± 0.003 for the second peak. The above results confirm that the experimental data for both triangular and cosine waves coincide with the simulation results.

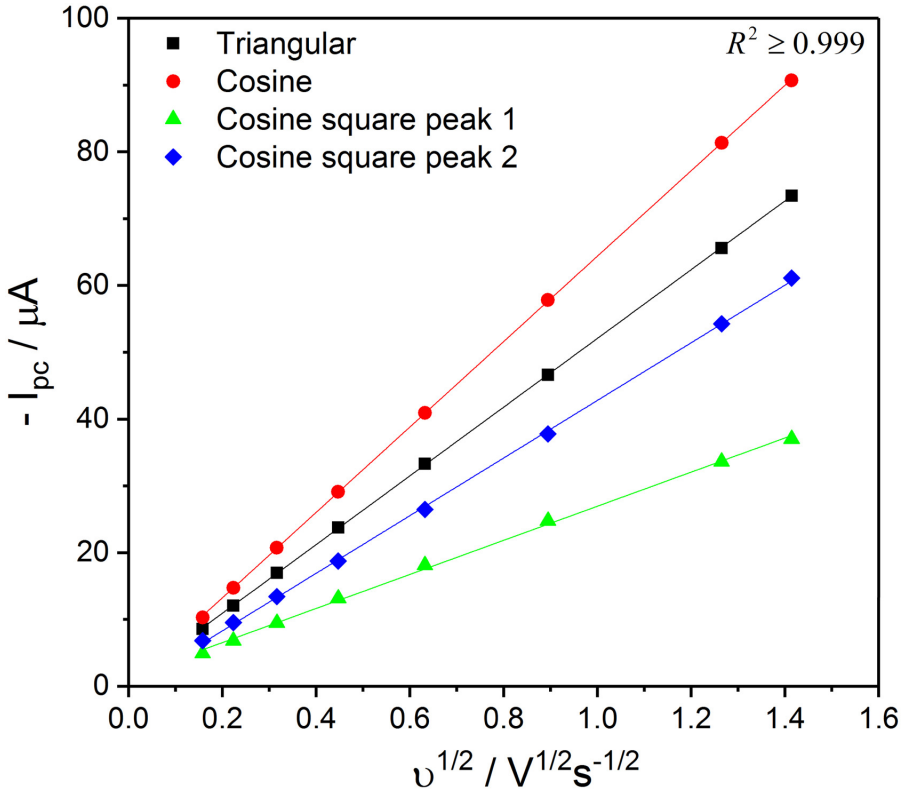


Figure 3.12: Plot of capacitive current-corrected cathodic peak currents against the square root of the scan rate using triangular, cosine, and cosine square potential waves ranging from 0.025 to 2 V s^{-1} in $[Ru(NH_3)_6]Cl_3$/0.10 M KCl solution at 298 K. The linear regressions are shown.

Analysis of the Voltammetric Behavior

Next, the change in voltammetric behavior is discussed when the potential window is shifted. To exploit the characteristic features arising from the cosine square potential wave for quantitative analysis, the cosine square wave was applied using different E_{centre} values. Examples of the experimental Faradaic-only voltammograms are displayed in Figure 3.13. These voltammograms were again recorded using the same GC electrode in 0.96 mM $[Ru(NH_3)_6]Cl_3$/0.10 M KCl solution at 298 K. The average scan rate is 0.05 V s^{-1}, which was achieved by setting the duration of

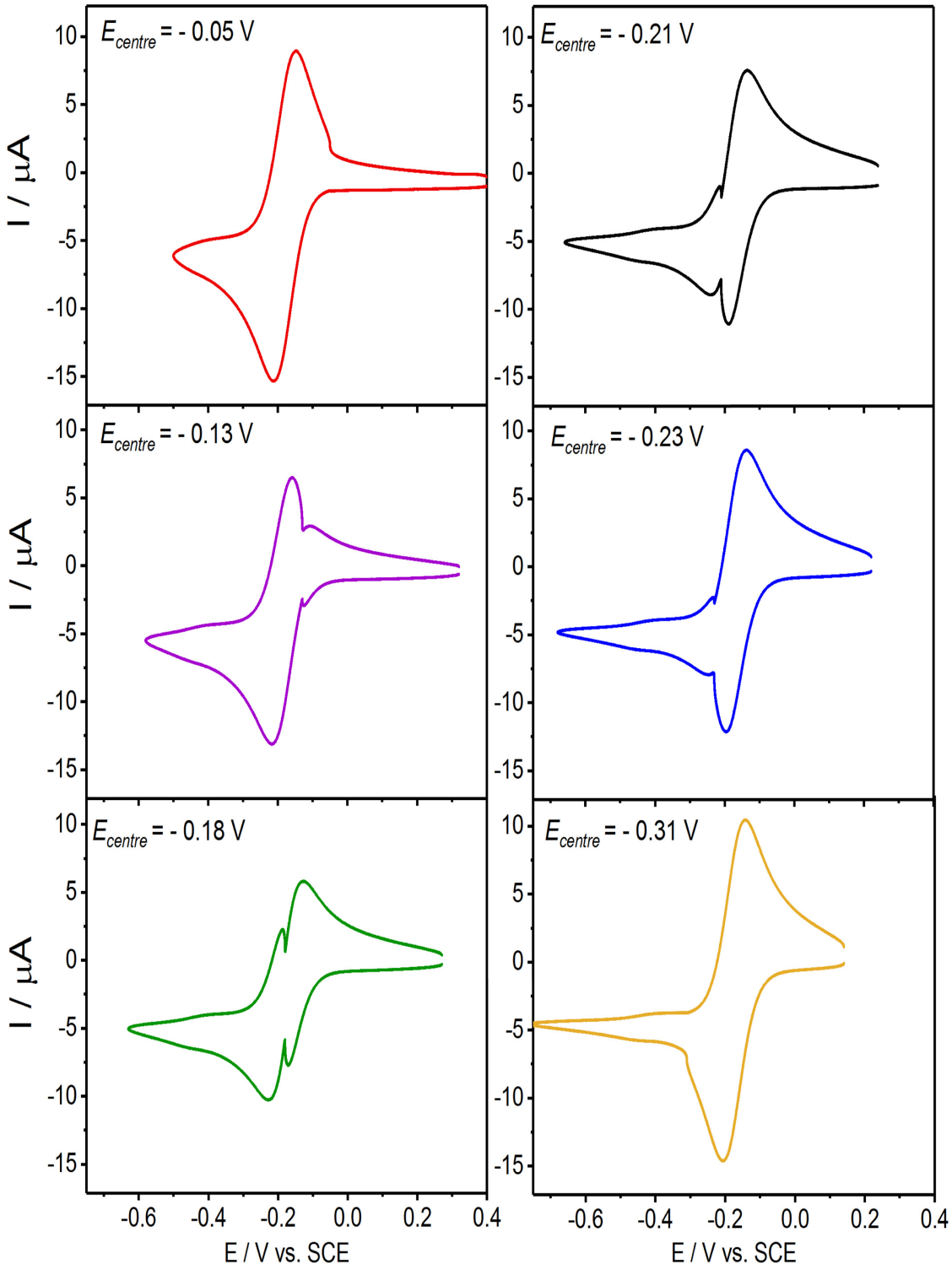


Figure 3.13: Capacitive current-corrected voltammograms obtained at GC electrode with cosine square potential waveform at different E_{centre} values in 0.96 mM $[Ru(NH_3)_6]Cl_3$/0.10 M KCl solution at an average scan rate of 0.05 V s^{-1}.

each single cycle to 36 s (the same duration time for the triangular sweep). The same series of voltammograms were recorded for the triangular and cosine potential waveforms. Both waveforms resulted in similar voltammograms with a single peak at the same potential independent of the applied potential window whereas the cosine square potential wave produced voltammograms with characteristic features such as the split peak, which were exploited for quantitative analysis as discussed below. The voltammograms obtained at varying E_{centre} values for the three methods are given in *Appendix*: A.2.

To analyze the unique behavior of the cosine square voltammograms, the experimental peak currents were plotted against the applied E_{centre} as shown in Figure 3.14. The dots represent the experimental results while the solid lines represent the simulation result.

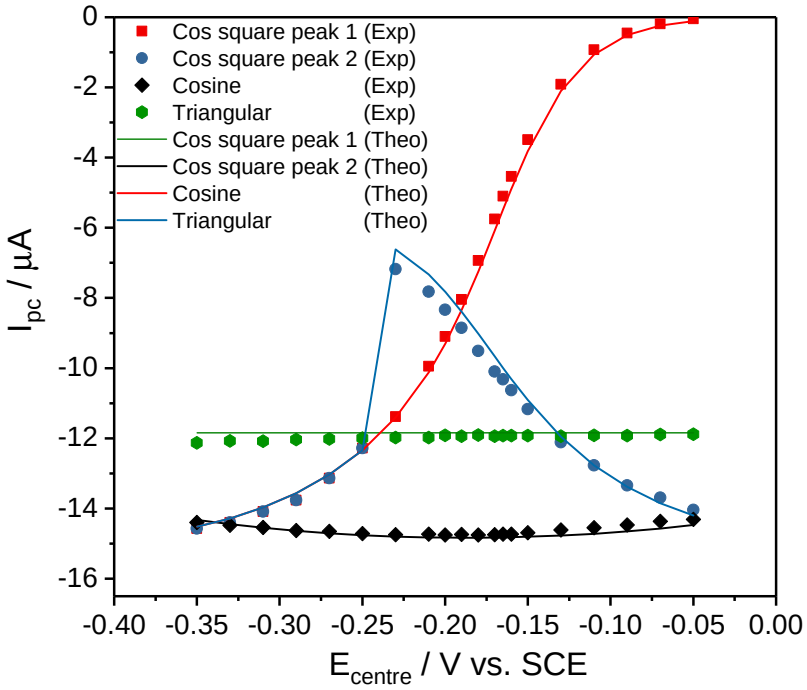


Figure 3.14: Plot of the cathodic peak currents (capacitive current-corrected) obtained from the corresponding voltammograms with the triangular, cosine, and cosine square waves using different E_{centre} values.

Notably, the intensity of the two peaks of the cosine square result varies as E_{centre} is shifted. At -0.25 < E_{centre} < -0.07 V, the peak spilts into two with the first peak dominating, and after the point of intersection in the plot, the second

peak becomes dominant. Meanwhile, at E_{center} values lower than -0.25 V, the two peaks merge and at E_{centre} values higher than -0.07 V, the first peak diminishes as expected from earlier discussion. The split of the peak can clearly be explained from the cosine square function (Equation (3.10)) and its waveshape (Figure 3.1). As explained in Section 3.3.3, at the midpoint of the potential window, a plateau is observed, which indicates a temporal hold of potential and causes a drop of current. For direct comparison with theory, the simulated peak currents from the finite difference method using the same parameters as given in Section 3.3 were also provided and show excellent agreement with the experimental results.

Determination of the Formal Potential of $[Ru(NH_3)_6]^{3+/2+}$

A more significant characteristic observed in the voltammetry with the cosine square potential waveform is the strong influence of E_{centre} on the peak-to-peak separation of the voltammogram. As shown in Figure 3.15, a drastic change in the peak-to-peak separation (potential jump) appears at certain E_{centre} values, which is also confirmed in the simulations. The minimum of this concave step at the jump gave a potential of -0.175 ± 0.001 V, and based on the previous analysis, the formal potential is determined given that $E_{shift} = E_{centre} - E_f^0$. Since the minimum is observed at $E_{shift} = 0$, E_{centre} and E_f^0 must be the same value thus giving $E_f^0 = -0.175 \pm 0.001$ V. The excellent fit between the experimental and simulated results, which were calculated based on the formal potential value above, shows that the peak-to-peak separation analysis of the voltammograms of the cosine square wave provides an alternative method to determine the formal potential of the $[Ru(NH_3)_6]^{3+/2+}$ system.

For comparison, E_f^0 was also determined from the midpoint of the voltammograms with triangular and cosine waves and a value of -0.178 ± 0.001 V was obtained from both methods; the error bars indicate the experimental error of the potentiostat. For further confirmation of the result, an independent experiment with a microelectrode in $[Ru(NH_3)_6]Cl_3$ solution was conducted and revealed $E_f^0 = -0.177 \pm 0.001$ V vs. SCE (see *Appendix*: A.2). The E_f^0 values obtained from the different methods are close to within an experimental error for the analog

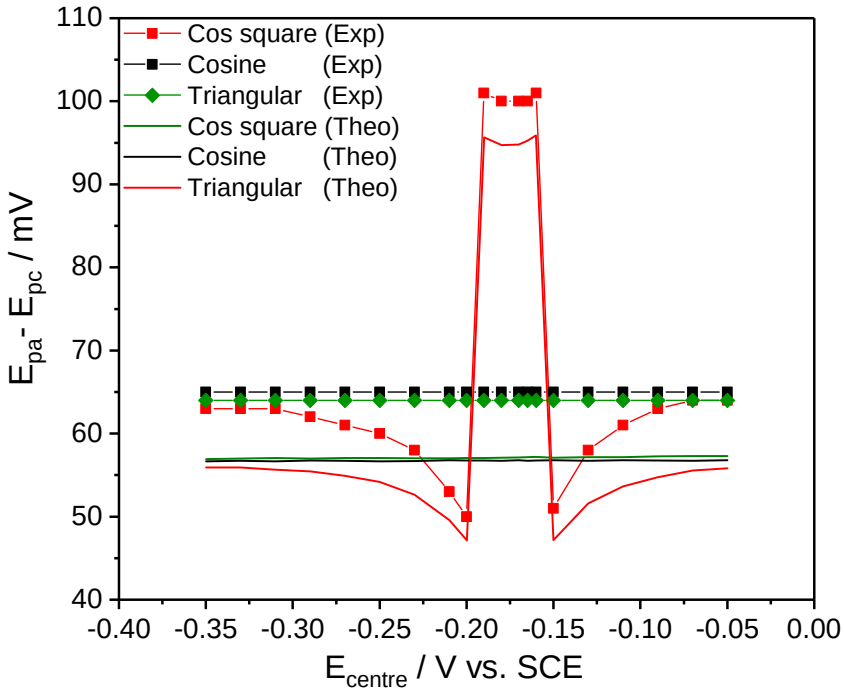


Figure 3.15: Plot of the peak-to-peak separation obtained from the corresponding capacitive current-corrected voltammograms using the triangular, cosine, and cosine square waves at different E_{centre} values.

potentiostat system of ± 1 mV, and hence validate the theory. For the voltammetry of the triangular wave, the peak-to-peak separation did not change with the potential shift and remained at a value of 64-65 mV, which is close to the theoretical 57 mV. It is noteworthy to mention that the few millivolts difference from the theoretical value of 57 mV is mostly due to slightly incomplete electrolytic support, and in turn a small non-compensated resistance in solution. A ratio of the supporting electrolyte to $[Ru(NH_3)_6]Cl_3$ concentrations of > 100 is required to achieve a full diffusion-only behavior [14].

3.5.4 Conclusions

The theory for a non-triangular potential wave cyclic voltammetry was experimentally verified at a macrodisc electrode for the reversible $[Ru(NH_3)_6]^{3+/2+}$ system. In contrast to the classical triangular potential wave, a cosine-based potential waveform was employed in cyclic voltammetry to reduce the discontinuity in the capacitive currents at the potential vertex, which inevitably occurs in the triangular cyclic

voltametry. The significant features arising from the voltammograms with cosine square potential wave provided a simple route to determine the formal potential of $[Ru(NH_3)_6]^{3+/2+}$; and a value of -0.175 V vs. SCE was obtained which agress with other methods (-0.177 V from microelectrode voltammetry). The verification of the theory is evident from the excellent agreement with the experimental results.

References

[1] Y. Uchida, E. Kätelhön, R. G. Compton, *Journal of Electroanalytical Chemistry* **2017**, *801*, 381–387.

[2] H. M. Amin, Y. Uchida, C. Batchelor-McAuley, E. Kätelhön, R. G. Compton, *Journal of Electroanalytical Chemistry* **2018**, *815*, 24–29.

[3] R. S. Nicholson, I. Shain, *Analytical Chemistry* **1964**, *36*, 706–723.

[4] R. G. Compton, C. E. Banks, *Understanding Voltammetry*, Imperial College Press, **2010**.

[5] A. J. Bard, L. R. Faulkner, *Electrochemical Methods: Fundamentals and Applications*, John Wiley & Sons Inc, **2000**.

[6] C. Batchelor-McAuley, E. Kätelhön, E. O. Barnes, R. G. Compton, E. Laborda, A. Molina, *ChemistryOpen* **2015**, *4*, 224–260.

[7] E. Kätelhön, *Research and Reviews in Electrochemistry* **2017**, *8*, E1–E2.

[8] K. Cinková, M. Clark, S. V. Sokolov, C. Batchelor-McAuley, Ľ. Švorc, R. G. Compton, *Electroanalysis* **2017**, *29*, 1006–1013.

[9] J. E. B. Randles, *Trans. Faraday Soc.* **1948**, *44*, 327–338.

[10] A. Ševčík, *Collect. Czech. Chem. Commun.* **1948**, *13*, 349–377.

[11] G. A. Mabbott, *Journal of Chemical Education* **1983**, *60*, 697.

[12] H. T. H. Chan, E. Kätelhön, R. G. Compton, *Journal of Electroanalytical Chemistry* **2017**, *799*, 126–133.

[13] M. C. Henstridge, E. Laborda, E. J. Dickinson, R. G. Compton, *Journal of Electroanalytical Chemistry* **2012**, *664*, 73–79.

[14] E. J. F. Dickinson, J. G. Limon-Petersen, N. V. Rees, R. G. Compton, *The Journal of Physical Chemistry C* **2009**, *113*, 11157–11171.

[15] N. Elgrishi, K. J. Rountree, B. D. McCarthy, E. S. Rountree, T. T. Eisenhart, J. L. Dempsey, *Journal of Chemical Education* **2018**, *95*, 197–206.

[16] D. H. Evans, K. M. O'Connell, R. A. Petersen, M. J. Kelly, *Journal of Chemical Education* **1983**, *60*, 290.

[17] C. Amatore, A. Oleinick, I. Svir, *Analytical Chemistry* **2008**, *80*, 7947–7956.

[18] S. Ching, R. Dudek, E. Tabet, *Journal of Chemical Education* **1994**, *71*, 602.

[19] J. Heinze, *Angewandte Chemie International Edition in English* **1984**, *23*, 831–847.

[20] C. Amatore, C. Pebay, L., A. Wang, J.-S. Warkocz, *Analytical Chemistry* **2010**, *82*, 6933–6939.

[21] C. N. Reilley, G. W. Everett, R. Johns, *Analytical Chemistry* **1955**, *27*, 483–491.

[22] K. Ngamchuea, S. Eloul, K. Tschulik, R. G. Compton, *Analytical Chemistry* **2015**, *87*, 7226–7234.

[23] R. G. Compton, E. Laborda, K. R. Ward, *Understanding Voltammetry: Simulation of Electrode Processes*, Imperial College Press, **2013**.

[24] J. Crank, *The Mathematics of Diffusion*, Oxford University Press, **1979**.

[25] H. Wang, L. Pilon, *Electrochimica Acta* **2012**, *64*, 130–139.

[26] M. J. A. Shiddiky, A. A. J. Torriero, J. M. Reyna-Gonzalez, A. M. Bond, *Analytical Chemistry* **2010**, *82*, 1680–1691.

[27] P. Kant, R. Kant, *The Journal of Physical Chemistry C* **2014**, *118*, 26599–26612.

[28] Y. Wang, J. G. Limon-Petersen, R. G. Compton, *Journal of Electroanalytical Chemistry* **2011**, *652*, 13–17.

4

Semi-circular Potential Waves in Voltammetry: Theory and Experiment

The previous chapter discussed the benefits of employing a cosine-based potential waveform to determine the formal potential of a reversible one-electron redox couple from theoretical and experimental approaches. This chapter builds on the idea of using a non-triangular potential waveform and introduces a semi-circular potential waveform. The work presented here are published in the '*Journal of Electroanalytical Chemistry* 2018, 818, 140-148' [1] and the '*Journal of Electroanalytical Chemistry* 2019, 836, 62-67' [2].

Contents

4.1 Introduction 74
4.2 Theory 75
4.2.1 Theoretical Model 75
4.2.2 Dimensionless Coordinates 77
4.2.3 Semi-circular Potential Sweep 78
4.2.4 Simulation via Finite Differences 81
4.3 Results and Discussion 82
4.3.1 Single Electrochemically Reversible Species: Linear versus Semi-circular Potential Waves 82
4.3.2 Two Species Linear versus Semi-circular Potential Sweeps 85
4.4 Conclusions 94
4.5 Experimental Verification 95
4.5.1 Chemicals 95
4.5.2 Instrumental 96

4.5.3 Results and Discussion 96
4.6 Conclusions 103

4.1 Introduction

As discussed in the previous chapter, typical cyclic voltammetry (CV) and linear-sweep voltammetry (LSV) employ a linear potential wave [3] in which the scan rate is constant throughout the voltammetric sweep, and is used to extract information such as analyte concentrations, diffusion constants, and kinetics of a redox system [4, 5]. The potential wave for linear voltammetry is expressed by the following equation:

$$E(t) = \pm\nu t + E(t = 0) \tag{4.1}$$

where the $\pm$ sign indicates oxidation or reduction and ν is the scan rate. Unlike cyclic voltammetry, linear-sweep voltammetry only considers the forward sweep and thus gives a linear wave rather than a triangular wave. For analytical applications, other techniques such as differential pulse voltammetry (DPV) and square wave voltammetry (SWV) are used because of their sensitivities and their abilities to effectively suppress the capacitive current effect on the voltammogram [6–10]. However, the interpretation of SWV is often very much more complex compared to cyclic or linear-sweep voltammetry where a linear wave (4.1) is applied [3, 11, 12].

This chapter proposes an alternative method to perform sweep voltammetry for electroanalysis using a semi-circular potential wave, which gives an instantaneously infinitely fast scan rate at the midpoint of the potential window. Since the current is proportional to the scan rate, the aformentioned feature greatly increases the current response at the potential at which the infinite scan rate is observed if this coincides with a Faradaic feature in the voltammetry. Additionally, the semi-circular potential waveform applies relatively slow voltage scan rates in other parts of its wave, thereby suppressing the current response in those regions. The analysis presented shows that these two features - instantaneously infinitely fast scan rate and relative suppression of current everywhere else - is beneficial in electroanalysis

of a mixture because the peak current of one species can be greatly amplified while the current resulting from other species are much suppressed.

4.2 Theory

In the following sections, the theoretical model is introduced and the semi-circular potential waveform is explained. Additionally, the dimensionless coordinates employed in the simulations are listed.

4.2.1 Theoretical Model

Two simple one-electron electrochemically-reversible reduction reactions of A to C and B to D were investigated simultaneously at a planar macroelectrode under diffusion-only conditions, where species A and C were assumed to have equal diffusion coefficients as did B and D, but the redox couples A/C and B/D may have different diffusion coefficients from each other:

$$\begin{aligned} A(aq) + e &\rightleftharpoons C(aq) \\ B(aq) + e &\rightleftharpoons D(aq) \end{aligned} \tag{4.2}$$

The system of interest was simulated under the assumption that sufficiently high concentration of supporting electrolyte was present in order to suppress migration [13–16] and ensured diffusion as the only means of mass transport of analyte to the electrode surface [17–19]. Although it is noted that when the scan duration time is long, convection [20–22] may need to be taken into consideration [23–25]. The transport of analytes is described via the one-dimensional diffusion equation given by Fick's Second Law [26, 27]:

$$\frac{\partial c_j}{\partial t} = D_j \frac{\partial^2 c_j}{\partial x^2} \tag{4.3}$$

where j is the species under study and D is its diffusion coefficient. For the reactions shown in Equation (4.2), $D_A = D_C$ and $D_B = D_D$ but $D_A \neq D_B$. Since the two reactions were independent of each other, boundary conditions were established

akin to that of a one-species reaction where it was assumed that initially only the reactant is present in the bulk solution [3, 26] and prior to applying the potential, the concentration of the reactant and product are uniform in space:

$$\begin{aligned} t \leq 0,\ \text{all}\, x,\ c_A = c_A^*,\ c_C = 0 \\ t \leq 0,\ \text{all}\, x,\ c_B = c_B^*,\ c_D = 0 \end{aligned} \tag{4.4}$$

As t increases, c_A, c_B, c_C, and c_D near the electrode surface vary but no change is observed at the outer boundary surface:

$$\begin{aligned} t > 0,\ x \to \infty,\ c_A = c_A^*,\ c_C = 0 \\ t > 0,\ x \to \infty,\ c_B = c_B^*,\ c_D = 0 \end{aligned} \tag{4.5}$$

Due to conservation of mass, the amount of A and B consumed at the electrode surface equal the amount of C and D produced, giving the conditions:

$$\begin{aligned} t > 0,\ x = 0,\ -\frac{\partial c_A}{\partial x} = \frac{\partial c_C}{\partial x} \\ t > 0,\ x = 0,\ -\frac{\partial c_B}{\partial x} = \frac{\partial c_D}{\partial x} \end{aligned} \tag{4.6}$$

assuming $D_A = D_C$ and $D_B = D_D$. Therefore, for the diffusion coefficients established above, the following conditions hold true for all space and time:

$$\begin{aligned} c_A + c_C = c_A^* \\ c_B + c_D = c_B^* \end{aligned} \tag{4.7}$$

The electrode kinetics can be described via the Butler-Volmer equation for a general one-electron reaction of $O(aq) + e \rightleftharpoons R(aq)$ where $O = A$ or B and $R = C$ or D, given as [16, 28, 29]:

$$j_{net} = k_0 exp\left[\frac{-\alpha F(E - E_f^0)}{RT}\right][O]_0 - k_0 exp\left[\frac{(1-\alpha)F(E - E_f^0)}{RT}\right][R]_0 \tag{4.8}$$

where j_{net} is the flux of the reactant to the electrode surface, k_0 is the standard electrochemical rate constant, $[O]_0$ and $[R]_0$ are the surface concentrations of the

reactant and product, respectively. α is the transfer coefficient [30, 31], F, R, and T have their usual meanings, E is the applied potential, and E_f^0 is the formal potential of the redox couple under investigation. The Butler-Volmer boundary condition - shown in Equation (4.8) - was implemented with a large k_0 to simulate a reversible limit. The flux of the species to the electrode surface is described via Fick's First Law, which can be written in the form:

$$j_O = -D_O \left(\frac{\partial c_O}{\partial x} \right)_{x=0} = -[k_{red}[O]_0 - k_{ox}[R]_0] \tag{4.9}$$

assuming equal diffusion coefficients for O and R. Using the relationships $\theta = \frac{F}{RT}(E - E_f^0)$, $k_{red} = k_0 e^{-\alpha\theta}$, and $k_{ox} = k_0 e^{(1-\alpha)\theta}$, Equation (4.9) can be written as:

$$D_O \left(\frac{\partial c_O}{\partial x} \right) = k_0 e^{-\alpha\theta}[O]_0 - k_0 e^{(1-\alpha)\theta}[R]_0 \tag{4.10}$$

Equation (4.9) and (4.10) give the concentration gradient of the reactant at the electrode surface. In the systems of interest, the A/C and B/D redox couple were both assumed to be fully reversible in which the electrode kinetics are fast compared to the mass transport and attain a Nernstian equilibrium [3, 32], thus the boundary condition in Equation (4.8) can be replaced by [11, 26]:

$$E = E_f^0 + \frac{RT}{F} ln \frac{[O]_0}{[R]_0} \tag{4.11}$$

The Nernst equation is used for systems with fast electrode kinetics whereas the Butler-Volmer equation encompasses systems with both, fast and slow electrode kinetics. The two systems of interest, the A/C and B/D redox couple, are electrochemically reversible and can thus be described with the Nernst equation.

4.2.2 Dimensionless Coordinates

The simulations were run using the dimensionless forms of the expressions given earlier using the conversion factors listed in Table 4.1.

Table 4.1: Dimensionless parameters. [26]

Parameter	Normalization
concentration	$C_j = \frac{c_j}{c_A^*}$
diffusion coefficient	$d_j = \frac{D_j}{D_A}$
spatial coordinate	$X = \frac{x}{\epsilon}$
time	$\tau = \frac{D_A t}{\epsilon^2}$
potential	$\theta = \left(\frac{F}{RT}\right)(E - E^0_{f,A/C})$
scan rate	$\sigma = \left(\frac{\epsilon^2}{D_A}\right)\left(\frac{F}{RT}\right)\nu$
current	$J = \frac{I}{\pi\epsilon F D_A c_A^*}$
rate constant	$K_0 = \frac{k_0\epsilon}{D_A}$

Given these expressions, Equation (4.3) can be written in its dimensionless form:

$$\frac{\partial C_j}{\partial \tau} = d_j \frac{\partial^2 C_j}{\partial X^2} \tag{4.12}$$

and Equation (4.9) becomes:

$$\frac{C_{O,1} - C_{O,0}}{h} = \frac{1}{d_j} K_0 f(\theta)\{C_{O,0} - [1 + C_R^* - C_{O,0}]e^{\theta}\} \tag{4.13}$$

where $C_{O,1}$ and $C_{O,0}$ correspond to the dimensionless concentrations of O at X_1 and X_0, respectively, $f(\theta) = e^{-\alpha\theta}$, and $h = X_1 - X_0$ assuming O and R have equal diffusion coefficients.

4.2.3 Semi-circular Potential Sweep

The goal of this project was to employ a potential wave with an instantaneously infinitely fast scan rate at some potential and a slow scan rate in other areas of the wave in order to selectively amplify the peak current of one species at its formal potential and suppress the current contribution of others for analytical applications. To this end, a semi-circular potential wave function was introduced which possesses all the desired features. As evident from Figure 4.1, the linear potential wave, as given by Equation (4.1), shows a constant scan rate throughout the duration time

but the semi-circular wave when centred at $\theta = 0$ has the highest instantaneous scan rate at $\theta = 0$ and rapidly decreases as the potential becomes further from zero.

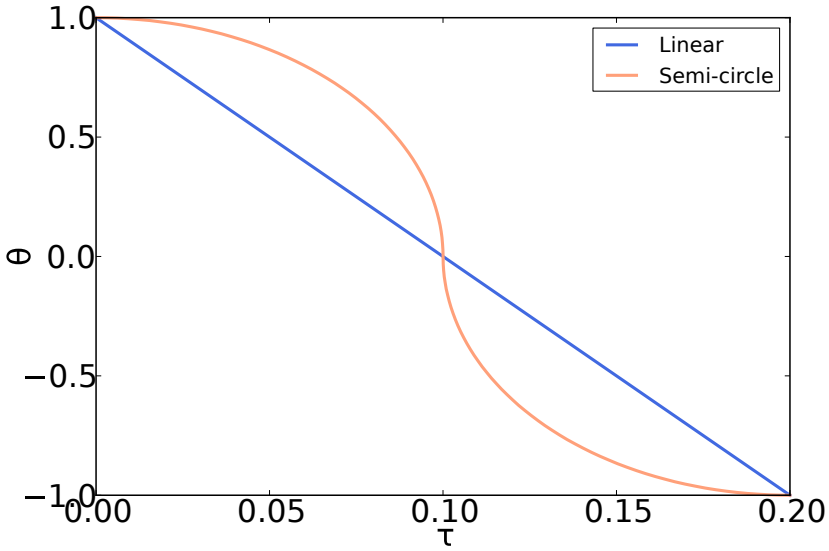


Figure 4.1: A schematic representation of the two potential waves centrered at $\theta = 0$ with an amplitude of 1. The blue line corresponds to the linear wave and the orange line corresponds to the semi-circular wave.

The semi-circle function is advantageous in a way that the potential wave displays the desired features and the equation is easily understood. The general form of a circle equation centred at (a, b) is given as:

$$(x - a)^2 + (y - b)^2 = r^2 \tag{4.14}$$

where a and b determine the shift from the point of origin defined as $(0, 0)$, and r is the radius. Solving Equation (4.14) for y yields:

$$y = \pm\sqrt{r^2 - (x - a)^2} + b \tag{4.15}$$

When applying Equation (4.15) to voltammetry, y represents the function of the potential E with respect to time t, r represents the amplitude A_0 of the wave in volts, x represents the time t, a represents the fraction of the maximum time when the centre of each semi-circle is observed thus defined as $a = ct_{max}$, and b

represents the shift along the y-axis and is replaced by the expression E_{avg}, which is the midpoint of the potential window defined as $E_{avg} = \frac{E_i+E_f}{2}$:

$$E(t) = \pm\sqrt{A_0^2 - [\nu(t - ct_{max})]^2} + E_{avg} \tag{4.16}$$

ν ensures that the duration time of the sweep remains constant between the linear and semi-circular method. Using the dimensional to dimensionless transformations given above, Equation (4.16) becomes:

$$\theta(\tau) = \pm\sqrt{\theta_{A_0}^2 - \sigma(\tau - c\tau_{max})^2} + \theta_{shift} \tag{4.17}$$

where θ_{A_0} is the dimensionless amplitude and σ is the dimensionless average scan rate obtained from the slope of the linear potential wave. In Figure 4.1, the first semi-circle wave is centred around $\tau = 0$ and the second semi-circle is centre around $\tau = \tau_{max}$, thus they were plotted using $c = 0$ and $c = 1$ respectively.

It was necessary to ensure the values within the square root was a positive value and thus the absolute value was taken. The discretized dimensionless form of Equation (4.17) is:

$$\theta(\tau_k) = \pm\sqrt{\left|\theta_{A_0}^2 - [\sigma \cdot (k \cdot \Delta\tau - c\tau_{max})]^2\right|} + \theta_{shift} \tag{4.18}$$

where k is the time step, $\Delta\tau$ is the difference between each time step defined as $\Delta\tau = \frac{\tau_{max}}{m}$ and $\tau_{max} = \frac{2\theta_{A_0}}{\sigma}$.

The justification for taking the absolute value and adding the σ term is given in the following. Using the transformations given, Equation (4.18) can be written in the form:

$$\theta(\tau_k) = \pm\sqrt{\left|\theta_{A_0}^2 - \left[4\theta_{A_0}^2 \cdot \left(\frac{k}{m} - c\right)^2\right]\right|} + \theta_{shift} \tag{4.19}$$

Figure 4.1 shows that the semi-circular potential wave must be described in terms of the first positive region and the second negative region, both of which have their own centre of origin expressed in terms of $c\tau_{max}$, where $c = 0$ and $c = 1$

for the first and second semi-circles, respectively. Assuming the wave is centred at 0 ($\theta_{shift} = 0$), Equation (4.19) gives:

$$\begin{aligned} \theta(\tau_k) &= \sqrt{\left|\theta_{A_0}^2 - \left[4\theta_{A_0}^2 \cdot \left(\frac{k}{m}\right)^2\right]\right|} \\ \theta(\tau_k) &= -\sqrt{\left|\theta_{A_0}^2 - \left[4\theta_{A_0}^2 \cdot \left(\frac{k}{m} - 1\right)^2\right]\right|} \end{aligned} \tag{4.20}$$

From Figure 4.1 the certain conditions Equation (4.18) must fulfill is known. At $k = 0$ and $k = m$, the potential must equal the positive and negative amplitude, respectively, and at $k = \frac{m}{2}$ the potential must equal 0. Substituting each k value yields $\theta(\tau_0) = \theta_{A_0}$, $\theta(\tau_{m/2}) = 0$, and $\theta(\tau_m) = -\theta_{A_0}$. From the above justifications, it is clear that the parameters introduced in Equation (4.18) are necessary in order to preserve the desired semi-circular features with varying average scan rates.

4.2.4 Simulation via Finite Differences

All simulations were performed using the finite difference method through discretization of the dimensionless diffusion equation and the backward implicit method as explained in Chapter 2. The theoretical model introduced above was implemented in *C++* and plotting was performed in *Python* with the packages *NumPy* and *matplotlib*. Thorough testing [33] was performed via convergence tests, the conservation of mass test, and comparing the peak currents and peak positions with theoretical values where available. It is, however, noted that the semi-circular method does not fully converge with respect to $\Delta\theta$ at the point of infinite scan rate and in its vicinity as explained in detail in *Appendix*: A.3.1. The infinite scan rate produces a singularity in the concentration gradient in which the current approaches infinity and the singularity becomes more refined with decreasing $\Delta\theta$. Despite these limitations, the results presented in the following sections are valid since the analysis does not consider the value of the peak flux but rather its position expressed in terms of θ_{shift}.[1]

[1] In experimental practice, infinite scan rate is not possible with a real potentiostat thus the potential at which the absolute maximum peak current is observed - expressed as E_{avg} - is used for analysis.

4.3 Results and Discussion

The results are divided into two sections where (a) the difference in the voltammetric behavior is discussed between the conventional linear and the newly proposed method for a one species system by shifting the potential window with respect to the formal potential of the A/C couple which was set to $E^0_{f,A/C} = 0$ and hence $\theta^0_{f,A/C} = 0$, and (b) the analytical application of the method is elaborated by discussing the features of a two species system using the same method. The transfer coefficient, α, was set to a constant value of 0.5 and all results are reported in dimensionless units with $\sigma = 10^4$ and $K_0 = 10^{10}$ while changing the θ_{shift} values. Other parameters used for the simulations were $\Delta\theta = 10^{-4}$, $\omega = 1.07$, and $h = 10^{-7}$ (definition given in Chapter 2).

4.3.1 Single Electrochemically Reversible Species: Linear versus Semi-circular Potential Waves

The initial focus was on one species, A, of the A/C couple, and the results were compared between linear and semi-circular potential waves as shown in Figure 4.2. The dimensionless formal potential of A/C was set to 0 and its dimensionless diffusion coefficient, $d_A = d_C$, was set to 1.0 according to Table 4.1. Figure 4.2 shows the voltammograms at certain θ_{shift} values where 4.2A corresponds to $\theta_{shift} = -10$, 4.2B corresponds to $\theta_{shift} = -8$, 4.2C corresponds to $\theta_{shift} = -4$, 4.2D corresponds to $\theta_{shift} = 0$, 4.2E corresponds to $\theta_{shift} = 2$, and 4.2F corresponds to $\theta_{shift} = 4$. The blue solid line represents the results obtained using the linear potential wave whereas the orange solid line represents results from the semi-circular potential wave. The arrows indicate the direction of the sweep and the dotted line shows the theoretical peak current for the linear results predicted by the Randles-Ševčík equation [34, 35] for an electrochemically reversible electron transfer given as [26, 28, 36]:

$$I_p = -0.446FA_{ele}c^*_j\sqrt{\frac{FD_j\nu}{RT}} \tag{4.21}$$

where A_{ele} is the area of the electrode, c^* is the concentration of the species j under study, $\frac{F}{RT}$ has its usual meaning, D is the diffusion coefficient of the said species, and ν is the scan rate. Equation (4.21) shows that the peak current has a square

root dependence on the scan rate [37]. Equation (4.21) can then be converted to a dimensionless form using the conversion factors from Table 4.1, giving:

$$J_p = -0.446 C_j \sqrt{d_j \sigma} \tag{4.22}$$

where $C_A = 1.0$.

The peak currents obtained through the linear potential wave did not show any variance with different θ_{shift} values as predicted, however, those obtained from the semi-circular potential wave showed a significant dependence on the θ_{shift} values. Looking at Figure 4.2A, not much difference is seen between the linear and semi-circular peak currents, but as θ_{shift} approaches 0, the peak current of the semi-circular potential wave voltammogram increases and at $\theta_{shift} = 0$ where the wave features an infinite scan rate at the formal potential, the peak goes to infinity. In other θ_{shift} values, a sharp peak was also observed. This is due to the singularity of the scan rate that forms in the semi-circular wave function at the midpoint of the potential window as can be seen in Figure 4.1. When this singularity occurs at the formal potential and in its immediate vicinity of the reduced species, an infinite increase in the peak current is observed and a small but sharp peak is observed at other θ_{shift} values. When the θ_{shift} was significantly negative with respect to the formal potential, no sharp peak was observed due to the relatively low sensitivity of the electrochemical reaction kinetics to changes in the applied potential in this potential region.

The fact that the peak current is significantly amplified at the formal potential when $\theta_{shift} = 0$ and suppressed at other θ_{shift} values makes the semi-circular potential sweep a more powerful tool for electroanalysis compared to the conventional linear method which shows no peak variance. The new method can thus be used to selectively detect individual species with different formal potentials and diffusion coefficients that are in a same mixture since the current contribution of one species will be augmented at its formal potential while the current of other species will be minimized, thereby making the interpretation of the results much more obvious and intuitive. Here, the window of the y-axis has been limited in order to better show

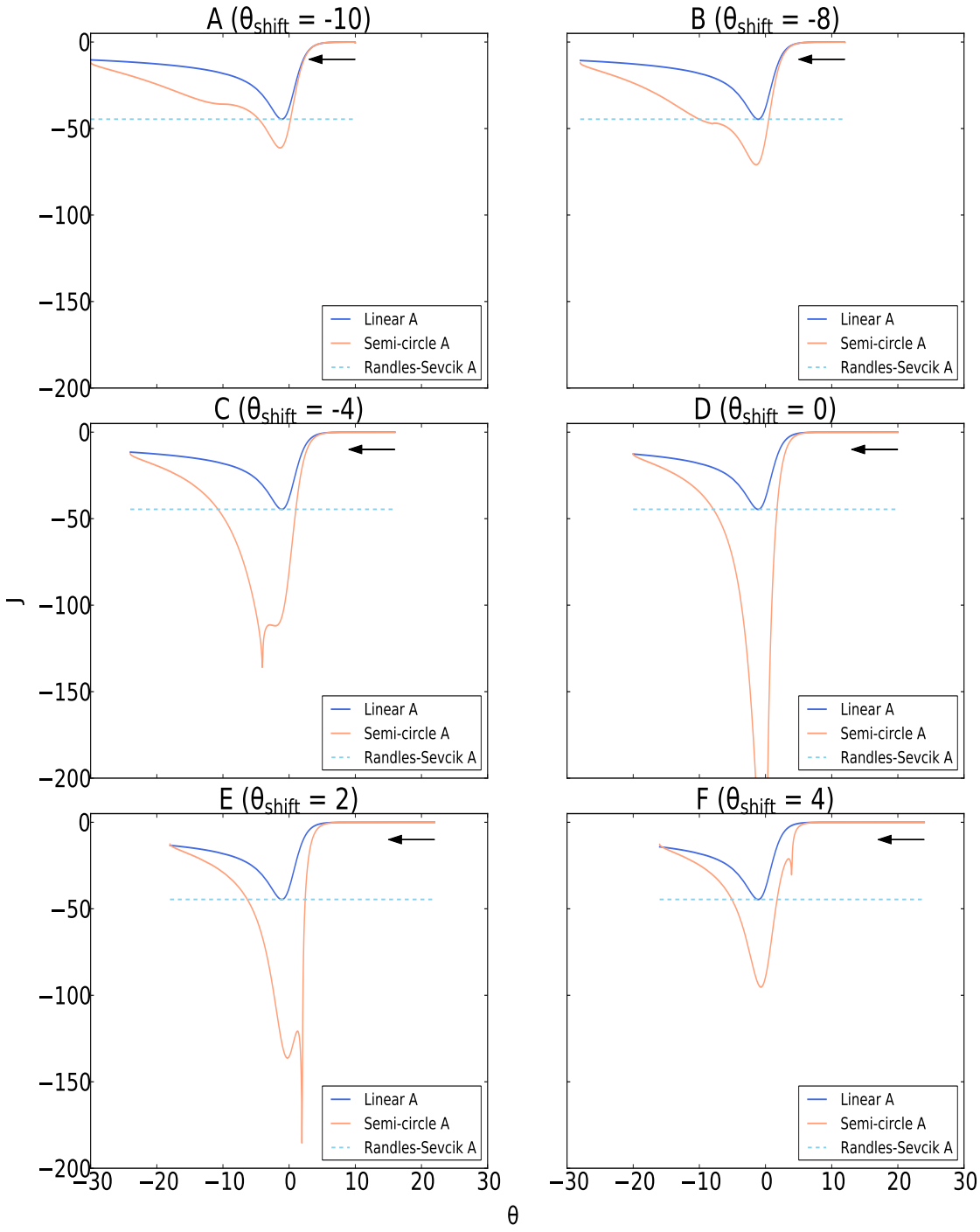


Figure 4.2: Voltammetric scan of species A obtained using linear and semi-circular potential waves at different θ_{shift} values where $\theta_f^0 = 0$ and $d_A = 1$. A is when $\theta_{shift} = -10$, B is when $\theta_{shift} = -8$, C is when $\theta_{shift} = -4$, D is when $\theta_{shift} = 0$, E is when $\theta_{shift} = 2$, and F is when $\theta_{shift} = 4$. The blue solid line represents the results from the linear potential wave and the solid orange line represents results from the semi-circular potential wave. The dotted line shows the peak current predicted by Equation (4.22).

the difference between the linear and semi-circular results. A more detailed version of Figure 4.2 and the following voltammograms are provided in *Appendix*: A.3.2.

4.3.2 Two Species Linear versus Semi-circular Potential Sweeps

The analytical applications of the semi-circular potential wave were explored next by comparing its voltammetric features with that obtained from a linear potential wave for a two species system containing the A/C couple and B/D couple where both systems were assumed to be electrochemically reversible. The formal potential difference was varied between the two redox couples to study the changes in the voltammetric response of both methods, starting with a formal potential difference of -8 dimensionless units, then -4, and lastly -2. In all cases, $d_A = d_C = 1.0$, $d_B = d_D = 0.5$, $C_A = 1.0$, $C_B = 1.0$, $K_0 = 10^{10}$, and $\theta^0_{f,A/C} = 0$.

Two Species with Formal Potential Difference of -8 Dimensionless Units

Figure 4.3 shows the results at the same θ_{shift} values as in Figure 4.2 but includes the voltammogram for the second species, B. The formal potential difference between the two species was set to -8 dimensionless units ($\theta^0_{f,B/D} = \theta^0_{f,A/C} - 8$), which, in dimensional term corresponds to approximately -0.21 V at 298 K. The light blue solid line represents results from the linear potential wave for species A, the bright blue solid line represents results from the linear potential wave for species B, the dark blue solid line represents the total dimensionless current of species A and B obtained from the linear potential wave, the light orange solid line represents results from the semi-circular potential wave for species A, the bright red solid line represents results from the semi-circular potential wave for species B, and the dark red solid line represents the total dimensionless current of species A and B obtained from the semi-circular potential wave. The light green dash line and the dark green dash-dotted line show the theoretical peak currents predicted by the dimensionless Randles-Ševčík equation (4.22) for species A and B, respectively.

Looking at the total dimensionless current for the linear potential wave, there are two peaks observed, each of which was a result of the contribution of the peak

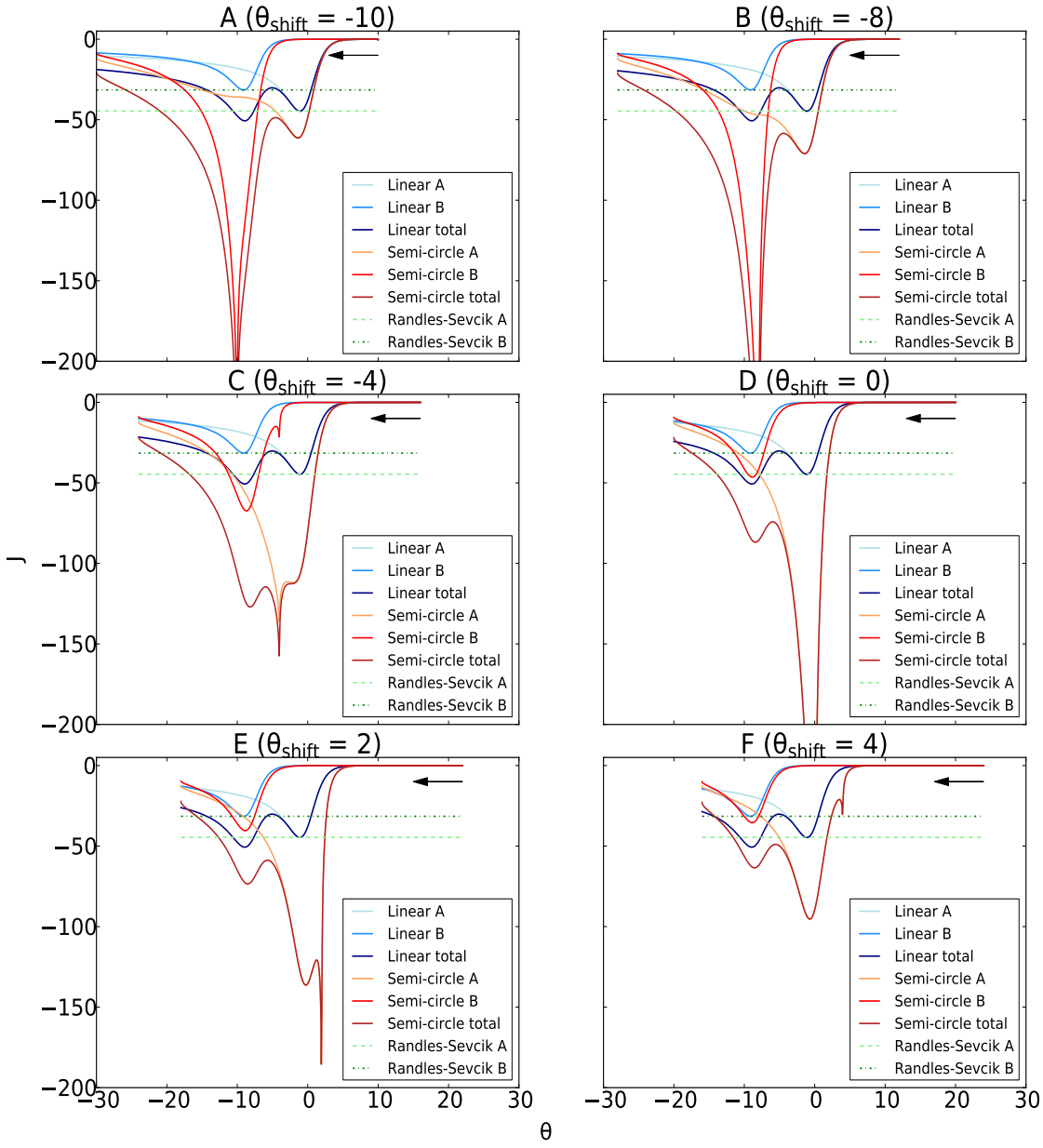


Figure 4.3: Voltammograms using linear and semi-circular potential waves at different θ_{shift} values for species A and B with a formal potential difference of -8 dimensionless units (-0.21 V). $\theta^0_{f,A/C} = 0$, and $d_A = 1.0$ while $d_B = 0.5$. A is when $\theta_{shift} = -10$, B is when $\theta_{shift} = -8$, C is when $\theta_{shift} = -4$, D is when $\theta_{shift} = 0$, E is when $\theta_{shift} = 2$, and F is when $\theta_{shift} = 4$. The blue solid lines correspond to results from the linear potential wave: light blue represents A, bright blue represents B, and dark blue represents the total dimensionless current $(A + B)$. The orange/red solid lines correspond to results from the semi-circular potential wave: light orange represents A, bright red represents B, and dark red represents the total dimensionless current $(A + B)$. The light green dash line and dark green dash-dotted line show the peak currents predicted by Equation (4.22) for species A and B, respectively.

current of species A and B. Since the individual peak currents do not change with varying θ_{shift}, the two peaks in the total current also remained constant with varying θ_{shift} values. Through simple examination, it is obvious that there were two species in this particular simulation where each species had a different formal potential based on the intensity of the two peaks and the potential at which they are observed. In addition, for this particular case, one of the peaks of the total current matches the horizontal line plotted by the dimensionless Randles-Ševčík equation using the dimensionless diffusion coefficient and concentration for species A. This is due to the fact that the potential at which this peak occurs is the region where species B does not react and thus most of the current contribution comes from species A. In such cases, Randles-Ševčík equation can be used to determine the diffusion coefficient of the current-contributing species. However, this is only applicable when the formal potential difference between species A and B is significant and the peak current of A is observed at a potential region where minimal or no reaction is observed for species B.

The total current of the semi-circular potential wave also shows there were two species within the same mixture, but significantly amplified the current contribution of one of the species near its formal potential while suppressing the other, thereby making the analysis much easier. From Figure 4.3A and 4.3B, it is clear that the peak current grows in 4.3B compared to 4.3A (full-scale figure provided in *Appendix*: A.3.2). It then diminishes in 4.3C, and increases significantly again in 4.3D. The subsequent figures 4.3E and 4.3F show a gradual decrease in the total peak current. Through simple observation it could be determined that the formal potential of A/C and B/D couple must be very close to 0 and -8 dimensionless units, respectively.

From the trend found in Figure 4.3, the semi-circular total dimensionless current was expected to show two potentials at which an absolute maximum dimensionless peak current would be observed with varying θ_{shift} values, and indeed this was the case as shown in Figure 4.4. Figure 4.4 shows the dimensionless peak currents plotted against the corresponding θ_{shift} values. The light orange dotted line represents peak currents for species A, the bright red dotted line represents peak currents for species

B, and the dark red dotted line represents peak curents of the total current. The plot for the total current shows that near $\theta_{shift} = 0$ and $\theta_{shift} = -8$, a maximum is observed and these two values correspond to the formal potential of species A and B, respectively. Therefore Figure 4.3 and 4.4 can be used to selectively detect individual species in a mixture and estimate their formal potentials.

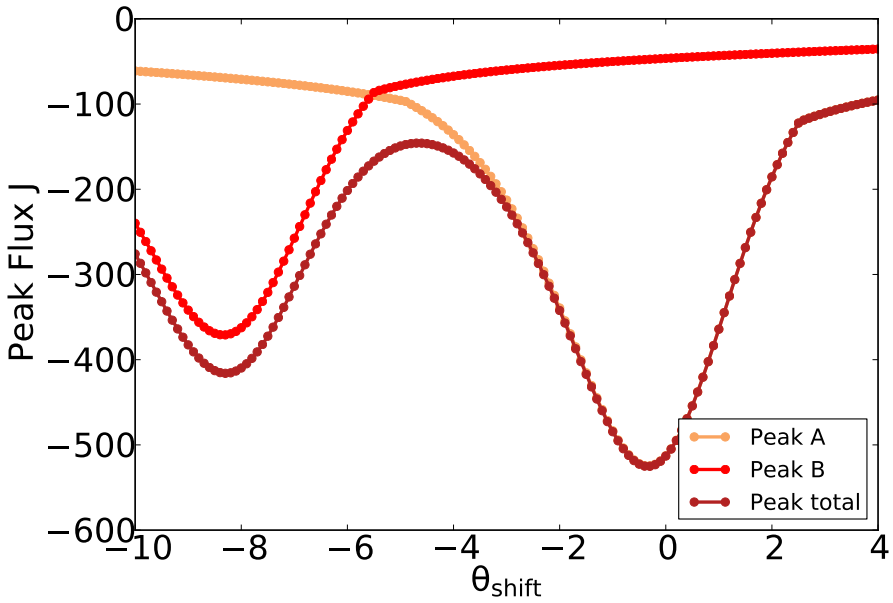


Figure 4.4: Peak flux plotted against the corresponding θ_{shift} value at which it was recorded for species A, B, and their total currents obtained through the semi-circular potential wave. The formal potential difference between the two species is -8 dimensionless units, and $d_A = 1.0$ and $d_B = 0.5$. The light orange dotted line represents peak currents for species A, the bright red dotted line represents peak currents for species B, and the dark red dotted line represents peak currents for the total current.

From the above analysis, it was clear that a semi-circular potential wave is a powerful tool for analyzing mixtures, however, Figure 4.3 shows that when the formal potential difference between two species is significant, the conventional linear potential wave is sensitive enough to detect them since two distinct peaks are observed in the total current. Therefore the limit of detection of the semi-circular potential wave was investigated next by decreasing the formal potential difference between species A and B.

Two Species with Formal Potential Difference of -4 Dimensionless Units

Figure 4.5 again shows the voltammetric results of species A and B with a formal potential difference of -4 dimensionless units ($\theta^0_{f,B/D} = \theta^0_{f,A/C} - 4$), which, in dimensional term corresponds to approximately -0.1 V at 298 K. The results were obtained using both, linear and semi-circular potential waves. Each figure uses the same color scheme as in Figure 4.3, however, the results are reported at different θ_{shift} values to better show the results at a θ_{shift} value near the formal potential of each species. Figure 4.5A corresponds to $\theta_{shift} = -6$, 4.5B corresponds to $\theta_{shift} = -4$, 4.5C corresponds to $\theta_{shift} = -2$, 4.5D corresponds to $\theta_{shift} = 0$, 4.5E corresponds to $\theta_{shift} = 2$, and 4.5F corresponds to $\theta_{shift} = 4$.

The two peaks of the linear total current that were clearly separate in Figure 4.3 are merged in Figure 4.5 and the current contributions from species A and B or their diffusion coefficients could not be distinguished. On the other hand, results from the semi-circular potential wave again show an infinite increase in the peak current around the formal potential of each species (full-scale figure provided in *Appendix*: A.3.2), indicating that this new method can be used for sensitive detection when the linear potential wave cannot.

Similar to Figure 4.4, Figure 4.6 shows the peak flux of the semi-circular method plotted against their corresponding θ_{shift} values at which they were recorded with the same color scheme as in Figure 4.4. Although the two maximum points in Figure 4.6 are not as pronounced as they were in Figure 4.4 due to the closeness in the formal potential of the two species, the two lowest points are still observable near a θ_{shift} of 0 and -4, which again correspond with the formal potential of species A and B, respectively, and is thus still within the limit of detection. Figure 4.5 and 4.6 show that a semi-circular potential wave can be used for selective detection of species under conditions where linear potential wave cannot.

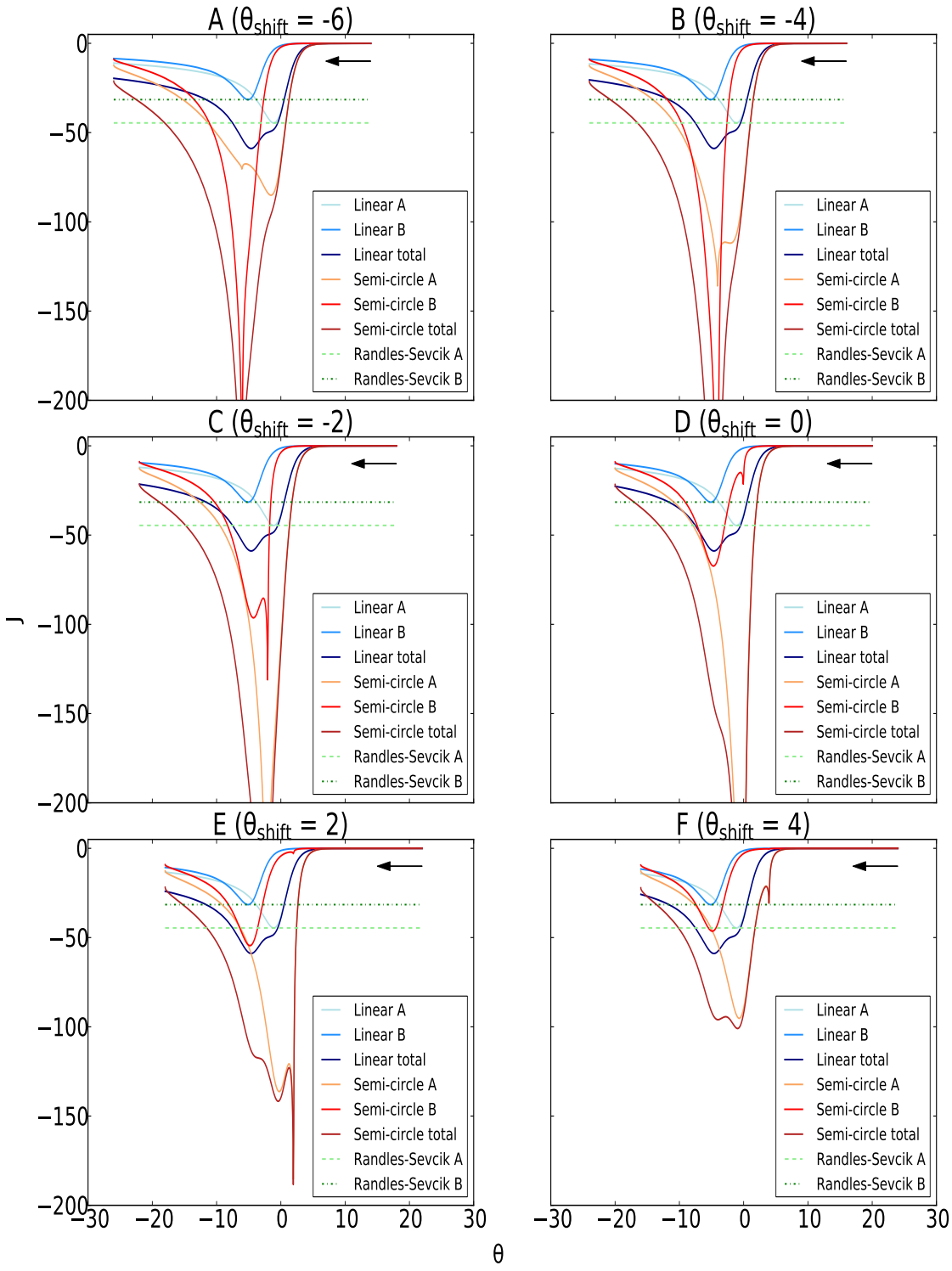


Figure 4.5: Voltammograms using linear and semi-circular potential waves at different θ_{shift} values for species A and B with a formal potential difference of -4 dimensionless units (-0.1 V). Formal potential of species $A = 0$, $d_A = 1.0$, and $d_B = 0.5$. A is when $\theta_{shift} = -6$, B is when $\theta_{shift} = -4$, C is when $\theta_{shift} = -2$, D is when $\theta_{shift} = 0$, E is when $\theta_{shift} = 2$, and F is when $\theta_{shift} = 4$. The same color scheme is used as in Figure 4.3.

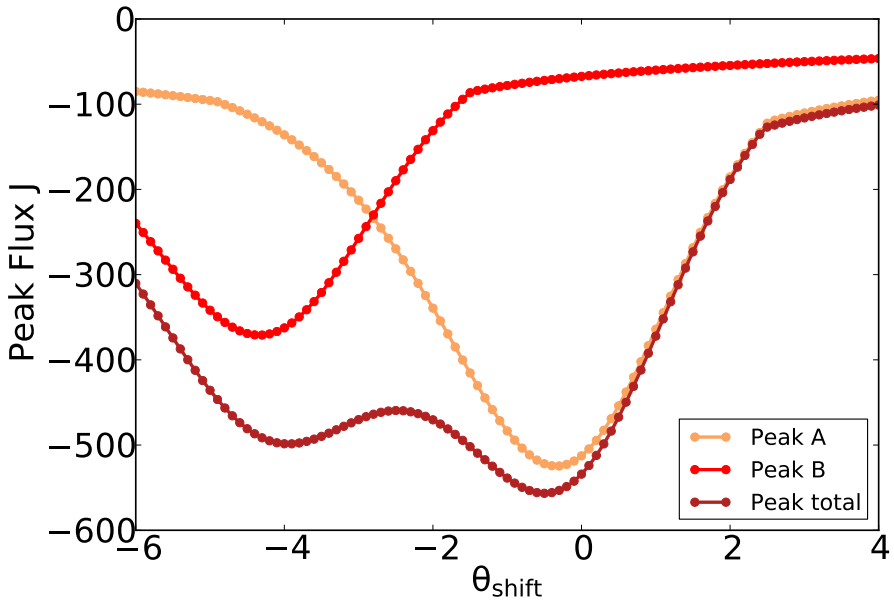


Figure 4.6: Peak flux plotted against the corresponding θ_{shift} value at which it was recorded for species A, B, and their total dimensionless currents obtained through the semi-circular potential wave. The formal potential difference between the two species is -4 dimensionless units, $d_A = 1.0$, and $d_B = 0.5$. The same color scheme is used as in Figure 4.4.

Two Species with Formal Potential Difference of -2 Dimensionless Units

Lastly, the formal potential difference between the two species was decreased even further to -2 dimensionless potential units ($\theta_{f,B/D} = \theta_{f,A/C} - 2$), which in dimensional term corresponds to -0.05 V at 298 K. The color scheme is the same as in Figures 4.3 and 4.5 but the results are reported at different θ_{shift} values. Figure 4.7A corresponds to $\theta_{shift} = -4$, 4.7B corresponds to $\theta_{shift} = -2$, 4.7C corresponds to $\theta_{shift} = -1$, 4.7D corresponds to $\theta_{shift} = 0$, 4.7E corresponds to $\theta_{shift} = 2$, and 4.7F corresponds to $\theta_{shift} = 4$.

Here, the two individual peaks of species A and B from the linear potential wave are completely merged in the total current making it impossible to detect the individual species or determine whether there are more than one species. Similarly, the results from semi-circular potential wave could not be used to detect the individual species as the θ_{shift} value at which the inifnite current is observed could not be associated with the formal potential of either of the species. The total

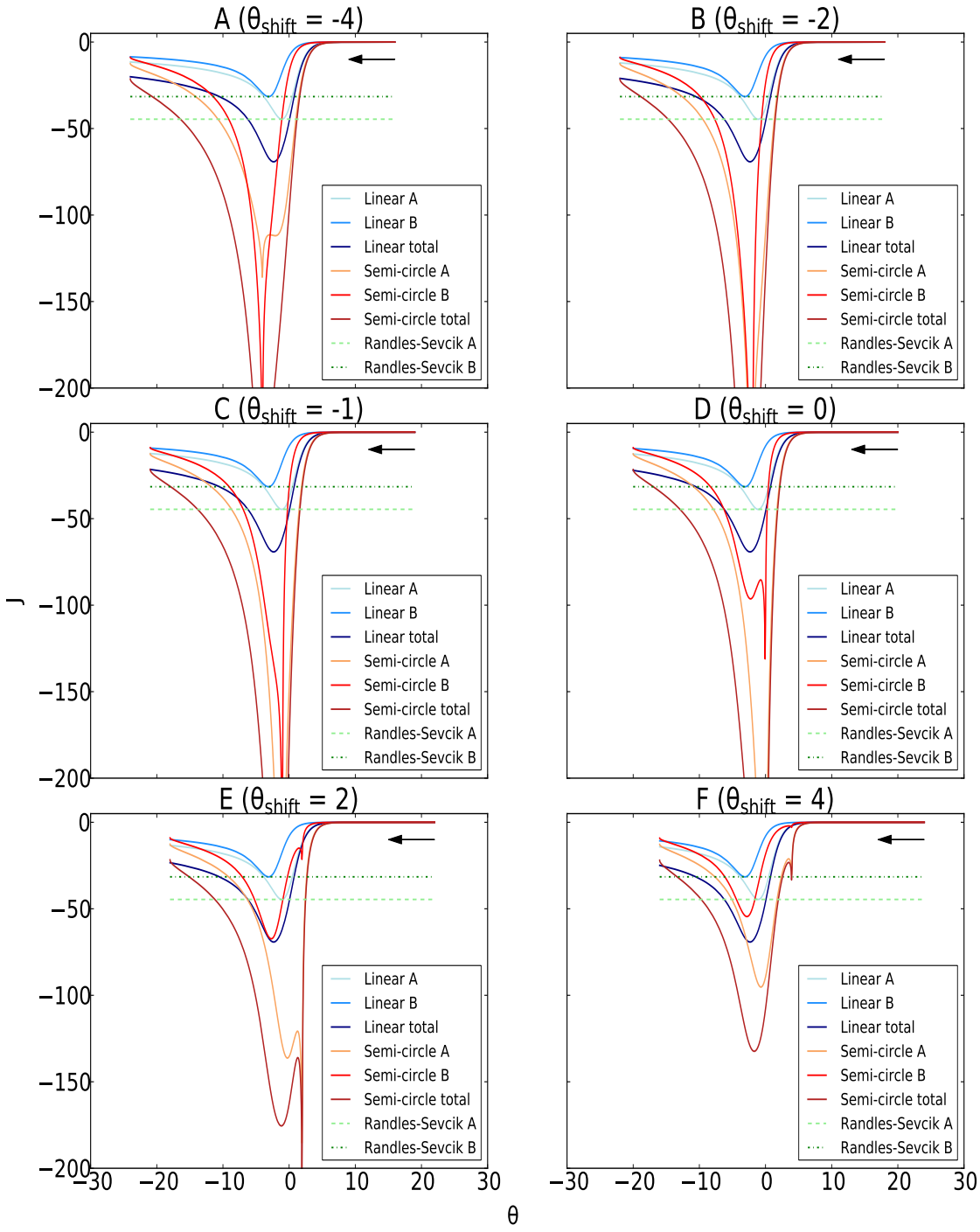


Figure 4.7: Voltammograms using linear and semi-circular potential waves at different θ_{shift} values for species A and B with a formal potential difference of -2 dimensionless units (-0.05 V). Formal potential of species $A = 0$, $d_A = 1.0$, and $d_B = 0.5$. A is when $\theta_{shift} = -4$, B is when $\theta_{shift} = -2$, C is when $\theta_{shift} = -1$, D is when $\theta_{shift} = 0$, E is when $\theta_{shift} = 2$, and F is when $\theta_{shift} = 4$. The same color scheme is used as in Figures 4.3 and 4.5.

current in Figures 4.7B, 4.7C, and 4.7D all appear to approach infinity, and this trend can be confirmed in Figure 4.8 as well.

Figure 4.8 shows the peak flux plotted against the θ_{shift} value when the formal potential difference between species A and B is -2 dimensionless units using the same color scheme as in Figures 4.4 and 4.6. Note the maximum point is observed at a θ_{shift} value close to -1, which does not correspond to the formal potential of either of the species. However, Figure 4.7 can be used to infer the presence of more than one species with small formal potential differences due to the wide range of θ_{shift} values where a very large peak is observed, and together with Figure 4.8 the range of θ_{shift} values in which the formal potential of species A and B might lie can be estimated. Looking at Figure 4.7, the total peak current of the semi-circular potential wave results approach infinity approximately between $\theta_{shift} = -2$ and $\theta_{shift} = 0$, and dramatically decreases in the positive θ_{shift} region. This feature can be seen in Figure 4.8 as well since the peak currents of the total current do not show much variance between the aforementioned range, and decreases rapidly in the far negative and positive regions.

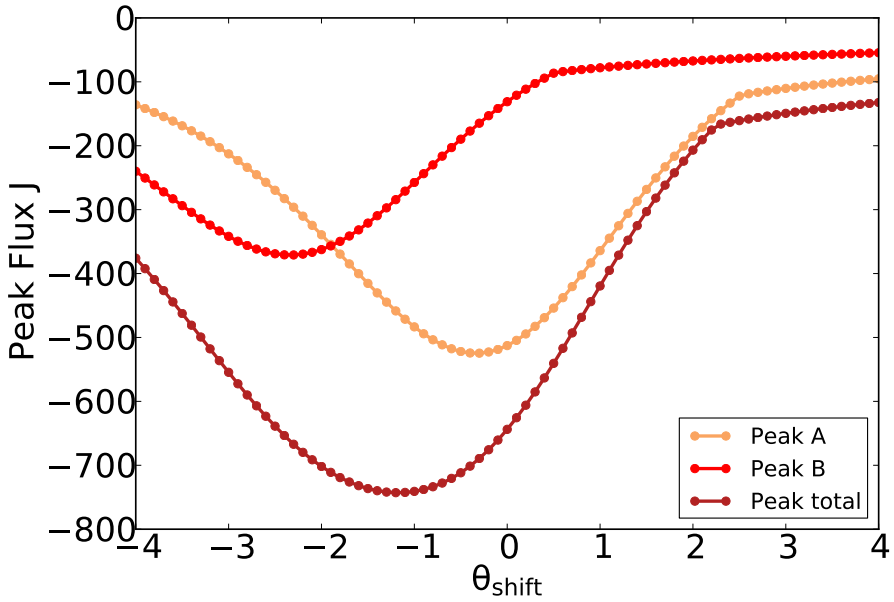


Figure 4.8: Peak flux plotted against the corresponding θ_{shift} value at which it was recorded for species A, B, and their total currents obtained through the semi-circular potential wave. The formal potential difference between the two species is -2 dimensionless units, $d_A = 1.0$, and $d_B = 0.5$. The same color scheme is used as in Figures 4.4 and 4.6.

From the results shown above, the conventional linear potential sweep is sensitive enough to detect individual species in a mixture when the formal potential difference is significant and in some occasions can be used to determine the diffusion coefficient of a specific species through the Randles-Ševčík equation. However, the results from the semi-circular potential wave are much easier to analyze because of the inifinite peak current observed at the formal potential of individual species and in its immediate vicinity. The semi-circular potential wave can further be used to distinguish individual species and detect their presence in situations where the linear potential wave cannot through the suppression and amplification of current contribution at varying θ_{shift} values.

For the analysis the potential window was shifted with respect to the formal potential of the A/C couple where $\theta^0_{f,A/C} = 0$ and thus $\theta_{shift} = \theta_{avg}$. In practice, the above analysis would be performed by repeatedly applying the semi-circular potential wave given in Equation (4.16) until an infinite peak is observed. It was shown earlier that the said infinite peak occurs when $\theta_{shift} = 0$ and in its immediate vicinity, thus the formal potential of the species in a mixture can be estimated through the analysis of the voltammograms by determining the E_{avg} value at which the aforementioned feature is observed.

4.4 Conclusions

This chapter introduced a novel approach in running voltammetric scans for electroanalysis on a mixture with two species, A and B, using a semi-circular potential wave with various θ_{shift} values where the wave was shifted with respect to the formal potential of one of the species. When the formal potential difference between the two species in a mixture was significantly large, the conventional linear and the new semi-circular potential waves could both selectively detect the species. However, in situations where the linear potential wave could not distinguish individual species due to the small formal potential difference, the semi-circular potential wave sensitively detected them by showing an infinite increase in the peak current near the formal potentials of the species in the mixture. Under

conditions where the formal potential difference between the two species was too small to sensitively detect them individually using either of the methods discussed, the semi-circular potential wave could still predict the presence of more than one species and estimate the potential range at which their formal potentials may be observed. The results and analysis thus showed that the new method complements the conventional linear potential wave for electroanalysis.

This work focused on the analytical application of the semi-circular voltammetry method. It is noted that the infinite scan rate at the apex of the potential wave maximizes the Faradaic current as well as the capacitive current [38] and thus the method operates in a manner such that both signal contributions are amplified. A prior careful determination of the capacitive background though enables the identification of the Faradaic current contribution. The method is suggested primarily as a tool for detecting the presence of a species via its electrochemical signal.

4.5 Experimental Verification

This section discusses the experimental verification of the semi-circular potential wave method. The changes in voltammetric response with varying E_{avg} (denoted in the following sections as E_{centre}) was investigated using the $[Ru(NH_3)_6]^{3+}/[Ru(NH_3)_6]^{+2}$ couple. All experiments were performed by Dr. Hatem M. A. Amin.

4.5.1 Chemicals

Hexaaminеruthenium(III) chloride ($[Ru(NH_3)_6]Cl_3$, "Ruhex", Aldrich, 98%) and potassium chloride (KCl, Aldrich, >99%) were used as received. All solutions were prepared with Milli-Q water with a resistivity of 18.2 MΩ cm at 298 K (Millipore Water Systems, U.K.). Prior to each experiment, all solutions were bubbled for at least 30 min with N_2 (99.998%, BOC, U.K.) and were then blanketed with N_2 during the measurement.

4.5.2 Instrumental

All electrochemical experiments (CV and LSV) were conducted using a three-electrode one-compartment glass cell with a glassy carbon disc (GC, 3.08 mm diameter, ALS Co. Ltd., Japan) as the working electrode, a saturated calomel electrode (SCE, ALS Co. Ltd., Japan) as the reference electrode and a Pt wire (GoodFellow, Cambridge, U.K.) as the counter electrode. All experiments were performed at 298 K and the temperature was kept constant using a water bath connected to a temperature controller (SCT1, Stuart, U.K.) inside a Faraday cage. A full discussion on the experimental setup is given in the published work [2].

4.5.3 Results and Discussion

This section is divided into three parts; the first part discusses the difference in voltammetric behavior between the linear and semi-circular potential wave methods, the second part analyzes the effect of the potential window shift on the voltammograms, and the third part shows how to determine the formal potential using the semi-circular method.

Voltammetry with Linear and Semi-circular Potential Waveforms

First the effect of the linear wave against the proposed semi-circular potential wave on the voltammetric behavior of the electrochemically reversible $[Ru(NH_3)_6]^{3+/2+}$ system is discussed. Figure 4.9 shows the voltammograms obtained using both linear and semi-circular potential waveforms for the potential range of 0.23 V to -0.67 V (E_{centre} = -0.22 V) at an average scan rate of 0.025 V s^{-1} in both, blank solution of 0.5 M KCl and in 0.265 mM $[Ru(NH_3)_6]Cl_3$/0.5 M KCl solution. In linear wave voltammetry, a peak for the reduction of Ru^{3+} appears at -0.23 V (see Figure 4.9(a)). The capacitive currents obtained using the semi-circular voltammetry are variable with a sharp peak at the midpoint of the applied potential window. This is, as explained earlier, due to the occurrence of the fastest scan rate in the immediate vicinity of this potential value. Since the capacitive current is directly proportional

to the scan rate, a large increase in capacitive current is observed at this potential while relatively low currents are seen everywhere else.

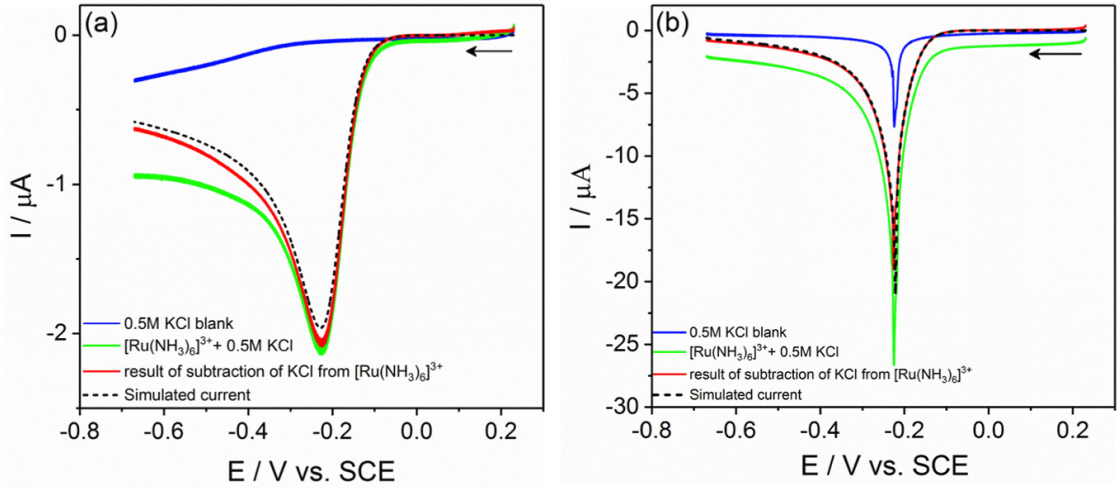


Figure 4.9: Voltammograms obtained using (a) linear and (b) semi-circular potential waveforms at a GC electrode in blank 0.5 M KCl solution (blue curves, capacitive currents) and in 0.265 mM $[Ru(NH_3)_6]Cl_3$/0.5 M KCl solution (green curves, Faradaic + capacitive currents) at an average scan rate of 0.025 V s^{-1}. The experimental Faradaic-only currents (red curves) were obtained by subtraction of the blue curve from the green curve and base line correction. The Faradaic currents obtained from the simulations are displayed as black dashed lines. The arrows show the direction of the potential sweep.

In all voltammograms, unless otherwise stated, the Faradaic-only currents (red curves) are plotted by subtracting the capacitive currents obtained in blank 0.5 M KCl solution (blue curves) from the measured currents in $[Ru(NH_3)_6]Cl_3$/0.5 M KCl solution (green curves) and the voltammograms are base-line corrected, as shown in Figure (4.9).

As expected, the voltammograms obtained from the semi-circular potential wave were different from those obtained using the conventional linear potential wave; the former resulted in a significantly larger peak current at -0.22 V than that obtained from the latter method for the same potential window, and the current declined at other potentials of the voltammogram (see Figure 4.9(b)). This noticeably high current response is, again, due to the fact that the semi-circular potential wave generates a dramatically elevated scan rate at the midpoint of the applied potential window and slower scan rates everywhere else. Consequently, when this increased scan rate occurs at and near the formal potential of $[Ru(NH_3)_6]^{3+/2+}$, a greater

flux of $[Ru(NH_3)_6]^{3+}$ to the electrode surface is achieved and thus a remarkable amplification of the peak current is observed. This method is therefore beneficial in electroanalysis because it possibly lowers the limit of detection of the species of interest by greatly amplifying the current response of such species, in particular when this species is present in a mixture with another species of similar formal potential.

The corresponding simulated currents (black dashed curves) are displyaed in Figure 4.9 where the diffusion coefficient was set to $5.5 \cdot 10^{-10}$ m^2 s^{-1} [39] and the same parameters were used as given in Section 4.3. The figure shows that the measured Faradaic currents are in good agreement with the simulated currents.

Analysis of The Semi-Circular Potential Scans at Shifted Potential Windows

In this and the following section, first the E_f^0 of $[Ru(NH_3)_6]^{3+/2+}$ is confirmed from triangular voltage scan voltammograms, second that value is used for the simulation of the semi-circular voltammograms, third the results of the simulation are compared with the corresponding experimental results for the semi-circular wave to validate the theoretical model, and fourth the used E_f^0 value is validated.

The influence of shifting the potential window on the voltammetric response of both the linear and semi-circular potential waves was investigated first. Figure 4.10 depicts the voltammograms obtained using triangular potential wave voltammetry in 0.265 mM $[Ru(NH_3)_6]Cl_3$/0.5 M KCl solution at 0.025 V s^{-1} and different potential windows.

It is clear from direct observation that the voltammetric response obtained is insensitive to the applied potential windows (i.e. different E_{centre} values). The triangular potential wave produces nearly identical voltammograms with single peaks at the same positions and magnitudes independent of the applied potential window. The formal potential is obtained from the midpoint between the reduction and oxidation peak potentials in the triangular voltammograms and a value of -200 $\pm$ 2 mV is obtained.

The semi-circular potential wave was also applied using different E_{centre} values ranging from -0.1 to -0.60 V in short intervals in the vicinity of the reduction peak.

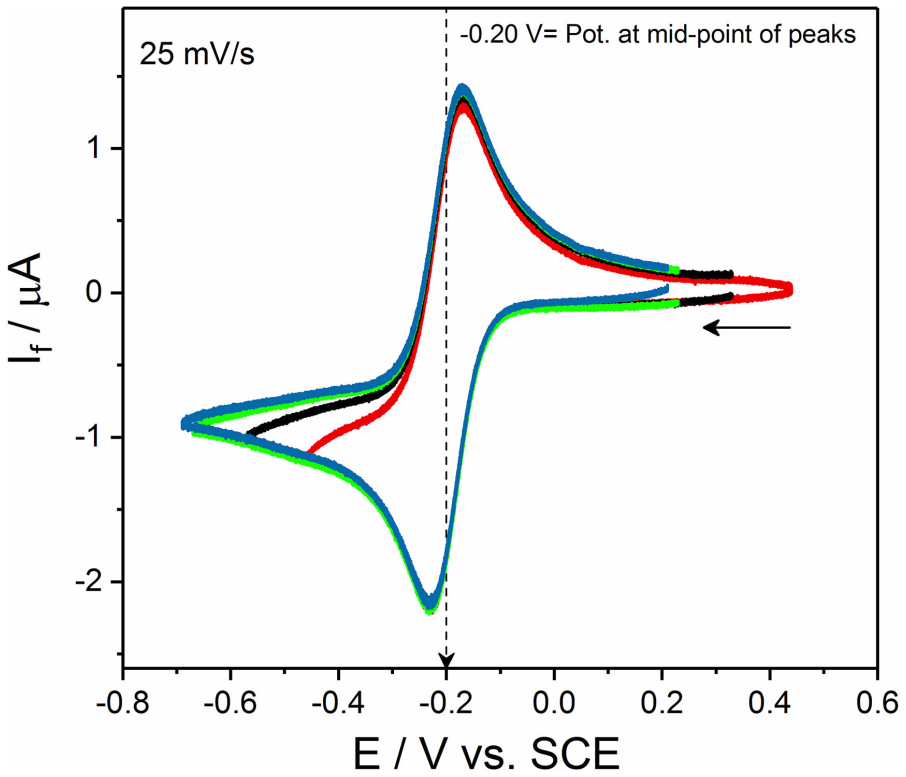


Figure 4.10: Capacitive current-corrected voltammograms obtained at a GC electrode with the triangular potential waveform

The voltammograms were recorded in 0.265 mM $[Ru(NH_3)_6]Cl_3$/0.5 M KCl solution at 298 K at the same GC working electrode. An average scan rate of 0.025 V s^{-1} was employed, which was achieved by setting the duration of each sweep to 36 s (the same duration length as the linear method). Figure 4.11 shows a couple of the resulting experimental and corresponding simulated voltammograms (using $E_f^0 = -200$ mV) of the semi-circular potential waveform at different potential windows. The used E_{centre} values are displayed in each graph.

In contrast to the linear wave voltammetry, the voltammetric behavior obtained from the semi-circular potential wave is dependent on the applied E_{centre} value. In all semi-circular potential wave voltammograms, the current is largely amplified especially at the potential where the fastest scan rate occurs, generating a sharp peak at this potential. At certain E_{centre} values, two distinct peaks are observed: a slightly amplified broad reduction peak at potentials far from the set E_{centre} value and a sharp peak at the fastest scan rate. The potential at which the sharp

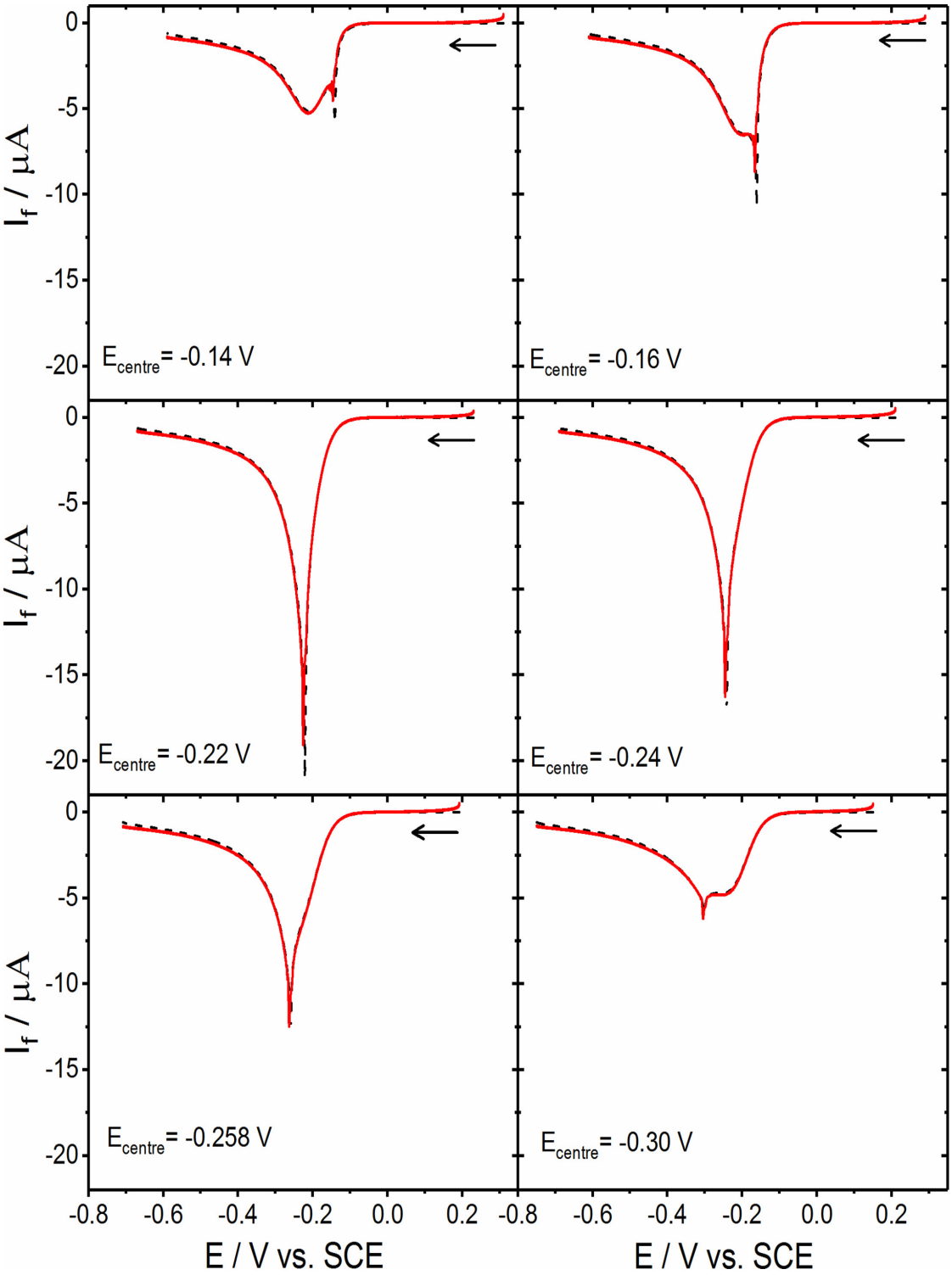


Figure 4.11: Capacitive current- and base line-corrected voltammograms obtained from experiment (solid red curves) and simulation (dashed black curves) at a GC electrode using the semi-circular potential waveform at different E_{centre} values in 0.265 mM $[Ru(NH_3)_6]Cl_3$/0.5 M KCl solution at an average scan rate of 0.025 V s^{-1}.

peak is observed is close to the applied E_{centre}.

Again, the emergence of a sharp peak in each voltammogram can be explained from the nature of the semi-circular wave function (4.16) and its waveshape (Figure 4.1). At the midpoint of the potential window, a steep slope is observed which means a temporary fast scan rate causing a significant rise in current, while relatively slower scan rates are applied everywhere else and the current decreases rapidly. The extent of the amplification of the peak current depends largely on the applied E_{centre} value as shown in figure 4.11. For example, at $E_{centre} = -0.14$, -0.16, and -0.30 V, the fastest applied scan rate occurs at potentials far from the formal potential of $[Ru(NH_3)_6]^{3+/2+}$, and the peak current is low, but as the E_{centre} value approaches the formal potential, the peak current increases dramatically (see curves at $E_{centre} = -0.22$ and -0.24 V) and reaches a maximum at an E_{centre} value where the fastest scan rate occurs few millivolts more negative than the formal potential of the species.

From the above results, it can be seen that the peak current obtained using the semi-circular potential wave is greatly amplified when the fastest scan rate is applied in the close vicinity of the foraml potential, while a much shorter sharp peak is seen when the fastest scan rate is applied at potentials far from the formal potential.

Determination of the Formal Potential of $[Ru(NH_3)_6]^{3+/2+}$

This section provides an analysis of all measured voltammograms and their absolute peak currents to determine the experimental E_{centre} at which the maximum peak current occurs. This value is then compared with simulation results. The advantage of the proposed method is that the current response of this method is significantly higher than that of the conventional LSV, and thus may reduce the limit of detection of the chemical species.

Figure 4.12 depicts the absolute maximum peak currents obtained experimentally (red spheres) at a scan rate of 0.025 V s^{-1} plotted against the corresponding E_{centre} values after the correction for capacitive currents and the base-line offset. The corresponding simulated peak currents (black diamonds) were further plotted

alongside the formal potential of -200 ± 2 mV as determined from Figure 4.10. In addition, the two peak positions, E_{centre}^{max}, as found experimentally and via the simulation were included at -214 ± 2 mV and -208 ± 2 mV, respectively. Errors indicate the resolution of the experimental and simulated data in terms of E_{centre}.

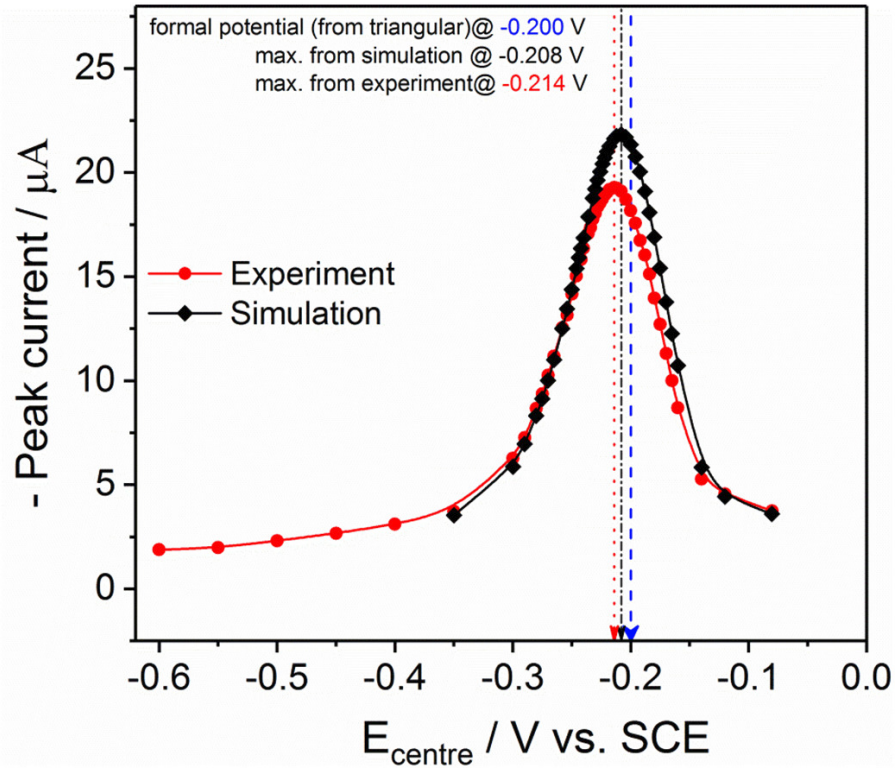


Figure 4.12: Plot of the maximum peak currents for different E_{centre} values using the semi-circular potential wave. Data were obtained for 0.265 mM $[Ru(NH_3)_6]Cl_3$/0.5 M KCl solution at 0.025 V s^{-1} from the corresponding experimental (correted for the capacitive current and the baseline, red speheres) and simulated (black diamonds) voltammograms. The formal potential estimated from the prior triangular voltammetry is indicated by the dashed blue line while the simulated potential of the maximum peak current calculated using the E_f^0 from the triangular wave voltammetry is indicated by the dash-dotted black line and the maximum peak current from the semi-circular experiment is indicated by the dotted red line.

Figure 4.12 shows good agreement between experiment and simulation, except for a different absolute magnitude of the simulated peak currents which, on one hand, is due to the infinite current response expected at an infinite scan rate and on the other the bandwidth limitations of the potentiostat. The combination of simulated and experimental data further allows the determination of the formal potential. The simulation reveals that, under the chosen experimental conditions,

the peak in the plot of the absolute maximum currents as a function of E_{centre}, E_{centre}^{max}, is offset from the formal potential by the theoretically predicted negative potential shift of $E_{centre}^{max} - E_f^0 = -8 \pm 2$ mV. This finding can be exploited, entirely independently from the prior measurements of the formal potential, to determine the formal potential of the $[Ru(NH_3)_6]^{3+/2+}$ couple experimentally from the semi-circular wave voltammetry. By simply calculating $E_f^0 = (E_{centre}^{max} + 8) \pm 2$ mV, the formal potential value of -206 ± 2mV is obtained from the semi-circular voltammetry. This value is in good agreement with the value determined from triangular voltammetry (-200 ± 2 mV), and the slight deviation of 6 ± 2 mV from simulation is attributed to bandwidth limitations of the digital-to-analogue converter which controls the electrode potential and an Ohmic drop at fast scan rates.

The above analysis shows the experimental validation of the semi-circular potential wave voltammetry and the use of this new method to measure the formal potential of $[Ru(NH_3)_6]^{3+/2+}$ redox couple.

4.6 Conclusions

Voltammetry with a semi-circular potential waveform was investigated and the theoretical predictions using the reversible $[Ru(NH_3)_6]^{3+/2+}$ redox couple at a macroelectrode were verified experimentally. Contrary to the classical linear potential wave, the semi-circular waveform has a characteristic feature that at the mid-point of the scanned potential window, a fast scan rate is obtained while relatively slower scan rates are found everywhere else. When the fastest scan rate appears within the close vicinity of the formal potential of $[Ru(NH_3)_6]^{3+/2+}$, a maximum in the absolute peak current is observed. The adjustment of the potential window allows the determination of the E_f^0 value making use of the near infinite current expected for scans centred at and near E_f^0.

References

[1] Y. Uchida, E. Kätelhön, R. G. Compton, *Journal of Electroanalytical Chemistry* **2018**, *818*, 140–148.

[2] H. M. A. Amin, Y. Uchida, E. Kätelhön, R. G. Compton, *Journal of Electroanalytical Chemistry* **2019**, *836*, 62–67.

[3] R. G. Compton, C. E. Banks, *Understanding Voltammetry*, Imperial College Press, **2010**.

[4] J. J. Van Benschoten, J. Y. Lewis, W. R. Heineman, D. A. Roston, P. T. Kissinger, *Journal of Chemical Education* **1983**, *60*, 772.

[5] M. Rudolph, D. P. Reddy, S. W. Feldberg, *Analytical Chemistry* **1994**, *66*, 589A–600A.

[6] J. G. Osteryoung, R. A. Osteryoung, *Analytical Chemistry* **1985**, *57*, 101–110.

[7] C. M. A. Brett, A. M. O. Brett, *Electrochemistry : Principles, Methods, and Applications*, Oxford University Press, **1993**.

[8] G. C. Barker, I. L. Jenkins, *Analyst* **1952**, *77*, 685–696.

[9] F. Scholz, *Electroanalytical Methods*, Springer-Verlag Berlin Heidelberg, **2010**.

[10] J. J. O'Dea, J. Osteryoung, R. A. Osteryoung, *Analytical Chemistry* **1981**, *53*, 695–701.

[11] A. J. Bard, L. R. Faulkner, *Electrochemical Methods: Fundamentals and Applications*, John Wiley & Sons Inc, **2000**.

[12] Á. Molina, J. González, *Pulse Voltammetry in Physical Electrochemistry and Electroanalysis: Theory and Applications (Monographs in Electrochemistry)*, Springer, **2016**.

[13] C. Amatore, A. Oleinick, I. Svir, *Analytical Chemistry* **2008**, *80*, 7947–7956.

[14] S. Ching, R. Dudek, E. Tabet, *Journal of Chemical Education* **1994**, *71*, 602.

[15] D. H. Evans, K. M. O'Connell, R. A. Petersen, M. J. Kelly, *Journal of Chemical Education* **1983**, *60*, 290.

[16] J. Heinze, *Angewandte Chemie International Edition in English* **1984**, *23*, 831–847.

[17] H. T. H. Chan, E. Kätelhön, R. G. Compton, *Journal of Electroanalytical Chemistry* **2017**, *799*, 126–133.

[18] M. C. Henstridge, E. Laborda, E. J. Dickinson, R. G. Compton, *Journal of Electroanalytical Chemistry* **2012**, *664*, 73–79.

[19] E. J. F. Dickinson, J. G. Limon-Petersen, N. V. Rees, R. G. Compton, *The Journal of Physical Chemistry C* **2009**, *113*, 11157–11171.

[20] J. K. Novev, S. Eloul, R. G. Compton, *The Journal of Physical Chemistry C* **2016**, *120*, 13549–13562.

[21] J. K. Novev, R. G. Compton, *Current Opinion in Electrochemistry* **2018**, *7*, 118–129.

[22] V. Sahore, A. Kreidermacher, F. Z. Khan, I. Fritsch, *Journal of The Electrochemical Society* **2016**, *163*, H3135–H3144.

[23] C. Amatore, C. Pebay, L., A. Wang, J.-S. Warkocz, *Analytical Chemistry* **2010**, *82*, 6933–6939.

[24] K. Ngamchuea, S. Eloul, K. Tschulik, R. G. Compton, *Analytical Chemistry* **2015**, *87*, 7226–7234.

[25] X. Gao, J. Lee, H. S. White, *Analytical Chemistry* **1995**, *67*, 1541–1545.

[26] R. G. Compton, E. Laborda, K. R. Ward, *Understanding Voltammetry: Simulation of Electrode Processes*, Imperial College Press, **2013**.

[27] J. Crank, *The Mathematics of Diffusion*, Oxford University Press, **1979**.

[28] K. R. Ward, M. Gara, N. S. Lawrence, R. S. Hartshorne, R. G. Compton, *Journal of Electroanalytical Chemistry* **2013**, *695*, 1–9.

[29] E. O. Barnes, X. Chen, P. Li, R. G. Compton, *Journal of Electroanalytical Chemistry* **2014**, *720-721*, 92–100.

[30] R. Guidelli, R. G. Compton, J. M. Feliu, E. Gileadi, J. Lipkowski, W. Schmickler, S. Trasatti, **2014**, *86*, 259–262.

[31] R. Guidelli, R. G. Compton, J. M. Feliu, E. Gileadi, J. Lipkowski, W. Schmickler, S. Trasatti, **2014**, *86*, 245–258.

[32] S. Benthin, B. Speiser, *Journal of Electroanalytical Chemistry* **2012**, *682*, 147–157.

[33] E. Kätelhön, R. G. Compton, *Analyst* **2015**, *140*, 2592–2598.

[34] J. E. B. Randles, *Trans. Faraday Soc.* **1948**, *44*, 327–338.

[35] A. Ševčík, *Collect. Czech. Chem. Commun.* **1948**, *13*, 349–377.

[36] M. J. A. Shiddiky, A. A. J. Torriero, J. M. Reyna-Gonzalez, A. M. Bond, *Analytical Chemistry* **2010**, *82*, 1680–1691.

[37] P. Kant, R. Kant, *The Journal of Physical Chemistry C* **2014**, *118*, 26599–26612.

[38] X.-S. Zhou, B.-W. Mao, C. Amatore, R. G. Compton, J.-L. Marignier, M. Mostafavi, J.-F. Nierengarten, E. Maisonhaute, *Chem. Commun.* **2016**, *52*, 251–263.

[39] Y. Wang, J. G. Limon-Petersen, R. G. Compton, *Journal of Electroanalytical Chemistry* **2011**, *652*, 13–17.

5

Application of Semi-circular Potential Waves in Voltammetry at a Microelectrode

So far this thesis has considered a one-dimensional diffusion system, modeling a redox reaction at a macrodisc electrode. In this chapter the discussion shifts to a reaction at a microdisc electrode, which requires a two-dimensional diffusion model using the semi-circular potential sweep introduced in the previous chapter. The work presented here is published in the '*Journal of Electroanalytical Chemistry* 2018, 823, 465-473' [1].

Contents

5.1 Introduction 108
5.2 Theory 109
5.2.1 Theoretical Model 109
5.2.2 Boundary Conditions 110
5.2.3 Dimensionless Coordinates 112
5.2.4 Semi-circular Potential Wave 113
5.2.5 Simulation via Finite Differences 114
5.3 Results and Discussion 115
5.3.1 Linear versus Semi-circular Potential Sweeps: 3 Different Scan Rates 115
5.3.2 Semi-circular Potential Sweeps: Different θ_{shift} Values . 121
5.4 Conclusions 128

5.1 Introduction

As introduced in Chapter 4, linear sweep voltammetry (LSV) is commonly performed through the application of a linear potential wave [2], where the scan rate is constant throughout the sweep. The resulting voltammograms give information regarding the redox system under investigation such as analyte concentrations, diffusion constants, and kinetic information [3, 4]. The linear potential wave is given as:

$$E(t) = \pm\nu t + E(t = 0) \tag{5.1}$$

where $E(t)$ is the applied potential with respect to time, $\pm$ shows whether the reaction is oxidative or reductive, and ν is the scan rate. In the previous chapter, a new method for carrying out voltammetry at a macroelectrode was introduced using a semi-circular potential wave, which creates a transiently infinitely fast scan rate at the midpoint of the potential window and slower scan rates everywhere else. The infinitely fast scan rate results in a significant increase in the current response while the slow scan rates in other areas reduce the current response. It was shown that the said new method is useful in electroanalytical applications and can be used for the selective detection of the presence of a species in a mixture.

This chapter further develops the concept and investigates the voltammetric response at a microdisc electrode when employing a semi-circular potential wave. Microelectrodes are widely used due to their advantages over macroelectrodes such as the reduced capacitance and ohmic drop, increased rates of mass transport, fast response time, and a steady-state current reponse [2, 5–10]. The analysis in the following sections show that the microdisc electrode exhibits an "infinite" peak current at the potential where the singularity in the scan rate is observed and suppresses the current response in other potential regions akin to macrodisc electrodes. These advantages make the semi-circular potential wave an advantageous tool for electroanalysis.

5.2 Theory

The following sections explain the theoretical model employed and re-introduce the semi-circular potential waveform applied in the simulation using dimensionless coordinates.

5.2.1 Theoretical Model

A simple one-electron electrochemically-reversible reduction reaction of A to B was studied at a microdisc electrode under diffusion-only conditions, where species A and B have equal diffusion coefficients:

$$A(aq) + e \rightleftharpoons B(aq) \tag{5.2}$$

The above system was simulated with diffusion as the only means of mass transport of analyte to the electrode surface [11–13] under the assumption of sufficiently high concentration of supporting electrolyte in order to suppress migration [14–17]. When the scan duration is long, convection [18–20] should be taken into consideration [7, 21, 22]. However, its effect is significantly reduced with decreasing electrode size [23]. The transport of analyte is hence described by Fick's Second Law expressed as [2, 24, 25]:

$$\frac{\partial c_j}{\partial t} = D_j \left(\frac{\partial^2 c_j}{\partial x^2} + \frac{\partial^2 c_j}{\partial y^2} + \frac{\partial^2 c_j}{\partial z^2} \right) \tag{5.3}$$

where j (= A or B) is the species under study and D is its diffusion coefficient. For a microelectrode simulation where the diffusion is not planar, Equation (5.3) must be written in cylindrical polar coordinates giving:

$$\frac{\partial c_j}{\partial t} = D_j \left(\frac{\partial^2 c_j}{\partial r^2} + \frac{1}{r}\frac{\partial c_j}{\partial r} + \frac{1}{r^2}\frac{\partial^2 c_j}{\partial \phi^2} + \frac{\partial^2 c_j}{\partial z^2} \right) \tag{5.4}$$

where z is the perpendicular distance from the electrode surface, r is the radial distance from the axis, and ϕ is the angle around the axis [2, 24]. Since concentration does not change with the angle, ϕ, Equation (5.4) is reduced to [2, 13, 24, 26, 27]:

$$\frac{\partial c_j}{\partial t} = D_j \left(\frac{\partial^2 c_j}{\partial r^2} + \frac{1}{r}\frac{\partial c_j}{\partial r} + \frac{\partial^2 c_j}{\partial z^2} \right) \tag{5.5}$$

5.2.2 Boundary Conditions

For a system using a macroelectrode, linear diffusion is observed and thus only the concentration change in the x direction, bounded by the electrode surface and the outer surface, is considered. However, microelectrodes introduce non-planar diffusion and therefore the concentration in the z and r directions must be considered, resulting in a two-dimensional rectangular simulation space [24] as explained in Chapter 2. Assuming the microelectrode is embedded in a planar supporting surface, the boundary line in the z direction is separated into two parts: one where it is bounded by the electrode surface and the outer surface, and the other bounded by the insulating supporting surface and the outer surface.

Given $D_A = D_B$, the following boundary conditions can be established under the assumption that initially only the reactant is present and prior to the experiment the concentration of reactant and product are uniform in space [2, 24]:

$$t \leq 0;\ \text{all } z,\ r;\ c_A = c_A^*;\ c_B = 0 \tag{5.6}$$

With increasing time, the concentration near the electrode surface varies but at the outer boundary surface no change in concentration is observed:

$$t > 0,\ z \to \infty,\ c_A = c_A^*,\ c_B = 0 \tag{5.7}$$

$$t > 0,\ r \to \infty,\ c_A = c_A^*,\ c_B = 0 \tag{5.8}$$

Furthermore, two no-flux boundaries are introduced: one at the insulating supporting surface, and the other at the cylindrical axis, $r = 0$. At a no-flux boundary, no change in concentration gradient is observed giving:

$$t > 0,\ r > \epsilon,\ \left(\frac{\partial c}{\partial z}\right)_{z=0} = 0 \tag{5.9}$$

$$t > 0,\ \text{all } z,\ \left(\frac{\partial c}{\partial r}\right)_{r=0} = 0 \tag{5.10}$$

where ϵ is the radius of the electrode. When the diffusion coefficients of the reactants and products are equal, conservation of mass predicts that the amount of A consumed at the electrode surface equals the amount of B produced:

$$t > 0,\ z = 0,\ -\frac{\partial c_A}{\partial z} = \frac{\partial c_B}{\partial z} \tag{5.11}$$

and the following relation holds true for all space and time:

$$c_A + c_B = c_A^* \tag{5.12}$$

The electrode kinetics is described through the Butler-Volmer equation given as:

$$j_{net} = k_0 exp\left[\frac{-\alpha F(E - E_f^0)}{RT}\right][A]_0 - k_0 exp\left[\frac{(1-\alpha)F(E - E_f^0)}{RT}\right][B]_0 \tag{5.13}$$

where j_{net} is the flux of the reactant to the electrode surface, k_0 is the standard electrochemical rate constant, $[A]_0$ and $[B]_0$ are the surface concentrations of species A and B respectively, α is the transfer coefficient [28, 29], F, R, and T hold their conventional significance, E is the applied potential, and E_f^0 is the formal potential of the A/B redox couple. The flux of species A, j_A, is also described via Fick's First Law. Assuming equal diffusion coefficients, D, it can be written as:

$$j_A = -D\left(\frac{\partial c_A(z,t)}{\partial z}\right)_{z=0} = -[k_{red}c_A(0,t) - k_{ox}c_B(0,t)] \tag{5.14}$$

and by subsituting the relationships $\theta = \frac{F}{RT}(E - E_{f,A/B}^0)$, $k_{red} = k_0 e^{-\alpha\theta}$, and $k_{ox} = k_0 e^{(1-\alpha)\theta}$, Equation (5.14) becomes:

$$D\left(\frac{\partial c_A(z,t)}{\partial z}\right) = k_0 e^{-\alpha\theta} c_A(0,t) - k_0 e^{(1-\alpha)\theta} c_B(0,t) \tag{5.15}$$

The system of interest was investigated under the assumption that the A/B couple is fully reversible by applying a very large k_0 value to the Butler-Volmer boundary condition, and hence Equation (5.13) becomes indistinguishable from the Nernst equation giving [30]:

$$E = E_f^0 + \frac{RT}{F} ln \frac{[A]_0}{[B]_0} \tag{5.16}$$

A related convergence test to ensure the reversibility of the system with the k_0 value used here is given in *Appendix*: A.4.1, which was conducted using the Butler-Volmer boundary conditions as above.

5.2.3 Dimensionless Coordinates

All simulations were run using the dimensionless coordinates of the equations given earlier and their conversion factors are listed in Table 5.1. Using these conversion factors, Fick's Second Law can be expressed in its dimensionless form:

$$\frac{\partial C}{\partial \tau} = d_j \left(\frac{\partial^2 C}{\partial R^2} + \frac{1}{R} \frac{\partial C}{\partial R} + \frac{\partial^2 C}{\partial Z^2} \right) \tag{5.17}$$

and Fick's First Law can be rewritten as:

$$\frac{C_{A,1} - C_{A,0}}{h} = \frac{1}{d_j} K_0 f(\theta) \{ C_{A,0} - [1 + C_B^* - C_{A,0}] e^{\theta} \} \tag{5.18}$$

where $C_{A,1}$ and $C_{A,0}$ are the dimensionless concentrations of species A at position Z_1 and Z_0, respectively, $f(\theta) = e^{-\alpha\theta}$, and $h = Z_1 - Z_0$ assuming A and B have equal diffusion coefficients.

Table 5.1: Dimensionless parameters.[24]

Parameter	Normalization
concentration	$C_j = \frac{c_j}{c_A^*}$
diffusion coefficient	$d_j = \frac{D_j}{D_A}$
z spatial coordinate	$Z = \frac{z}{\epsilon}$
r spatial coordinate	$R = \frac{r}{\epsilon}$
time	$\tau = \frac{D_A t}{\epsilon^2}$
potential	$\theta = \left(\frac{F}{RT}\right)(E - E^0_{f,A/B})$
scan rate	$\sigma = \left(\frac{\epsilon^2}{D_A}\right)\left(\frac{F}{RT}\right)\nu$
current	$J = \frac{I}{2\pi\epsilon F D_A c_A^*}$
rate constant	$K^0 = \frac{k^0\epsilon}{D_A}$

5.2.4 Semi-circular Potential Wave

The semi-circular potential waveform and the conventional linear waveform (5.1) were employed in this project. The equation used to describe the semi-circular potential waveform is:

$$\theta(\tau) = \pm\sqrt{\left|\theta_{A_0}^2 - [\sigma \cdot (\tau - c\tau_{max})]^2\right|} + \theta_{shift} \tag{5.19}$$

where $\theta(\tau)$ is the dimensionless potential with respect to dimensionless time, θ_{A_0} is the dimensionless amplitude, σ is the dimensionless average scan rate defined as the slope of the linear wave, c is the fraction of the maximum time when the centre of each semi-circle is observed, $\tau_{max} = \frac{2\theta_{A_0}}{\sigma}$, and θ_{shift} is the potential shift defined as $\theta_{shift} = \theta_{avg} - \theta_f^0$. From Table 5.1, θ_f^0 is by definition equal to 0 and hence $\theta_{shift} = \theta_{avg}$ where θ_{avg} is the midpoint of the potential window. A more detailed discussion on the derivation of Equation (5.19) is provided in Chapter 4. The key feature of the semi-circular potential wave is that it produces an instantaneously infinite scan rate at the mid-point of the wave and a slower scan rate at all other areas thereby amplifying the current response within a very narrow potential range and suppressing it at other potential regions, making it suitable for analytical applications.

Figure 5.1 shows the linear and the semi-circular potential waves centred at $\theta = 0$ with $\theta_{A_0} = 1$. For this figure, the first half of the semi-circular potential wave was plotted using $c = 0$ and the second half was plotted using $c = 1$. As can be seen, the scan rate for the linear potential wave is constant throughout the entire sweep while the semi-circular potential wave shows significant changes in temporal scan rate throughout the sweep. At $t = 0$ and $t = t_{max}$, the scan rates are close to zero but at $\theta = 0$, the instantaneous scan rate approaches infinity due to the infinite value of $\frac{\partial\theta}{\partial\tau}$. It is known through conventional CV and LSV that increased scan rates lead to greater flux [2] and thus the transiently infinitely fast scan rate arising from the semi-circular potential wave will result in an infinite current response if the infinitely fast scan rate is reached near the formal potential.

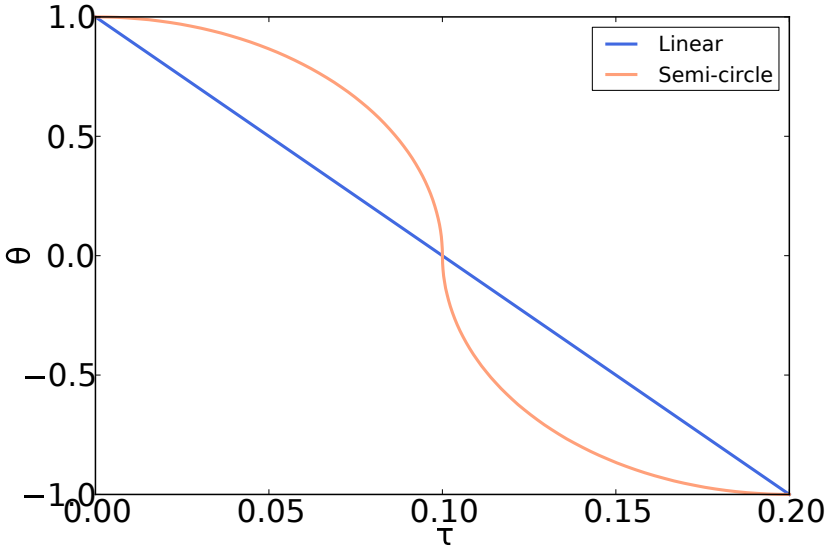


Figure 5.1: A schematic representation of the two potential waves centrered at $\theta = 0$ with an amplitude of 1. The blue line corresponds to the linear wave and the orange line corresponds to the semi-circular wave.

5.2.5 Simulation via Finite Differences

All results were obtained through the application of the ADI (alternating direction implicit) method by discretizing the dimensionless diffusion equation to solve the system [24, 27, 31] (details provided in Chapter 2). The simulation was performed in *C++* with *OpenMP* for parallel simulation while the plotting was

done in *Python* using packages *NumPy* and *matplotlib*. As part of the testing [32], peak currents were compared with theoretical values and convergence tests were performed as explained in Chapter 2.

5.3 Results and Discussion

The results are divided into two sections in which first the results from the linear and semi-circular potential waves are presented at three different scan rates of $\sigma = 10^3$, 10^1, and 10^{-1}, and second the voltammetric features obtained from the semi-circular potential wave when θ_{shift} is varied are discussed. For all results shown, the formal potential of the A/B couple was set to 0, the transfer coefficient, α, was set to 0.5 and the dimensionless standard electrochemical rate constant, K_0 was set to 10^{10} to ensure full reversibility of the redox system. The other parameters employed for simulation were $\Delta\theta = 10^{-4}$, $\omega = 1.1$, and $h = 10^{-6}$ (definition given in Chapter 2).

5.3.1 Linear versus Semi-circular Potential Sweeps: 3 Different Scan Rates

This section focuses on the voltammetric differences between the linear and semi-circular potential waves at three different scan rates of $\sigma = 10^3$, 10^1, and 10^{-1}. Figure 5.2 shows the voltammetric response of both, linear and semi-circular potential waves at $\sigma = 10^3$ and $\theta_{shift} = 0$.

The blue solid line represents the result obtained from the linear potential wave and the orange solid line represents the result obtained from the semi-circular potential wave. The blue-green solid horizontal line represents the peak current for a reversible system at a microelectrode using a linear potential wave predicted by the following empirical expression [24]:

$$I_p = -4F\epsilon c_j^* D_j (0.34e^{-0.66\sqrt{\sigma}} + 0.66 - 0.13e^{-11/\sqrt{\sigma}} + 0.351\sqrt{\sigma}) \tag{5.20}$$

Under conditions where $\sigma \to 0$, Equation (5.20) simplifies to:

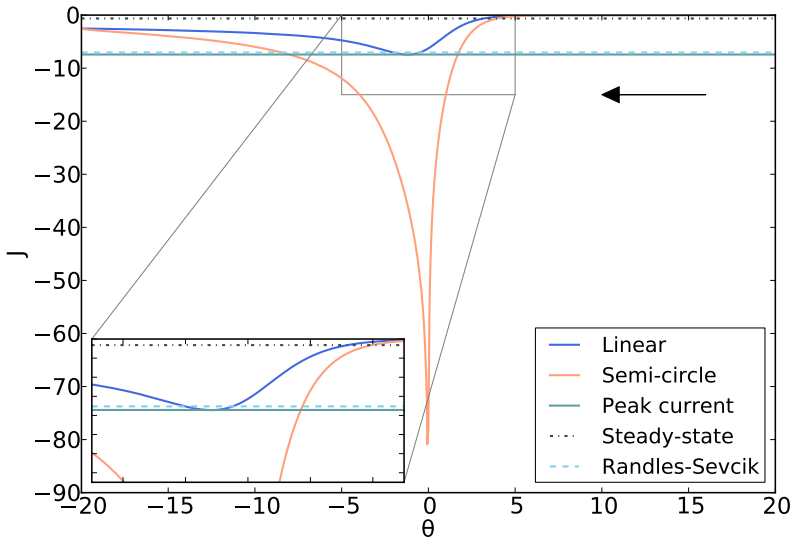


Figure 5.2: Voltammetric response using linear and semi-circular potential waves at $\sigma = 10^3$ and $\theta_{shift} = 0$. The blue solid line represents the linear potential wave result and the orange solid line represents the semi-circular potential wave result. The blue-green solid horizontal line, the dark blue dash-dotted horizontal line, and the light blue dashed horizontal line represent the theoretical peak current of a reversible system at a microelectrode using a linear potential wave predicted by Equation (5.23), (5.24), and (5.25), respectively. The arrow indicates the direction of the sweep.

$$I_{lim,ss} = -4F\epsilon c_j^* D_j \tag{5.21}$$

where steady-state limiting current is observed and is presented as a dark blue dash-dotted line in Figure 5.2. The light blue dashed line represents the peak current of a reversible system at a macroelectrode for a linear potential wave predicted by the Randles-Ševčík equation [33, 34] given as:

$$I_p = -0.446FA_{ele}c_j^*\sqrt{\frac{FD_j\nu}{RT}} \tag{5.22}$$

where A_{ele} is the area of the electrode. The arrow shows the direction of the sweep. For all results plotted, the dimensionless forms of Equations (5.20), (5.21), and (5.22) were used, giving the following three equations respectively:

$$J_p = -\frac{2}{\pi}C_j^* d_j(0.34e^{-0.66\sqrt{\sigma}} + 0.66 - 0.13e^{-11/\sqrt{\sigma}} + 0.351\sqrt{\sigma}) \tag{5.23}$$

$$J_{lim,ss} = -\frac{2}{\pi} C_j^* d_j \tag{5.24}$$

$$J_p = -0.223 C_j^* \sqrt{d_j \sigma} \tag{5.25}$$

where $C_j^* = 1$ and $d_j = 1$ for species A.

From immediate observation, it is clear that the result from the semi-circular potential wave has a significantly larger peak current compared to that from the linear potential wave, and the peak current approaches infinity at $\theta = 0$ and rapidly falls off in all other areas as predicted earlier. In Figure 5.2 the peak current from the linear potential wave matches the value predicted by Equation (5.23) but differs slightly from that predicted by Equation (5.25). This is because although the scan rate is relatively fast, it is not fast enough to converge the two expressions. In a later section other cases with higher scan rates are investigated and show that at very fast scan rates, Equations (5.23) and (5.25) predict the same value.

Figure 5.3 again shows the voltammetric response of both, linear and semi-circular potential waves but at a different scan rate of $\sigma = 10^1$ while maintaining the same potential shift value of $\theta_{shift} = 0$. The same color scheme was used as in

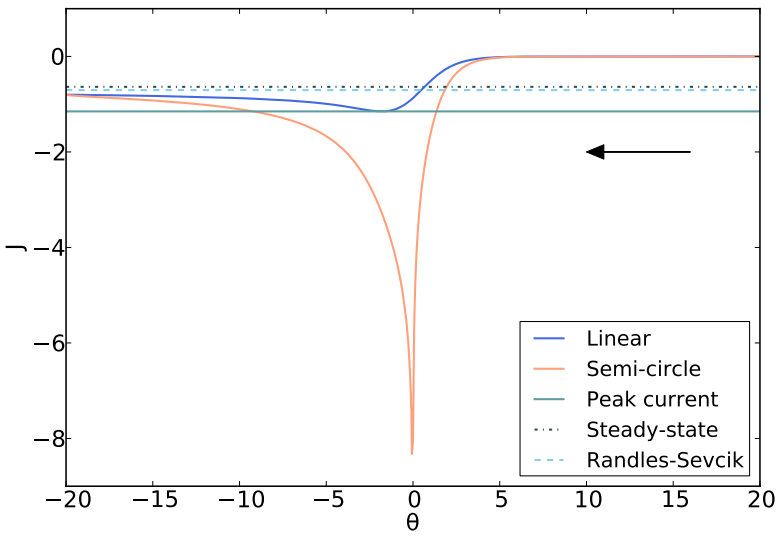


Figure 5.3: Voltammetric response using linear and semi-circular potential waves at $\sigma = 10^1$ and $\theta_{shift} = 0$. Further detail is provided in the caption of Figure 5.2.

Figure 5.2. Here the current response is reduced by approximately a tenth, but the overall behavior is the same as in Figure 5.2 with the semi-circular potential wave result showing a significantly higher peak current at $\theta = 0$ and relatively low currents everywhere else. Figure 5.3 also shows that the peak current obtained from the linear potential wave diverges further from the value predicted by the Randles-Ševčík equation due to the slower scan rate, and instead, approaches a steady-state as can be seen from the closeness between the blue-green solid horizontal line and dark blue dash-dotted horizontal line.

Figure 5.4 shows the linear and semi-circular potential wave current response at $\sigma = 10^{-1}$ and $\theta_{shift} = 0$. Again, the same color scheme is used as in Figures 5.2 and 5.3. The result from the linear potential wave shows a near steady-state response with little visible peak, and the blue-green solid horizontal line is nearly converged with the dark blue dash-dotted line, confirming the near steady-state limit. The result from the semi-circular potential wave is similar to that from the linear potential wave and can be seen approaching a steady-state limit but still shows a sharp peak at $\theta = 0$, although the value is much smaller compared to that seen in Figure 5.2.

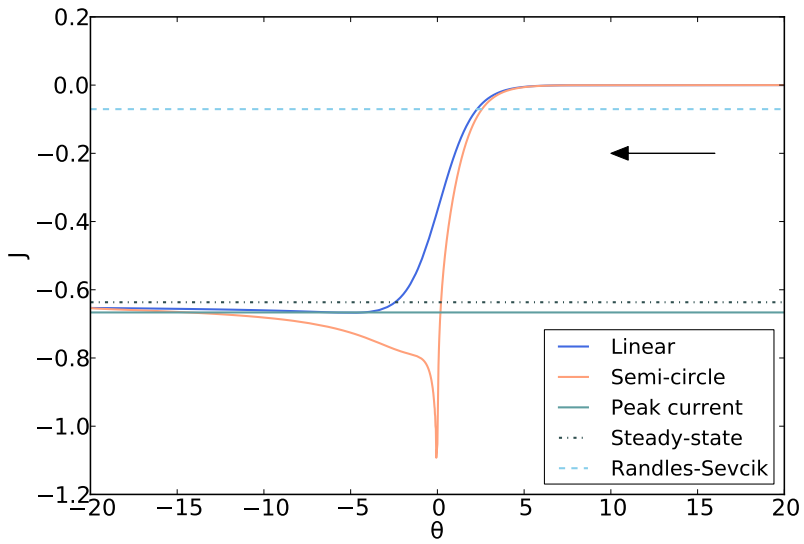


Figure 5.4: Voltammetric response using linear and semi-circular potential waves at $\sigma = 10^{-1}$ and $\theta_{shift} = 0$. Further detail is provided in the caption of Figure 5.2.

Results using scan rates of 10^3, 10^1, and 10^{-1} were explored because interesting

voltammetric features arise from the semi-circular potential wave at the transitioning stage from a fully voltammetric response to a fully steady-state limit. Two extreme cases are shown below: one when the scan rate is very fast and one when it is very slow.

Figure 5.5 shows the voltammetric response using the linear and semi-circular potential wave at $\sigma = 10^8$ and $\theta_{shift} = 0$ with the same color scheme as in Figures 5.2, 5.3, and 5.4. As discussed earlier, when $\sigma \to \infty$, a planar diffusion is observed [35–37] at the electrode surface, resulting in a macroelectrode voltammetry behavior. As a result, Equation (5.23) converges with the Randles-Ševčík expression and predicts the same peak current value, which can be seen through the perfect overlap of the blue-green solid horizontal line and the light blue dashed horizontal line in Figure 5.5. The voltammetric features observed here are mostly identical to that in Figure 5.2, except the current response is much larger in Figure 5.5 due to the faster scan rate.

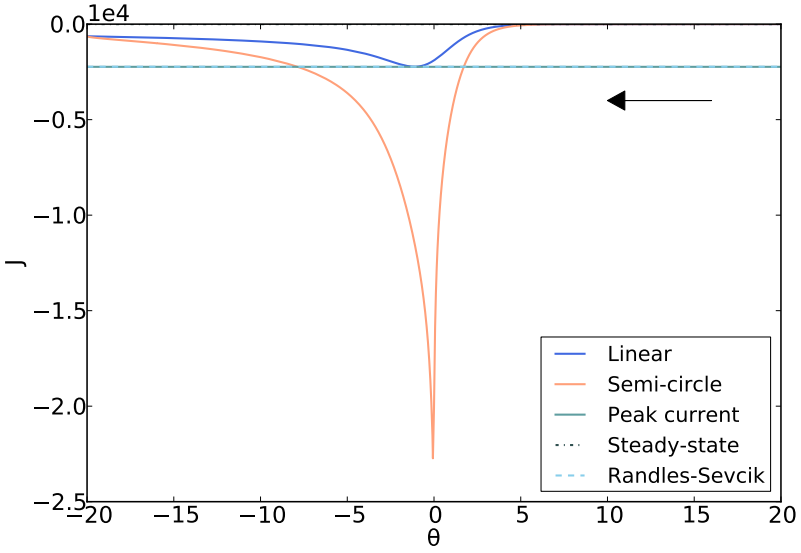


Figure 5.5: Voltammetric response using linear and semi-circular potential waves at $\sigma = 10^8$ and $\theta_{shift} = 0$. Further detail is provided in the caption of Figure 5.2.

Figure 5.6 shows the voltammetric response of the linear and semi-circular potential wave at $\sigma = 10^{-4}$ and $\theta_{shift} = 0$, again using the same color scheme as in Figures 5.2, 5.3, 5.4, and 5.5. The current shows a full steady-state behavior and Equations (5.23) and (5.24) predict the same value, which can be seen through

the overlap of the blue-green solid horizontal line and the dark blue dash-dotted horizontal line. Under full steady-state conditions, current is independent of the scan rate [38] and hence the transiently infinitely fast scan rate produced by the semi-circular potential wave does not show much effect on the current response compared to that obtained from a linear potential wave, producing nearly identical curves as evident from the overlap of the blue and orange solid lines in Figure 5.6. In such cases, the semi-circular potential wave does not hold any advantage over the conventional linear method.

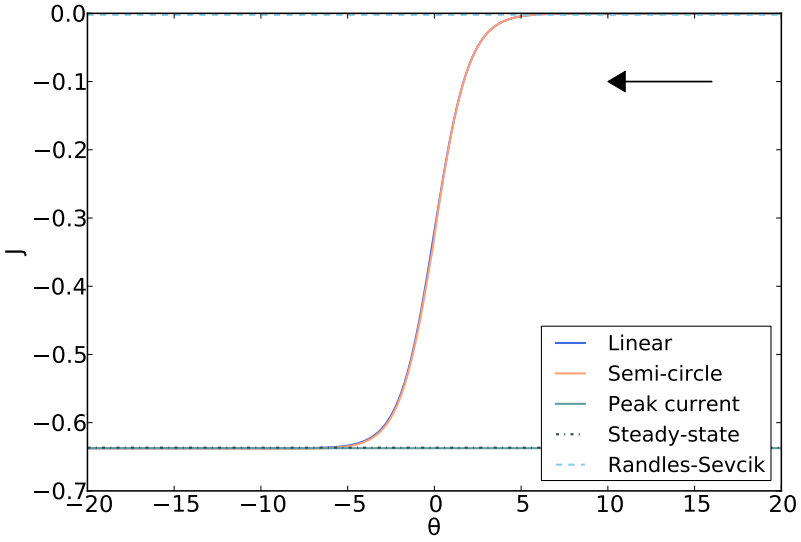


Figure 5.6: Voltammetric response using linear and semi-circular potential waves at $\sigma = 10^{-4}$ and $\theta_{shift} = 0$. Further detail is provided in the caption of Figure 5.2.

The analysis of Figures 5.2, 5.3, and 5.4 shows that under non-steady-state conditions the current response obtained from the semi-circular potential wave is significantly amplified especially at the potential where the singularity in the scan rate is observed, which, in the above three cases, is $\theta = 0$ - at the formal potential of the A/B couple. Next, the potential window was shifted by changing the θ_{shift} value in order to examine the voltammetric behavior when the singularity in the scan rate occurs at a potential different from the formal potential.

5.3.2 Semi-circular Potential Sweeps: Different θ_{shift} Values

This section investigates the effect of varying θ_{shift} values on the voltammetric response when using a semi-circular potential wave. As in section 5.3.1, scan rates of $\sigma = 10^3$, $\sigma = 10^1$, and $\sigma = 10^{-1}$ were used.

Figure 5.7 shows the voltammetric response using the semi-circular potential wave at $\sigma = 10^3$ with varying θ_{shift} values. Figure 5.7A corresponds to $\theta_{shift} = -4$, Figure 5.7B corresponds to $\theta_{shift} = -2$, Figure 5.7C corresponds to $\theta_{shift} = -1$, Figure 5.7D corresponds to $\theta_{shift} = 0$, Figure 5.7E corresponds to $\theta_{shift} = 2$, and Figure 5.7F corresponds to $\theta_{shift} = 4$.

In all figures, a sharp peak is visible and the potential at which it is observed equals the potential at which the singularity in the scan rate occurs. However, the amplification of the peak differs greatly depending on the θ_{shift} value. When the singularity occurs in the far negative region relative to the formal potential of the redox couple as in Figure 5.7A, the peak current is low because much of the material is consumed at the electrode surface and thus increasing the scan rate has little effect on the electron transfer. As θ_{shift} is moved closer to the formal potential such as in Figures 5.7B, 5.7C, and 5.7D the peak current increases. In these regions, the system is much more sensitive to changes in the applied potential and thus show significant increase in the peak current. In Figure 5.7E, the singularity occurs at a higher potential relative to the formal potential, causing more materials to be consumed at that point resulting in the small sharp peak. However, as shown in Figure 5.1, the local scan rate rapidly decreases after the singularity which results in the decrease in the current after the sharp peak in Figure 5.7E but then near the formal potential, a local absolute maximum is observed due to the diffusive current. In the far positive potential region relative to the formal potential as shown in Figure 5.7F, very little reaction is observed and thus the transiently infinitely fast scan rate does not influence the current response much and the peak current is controlled by diffusion.

Figure 5.8 shows the voltammetric response using the semi-circular potential wave at $\sigma = 10^1$. The results are reported using the same θ_{shift} values as in Figure

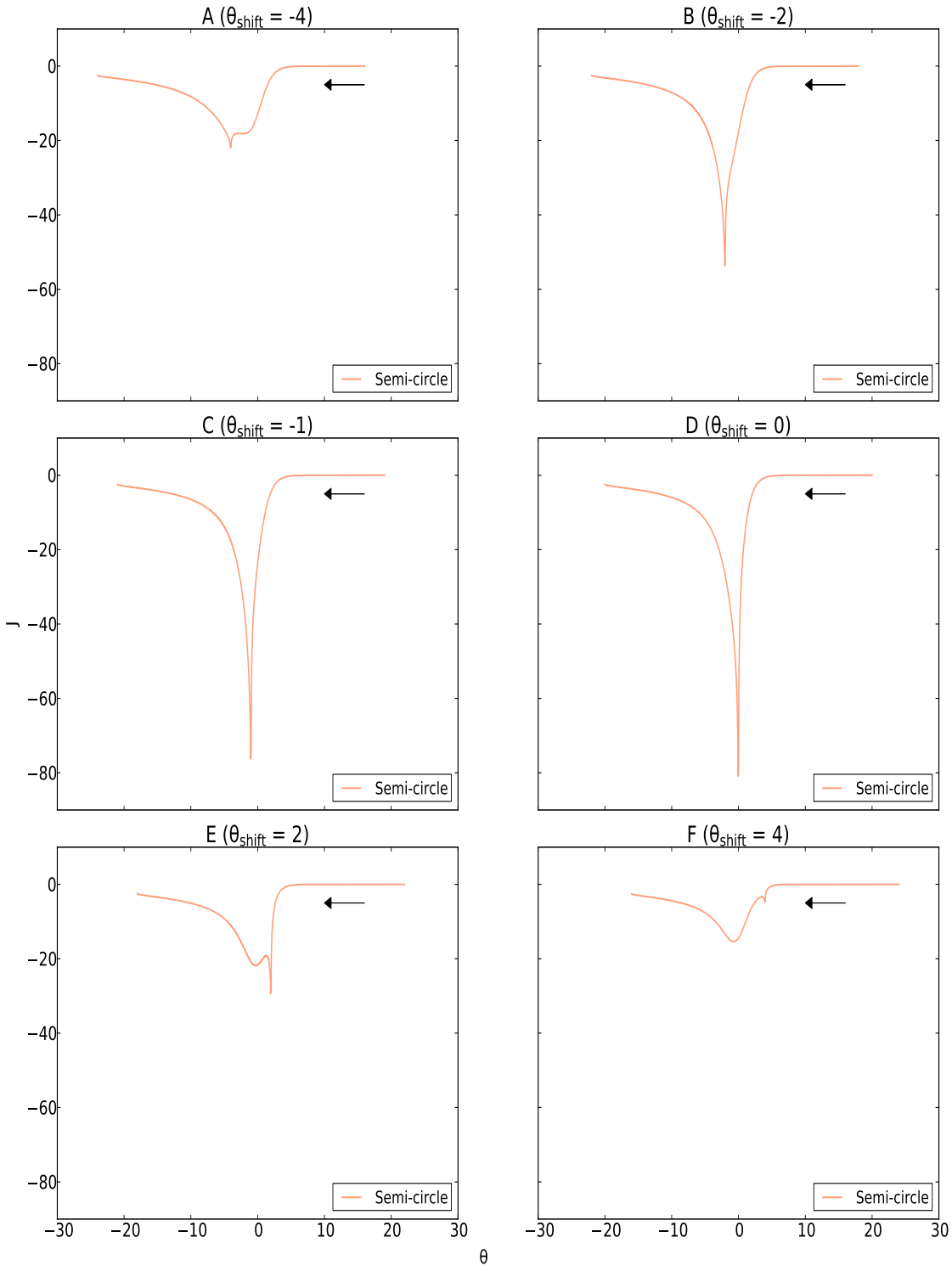


Figure 5.7: Voltammetric response using the semi-circular potential wave at $\sigma = 10^3$ with varying θ_{shift} values. A corresponds to $\theta_{shift} = -4$, B corresponds to $\theta_{shift} = -2$, C corresponds to $\theta_{shift} = -1$, D corresponds to $\theta_{shift} = 0$, E corresponds to $\theta_{shift} = 2$, and F corresponds to $\theta_{shift} = 4$. The arrows indicate the direction of the sweep.

5.7 and very similar behavior is noted. When θ_{shift} is significantly negative relative to the formal potential, little effect of the singularity is visible whereas when θ_{shift} is close to the formal potential, significant increase in the peak current is seen. When the θ_{shift} is slightly positive relative to the formal potential, two peaks occur: one resulting from the singularity of the potential wave and the other resulting from diffusion. In the far positive region where the electrode potential is not negative enough, the singularity has minimal effect on the current response.

Figure 5.9 shows the voltammetric response using the semi-circular potential wave at $\sigma = 10^{-1}$. The results are again reported using the same θ_{shift} values as in Figures 5.7 and 5.8. Since the system is near-steady-state due to the slow scan rate, the overall current is much lower but the unique current response arising from the semi-circular potential wave can still be identified. Figure 5.9A shows a very slight amplification of the peak current, which grows as θ_{shift} becomes closer to the formal potential as shown in Figures 5.9B and 5.9C. One interesting feature to note is that unlike in Figures 5.7 and 5.8, the maximum peak current is observed at $\theta_{shift} = -1$. This is caused by the fact that the instantaneously infinite scan rate of the potential wave coincides with the potential at which the diffusional peak current, i.e. the peak that arises from the diffusive mass transport along the concentration gradient rather than the temporarily accelerated scan rate, is observed, thereby enhancing the current response. This analysis becomes more apparent in Figures 5.9D, 5.9E, and 5.9F. Figure 5.9D is the same voltammogram as the semi-circular result in Figure 5.4 and shows a slight "dip". In Figures 5.9B and 5.9C, a steep and rapid decrease in current is observed after the peak current until it levels off in the far negative potential region whereas in Figure 5.9D, the current decreases significantly after $\theta_{shift} = 0$ but then the curve becomes less steep before leveling off. This slight decrease in the steepness of the curve, referred to as the "dip", is caused by the diffusional current. Figure 5.9E shows the diffusional current more prominently at around $\theta = -1$, and as θ_{shift} becomes increasingly positive, the sharp current response becomes less visible.

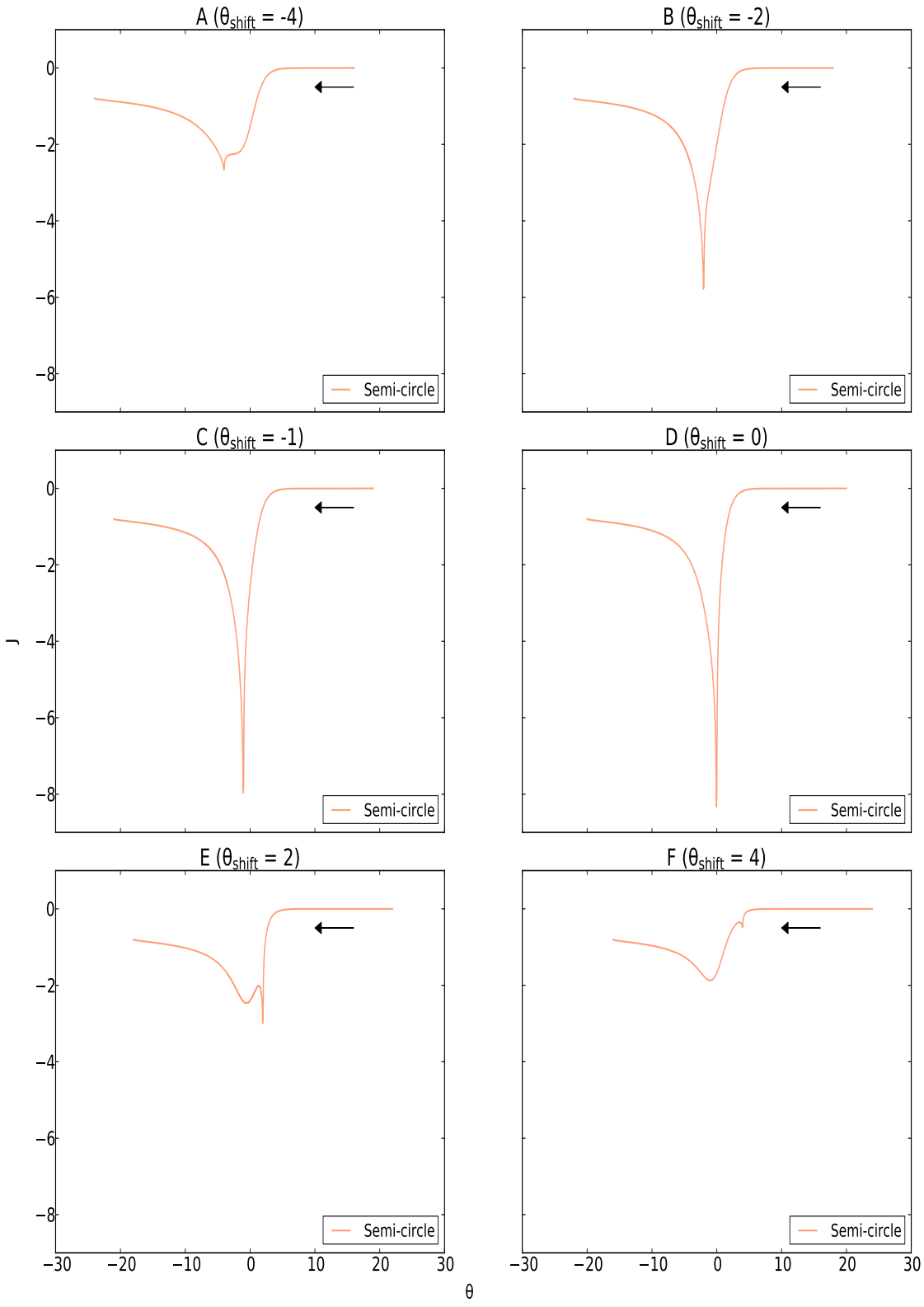


Figure 5.8: Voltammetric response using the semi-circular potential wave at $\sigma = 10^1$ with varying θ_{shift} values. Further detail is provided in the caption of Figure 5.7.

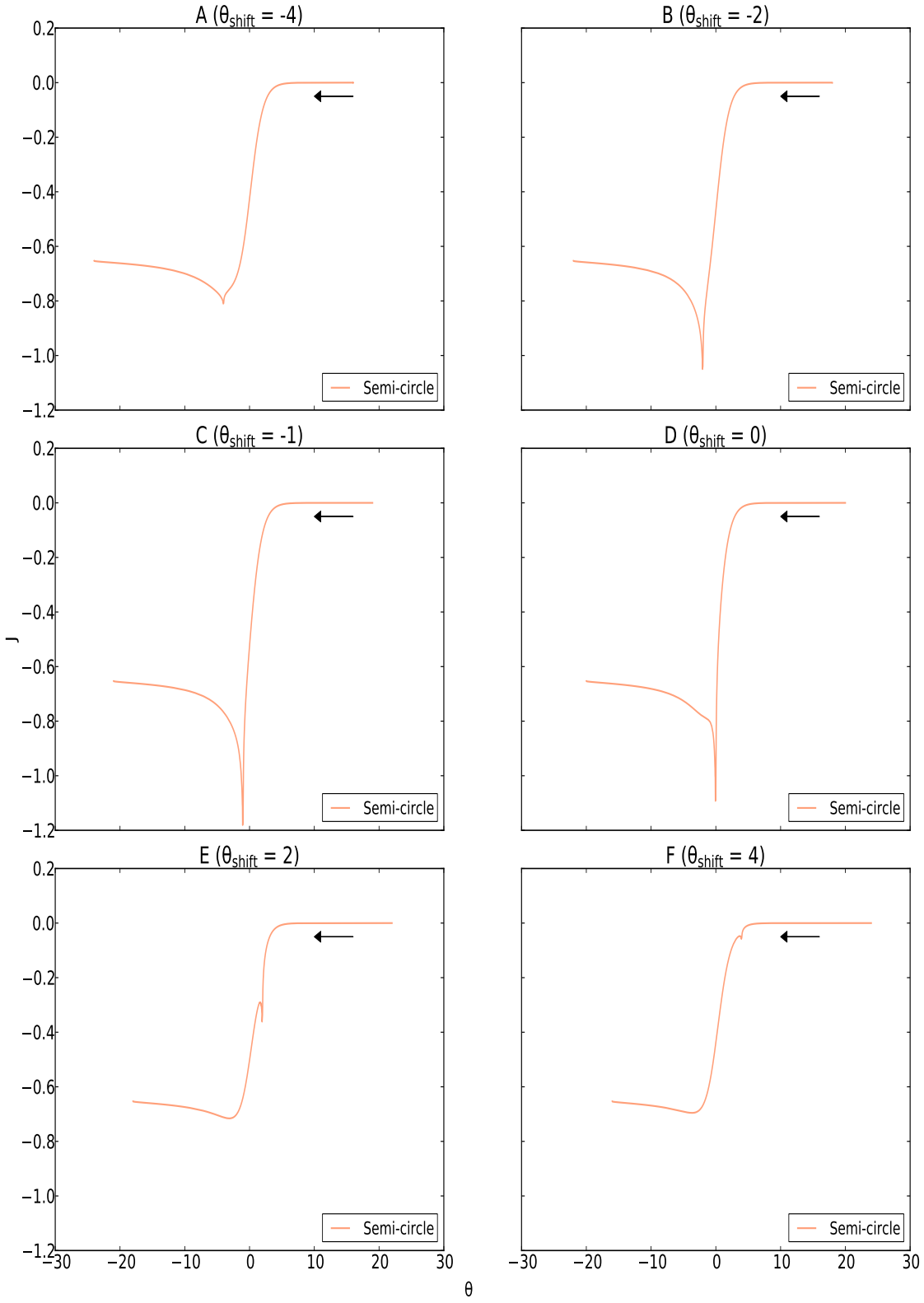
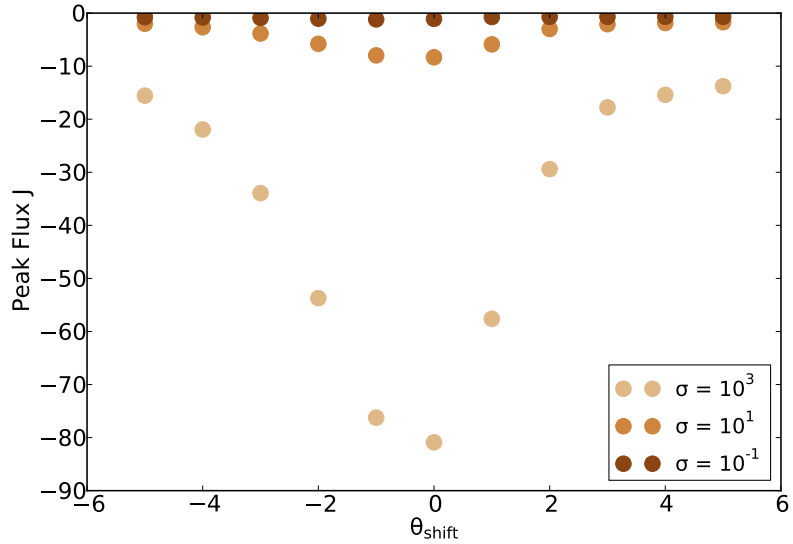


Figure 5.9: Voltammetric response using the semi-circular potential wave at $\sigma = 10^{-1}$ with varying θ_{shift} values. Further detail is provided in the caption of Figure 5.7.

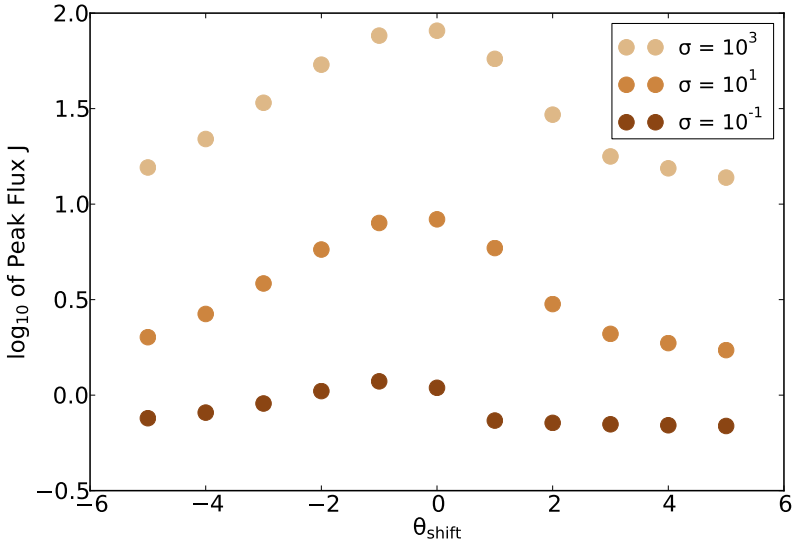
The change in peak currents with respect to the θ_{shift} values is presented clearly in Figures 5.10(a) and 5.10(b). Figure 5.10(a) shows the dimensionless peak currents plotted against the θ_{shift} values at which they are observed and Figure 5.10(b) shows the $\log_{10}$ of the absolute dimensionless peak currents plotted against their respective θ_{shift} values. Both figures use the same color scheme where the beige dots represent results from $\sigma = 10^3$, the brown dots represent results from $\sigma = 10^1$, and the dark brown dots represent results from $\sigma = 10^{-1}$. As evident, peak flux increases as θ_{shift} approaches 0 from reasons discussed earlier. However, from Figures 5.10(a) and 5.10(b), it is unclear whether the absolute maximum occurs at $\theta_{shift} = 0$ or somewhere between $\theta_{shift} = -1$ and $\theta_{shift} = 0$. In order to determine the exact potential at which the absolute maximum peak flux is observed, the θ_{shift} values must be more refined near the formal potential but for high scan rates such as $\sigma = 10^3$, the absolute maximum peak flux is assumed to be observed at a θ_{shift} value similar to that shown in Chapter 4.

From the results presented in Sections 5.3.1 and 5.3.2, the semi-circular potential wave exhibits similar advantages at a microelectrode as it does at a macroelectrode. The method introduced here gives the opportunity of amplifying a peak that would otherwise be too small to be seen in conventional linear wave voltammetry, such as when the potentiostat's signal-to-noise ratio exceeds the peak current in the conventional case and is thus ideal for electroanalysis. The technique may also be used to detect the presence of one species in a solution comprising multiple electroactive analytes where otherwise differential pulse or square wave voltammetry might be needed [39–44].

For the simulation, since $\theta^0_{f,A/B} = 0$, the θ_{shift} expression is reduced to $\theta_{shift} = \theta_{avg}$. However in experimental practice, the above analysis would be performed by repeatedly applying the dimensional semi-circular equation (refer to Chapter 4) where E_{avg} is the controlled parameter until an "infinite" peak or an absolute maximum peak is observed. Since, depending on σ, the infinite peak occurs at $\theta_{shift} = 0$ or in its immediate vicinity, as shown through the above analysis, by



(a) Dimensionless peak currents plotted against the corresponding θ_{shift} values at which they were observed for scan rates 10^3, 10^1, and 10^{-1}. The beige dots represent results from $\sigma = 10^3$, the brown dots represent results from $\sigma = 10^1$, and the dark brown dots represent results from $\sigma = 10^{-1}$.



(b) $\log_{10}$ of the absolute dimensionless peak currents in (a) plotted against the θ_{shift} values. The same color scheme is used as in (a).

Figure 5.10

determining the E_{avg} value at which the absolute maximum current is observed, the formal potential of a species can be estimated.

5.4 Conclusions

A simple one-electron electrochemically reversible reaction was investigated using a semi-circular potential wave and the potential window was shifted to study the resulting changes in voltammetric response at a microelectrode. The transiently infinitely fast scan rate at the midpoint of the potential wave results in an "infinite" peak current when the midpoint potential is at the formal potential of a redox system or in its immediate vicinity. The unique voltammetric features resulting from the semi-circular potential wave is suitable for electroanalysis and hence complements and in some situations can replace the conventional linear scan voltammetry.

The analysis shows that the semi-circular potential wave exhibits similar advantages at microelectrodes as it does at macroelectrodes. This significantly broadens the applicability of this new voltammetric technique. Due to their advanced mass transport characteristics, reduced capacitive effect, and their applicability in many scientific fields, microelectrodes have become a very popular electrode in electroanalysis [10, 45]. Since changing the voltammetric wave often only requires comparably small amendments to many electrochemical set-ups and microelectrodes are so commonly used, the presented work dramatically advances the availability of this new and exciting method to a wider scientific community.

References

[1] Y. Uchida, E. Kätelhön, R. G. Compton, *Journal of Electroanalytical Chemistry* **2018**, *823*, 465–473.

[2] R. G. Compton, C. E. Banks, *Understanding Voltammetry*, Imperial College Press, **2010**.

[3] J. J. Van Benschoten, J. Y. Lewis, W. R. Heineman, D. A. Roston, P. T. Kissinger, *Journal of Chemical Education* **1983**, *60*, 772.

[4] M. Rudolph, D. P. Reddy, S. W. Feldberg, *Analytical Chemistry* **1994**, *66*, 589A–600A.

[5] R. Forster, *Chemical Society Reviews* **1994**, *23*, cited By 173, 289–297.

[6] M. Fleischmann, S. Pons, *Analytical Chemistry* **1987**, *59*, 1391A–1399A.

[7] C. Amatore, C. Pebay, L., A. Wang, J.-S. Warkocz, *Analytical Chemistry* **2010**, *82*, 6933–6939.

[8] C. Amatore, E. Maisonhaute, G. Simonneau, *Electrochemistry Communications* **2000**, *2*, 81–84.

[9] R. G. Compton, J. C. Eklund, L. Nei, *Journal of Electroanalytical Chemistry* **1995**, *381*, 87–93.

[10] I. Montenegro, M. A. Queirós, J. L. Daschbach, *Microelectrodes: Theory and Applications*, *Vol. 197*, Kluwer Academic Press: Dordrecht, The Netherlands, **1991**.

[11] H. T. H. Chan, E. Kätelhön, R. G. Compton, *Journal of Electroanalytical Chemistry* **2017**, *799*, 126–133.

[12] M. C. Henstridge, E. Laborda, E. J. Dickinson, R. G. Compton, *Journal of Electroanalytical Chemistry* **2012**, *664*, 73–79.

[13] E. J. F. Dickinson, J. G. Limon-Petersen, N. V. Rees, R. G. Compton, *The Journal of Physical Chemistry C* **2009**, *113*, 11157–11171.

[14] C. Amatore, A. Oleinick, I. Svir, *Analytical Chemistry* **2008**, *80*, 7947–7956.

[15] S. Ching, R. Dudek, E. Tabet, *Journal of Chemical Education* **1994**, *71*, 602.

[16] D. H. Evans, K. M. O'Connell, R. A. Petersen, M. J. Kelly, *Journal of Chemical Education* **1983**, *60*, 290.

[17] J. Heinze, *Angewandte Chemie International Edition in English* **1984**, *23*, 831–847.

[18] J. K. Novev, S. Eloul, R. G. Compton, *The Journal of Physical Chemistry C* **2016**, *120*, 13549–13562.

[19] J. K. Novev, R. G. Compton, *Current Opinion in Electrochemistry* **2018**, *7*, 118–129.

[20] V. Sahore, A. Kreidermacher, F. Z. Khan, I. Fritsch, *Journal of The Electrochemical Society* **2016**, *163*, H3135–H3144.

[21] K. Ngamchuea, S. Eloul, K. Tschulik, R. G. Compton, *Analytical Chemistry* **2015**, *87*, 7226–7234.

[22] X. Gao, J. Lee, H. S. White, *Analytical Chemistry* **1995**, *67*, 1541–1545.

[23] C. Amatore, C. Pebay, L. Thouin, A. Wang, *Electrochemistry Communications* **2009**, *11*, 1269–1272.

[24] R. G. Compton, E. Laborda, K. R. Ward, *Understanding Voltammetry: Simulation of Electrode Processes*, Imperial College Press, **2013**.

[25] J. Crank, *The Mathematics of Diffusion*, Oxford University Press, **1979**.

[26] K. R. Ward, N. S. Lawrence, R. S. Hartshorne, R. G. Compton, *Journal of Electroanalytical Chemistry* **2012**, *683*, 37–42.

[27] J. Heinze, *Journal of Electroanalytical Chemistry and Interfacial Electrochemistry* **1981**, *124*, 73–86.

[28] R. Guidelli, R. G. Compton, J. M. Feliu, E. Gileadi, J. Lipkowski, W. Schmickler, S. Trasatti, **2014**, *86*, 259–262.

[29] R. Guidelli, R. G. Compton, J. M. Feliu, E. Gileadi, J. Lipkowski, W. Schmickler, S. Trasatti, **2014**, *86*, 245–258.

[30] A. J. Bard, L. R. Faulkner, *Electrochemical Methods: Fundamentals and Applications*, John Wiley & Sons Inc, **2000**.

[31] S. Eloul, R. G. Compton, *Journal of Electroanalytical Chemistry* **2016**, *771*, 50–55.

[32] E. Kätelhön, R. G. Compton, *Analyst* **2015**, *140*, 2592–2598.

[33] J. E. B. Randles, *Trans. Faraday Soc.* **1948**, *44*, 327–338.

[34] A. Ševčík, *Collect. Czech. Chem. Commun.* **1948**, *13*, 349–377.

[35] D. O. Wipf, E. W. Kristensen, M. R. Deakin, R. M. Wightman, *Analytical Chemistry* **1988**, *60*, 306–310.

[36] C. Andrieux, D. Garreau, P. Hapiot, J. Pinson, J. Savéant, *Journal of Electroanalytical Chemistry and Interfacial Electrochemistry* **1988**, *243*, 321–335.

[37] A. Fitch, D. H. Evans, *Journal of Electroanalytical Chemistry and Interfacial Electrochemistry* **1986**, *202*, 83–92.

[38] A. M. Bond, K. B. Oldham, C. G. Zoski, *Analytica Chimica Acta* **1989**, *216*, 177–230.

[39] J. G. Osteryoung, R. A. Osteryoung, *Analytical Chemistry* **1985**, *57*, 101–110.

[40] C. M. A. Brett, A. M. O. Brett, *Electrochemistry : Principles, Methods, and Applications*, Oxford University Press, **1993**.

[41] G. C. Barker, I. L. Jenkins, *Analyst* **1952**, *77*, 685–696.

[42] F. Scholz, *Electroanalytical Methods*, Springer-Verlag Berlin Heidelberg, **2010**.

[43] J. J. O'Dea, J. Osteryoung, R. A. Osteryoung, *Analytical Chemistry* **1981**, *53*, 695–701.

[44] Á. Molina, J. González, *Pulse Voltammetry in Physical Electrochemistry and Electroanalysis: Theory and Applications (Monographs in Electrochemistry)*, Springer, **2016**.

[45] D. K. Cope, D. E. Tallman, *Journal of Electroanalytical Chemistry and Interfacial Electrochemistry* **1990**, *285*, 79–84.

6

Determining Kinetic Parameters Through Semi-circular Potential Wave Voltammetry at Microelectrodes

This chapter applies the semi-circular potential wave voltammetry introduced in Chapters 4 and 5 to electrode kinetic studies at a microdisc electrode. The work presented here is based on work published in the '*Journal of Electroanalytical Chemistry* 2019, 835, 60-66' [1].

Contents

6.1 Introduction 132
6.2 Theory 133
6.2.1 Theoretical Model 133
6.2.2 Boundary Conditions 134
6.2.3 Dimensionless Coordinates 135
6.2.4 Semi-circular Potential Wave 136
6.2.5 Simulation via Finite Differences 138
6.3 Results and Discussion 138
6.3.1 Linear versus Semi-circular Potential Sweeps: 1.0 V s^{-1} Scan Rate 138
6.3.2 Determining k_0 141
6.3.3 Linear versus Semi-circular Potential Sweeps: 100.0 mV s^{-1} Scan Rate 146
6.4 Conclusions 147

6.1 Introduction

As discussed in Chapters 4 and 5, linear sweep voltammetry (LSV) and cyclic voltammetry (CV) are widely used to study electrochemical reactions [2] and to provide insight into the thermodynamics of a redox process and the kinetics of heterogeneous electron transfer [3]. Both methods employ individual or sequences of linear potential sweeps [4] of the form:

$$E(t) = \pm\nu t + E(t = 0) \tag{6.1}$$

where $E(t)$ is the applied potential as a function of time, t, and ν is the scan rate defined as the slope of the wave.

Linear sweep- and cyclic voltammograms are commonly studied to determine the kinetics of a redox reaction while a number of different approaches can be pursued. Oldham et al. [5] have proposed a method to determine formal potentials, standard electrochemical rate constants, and electrochemical transfer coefficients using the quartile potentials ($E_{1/4}$, $E_{1/2}$, and $E_{3/4}$) of a steady-state voltammogram measured at a microdisc electrode. Mirkin and Bard [6] later advanced and extended the analysis of steady-state voltammograms to include the voltammetry of any uniformly-accessible electrode. In addition, fast scan approaches have been proven to be beneficial in the measurement of fast standard electrochemical rate constants as shown by the Wightman group [7] and can be further accelerated to the megavolts per second range as reported by Amatore et al. [8].

In Chapters 4 and 5, an alternative method to LSV was introduced and discussed, which employs a semi-circular potential waveform rather than a linear wave. The semi-circular wave produces a transiently infinitely fast scan rate at the midpoint of the potential window which can be exploited to enable the selective amplification of current responses in potential regions set by the experimentalist. This chapter further develops the semi-circle voltammetry and proposes an alternative method to measure the standard electrochemical rate constant through simple analysis of voltammograms measured at microdisc electrodes. The technique is advantageous

in that the application of such a potential wave requires only small changes to any existing electrochemical set-up, and the analysis is straight-forward.

6.2 Theory

The following sections introduce the theoretical model used and explain the waveforms employed in the simulation. Further, the conversion between the dimensional and dimensionless coordinates used in the simulation (also provided in Chapter 5) are listed.

6.2.1 Theoretical Model

A simple one-electron reduction reaction of A to B was investigated with varying rate constants at a microdisc electrode where diffusion is the only means of mass transport, and species A and B have equal diffusion coefficients:

$$A(aq) + e \rightleftharpoons B(aq) \tag{6.2}$$

The above reaction was simulated under the assumption that a sufficiently high concentration of supporting electrolyte is present in order to suppress migration [3, 9–12]. With long scan durations, convection [13–15] may need to be taken into account [16–18], although its effect is significantly reduced with decreasing electrode size [19]. The transport of analyte for the above system is thus expressed through the diffusion equation given as [4, 20, 21]:

$$\frac{\partial c_j}{\partial t} = D_j \left(\frac{\partial^2 c_j}{\partial x^2} + \frac{\partial^2 c_j}{\partial y^2} + \frac{\partial^2 c_j}{\partial z^2} \right) \tag{6.3}$$

where j is the species of interest and D is its diffusion coefficient. More conveniently, the diffusion to a microdisc electrode can be expressed in cylindrical polar coordinates:

$$\frac{\partial c_j}{\partial t} = D_j \left(\frac{\partial^2 c_j}{\partial r^2} + \frac{1}{r}\frac{\partial c_j}{\partial r} + \frac{1}{r^2}\frac{\partial^2 c_j}{\partial \phi^2} + \frac{\partial^2 c_j}{\partial z^2} \right) \tag{6.4}$$

where z is the perpendicular distance from the electrode surface, r is the radial distance from the longitudinal axis, and ϕ is the azimuth [4, 20]. In the model discussed, the longitudinal axis passes through the centre of the microdisc electrode thereby creating a rotationally symmetric system. Thus there will be no change in flux with respect to angle ϕ and Equation (6.4) is reduced to [4, 20, 22–24]:

$$\frac{\partial c_j}{\partial t} = D_j \left(\frac{\partial^2 c_j}{\partial r^2} + \frac{1}{r}\frac{\partial c_j}{\partial r} + \frac{\partial^2 c_j}{\partial z^2} \right) \tag{6.5}$$

6.2.2 Boundary Conditions

Assuming $D_A = D_B$ and that prior to the experiment only the reactant is present, the following boundary conditions can be established:

$$t \leq 0;\ \text{all } z,\ r;\ c_A = c_A^*;\ c_B = 0 \tag{6.6}$$

As t increases, the concentration at the electrode surface varies but no change is observed at the outer boundary surface:

$$t > 0,\ z \to \infty,\ c_A = c_A^*,\ c_B = 0 \tag{6.7}$$

$$t > 0,\ r \to \infty,\ c_A = c_A^*,\ c_B = 0 \tag{6.8}$$

In addition, two no-flux boundaries are introduced where no change in the concentration gradient is observed. One is set at the insulating supporting surface, and the other at the cylindrical axis, $r = 0$, due to the rotational symmetry, giving:

$$t > 0,\ r > \epsilon,\ \left(\frac{\partial c}{\partial z}\right)_{z=0} = 0 \tag{6.9}$$

$$t > 0,\ \text{all } z,\ \left(\frac{\partial c}{\partial r}\right)_{r=0} = 0 \tag{6.10}$$

where ϵ is the radius of the electrode. Conservation of mass predicts that the amount of A consumed at the electrode surface equals the amount of B produced which, under the assumption that species A and B have equal diffusion coefficients, gives:

$$t > 0,\ r \leq \epsilon,\ z = 0,\ \ -\frac{\partial c_A}{\partial z} = \frac{\partial c_B}{\partial z} \tag{6.11}$$

and the following condition holds true for all space and time:

$$c_A + c_B = c_A^* \tag{6.12}$$

Since this chapter focuses on the effect of the standard electrochemical rate constant on semi-circular potential wave voltammetry, the Butler-Volmer model was inplemented to describe the electrode kinetics:

$$j_{net} = k_0 exp\left[\frac{-\alpha F(E - E_f^0)}{RT}\right][A]_0 - k_0 exp\left[\frac{(1-\alpha)F(E - E_f^0)}{RT}\right][B]_0 \tag{6.13}$$

where j_{net} is the flux of the reactant to the electrode surface, k_0 is the standard electrochemical rate constant, $[A]_0$ and $[B]_0$ are the surface concentrations of species A and B respectively, α is the transfer coefficient [25, 26], F, R, and T, hold their usual meanings, E is the electrode potential, and E_f^0 is the formal potential of the A/B redox couple. Since the flux of A, j_A, can also be expressed via Fick's First Law, assuming $D_A = D_B$, it can be written as:

$$j_A = -D\left(\frac{\partial c_A(z,t)}{\partial z}\right)_{z=0} = -\left[k_{red}c_A(0,t) - k_{ox}c_B(0,t)\right] \tag{6.14}$$

Substituting the relationships $\theta = \frac{F}{RT}(E - E_{f,A/B}^0)$, $k_{red} = k_0 e^{-\alpha\theta}$, and $k_{ox} = k_0 e^{(1-\alpha)\theta}$, Equation (6.14) is expressed in terms of the standard electrochemical rate constant:

$$D\left(\frac{\partial c_A(0,t)}{\partial z}\right)_{z=0} = k_0 e^{-\alpha\theta}c_A(0,t) - k_0 e^{(1-\alpha)\theta}c_B(0,t) \tag{6.15}$$

6.2.3 Dimensionless Coordinates

Table 6.1 shows the conversion factors between dimensional and dimensionless coordinates, and all simulations were run using dimensionless coordinates. From Table 6.1, Fick's Second Law can be rewritten in terms of dimensionless coordinates:

$$\frac{\partial C}{\partial \tau} = d_j \left(\frac{\partial^2 C}{\partial R^2} + \frac{1}{R}\frac{\partial C}{\partial R} + \frac{\partial^2 C}{\partial Z^2} \right) \tag{6.16}$$

and Equation (6.15) becomes:

$$\frac{C_{A,1} - C_{A,0}}{h} = \frac{1}{d_j} K_0 f(\theta) \{ C_{A,0} - [1 + C_B^* - C_{A,0}] e^{\theta} \} \tag{6.17}$$

where $C_{A,1}$ and $C_{A,0}$ are the dimensionless concentrations of species A at position Z_1 and Z_0, respectively, $f(\theta) = e^{-\alpha\theta}$, and $h = Z_1 - Z_0$ assuming A and B have equal diffusion coefficients.

Table 6.1: Dimensionless parameters. [20]

Parameter	Normalization
concentration	$C_j = \frac{c_j}{c_A^*}$
diffusion coefficient	$d_j = \frac{D_j}{D_A}$
z spatial coordinate	$Z = \frac{z}{\epsilon}$
r spatial coordinate	$R = \frac{r}{\epsilon}$
time	$\tau = \frac{D_A t}{\epsilon^2}$
potential	$\theta = \left(\frac{F}{RT}\right)(E - E^0_{f,A/B})$
scan rate	$\sigma = \left(\frac{\epsilon^2}{D_A}\right)\left(\frac{F}{RT}\right)\nu$
current	$J = \frac{I}{2\pi\epsilon F D_A c_A^*}$
rate constant	$K_0 = \frac{k_0 \epsilon}{D_A}$

6.2.4 Semi-circular Potential Wave

The semi-circular potential wave employed in this chapter is described via the equation below:

$$\theta(\tau) = \pm\sqrt{\left|\theta_{A_0}^2 - [\sigma \cdot (\tau - c\tau_{max})]^2\right|} + \theta_{shift} \tag{6.18}$$

where $\theta(\tau)$ is the dimensionless potential with respect to dimensionless time, θ_{A_0} is the dimensionless amplitude, σ is the dimensionless average scan rate defined as the slope of the linear wave, c is the fraction of the maximum time when the centre of each semi-circle is observed, $\tau_{max} = \frac{2\theta_{A_0}}{\sigma}$, and $\theta_{shift} = \theta_{avg} - \theta_f^0$. θ_f^0 is the

dimensionless formal potential of the A/B couple, which, by definition, is 0 and thus $\theta_{shift} = \theta_{avg}$ where θ_{avg} is the midpoint of the potential window. The scan rate of the semi-circular potential wave changes with respect to time such that it produces an instantaneously infinite scan rate at the mid-point of the wave and slower scan rates at all other areas. These features result in a selective current amplification at the transiently infinite scan rate and suppression at the slower scan rates. Further detail on the derivation of Equation (6.18) is provided in Chapter 4.

Figure 6.1 shows the two potential waves employed; the blue line represents the conventional linear wave and the orange line represents the semi-circular wave centered at $\theta = 0$ with $\theta_{A_0} = 1$. In Figure 6.1, the semi-circular potential wave is plotted using $c = 0$ and $c = 1$ for the first and second half of the wave, respectively. From simple observation, it is clear that the scan rate of the linear potential wave is constant throughout the entire sweep whereas the scan rate of the semi-circular potential wave changes throughout the scan where at the midpoint an instantaneously infinite scan rate is observed.

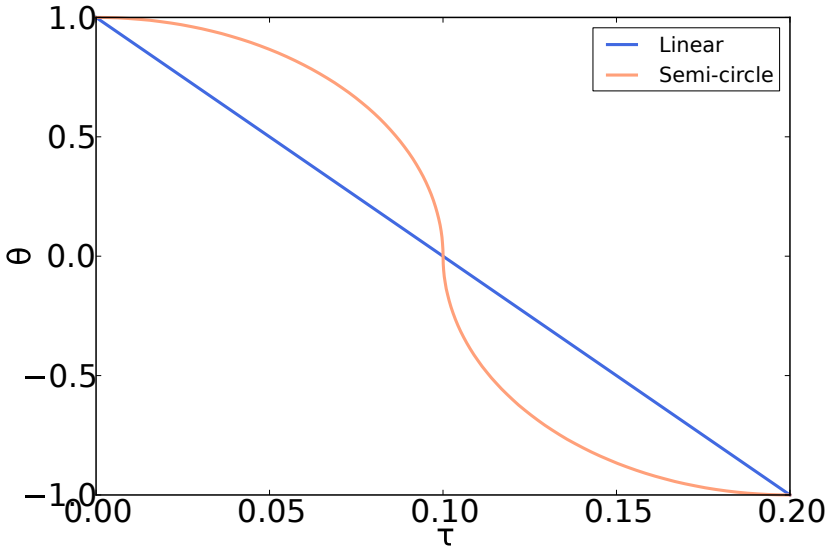


Figure 6.1: A schematic representation of the two potential waves centrered at $\theta = 0$ with an amplitude of 1. The blue line corresponds to the linear wave and the orange line corresponds to the semi-circular wave.

6.2.5 Simulation via Finite Differences

All results reported were obtained by solving the discretized dimensionless diffusion equation through the use of the ADI (alternating direction implicit) method [20, 24, 27] as explained in Chapter 2. The simulations were written in *C++* with *OpenMP* which allows for parallel computing and the plotting was done in *Python* with the packages *NumPy* and *matplotlib*. Testing [28] was performed by comparing simulated peak flux with the semi-empirically predicted value where applicable and through convergence tests. The convergence test results are presented in *Appendix*: A.5.1.

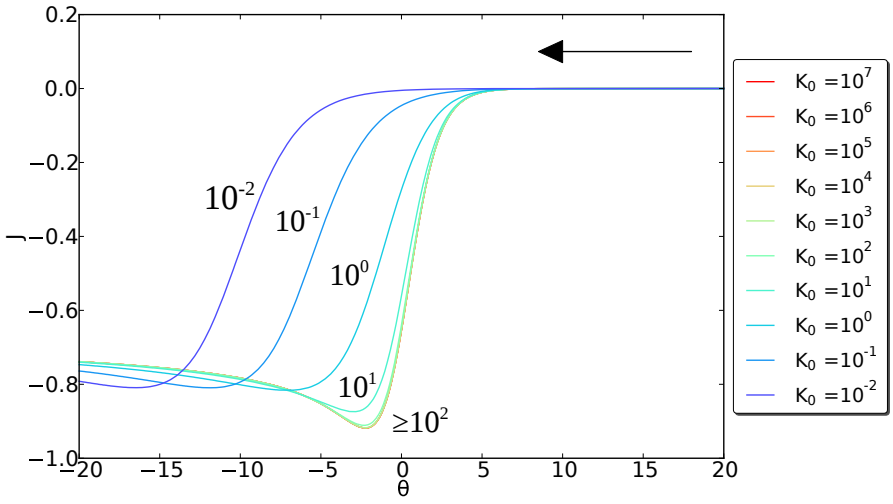
6.3 Results and Discussion

The following sections discuss the new opportunities for determining the standard electrochemical rate constant, k_0, of a redox system via the application of a semi-circular potential wave. First, the voltammetric features that emerge from the semi-circular potential wave and its increased sensitivity to electrode kinetics is discussed at a relatively fast average scan rate of 1.0 V s^{-1}. The second section shows how the voltammograms may be used to determine the rate constant, and the third section illustrates that the same analysis can be applied with a slower average scan rate of 100.0 mV s^{-1}. All data is calculated for a transfer coefficient of 0.5 unless otherwise specified to reflect common experimental situations where typical α values [20] are in the range of $0.3 < \alpha < 0.7$. The other parameters employed for simulation were $\Delta\theta = 10^{-4}$, $\omega = 1.1$, and $h = 10^{-6}$ (definition given in Chapter 2).

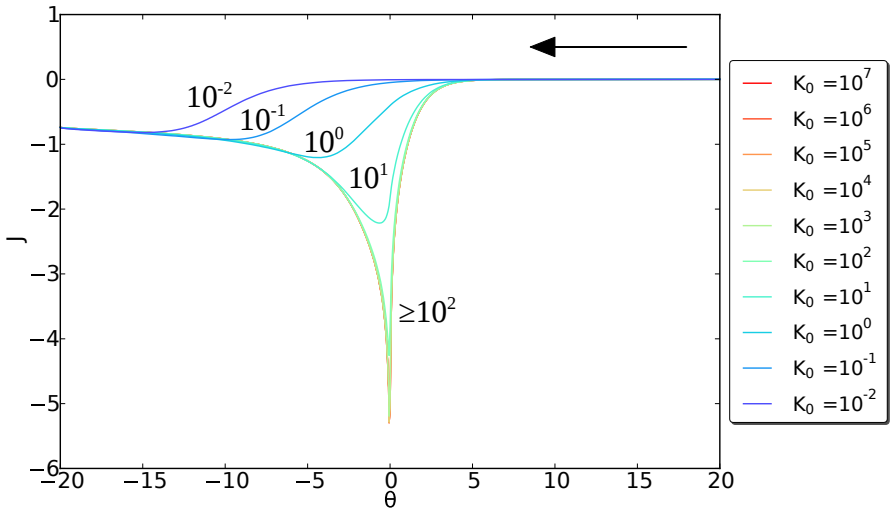
6.3.1 Linear versus Semi-circular Potential Sweeps: 1.0 V s^{-1} Scan Rate

This section explores the differences between linear and semi-circular potential wave voltammetry using an average scan rate of 1.0 V s^{-1}, which, in dimensionless terms corresponds to $\sigma = 3.89$ when $\epsilon = 10^{-5}$ m, $D = 10^{-9}$ m^2 s^{-1}, and $T = 298$ K. Figures 6.2(a) and 6.2(b) show the voltammetric response using the linear and semi-circular potential waves, respectively, with varying K_0's. The plots are color-coded and the corresponding K_0 values are listed in the label. The arrow indicates the direction

of the sweep. In both figures, the system approaches the irreversible limit (lower K_0) where the graphs are shifted towards the left and approaches the reversible limit (higher K_0) towards the right where the shape of the voltammogram is almost independent of the value of K_0. The linear results show very little to almost no peaks depending on the K_0 whereas the semi-circular results show a sharp peak for fast K_0's and comparably little current response for low K_0's for reasons discussed below.



(a) Dimensionless current responses using linear potential waves.



(b) Dimensionless current responses using semi-circular potential waves.

Figure 6.2: Dimensionless current responses using (a)linear potential waves and (b)semi-circular potential waves with various K_0 values and $\sigma = 3.89$ evaluated for $\theta_{shift} = 0$ and $\alpha = 0.5$. Each voltammogram is color-coded and the corresponding K_0 values are listed in the label and the arrow indicates the direction of the sweep. The graphs approach the irreversible limit (low K_0) towards the left and reversible limit (high K_0) towards the right.

Figure 6.2(a) shows the results obtained from the linear potential wave with varying K_0 values. Due to the relatively fast scan rate, the system does not attain a full steady-state, and as can be seen, some of the plots with higher K_0's show peaks, which are typical features observed in non-steady-state linear sweep voltammetry. As K_0 decreases the peak diminishes and less analyte is consumed. This behavior is due to the fact that with slower electrode kinetics, higher overpotential is required to drive the reaction and hence shifts the voltammetric curve as shown most clearly through the three left-most graphs in Figure 6.2(a). A shift indicates that a current response is seen at more negative potentials, while the slower kinetics reduce the peak flux as the response is limited by the electrode kinetics and not the mass transport.

Figure 6.2(b) shows the results obtained from the semi-circular potential wave with varying K_0 values and the general trend is similar to that seen in Figure 6.2(a). With very high K_0 values such as 10^7, the system is fully reversible and the voltammogram shows a sharp peak as expected from Chapter 5. With decreasing K_0, the current response decreases as well and approaches a near steady-state. A noticeable feature in Figure 6.2(b) is the appearance of the sharp peak with increasing K_0 values, which can be explained through the Butler-Volmer model. With very high standard electrochemical rate constants, the Butler-Volmer expression becomes indistinguishable from the Nernst equation giving [29]:

$$E = E_f^0 + \frac{RT}{F} ln \frac{[A]_0}{[B]_0} \tag{6.19}$$

hence the dimensionless form is:

$$\theta = ln \frac{C_{A,0}}{C_{B,0}} \tag{6.20}$$

The Nernst equation shows the ratio of the concentrations of A to B at the electrode surface, and reflects the term e^θ where θ is the dimensionless potential. Therefore any change in the potential is directly reflected in the concentration and consequently the voltammogram. The semi-circular potential wave shows significant potential changes at the midpoint of the wave and the effect of this behavior is manifested in the infinite peak flux observed in Figure 6.2(b) for plots with very high K_0 values.

On the other hand, when the electrode kinetics are sluggish, a Butler-Volmer model as given in Equation (6.17) must be used to describe the concentration gradient at the electrode surface. This model no longer gives the direct concentration ratio at the electrode surface but rather the gradient, which is a function of the rate constant and the applied potential. As K_0 decreases, so do the contribution of the $e^{-\alpha\theta}$ and $e^{(1-\alpha)\theta}$ terms to the overall flux. As such, if the value of K_0 is small enough, changes in the potential, however significant, will not affect the flux in a way expected for systems with high K_0 values to produce a sharp peak. At low K_0 values, the reaction is slow and is therefore less limited by diffusive mass transport, which explains why there is no peak.

From Figures 6.2(a) and 6.2(b), it is clear that the results obtained using the semi-circular potential wave are more sensitive to the changes in electrode kinetics and produces unique voltammetric curves with respect to K_0.

6.3.2 Determining k_0

The two figures presented in Section 6.3.1 were calculated for $\theta_{shift} = 0$ and $\alpha = 0.5$, and show that the voltammograms obtained using a semi-circular potential wave produce characteristic curves depending on the K_0, which can be used for the determination of the rate constant. Experimentally, this would be done by running an LSV with a semi-circular potential wave using a potential window symmetric with respect to E_f^0 and comparing its voltammetric curve with a simulated curve. In practice, the peak current of the high rate constant voltammogram may be filtered due to the limitation of the potentiostat and thus when comparing experimental data to simulated data, the curve prior to the infinite scan rate is considered. Once the experimental voltammogram is obtained, a simulation is run with various K_0's and by superimposing the capacitive current-corrected experimental and simulated curves, the rate constant can be determined or estimated with high accuracy.

The advantage of the semi-circular method is its increased sensitivity to the k_0 in the high k_0 region. Figure 6.2(a) shows that between $K_0 = 10^1$ and $K_0 = 10^2$, very little difference is seen in the voltammograms whereas Figure 6.2(b) shows

a significant change in the shape of the the curves between these two K_0 values thereby adding a one order greater magnitude sensitivity.

It should be noted that all results reported in Figure 6.2 and the following were obtained for $\theta_{shift} = 0$ and thus when applied to experimental practice, the formal potential of the redox couple must be available to ensure that the potential wave is symmetric with respect to the formal potential. Additionally, the transfer coefficient, α, must be known for simulation. It is further noted that the analysis of the semi-circular potential wave result discussed above is only applicable for near steady-state systems where the voltammetric curve shows appreciable change with respect to varying K_0's. For systems recorded at very slow scan rates, the current approaches a full steady-state such as that shown in Figure 6.3 and the semi-circular potential wave shows very little to no effect on the voltammetric curve. Consequently, the linear and semi-circular potential waves produce nearly identical results and the latter method loses its advantage.

Figures 6.3(a) and 6.3(b) show the voltammetric response when the scan rate is $\sigma = 10^{-4}$ for the same K_0's as reported in Figures 6.2(a) and 6.2(b). The pink dashed line shows the steady-state limiting current predicted by the following expression [20]:

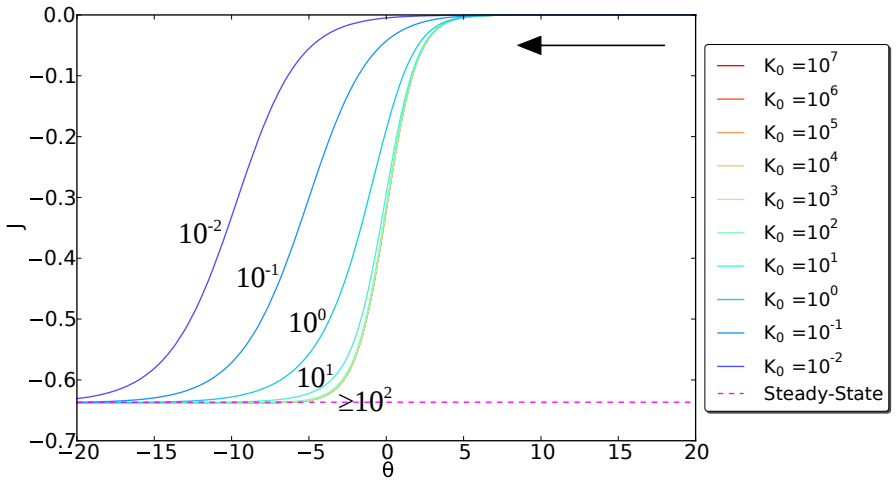
$$I_{lim,ss} = -4F\epsilon c_j^* D_j \tag{6.21}$$

which in dimensionless term is:

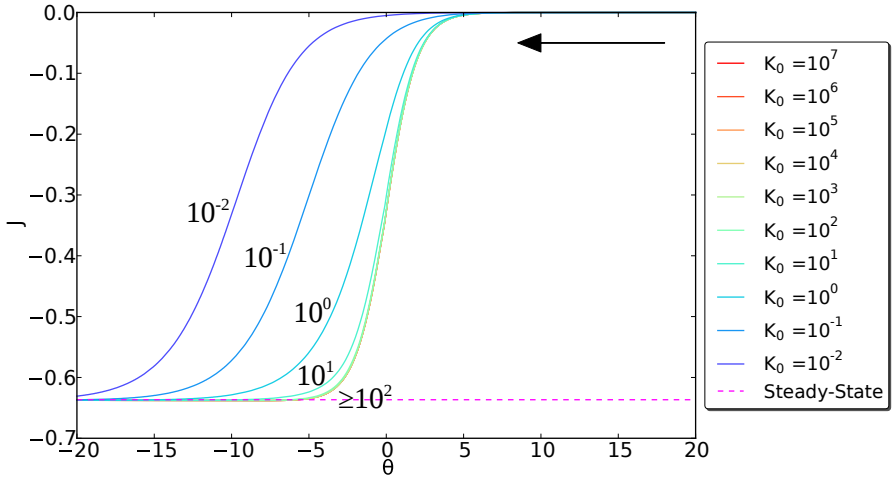
$$J_{lim,ss} = -\frac{2}{\pi} C_j^* d_j \tag{6.22}$$

where $C_j^* = 1$ and $d_j = 1$ for species A.

All linear results converge to a steady value indicating the system is in the full steady-state limit, and from simple observation it is clear that the two figures produce nearly identical curves for every K_0 value. One might expect to see a relatively sharp peak in the semi-circular results at the midpoint of the potential window for high K_0 values, however, this is not the case. The reason is that since the system is near the steady-state and, at all times, the diffusion is fast compared to the reaction kinetics, changes in scan rate are less reflected in the current response.



(a) Dimensionless current response using linear potential waves.

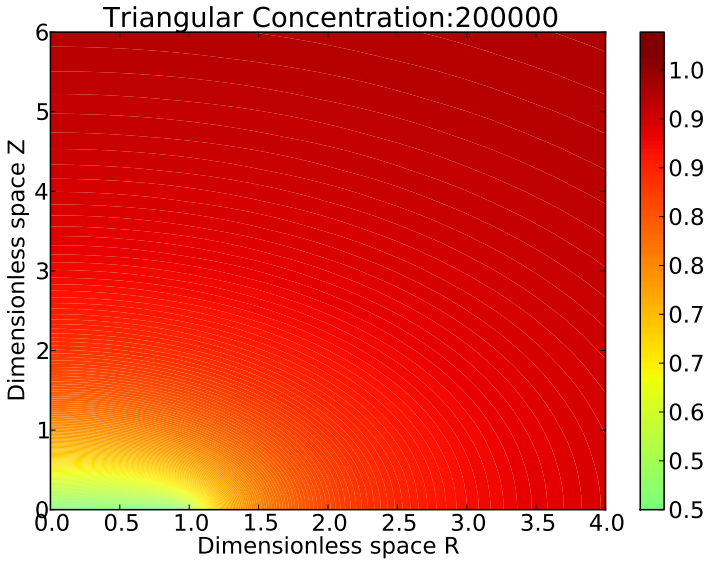


(b) Dimensionless current response using semi-circular potential waves.

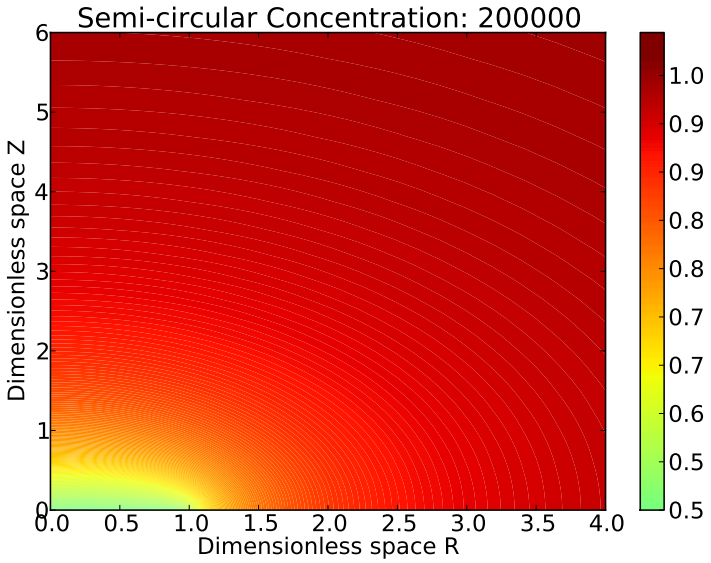
Figure 6.3: Dimensionless current responses using (a) linear potential wave and (b) semi-circular potential wave with various K_0 values and $\sigma = 10^{-4}$. The pink dashed line represents the steady-state limiting flux predicted by Equation (6.22). Further detail is provided in the caption of Figure 6.2.

The semi-circular concentration profile was compared against that obtained using a linear potential wave when the dimensionless potential is zero in order to further check whether the two methods produce identical current responses. Figures 6.4(a) and 6.4(b) show the concentration profiles obtained from the linear and semi-circular potential waves, respectively at the timestep $\tau = 200000$ and $K_0 = 10^7$. This particular timestep was chosen because it is when $\theta(\tau) = 0$ for both waves and is where the transiently infinite scan rate is observed in the semi-circular potential wave. Hence any discrepancies between the two methods will

be reflected maximally at this timestep.



(a) Linear concentration profile at $\tau = 200000$ and $\theta(\tau) = 0$.

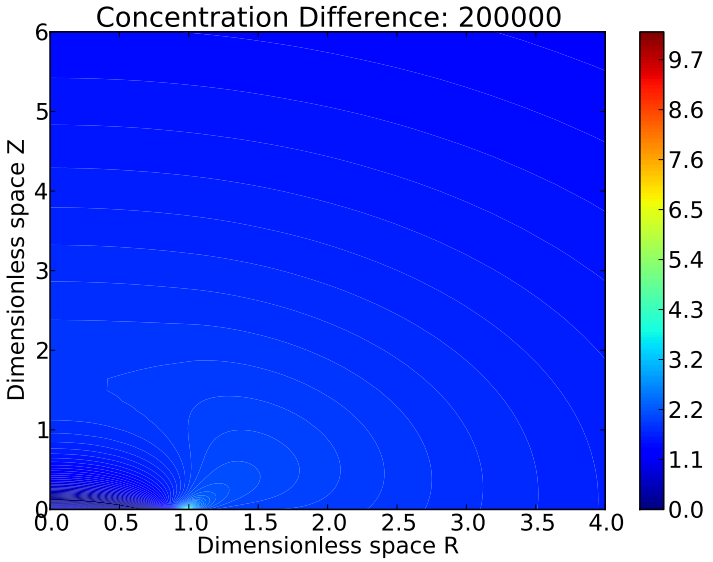


(b) Semi-circular concentration profile at $\tau = 200000$ and $\theta(\tau) = 0$.

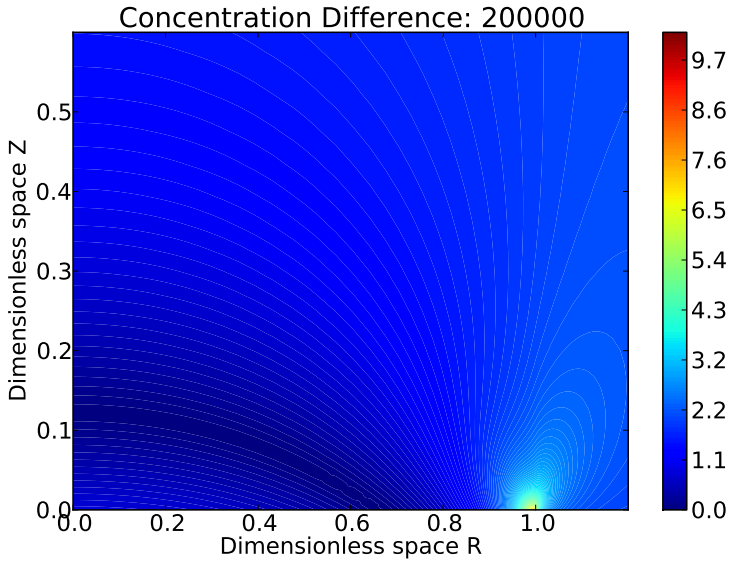
Figure 6.4

Simple examination of the two figures give the impression that the two concentration profiles are effectively equal across the entire space. A depletion of species at and near the electrode surface is seen, represented via the light green and yellow with a radial diffusion near the edge at $R = 1$. Since the real difference between the two concentration profiles cannot be determined through observation, their percent

differences were plotted additionally as shown in Figures 6.5(a) and 6.5(b).



(a) Percent difference between Figures 6.4(a) and 6.4(b).



(b) Zoomed up version of (a).

Figure 6.5

Figure 6.5(a) shows the percent difference between Figures 6.4(a) and 6.4(b), and Figure 6.5(b) shows a zoomed up version of Figure 6.5(a) for clarity. From Figure 6.5(b) it can be seen that the biggest percent difference is observed at the edge of the electrode at $R = 1$, as shown through the bright colors. This is expected because this is where radial diffusion occurs and thus changes in the diffusion will

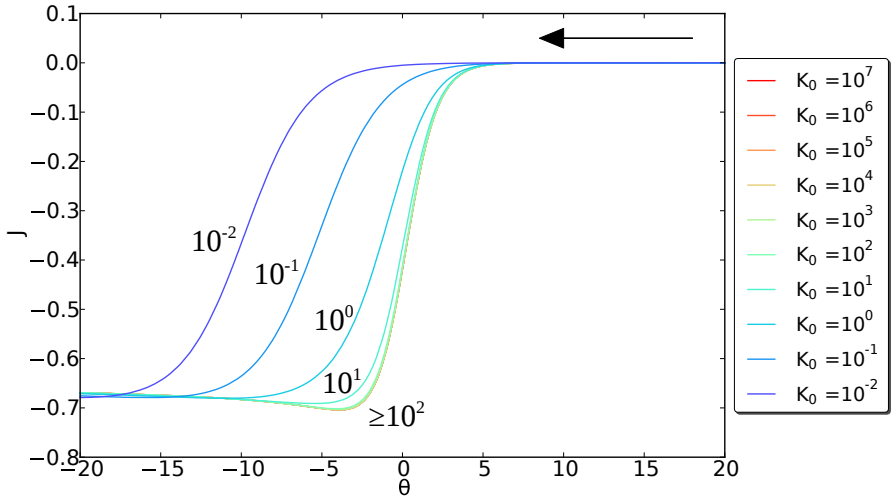
be pronounced most significantly in this area.

From the analysis of Figure 6.5(b), it is clear that even though the concentration profiles obtained from the linear and semi-circular potential wave methods are very similar, there are differences, which reach up to approximately 10% for the chosen set of parameters. Nevertheless, the difference reflected in the current response is negligible and both methods achieve a full steady-state. Consequently, the semi-circular method loses its advantage over the linear method and hence cannot be used for the determination of k_0 through its curve shape.

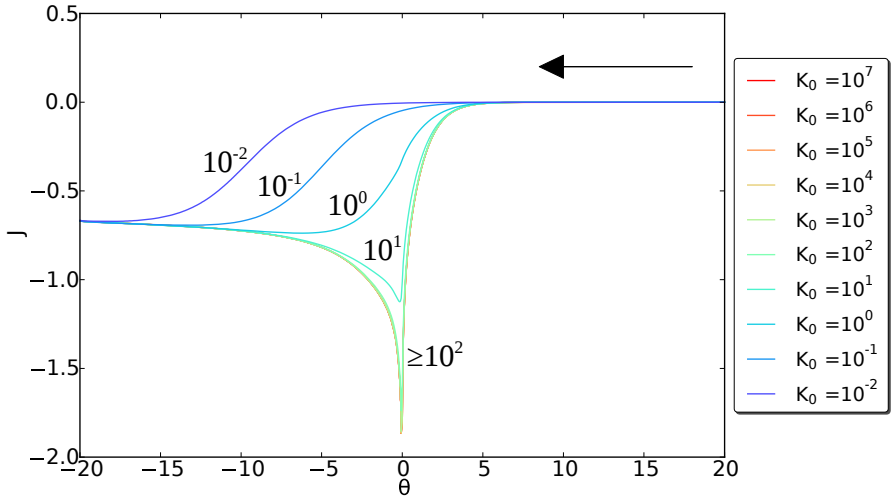
6.3.3 Linear versus Semi-circular Potential Sweeps: 100.0 mV s^{-1} Scan Rate

The analysis in Section 6.3.1 was performed for results obtained using a relatively fast average scan rate of 1.0 V s^{-1}. This section shows that similar trends and sensitivities can be observed using a scan rate of 100.0 mV s^{-1}, which gives a near steady-state response for all K_0's when the conventional linear potential wave is employed. Other parameters are the same as reported earlier where $\epsilon = 10^{-5}$ m, $D = 10^{-9}$ m^2 s^{-1}, and $T = 298$ K, giving $\sigma = 0.389$. Figures 6.6(a) and 6.6(b) correspond to the linear and semi-circular voltammograms recorded at the same K_0 values as in Figures 6.2(a) and 6.2(b), respectively.

In Figure 6.6(a), very little difference is seen between the voltammograms of $K_0 = 10^1$ and $K_0 = 10^2$. On the other hand, the semi-circular voltammograms (Figure 6.6(b)) for the said K_0 values show significant difference in the curve shape, showing that the k_0 determination can be performed for slower scan rates. In addition to the analysis of the first half of the voltammetric curve, the general shape of the overall curve may be used as an indication of the region of k_0 of the system since at $K_0 = 10^2$ a sharp peak is observed whereas at $K_0 = 10^1$ a smoother, less steep peak is recorded.



(a) Dimensionless current responses using linear potential waves.



(b) Dimensionless current responses using semi-circular potential waves.

Figure 6.6: Dimensionless current responses using (a)linear potential wave and (b)semi-circular potential wave with various K_0 values and $\sigma = 0.389$. Further detail is provided in the caption of Figure 6.2.

6.4 Conclusions

This chapter introduced an alternative way of determining the standard electrochemical rate constant via the application of a semi-circular potential wave at a microdisc electrode. To this end, a one-electron reduction reaction of A to B was investigated with varying dimensionless kinetic parameters, K_0. The results show that the semi-circular potential wave approach can measure K_0 values one order magnitude greater than the values that can be measured via the conventional

linear potential wave approach. The presented data allows experimentalists to determine the rate constant of a redox system under study by comparing their voltammograms with simulated curves.

References

[1] Y. Uchida, E. Kätelhön, R. G. Compton, *Journal of Electroanalytical Chemistry* **2019**, *835*, 60–66.

[2] G. A. Mabbott, *Journal of Chemical Education* **1983**, *60*, 697.

[3] J. Heinze, *Angewandte Chemie International Edition in English* **1984**, *23*, 831–847.

[4] R. G. Compton, C. E. Banks, *Understanding Voltammetry*, Imperial College Press, **2010**.

[5] K. B. Oldham, J. C. Myland, C. G. Zoski, A. M. Bond, *Journal of Electroanalytical Chemistry and Interfacial Electrochemistry* **1989**, *270*, 79–101.

[6] M. V. Mirkin, A. J. Bard, *Analytical Chemistry* **1992**, *64*, 2293–2302.

[7] D. O. Wipf, E. W. Kristensen, M. R. Deakin, R. M. Wightman, *Analytical Chemistry* **1988**, *60*, 306–310.

[8] C. Amatore, E. Maisonhaute, G. Simonneau, *Electrochemistry Communications* **2000**, *2*, 81–84.

[9] C. Amatore, A. Oleinick, I. Svir, *Analytical Chemistry* **2008**, *80*, 7947–7956.

[10] S. Ching, R. Dudek, E. Tabet, *Journal of Chemical Education* **1994**, *71*, 602.

[11] D. H. Evans, K. M. O'Connell, R. A. Petersen, M. J. Kelly, *Journal of Chemical Education* **1983**, *60*, 290.

[12] U. Kalapathy, D. E. Tallman, S. Hagen, *Journal of Electroanalytical Chemistry* **1992**, *325*, 65–81.

[13] J. K. Novev, S. Eloul, R. G. Compton, *The Journal of Physical Chemistry C* **2016**, *120*, 13549–13562.

[14] J. K. Novev, R. G. Compton, *Current Opinion in Electrochemistry* **2018**, *7*, 118–129.

[15] V. Sahore, A. Kreidermacher, F. Z. Khan, I. Fritsch, *Journal of The Electrochemical Society* **2016**, *163*, H3135–H3144.

[16] C. Amatore, C. Pebay, L., A. Wang, J.-S. Warkocz, *Analytical Chemistry* **2010**, *82*, 6933–6939.

[17] K. Ngamchuea, S. Eloul, K. Tschulik, R. G. Compton, *Analytical Chemistry* **2015**, *87*, 7226–7234.

[18] X. Gao, J. Lee, H. S. White, *Analytical Chemistry* **1995**, *67*, 1541–1545.

[19] C. Amatore, C. Pebay, L. Thouin, A. Wang, *Electrochemistry Communications* **2009**, *11*, 1269–1272.

[20] R. G. Compton, E. Laborda, K. R. Ward, *Understanding Voltammetry: Simulation of Electrode Processes*, Imperial College Press, **2013**.

[21] J. Crank, *The Mathematics of Diffusion*, Oxford University Press, **1979**.

[22] K. R. Ward, N. S. Lawrence, R. S. Hartshorne, R. G. Compton, *Journal of Electroanalytical Chemistry* **2012**, *683*, 37–42.

[23] E. J. F. Dickinson, J. G. Limon-Petersen, N. V. Rees, R. G. Compton, *The Journal of Physical Chemistry C* **2009**, *113*, 11157–11171.

[24] J. Heinze, *Journal of Electroanalytical Chemistry and Interfacial Electrochemistry* **1981**, *124*, 73–86.

[25] R. Guidelli, R. G. Compton, J. M. Feliu, E. Gileadi, J. Lipkowski, W. Schmickler, S. Trasatti, **2014**, *86*, 259–262.

[26] R. Guidelli, R. G. Compton, J. M. Feliu, E. Gileadi, J. Lipkowski, W. Schmickler, S. Trasatti, **2014**, *86*, 245–258.

[27] S. Eloul, R. G. Compton, *Journal of Electroanalytical Chemistry* **2016**, *771*, 50–55.

[28] E. Kätelhön, R. G. Compton, *Analyst* **2015**, *140*, 2592–2598.

[29] A. J. Bard, L. R. Faulkner, *Electrochemical Methods: Fundamentals and Applications*, John Wiley & Sons Inc, **2000**.

7

Cathodic Stripping Voltammetry using Semi-circular Potential Waves for Increased Sensitivity of Detection

This chapter explores the application of the semi-circular potential wave introduced in Chapter 4 to stripping voltammetry. The work presented here has been published in the '*Journal of Electroanalytical Chemistry* 2019, 848, 113290' [1].

Contents

7.1 Introduction 152
7.2 Theory 153
7.2.1 Theoretical Model 153
7.2.2 Dimensionless Coordinates 155
7.2.3 Semi-circular Potential Wave 156
7.2.4 Simulation via Finite Difference 157
7.3 Results and Discussion 157
7.3.1 Effect of Potential Window Shift 158
7.3.2 Features of Semi-circular Potential Wave Voltammetry . 161
7.3.3 Experimental Applications 167
7.4 Conclusions 168

7.1 Introduction

Stripping voltammetry allows the detection of metals, metal complexes [2, 3] and organic substances at low concentrations [4] making it a valuable technique for trace analysis [5–8]. Methods can be categorized into three types: anodic (ASV), cathodic (CSV), and adsorptive (AdSV). This chapter focuses on CSV, which, computationally is equivalent to ASV. Both, CSV and ASV require a pre-concentration step where the analyte is electrodeposited on the electrode surface by applying the appropriate potential for a certain amount of time followed by the dissolution step [4, 9–11]. On the other hand, in AdSV, the analyte adsorbs on the electrode surface via other physical or chemical interactions which may not involve a charge transfer with the electrode [9, 12, 13]. The analysis in all three methods is conventionally carried out by changing the applied potential linearly with respect to time to either a negative or positive value depending on the desired reaction [14–17]:

$$E(t) = \pm\nu t + E(t = 0) \tag{7.1}$$

The current response recorded via stripping voltammetry can be used to obtain analytical information such as the identity of the analyte through the peak potential and its concentration through the peak current [18] and the charge under the curve [9]. Stripping voltammetry is generally regarded as a highly sensitive method [19–21] with detection limits going as low as 10^{-10} M in some cases [22].

This chapter proposes a new method for stripping voltammetry that enhances the sensitivity of detection through the application of a semi-circular potential wave rather than the linear potential wave (7.1). It is shown that the semi-circular potential wave increases the peak current and produces a characteristic voltammetric curve for a given potential window and formal potential, and its shape changes with the shift of the potential window. The increased current allows the determination of surface concentrations and the characteristic curve is useful in identifying species of interest. It is noted that the classical system would be one using a mercury

film electrode, however, the herein introduced model can be extended to similar systems with a conducting film.

7.2 Theory

In the following sections, a theoretical model for stripping voltammetry with a semi-circular potential waveform is explained and dimensionless coordinates are introduced. Furthermore, the semi-circular wave is discussed and a description of the simulation method employed is given.

7.2.1 Theoretical Model

A one-electron electrochemically-reversible reduction of A to B was investigated where species A is adsorbed to the electrode in a film of thickness d and B is in solution.

$$A\,(ads) + e \rightleftharpoons B\,(sol) \tag{7.2}$$

As the system is fully reversible, it establishes a Nernstian equilibrium at the electrode surface at all times [4, 23]:

$$\begin{aligned} E &= E_f^0 + \frac{RT}{F} ln \frac{c_A^0}{c_B^0} \\ &= E_f^0 + \frac{RT}{F} ln \frac{c_A^s}{dc_B} \end{aligned} \tag{7.3}$$

where E is the electrode potential, E_f^0 is the formal potential of the A/B couple, R, T and F hold their usual meanings, and c_A^0 and c_B^0 are the volume concentrations of species A and B at the electrode surface, respectively. Here, since A is adsorbed to the electrode, its concentration is expressed in terms of a surface concentration c_A^s ([mol cm^{-2}]), which, divided by the film thickness, d, gives the volume concentration c_A^0 at the electrode surface. Consequently, only the mass transport of B is considered which is modeled via Fick's Second Law in one dimension [22, 24]:

$$\frac{\partial c_B}{\partial t} = D_B \frac{\partial^2 c_B}{\partial x^2} \tag{7.4}$$

where D_B is the diffusion coefficient of B.

In order to simulate the given system, five equations must be considered. First is the Nernst equation as given in Equation (7.3), which dictates the reaction at the electrode/solution interface. Second is the diffusion of B as shown through Equation (7.4). Additionally, the fluxes of species A and B and the conservation of mass must be considered as expressed by Equations (7.5), (7.6), and (7.7), respectively.

$$j_A = \frac{\partial c_A^s}{\partial t} \tag{7.5}$$

$$j_B = -D_B \frac{\partial c_B}{\partial x} \tag{7.6}$$

$$j_A = -j_B \tag{7.7}$$

j_A is the reaction rate density of A in moles per unit per surface area [mol s^{-1} m^{-2}], the rate at which the species reacts per surface area. For j_B, the reaction rate density is equivalent to the flux density in a normal direction away from the electrode surface.

Boundary conditions must be established to solve the diffusion equation. Initially, only A exists at the electrode surface in which the concentration is assumed to be uniform within the film, and the solution concentration of all species is uniformly zero across all space.

$$\begin{aligned} t \leq 0,\ x = 0,\ c_A = c_A^s,\ c_B = 0 \\ t \leq 0,\ x > 0,\ c_A = 0,\ c_B = 0 \end{aligned} \tag{7.8}$$

As t increases, A is consumed and B is released into the bulk solution but the concentrations of both species remain 0 at the outer boundary:

$$t > 0,\ x \to \infty,\ c_A = 0,\ c_B = 0 \tag{7.9}$$

7.2.2 Dimensionless Coordinates

Table 7.1 introduces the dimensionless coordinate transformations used in the simulation akin to those reported in the previous chapters [22]. For this model, however, the parameters are normalized with respect to the film thickness, d, rather than the electrode radius, ϵ, and c_A^* is the initial volume concentration of species A on the electrode surface.

Table 7.1: Dimensionless parameters. [22]

Parameter	Normalization
concentration A	$C_A = \frac{c_A^s}{dc_A^*}$ where $c_A^* = \frac{c_A^s}{d}$ at $t = 0$
concentration B	$C_B = \frac{c_B}{c_A^*}$
diffusion coefficient	$d_B = \frac{D_B}{D_B} = 1$
spatial coordinate	$X = \frac{x}{d}$
time	$\tau = \frac{D_B t}{d^2}$
potential	$\theta = \left(\frac{F}{RT}\right)(E - E_f^0)$
scan rate	$\sigma = \left(\frac{d^2}{D_B}\right)\left(\frac{F}{RT}\right)\nu$
current	$J_A = \frac{dI}{\pi\epsilon^2 F D_B c_A^*}$

Given the transformations in Table 7.1, Equations (7.3), (7.4), (7.5), (7.6), and (7.7) can be rewritten in dimensionless coordinates as follow:

$$e^{\theta} = \frac{C_A^0}{C_B^0} \tag{7.10}$$

$$\frac{\partial C_B}{\partial \tau} = \frac{\partial^2 C_B}{\partial X^2} \tag{7.11}$$

$$J_A = \frac{\partial C_A^0}{\partial \tau} \tag{7.12}$$

$$J_B = -\frac{\partial C_B}{\partial X}\bigg|_{X=0} \tag{7.13}$$

$$J_A = -J_B \tag{7.14}$$

where C_A^0 and C_B^0 are the dimensionless volume concentrations of A and B at the electrode surface respectively. An important difference to note between the dimensional and dimensionless expressions is the change in the concentration of A. The former is written in terms of a surface concentration whereas the latter is written in terms of a volume concentration. As a result, the film thickness becomes irrelevant to the simulation model.

7.2.3 Semi-circular Potential Wave

The conventional linear wave and the semi-circular wave established in the previous chapters were applied. The semi-circular potential wave is given as:

$$\theta(\tau) = \pm\sqrt{\left|\theta_{A_0}^2 - \left[\sigma \cdot (\tau - c\tau_{max})\right]^2\right|} + \theta_{shift} \tag{7.15}$$

where $\theta(\tau)$ is the dimensionless potential with respect to dimensionless time, τ, and θ_{A_0} is the dimensionless amplitude of the wave, σ is the dimensionless average scan rate defined as the slope of the linear wave, c is the fraction of the maximum time when the centre of each semi-circle is observed, $\tau_{max} = \frac{2\theta_{A_0}}{\sigma}$, and $\theta_{shift} = \theta_{avg} - \theta_f^0$ in which θ_{avg} is the midpoint of the potential window. θ_f^0 is the dimensionless formal potential of the A/B couple which is zero in accordance with the definition of the dimensionless coordinate transformations. When running experiments, E_{avg} is the key parameter to consider rather than the θ_{shift}, where E_{avg} is the average of the potential window defined as $E_{avg} = \frac{E_{initial}+E_{final}}{2}$. In contrast to the conventional linear waveform where the effect of varied scan rates is of interest, in the semi-circular waveform method, the effect of the set potential window relative to E_f^0 on the current response is of the main interest as explained in later sections.

Figure 7.1 shows the two potential waves used; the blue line represents the linear potential wave and the green line represents the semi-circular potential wave, both centred at $\theta = 0$, i.e. $\theta_{shift} = 0$, and $\theta_{A_0} = 20$. The linear potential wave features a constant scan rate throughout the entire sweep as evident from the figure, whereas the semi-circular potential wave exhibits different temporal scan rates with

an instantaneously infinitely fast scan rate at the mid-point of the potential wave. It is this latter feature which offers the enhanced sensitivity.

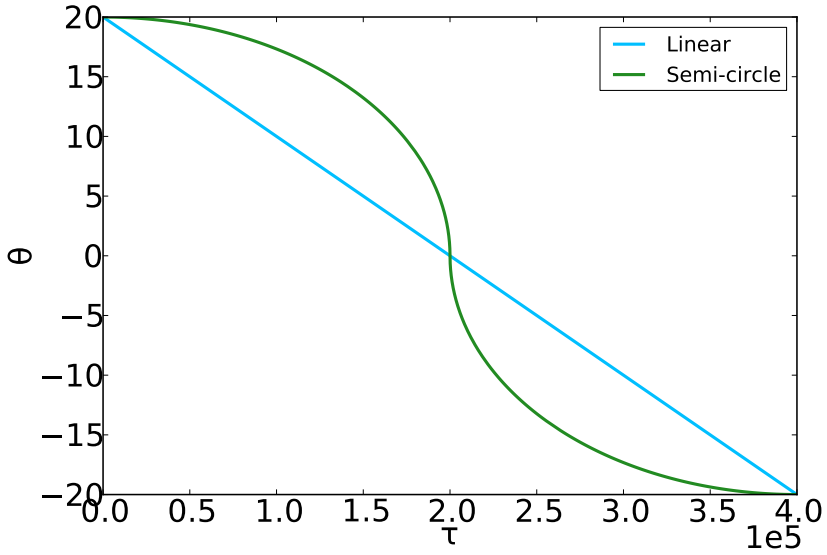


Figure 7.1: A schematic representation of linear and semi-circular potential wave graphs centered at 0 with an amplitude of 20. The blue line corresponds to the linear wave and the green line corresponds to the semi-circular wave. Similar schematic representations are provided in Chapters 5 and 6.

7.2.4 Simulation via Finite Difference

The simulation was performed by solving the discretized dimensionless diffusion equation via the finite difference method in *C++* [22] and plotting was done in *Python* using the packages *NumPy* and *matplotlib*. Numerous tests [25] were conducted by comparing simulated results with theoretical expressions where available and through conservation of mass tests.

7.3 Results and Discussion

The following sections discuss the characteristic features arising from the application of a semi-circular potential wave in CSV and their advantage in detecting analytes at low concentrations. All results are reported for a dimensionless scan rate of $\sigma = 10^{-4}$ unless otherwise specified. $\sigma = 10^{-4}$ corresponds to approximately $\nu = 257$ mV s^{-1}

assuming $D_B = 10^{-9}$ m^2 s^{-1}, $d = 10^{-7}$ m, and $T = 298$ K. Other parameters used in simulation were $\Delta\theta = 10^{-4}$, $\omega = 1.07$, and $h = 10^{-4}$ (definition given in Chapter 2).

7.3.1 Effect of Potential Window Shift

Based on the potential waveform, characteristic voltammograms can be expected from the semi-circular method. The following section investigates how the voltammetric features depend on shifts of the potential window chosen for the semi-circular potential wave.

Figure 7.2 shows four voltammograms recorded at different θ_{shift} values (defined in Section 7.2.3) where Figure 7.2A is for $\theta_{shift} = 0$, Figure 7.2B is for $\theta_{shift} = 5$,

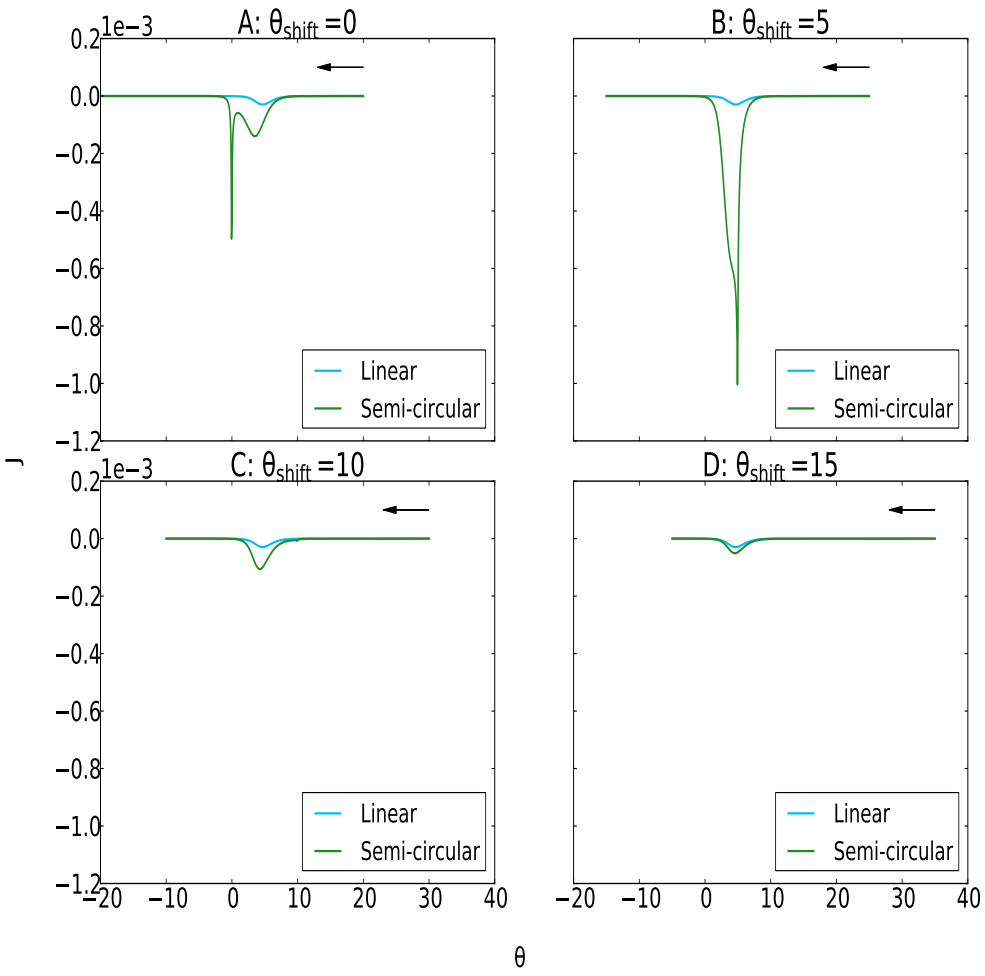


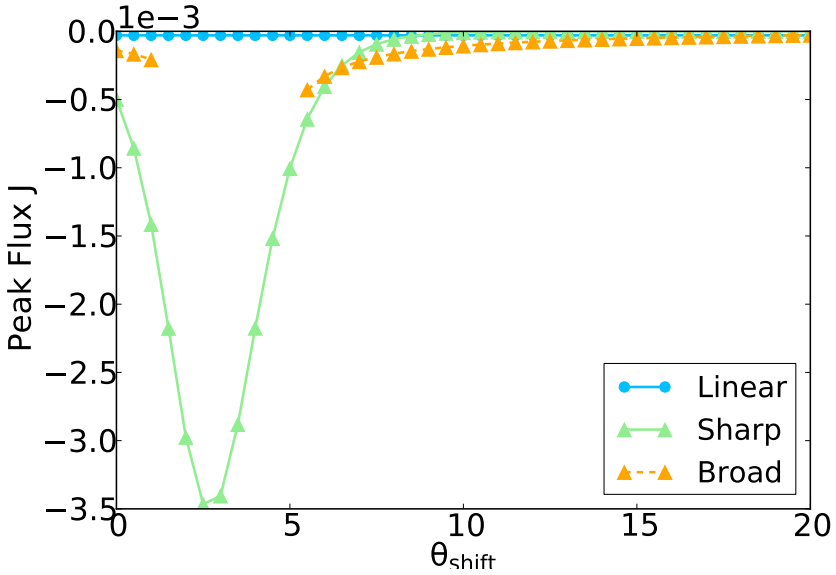
Figure 7.2: Voltammograms plotted for various θ_{shift} values. A corresponds to $\theta_{shift} = 0$, B corresponds to $\theta_{shift} = 5$, C corresponds to $\theta_{shift} = 10$, and D corresponds to $\theta_{shift} = 15$.

Figure 7.2C is for $\theta_{shift} = 10$, and Figure 7.2D is for $\theta_{shift} = 15$. In all figures, the blue line represents the result from the linear wave and the green line represents the result from the semi-circular wave. Figure 7.2A shows a broad peak and a sharp peak. The voltammetric shape when $\theta_{shift} = 0$ is discussed in more detail in Section 7.3.2. At a more positive θ_{shift} of 5, one big peak is seen such as in Figure 7.2B, and then at a more significantly positive θ_{shift}, the sharp peak diminishes and only the broad peak is observable.

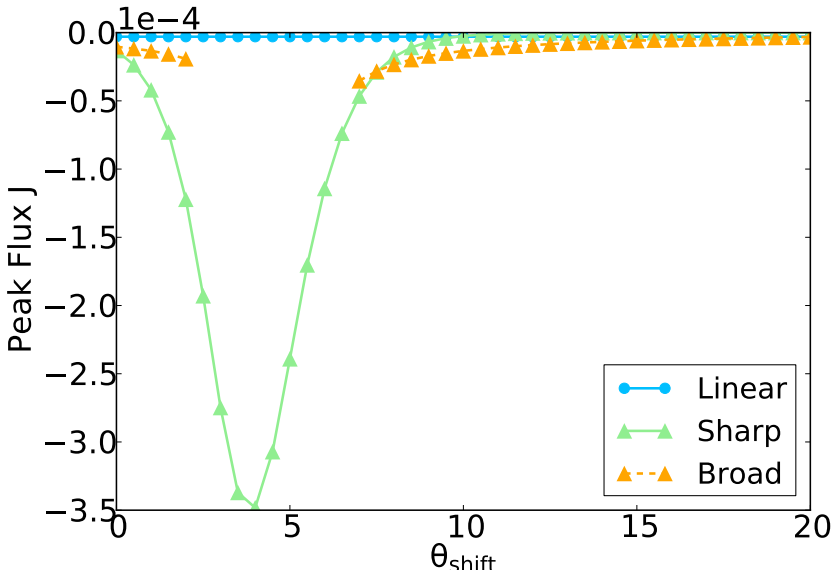
In 7.2B, the two peaks seen in 7.2A merge and the current response is much larger than that obtained from the linear potential wave. This can be understood as, at $\theta = 5$, the potential at which the infinitely fast scan rate occurs coincides with the potential region where the broad peak is otherwise observed. In 7.2C the sharp peak is very small and in 7.2D only one peak is observed, which features a different shape than the peak in 7.2B. Here, the infinitely fast scan rate responsible for the sharp peak occurs at a highly positive potential where very little to no reaction can proceed and thus does not affect the current response much. In addition, the temporal scan rate at the potential region where the reaction takes place is relatively slow and produces a current response similar to that of the linear method.

The effect of the potential window shift is more apparent when the peak flux of each voltammogram is plotted against its corresponding θ_{shift} values as in Figure 7.3(a). The solid blue circular line represents the peak flux obtained from the linear sweep method, the solid light green triangular line represents the peak flux of the sharp peak from the semi-circular waveform method, and the dashed orange triangular line represents the peak flux of the broad peaks. The peak flux from the linear method shows no variance with respect to θ_{shift}, while the sharp peaks show a significant change in value depending on the shift. The broad peaks appear in the lower θ_{shift} and in the higher θ_{shift} regions.

The linear method produces the same peak flux regardless of the potential shift since the wave provides a constant scan rate throughout the sweep. In contrast, the semi-circular method exhibits an absolute maximum peak flux at a specific θ_{shift}, and this value varies depending on the scan rate. The reason the broad peak



(a) Dimensionless peak flux plotted against corresponding θ_{shift} values at $\sigma = 10^{-4}$.



(b) Dimensionless peak flux plotted against corresponding θ_{shift} values at $\sigma = 10^{-5}$.

Figure 7.3: Peak flux values plotted against varying θ_{shift} values at (a) $\sigma = 10^{-4}$ and (b) $\sigma = 10^{-5}$. The solid blue circular line represents the peak flux from the linear method, the solid light green triangular line represents the peak flux of the sharp peak from the semi-circular method, and the dashed orange triangular line represents the peak flux of the broad peak from said method.

currents are not plotted at certain θ_{shift} values is because in this potential range, the two peaks merge and have thus been plotted as a single sharp peak in the Figure.

Figure 7.3(b) also plots the dimensionless peak flux against the corresponding θ_{shift} values but at a different scan rate of $\sigma = 10^{-5}$. While the absolute maximum peak flux is observed at $\theta_{shift} = 2.5$ in Figure 7.3(a), in Figure 7.3(b) it is observed at $\theta_{shift} = 4$ hence illustrating the scan rate dependency of the method.

7.3.2 Features of Semi-circular Potential Wave Voltammetry

As evident from the previous section, the semi-circular method introduces attractive features to the voltammetric response. This section discusses the difference in voltammetric features between the linear and semi-circular potential waves when $\theta_{shift} = 0$. Figure 7.4 shows the dimensionless current responses for linear and semi-circular potential waves at $\theta_{shift} = 0$ where the blue line represents the result from the linear wave and the green line represents the result from the semi-circular wave. The pink horizontal and vertical dashed lines are the theoretically predicted peak current and peak potential values plotted from the dimensionless expression of Equations (7.16) [19, 26–28] and (7.17) [27][1], respectively:

$$I_{peak} = 0.2975nFA_{ele}\sigma' dc_A^* \tag{7.16}$$

$$n(E_p - E_f^0) = -1.43 + 12.85\, ln\left(\frac{d^2\sigma'}{D_B}\right)\ [mV] \tag{7.17}$$

where n is the number of electrons involved in the reaction (here, $n = 1$), A_{ele} is the area of the electrode, and $\sigma' = \frac{nF}{RT}\nu$. The dimensionless expression of Equations (7.16) and (7.17) are given as:

$$J_{peak} = 0.2975\sigma \tag{7.18}$$

and

$$\theta_p = [-1.43 + 12.85ln(\sigma)] \cdot 10^{-3} \cdot \frac{F}{RT} \tag{7.19}$$

[1]It is noted that the respective equation is misprinted in the original publication [27] which has been corrected in Equation (7.17).

It is noted that while the recorded flux of B is a positive value, the plotted dimensionless current is negative as per convention to show a reduction is modelled and thus the theoretically predicted values in Figure 7.4 are plotted by taking the negative of Equations (7.18) and (7.19).

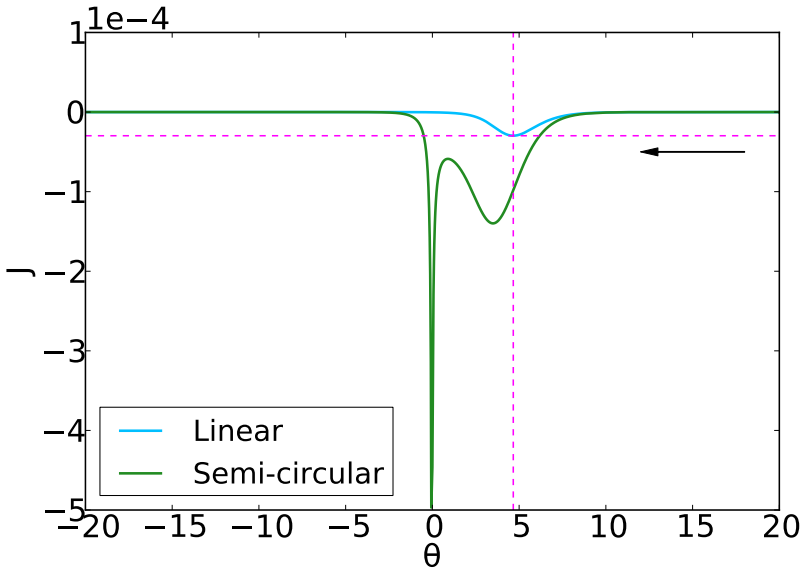


Figure 7.4: Dimensionless current response using linear and semi-circular potential waves at $\theta_{shift} = 0$. The blue line represents the result from the linear wave while the green line represents the result from the semi-circular wave. The pink horizontal and vertical dashed lines are the peak current and peak potential values predicted from Equations (7.18) and (7.19).

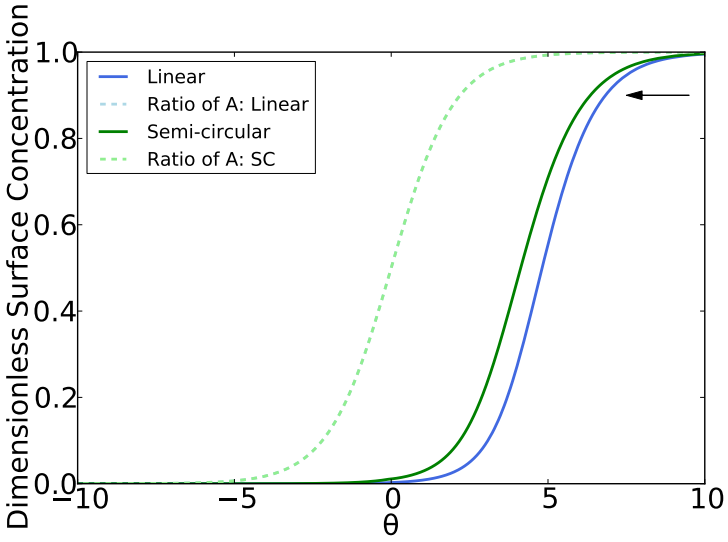
From Figure 7.4, it is clear that the semi-circular potential wave gives a significantly larger current response compared to the linear method, which results in a higher sensitivity. As seen in Figure 7.1, semi-circular potential wave gives rise to different temporal scan rates throughout the sweep with an instantaneously infinitely fast scan rate at the mid-point of the potential window. The larger current response is due to the increase in temporal scan rate in the potential region where the electrochemical reaction occurs. The different temporal scan rates also explain the presence of a double peak. In Figure 7.4, a broad peak is seen near the region where the peak is observed for the linear wave and, in addition, a sharp peak later in the sweep. There are two factors affecting the broad peak: one is the increasing scan rate and the other is the depletion of A. When the reaction starts near $\theta = 10$,

a large amount of A is at the electrode which is consumed at an increasing rate along with an increasing scan rate, resulting in a higher current. In contrast to the linear wave voltammogram where the current falls off past $\theta = 5$ due to depletion of the materials, the current in the semi-circular voltammogram continues to grow because of the effect of the increasing scan rate. Beyond $\theta = 3$, the depletion dominates and the current falls until a sharp peak is observed. At this potential most of A has been consumed but the speed at which the ratio of A to B is altered at the interface as a consequence of the Nernst equation surpasses the speed at which B can diffuse, resulting in a large concentration gradient at the electrode surface, and, following Fick's First Law, in a large flux.

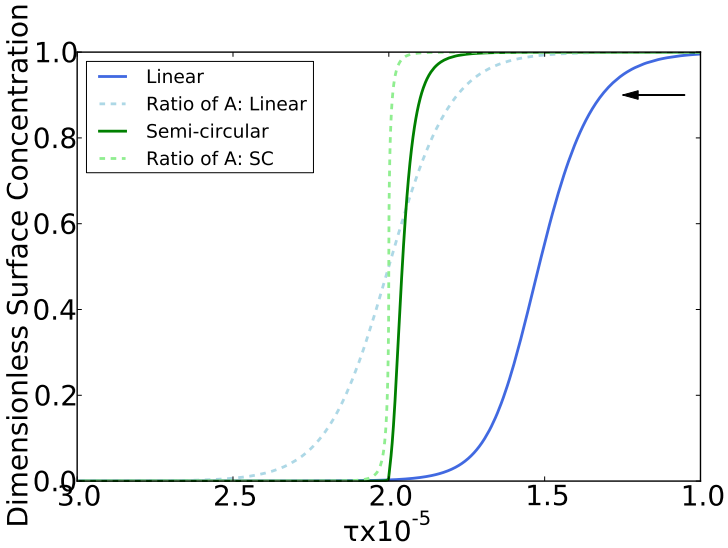
In order to better understand the origins of the two peaks, the change in the surface concentration of A and the solution concentration of B over time was analyzed. Figure 7.5(a) shows the dimensionless surface volume concentrations of A and the ratio of the surface volume concentrations of A given as:

$$Ratio_A = \frac{C_A^0}{C_A^0 + C_B^0} = \frac{1}{e^{-\theta} + 1} \tag{7.20}$$

which are plotted against the dimensionless potential, θ. The ratio is defined in such a way that its values vary between one and zero for simplicity and shows changes in the surface volume concentration of A, C_A^0, relative to the total surface volume concentration of A and B, $C_A^0 + C_B^0$, as the reaction progresses. The blue solid line in Figure 7.5(a) represents the surface volume concentration of A when a linear wave is applied and the green solid line represents the surface volume concentration of A when a semi-circular potential wave is applied. The light blue and light green dashed lines show the ratio of the surface volume concentrations of A to the surface volume concentrations of $A + B$ using the linear and semi-circular waves, respectively. Figure 7.5(b) shows the surface volume concentrations and the surface volume concentration ratios of A plotted against dimensionless time, τ, using the same color scheme as in Figure 7.5(a). It should be noted that for direct comparison of Figure 7.5(a) and 7.5(b), the time axis in 7.5(b) increases to the left.



(a) Surface concentration of A and ratios of A (7.20) plotted against the dimensionless potential, θ.



(b) Surface concentration of A and ratios of A (7.20) plotted against the dimensionless time, τ.

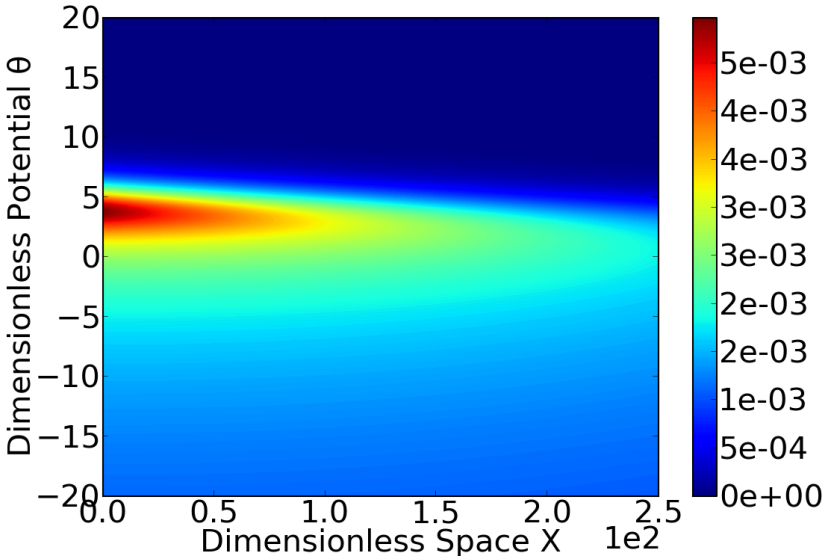
Figure 7.5: (a) shows the change in dimensionless surface volume concentration of A and the ratio of A (7.20) with respect to potential. The blue solid line represents the surface volume concentration of A when a linear wave is applied and the green solid line represents the surface volume concentration of A when a semi-circular potential wave is applied. The light blue and light green dashed lines show the ratio of the surface volume concentration of A to the surface volume concentration of $A+B$ for the linear and semi-circular method, respectively, which perfectly overlap in (a). The arrow represents the direction of the sweep. (b) shows the change in dimensionless surface volume concentration of A and the ratio of A with respect to time. Note that for direct comparability, the time axis points to the left. The same color schemes are employed as in (a).

Figure 7.5(a) shows a shift between the plot of the ratios (dashed line) and the surface volume concentrations (solid line) while the two plots of the concentration ratios for the linear and semi-circular potential overlap perfectly. The shift between the ratios and the surface volume concentration plots can be understood from the diffusion of B. At $\theta = 10$, a small amount of A is already consumed and B is produced, which diffuses away. Meanwhile the ratio (7.20) is defined by the Nernst equation throughout the sweep and must hold true at all times. Therefore, more A is consumed as more B diffuses away from the electrode to satisfy the Nernst equilibrium and changes in the surface volume concentrations are shifted with respect to changes in the ratios. The two ratio plots obtained from the linear and semi-circular potential waves overlap perfectly because, as stated and evident from Equation (7.20), the ratio is determined by the Nernst equilibrium which is only dependent on the potential and thus the potential wave shape does not affect the shape of the concentration ratio curve when plotted against θ.

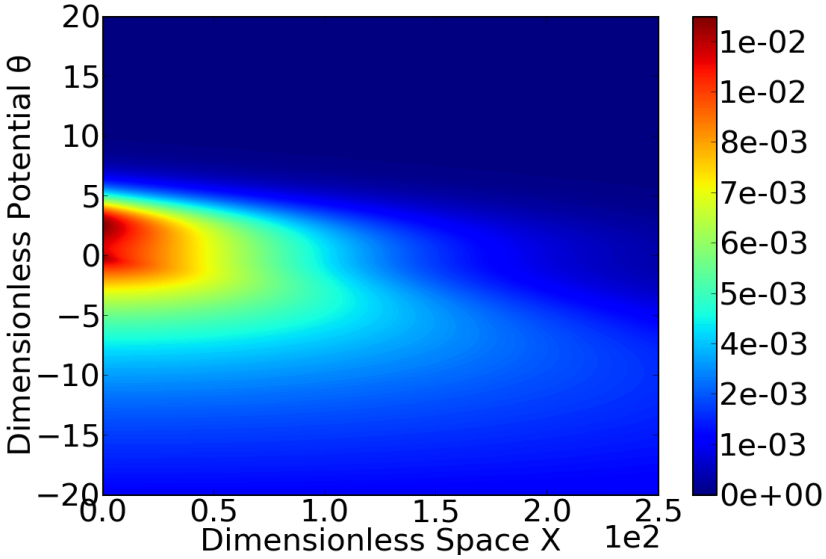
When the concentration ratios are plotted against the dimensionless time, τ, as in Figure 7.5(b), a significant difference is observed in the curve obtained from the two methods. The linear wave results exhibit the same trend as in Figure 7.5(a) whereas the semi-circular wave results show a much steeper curve for both, the surface volume concentration and the ratio. The reaction for a semi-circular potential wave begins at a much later time compared to the linear method and the reaction occurs within a more narrow time frame giving the surface volume concentration a steep slope.

The observations can be explained by the scan rate difference between the two methods. From Figure 7.1, it is clear that the temporal scan rate of the semi-circular method at the potential at which the reaction starts is already much faster than that of the linear method. As the reaction starts with a faster scan rate, there is less time for B to diffuse, causing a build-up of B at the electrode surface. The build-up of B hinders the reaction which must satisfy the Nernst equilibrium and thus less A is converted until B diffuses into the solution. Comparing the linear and the semi-circular wave, this results in a smaller shift of the latter surface volume concentration curve with respect to the corresponding ratio.

Next, the change in solution concentrations of B over time was considered and the solution concentrations of B with respect to dimensionless potential, θ, and dimensionless space, X, were plotted where Figures 7.6(a) and 7.6(b) correspond to linear and semi-circular results, respectively.



(a) Solution concentration of B with linear potential wave.



(b) Solution concentration of B with semi-circular potential wave.

Figure 7.6: The two figures show the solution concentrations when (a) a linear potential wave is applied, and (b) a semi-circular potential wave is applied. The colorbar on the right hand side of the figure represents the dimensionless concentration.

The linear method shows one peak extending far into the spatial grid whereas

the semi-circular method shows two peaks closer towards the electrode surface. The recorded maximum concentration values differ between the two methods giving the semi-circular method a higher concentration value. The peak in Figure 7.6(a) corresponds to the peak flux of the linear potential wave result observed in Figure 7.4. Figure 7.6(b) displays two occasions where a build up of concentration occurs: one corresponding to the broad current peak and the other to the sharp current peak. The higher concentration value of B in the semi-circular plot is due to the fact that in the said method, the reaction progresses within a very narrow time frame causing a rapid build-up of B at the interface.

To summarize, the double peaks of the semi-circular method in Figure 7.4 arise from the interplay between different temporal scan rates and the mass transport of B throughout the sweep. The broad peak is due to the increasing scan rate of the potential wave, which consumes A at an increasing rate giving a higher current response compared to the linear method. Between $\theta = 3$ and $\theta = 1$, the current drops since the low surface concentration of A dominates the effect of increasing scan rate. At $\theta = 0$, the scan rate approaches infinity (a jump in the potential value) and thus despite the low concentration of A at the interface, the Nernst equilibrium pushes the reaction to proceed forward very quickly. As a result, a large gradient is produced at the electrode surface and gives the sharp peak.

7.3.3 Experimental Applications

This section discusses the experimental application of the above method. The biggest advantage of the semi-circular potential wave is its ability to significantly amplify the current as evident from Figure 7.4. By integrating the voltammogram obtained, one can very easily determine the initial surface concentration of A via:

$$c_A^s = \frac{\int_0^{t_{max}} I(t)dt}{FA_{ele}} \tag{7.21}$$

where t_{max} is the final time, F is the Faraday constant, and A_{ele} is the area of the electrode.

Figure 7.2 has further shown that each potential shift produces a characteristic voltammogram that is specific to the formal potential of the analyte. This feature can be exploited when conducting an experimental analysis; Following a careful calibration of an experimental set-up for a specific species, characteristic changes in the shape of the voltammogram can be used to identify interferences with other analytes in a sensing context and may enable the determination of the identity of the species detected. To this end, a sequence of experiments is conducted using solutions that contain known concentrations of known species. The peak currents and voltammetric shapes are determined and then used as a reference in the analysis of unknown solutions.

7.4 Conclusions

This chapter explored a novel method to run CSV using a semi-circular potential wave, which gives a much more sensitive current response compared to the conventional linear wave and hence could be used to detect materials at a lower concentration. The increased peak current makes the analysis of the initial surface concentration easier while the more characteristic voltammetric curves obtained allows the identification of the species under investigation via its formal potential.

References

[1] Y. Uchida, E. Kätelhön, R. G. Compton, *Journal of Electroanalytical Chemistry* **2019**, *848*, 113290.

[2] J. Barón-Jaimez, M. R. Joya, J. Barba-Ortega, *Journal of Physics: Conference Series* **2013**, *466*, 012023.

[3] T. A. O'Shea, K. H. Mancy, *Analytical Chemistry* **1976**, *48*, 1603–1607.

[4] R. G. Compton, C. E. Banks, *Understanding Voltammetry*, Imperial College Press, **2010**.

[5] K. Wikiel, Z. Kublik, *Journal of Electroanalytical Chemistry and Interfacial Electrochemistry* **1984**, *165*, 71–85.

[6] E. P. Achterberg, C. Braungardt, *Analytica Chimica Acta* **1999**, *400*, 381–397.

[7] C. M. G. van den Berg, *Journal of Electroanalytical Chemistry and Interfacial Electrochemistry* **1986**, *215*, 111–121.

[8] C. Colombo, C. M. G. van den Berg, *Analytica Chimica Acta* **1997**, *337*, 29–40.

[9] J. Davis, D. H. Vaughan, D. Stirling, L. Nei, R. G. Compton, *Talanta* **2002**, *57*, 1045–1051.

[10] T. R. Copeland, R. K. Skogerboe, *Analytical Chemistry* **1974**, *46*, 1257A–1268a.

[11] C. Agra-Gutiérrez, J. C. Ball, R. G. Compton, *The Journal of Physical Chemistry B* **1998**, *102*, 7028–7032.

[12] W. Yue, A. Bange, B. L. Riehl, B. D. Riehl, J. M. Johnson, I. Papautsky, W. R. Heineman, *Electroanalysis* **2012**, *24*, 1909–1914.

[13] M. G. Paneli, A. Voulgaropoulos, *Electroanalysis* **1993**, *5*, 355–373.

[14] W. T. D. Vries, E. V. Dalen, *Journal of Electroanalytical Chemistry (1959)* **1964**, *8*, 366–377.

[15] J. Schiewe, K. B. Oldham, J. C. Myland, A. M. Bond, V. A. Vicente-Beckett, S. Fletcher, *Analytical Chemistry* **1997**, *69*, 2673–2681.

[16] J. Buffle, *Journal of Electroanalytical Chemistry and Interfacial Electrochemistry* **1981**, *125*, 273–294.

[17] S. M. Roda, R. D. Greenland, R. L. Bornschein, P. B. Hammond, *Clinical Chemistry* **1988**, *34*, 563–7.

[18] P. L. Brezonik, P. A. Brauner, W. Stumm, *Water Research* **1976**, *10*, 605–612.

[19] Z. Stojek, Z. Kublik, *Journal of Electroanalytical Chemistry and Interfacial Electrochemistry* **1979**, *105*, 247–259.

[20] C. Kokkinos, I. Raptis, A. Economou, T. Speliotis, *Procedia Chemistry* **2009**, *1*, 1039–1042.

[21] T. Florence, *Journal of Electroanalytical Chemistry and Interfacial Electrochemistry* **1979**, *97*, 219–236.

[22] R. G. Compton, E. Laborda, K. R. Ward, *Understanding Voltammetry: Simulation of Electrode Processes*, Imperial College Press, **2013**.

[23] G. A. Mabbott, *Journal of Chemical Education* **1983**, *60*, 697.

[24] J. Crank, *The Mathematics of Diffusion*, Oxford University Press, **1979**.

[25] E. Kätelhön, R. G. Compton, *Analyst* **2015**, *140*, 2592–2598.

[26] W. D. Vries, E. van Dalen, *Journal of Electroanalytical Chemistry and Interfacial Electrochemistry* **1967**, *14*, 315–327.

[27] C. M. A. Brett, A. M. C. F. O. Brett, *Journal of Electroanalytical Chemistry and Interfacial Electrochemistry* **1989**, *262*, 83–95.

[28] J. C. Ball, R. G. Compton, *Electroanalysis* **1997**, *9*, 765–769.

8
Conclusions

This thesis set out to introduce and study new methods to run voltammetry using a non-linear potential waveform for electroanalysis. The waveforms explored were cosine-based and semi-circular, each of which were shown to possess advantages over the conventional linear potential sweep method.

When running cyclic voltammetry, the linear potential wave necessarily introduces capacitive perturbations in the current response due to the discontinuity at the point of reversal. The cosine-based potential waveform greatly reduces this capacitive effect on the recorded current, especially at the said point given the continuous nature of the wave. In addition, the cosine-square potential wave gives rise to a double peak in the voltammogram, which can be used to sensitively determine the formal potential of an electrochemically reversible redox couple under investigation at a macrodisc electrode with ease using the peak-to-peak separation. The peak-to-peak separation value varies in intensity with respect to the difference between E_{avg} and the formal potential, E_f^0, and shows a sharp increase at and near $E_{avg} - E_f^0 = 0$ where E_{avg} is the midpoint of the potential window. This can be exploited to determine the formal potential. It was validated experimentally that the cosine-based potential wave indeed reduces the capacitive effect and that the peak-to-peak separation of a cosine-square potential wave voltammetry can be used as a tool to determine the formal potential.

Similarly, the semi-circular potential wave also provides an alternative approach to determining the formal potential of an electrochemically reversible redox couple through potential-sweep voltammetry based on the peak current with respect to the potential window shift. The semi-circular potential wave voltammogram produces, at least in principle, an infinite peak current at and in the vicinity of E_f^0, and thus running multiple LSV's at a macrodisc electrode with various potential windows and recording the peak current with respect to E_{avg} provides a way to estimate the formal potential which corresponds to the E_{avg} at which the minimum current is seen. Note that this is not infinite in practice because of instrumental limitations. Further, the semi-circular potential wave enhances the current response in the region where the temporal scan rate is fast and suppresses the current response in all other regions, making it suitable for electroanalysis for solutions containing more than one species. It was shown that the semi-circular potential wave voltammetry can detect the presence of multiple species and give an estimate of their formal potentials in situations where the conventional linear sweep method cannot. The experimental analysis showed that the analysis of the plot of the peak current against E_{avg} can successfully and sensitively estimate the formal potential of the redox couple under study.

The analysis of semi-circular potential wave voltammetry at a microdisc electrode showed similar trends as observed at a macrodisc electrode. The transiently infinitely fast scan rate at the midpoint of the potential window enhances the current response whereas the slow scan rates in all other areas suppress the current response. The fact that similar analysis can be conducted at a microdisc electrode greatly increases the applicability of the method since microelectrodes have become a standard in electroanalysis.

Semi-circular potential wave voltammetry at a microdisc electrode presents a new opportunity for kinetic studies using the unique current response. The shape of the voltammogram is sensitive to the standard electrochemical rate constant, and can hence be used to determine the k_0 value of a redox system under study. The increased sensitivity allows one order greater magnitude detection limit of k_0

compared to the conventional linear potential wave method, and can thus both complement and extend the existing analysis.

Stripping voltammetry is often used for trace analysis due to its sensitivity. Semi-circular potential wave voltammetry was shown to provide further sensitivity through its very large peak current and distinct voltammetric curves with respect to the formal potential. The increased current response allows for an easy analysis of the initial surface concentration of the reactant and the characteristic voltammograms can be used for the identification of the species under investigation through its formal potential.

This thesis has shown that the application of a cosine-based and semi-circular potential wave provides new and exciting opportunities for electroanalysis. The cosine-based potential waves exhibits a continuous curve thereby reducing the capacitive effect on the voltammetric curve and also provides new methods to determine the formal potential of a redox couple. The semi-circular potential wave effectively suppresses and enhances the current response to selectively detect and identify individual species in a mixture. Further, the semi-circular voltammogram can be used for the determination of standard electrochemical rate constants due to its sensitivity to k_0, and also increases the sensitivity in stripping voltammetry.

Appendices

A Appendix

A.1 Butler-Volmer Derivation

Given the following one-electron transfer process:

$$A + e^{-} \rightleftharpoons B \tag{A.1}$$

the flux is related to the current through the expression:

$$I = -FA_{ele}j_{net} \tag{A.2}$$

where

$$j_{net} = k_{red}[A]_0 - k_{ox}[B]_0 \tag{A.3}$$

The Arrhenius equation relates the rate constants to the Gibbs energy of activation via:

$$k_{red} = A_{red}exp\left(-\frac{\Delta G^{\ddagger}_{red}}{RT}\right) \tag{A.4}$$

$$k_{ox} = A_{ox}exp\left(-\frac{\Delta G^{\ddagger}_{ox}}{RT}\right) \tag{A.5}$$

where A_{red} and A_{ox} are the pre-exponential factors, and $G^{\ddagger}_{red}$ and $G^{\ddagger}_{ox}$ are the standard Gibbs energy of activation ([J mol^{-1}]). Figure A.1 shows a schematic representation of the Gibbs' energy-reaction coordinate diagram in which the blue curve represents the reactant energy when the electrode potential is E^0_f where $G^{\ddagger}_{0,red}$ and $G^{\ddagger}_{0,ox}$ are the activation energies. The red curve shows how the energy changes with respect to the applied potential, E.

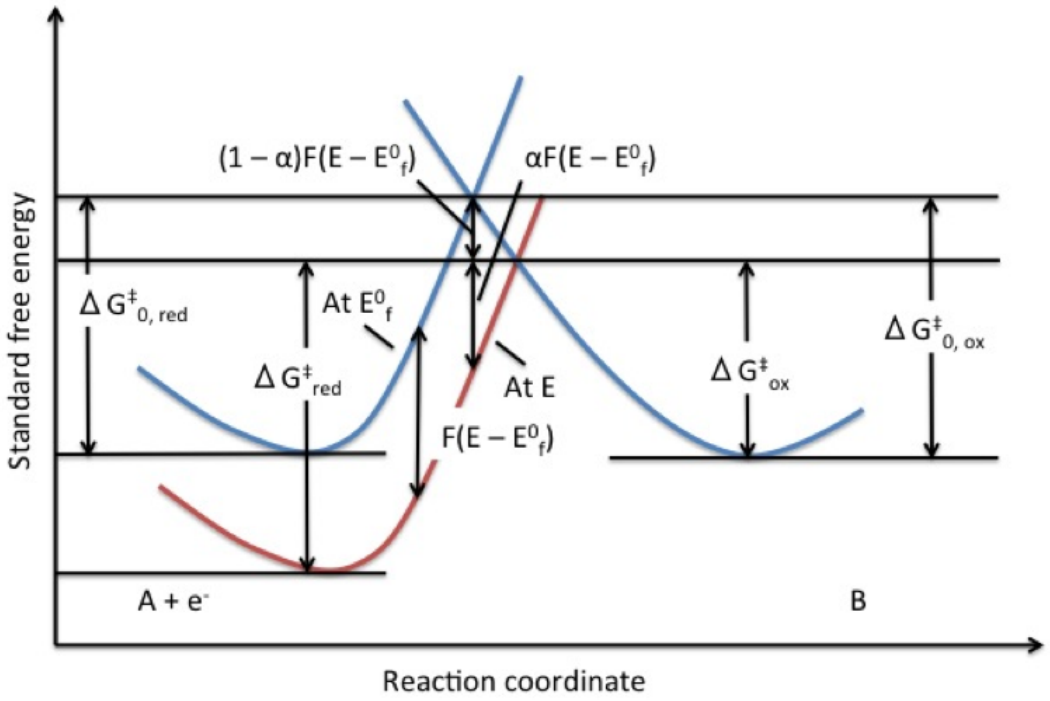


Figure A.1: Schematic representation of the effect of potential change on the standard Gibbs' energy of activation for a one-electron transfer process.

The change in Gibbs energy, ΔG, can be expressed relative to the potential through the expression $\Delta G = -nF\Delta E = -nF(E - E^0_f)$ where n is the number of electrons involved in the reaction (in this case, $n = 1$). When $E > E^0_f$, the energy barrier for oxidation, $\Delta G^{\ddagger}_{ox}$ becomes less than $\Delta G^{\ddagger}_{0,ox}$ by a fraction of the total energy change. The fraction is expressed in terms of α, the transfer coefficient, which can range between $0 < \alpha < 1$. The Gibbs energy of the reactant and product can thus be expressed as a function of α and E:

$$\Delta G^{\ddagger}_{red} = \Delta G^{\ddagger}_{0,red} + \alpha F(E - E^0_f) \tag{A.6}$$

$$\Delta G^{\ddagger}_{ox} = \Delta G^{\ddagger}_{0,ox} - (1-\alpha) F(E - E^0_f) \tag{A.7}$$

Substituting Equations (A.6) and (A.7) in Equations (A.4) and (A.5) yield:

$$k_{red} = A_{red} exp\left(\frac{-\Delta G^{\ddagger}_{0,red}}{RT}\right) exp\left[\frac{-\alpha F(E - E^0_f)}{RT}\right] \tag{A.8}$$

$$k_{ox} = A_{ox} exp\left(\frac{-\Delta G^{\ddagger}_{0,ox}}{RT}\right) exp\left[\frac{(1-\alpha) F(E - E^0_f)}{RT}\right] \tag{A.9}$$

Using the relations $k_{0,red} = A_{red} exp\left(\frac{-\Delta G^{\ddagger}_{0,red}}{RT}\right)$ and $k_{0,ox} = A_{ox} exp\left(\frac{-\Delta G^{\ddagger}_{0,ox}}{RT}\right)$, Equations (A.8) and (A.9) can be expressed as:

$$k_{red} = k_{0,red} exp\left[\frac{-\alpha F(E - E^0_f)}{RT}\right] \tag{A.10}$$

$$k_{ox} = k_{0,ox} exp\left[\frac{(1-\alpha) F(E - E^0_f)}{RT}\right] \tag{A.11}$$

and Equation (A.3) becomes:

$$j_{net} = k_{0,red} exp\left[\frac{-\alpha F(E - E^0_f)}{RT}\right][A]_0 - k_{0,ox} exp\left[\frac{(1-\alpha) F(E - E^0_f)}{RT}\right][B]_0 \tag{A.12}$$

When the system is at equilibrium, $[A]_0 = [B]_0$, $E = E^0_f$, and $j_{net} = 0$ to give:

$$E = E^0_f + \frac{RT}{F} ln\left(\frac{[A]}{[B]}\right) - ln\left(\frac{k_{0,ox}}{k_{0,red}}\right) \tag{A.13}$$

and thus $k_{0,red} = k_{0,ox} = k_0$ to produce the Nernst equation. Based on Equations (A.8) to (A.13), the rate constants k_{red} and k_{ox} can be written in terms of the standard electrochemical rate constant, k_0:

$$k_{red} = k_0 exp\left[\frac{-\alpha F(E - E^0_f)}{RT}\right] \tag{A.14}$$

$$k_{ox} = k_0 exp\left[\frac{(1-\alpha) F(E - E^0_f)}{RT}\right] \tag{A.15}$$

which gives the Butler-Volmer expression:

$$j_{net} = k_0 exp\left[\frac{-\alpha F}{RT}(E - E_f^0)\right][A]_0 - k_0 exp\left[\frac{\beta F}{RT}(E - E_f^0)\right][B]_0 \qquad \text{(A.16)}$$

A.2 Chapter 3 Additional Figures

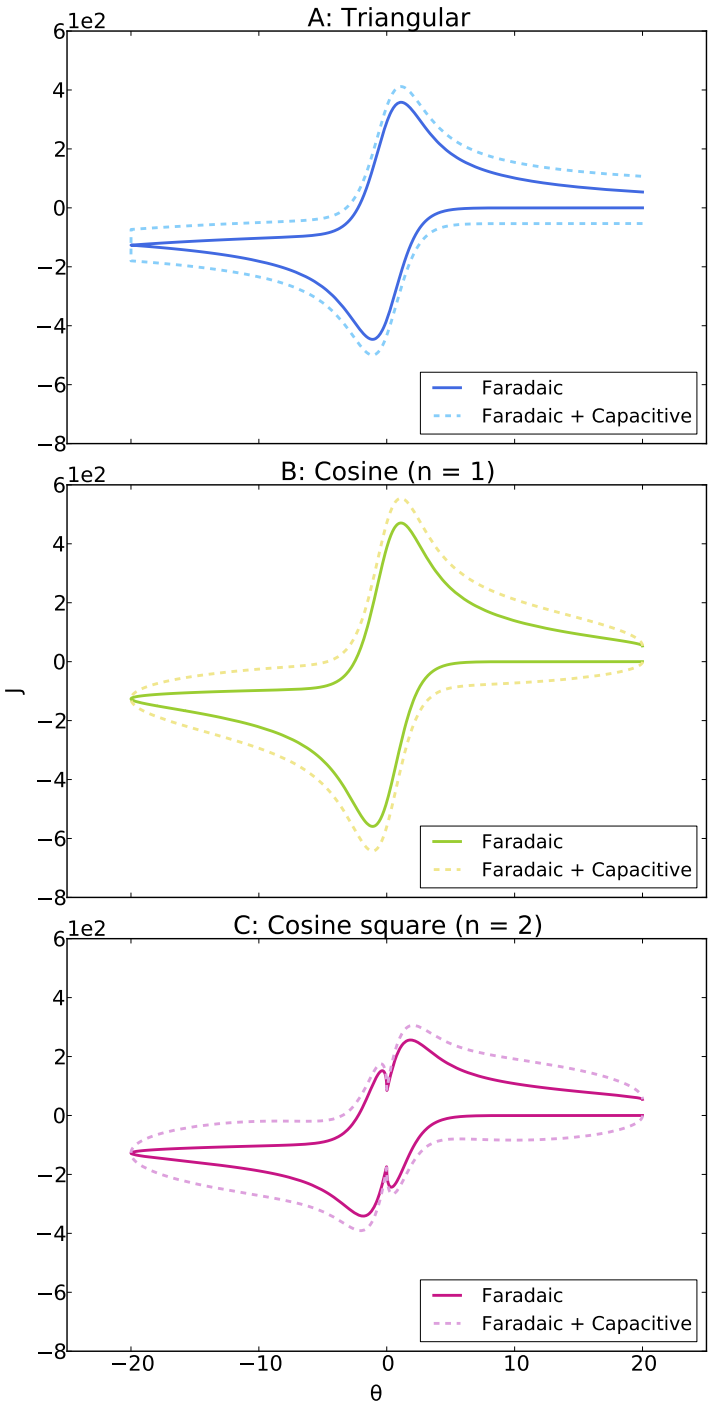
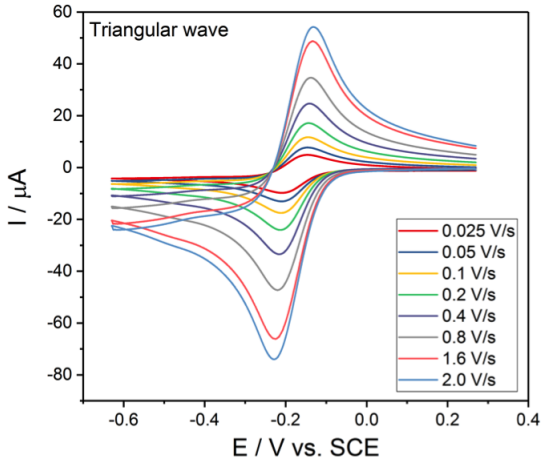
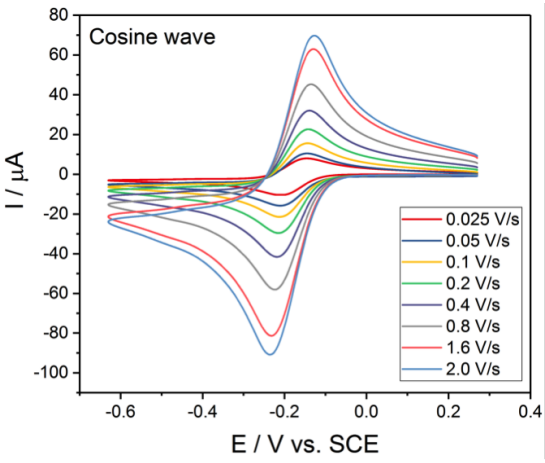


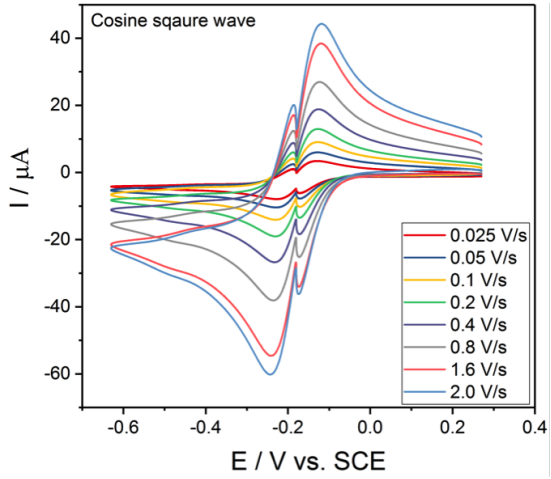
Figure A.2: A comparison between voltammograms with and without capacitive perturbations at $\sigma = 10^6$ and $\theta_{shift} = 0$ for $C_{dl} = 20$ µF cm^{-2}. Each figure is labeled with the corresponding potential wave: A is for triangular, B is for cosine when $n = 1$, and C is when $n = 2$. The solid curves represent the dimensionless Faradaic current and the dashed curves represent the total current (Faradaic + capacitive).



(a) Triangular voltammogram.

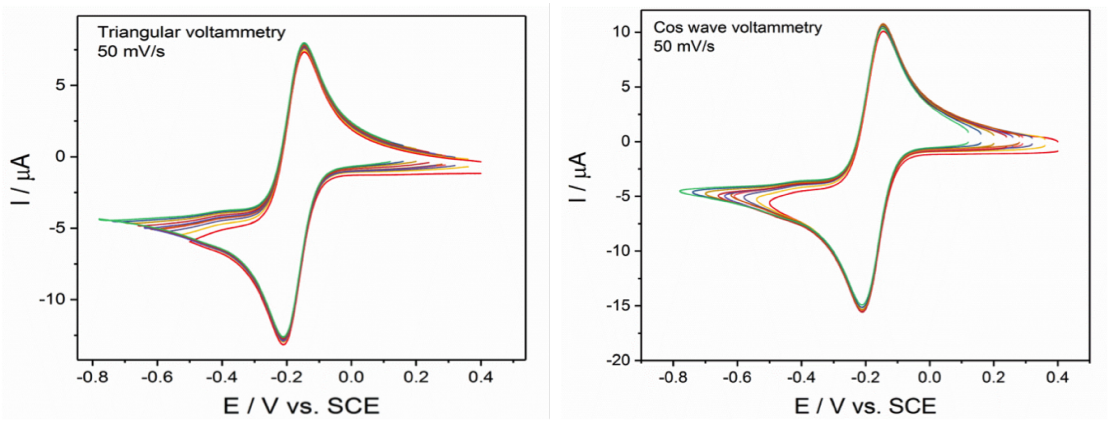


(b) Cosine voltammogram.

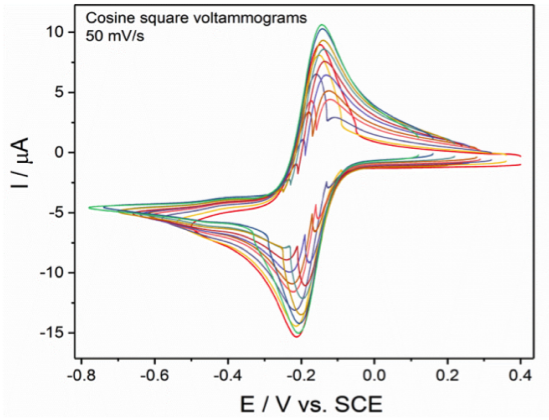


(c) Cosine square voltammogram.

Figure A.3: Capacitive current-corrected voltammograms obtained at GC electrode using (a) triangular, (b) cosine, (c) cosine square potential waves at scan rates from 0.025 to 2 V s^{-1} in 0.96 mM $[Ru(NH_3)_6]Cl_3$/0.10 M KCl solution at 298 K.



(a) Triangular voltammogram. **(b)** Cosine voltammogram.



(c) Cosine square voltammogram

Figure A.4: Capacitive current-corrected voltammograms obtained at GC electrode with (a) triangular, (b) cosine, and (c) cosine square potential waves at different E_{centre} values in 0.96 mM $[Ru(NH_3)_6]Cl_3$/0.10 M KCl solution at an average scan rate of 0.05 V s^{-1} at 298 K.

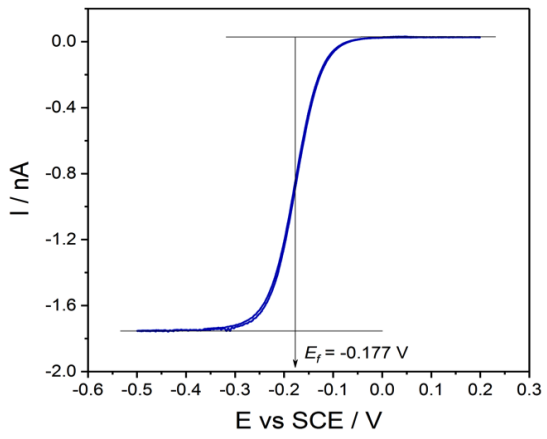


Figure A.5: Steady-state voltammogram of an apoxy-coated carbon fibre (9 µm diameter, GoodFellow, U.K.) microelectrode in 1 mM $[Ru(NH_3)_6]Cl_3$/0.10 M KCl solution.

A.3 Chapter 4 Additional Figures

This section explains the reason the semi-circular voltammogram does not converge with respect to $\Delta\theta$ at infinite scan rate, and also provides a full-scale figure of the voltammograms provided in the main text in Chapter 4.

A.3.1 $\Delta\theta$ Convergence

$\Delta\theta$ is the discretized dimensionless potential which indicates how much the potential changes between each time step when a linear potential wave is employed. Time is also discretized and $\Delta\theta$ is used to calculate the difference between each time step, defined in the main text as $\Delta\tau = \frac{\tau_{max}}{m}$, but can also be defined as $\Delta\tau = \frac{\Delta\theta}{\sigma}$. The discritized semi-circular potential wave equation is:

$$\theta(\tau_k) = \pm\sqrt{\left|\theta_{A_0}^2 - \left[\sigma \cdot (k \cdot \Delta\tau - c\tau_{max})\right]^2\right|} + \theta_{shift} \tag{A.17}$$

Equation (A.17) shows that the potential is dependent on $\Delta\tau$ which is dependent on $\Delta\theta$, and consequently any changes in $\Delta\theta$ will directly be reflected in the sequence of simulated discrete potential values. A smaller $\Delta\tau$ means the difference in potential between corresponding time steps for the semi-circular method is smaller and will provide a more refined current response, which will be reflected in the peak flux value as shown in Figure A.6.

Figure A.6 shows the peak flux plotted against the corresponding $\Delta\theta$ values used when $\theta_{shift} = 0$ where the blue dots represent results obtained from the linear potential wave and the orange diamonds represent results obtained from the semi-circular potential wave. The other two parameters, h and ω were set to the same value as reported in the main text. With decreasing $\Delta\theta$, the absolute peak flux value obtained from the semi-circular potential wave increases indicating the system does not converge with respect to $\Delta\theta$ at infinite scan rate.

The reason for this can be understood by considering the rate of change in concentration, $\frac{\partial C}{\partial \tau}$. As mentioned earlier, decreasing $\Delta\theta$ decreases $\Delta\tau$. At the point of infinite scan rate, the potential jumps from one value to another causing

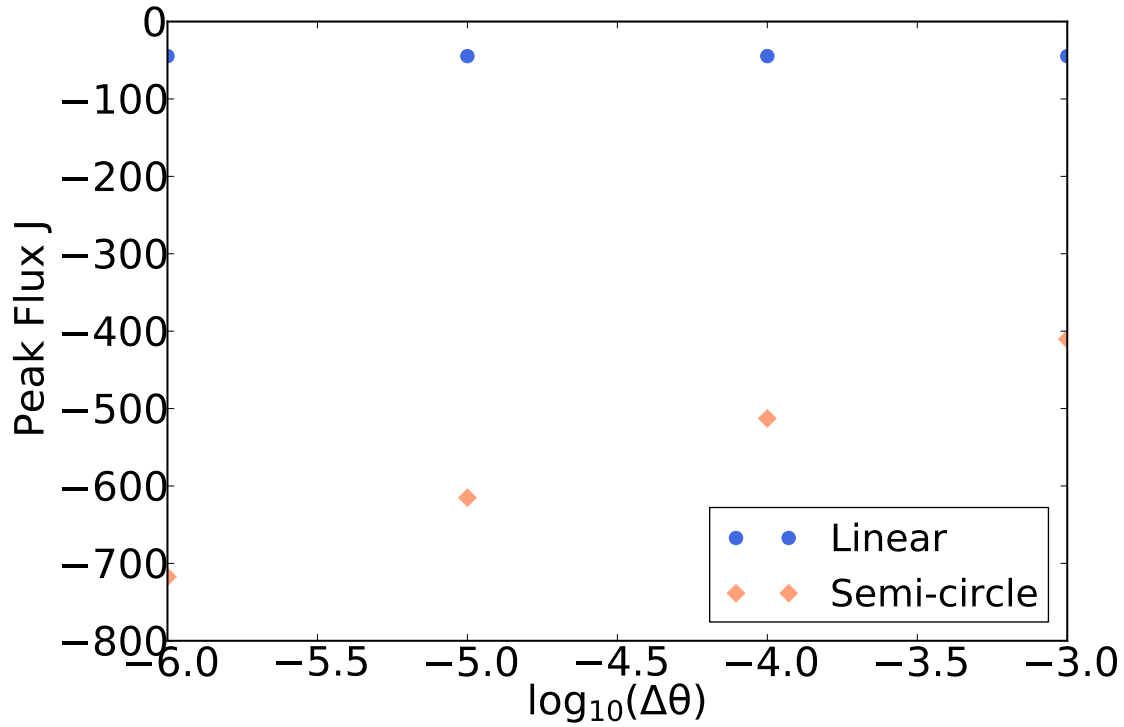
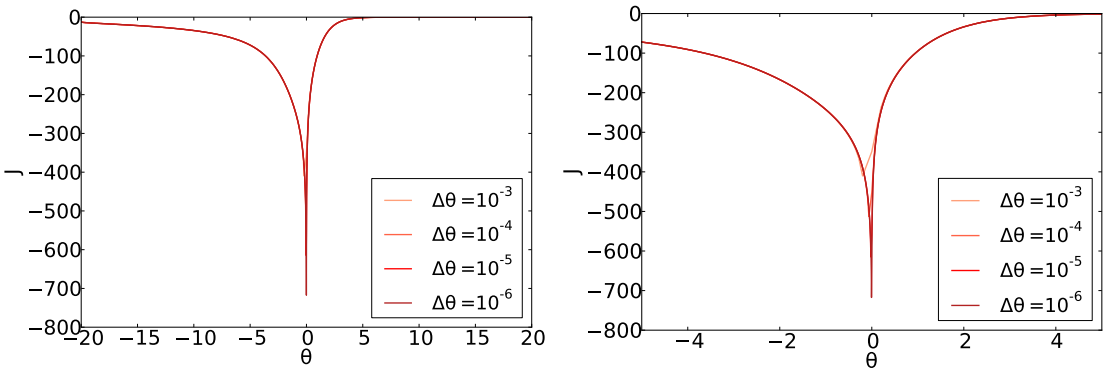


Figure A.6: Peak flux of linear and semi-circular results plotted against $\log_{10}$ of the corresponding $\Delta\theta$ values at $\sigma = 10^4$. The blue dots represent results obtained using the linear potential wave and the orange diamonds represent results obtained using the semi-circular potential wave.

an instantaneous change in the surface concentration as dictated by the Nernst equation and smaller the $\Delta\theta$, the faster the rate. Consequently, the materials have less time to diffuse from the electrode surface thereby resulting in a larger gradient at the electrode surface which leads to the singularity in the peak flux. Figures A.7(a) and A.7(b) show the semi-circular voltammograms obtained using the same $\Delta\theta$ values as in Figure A.6. It is clear that the flux approaches infinity at the midpoint of the potential where the scan rate approaches infinity, and the value increases with decreasing $\Delta\theta$. It can also be seen that even though the dimensionless current at the infinite scan rate and in its near vicinity do not converge, the results converge everywhere else since in those regions the rate of change in concentration is relatively slow enough that the materials are able to diffuse.



(a) Semi-circular voltammograms with varying $\Delta\theta$ values.

(b) Zoomed-up semi-circular voltammograms with vaying $\Delta\theta$ values.

Figure A.7: Figure (a) shows the voltammograms obtained using the semi-circular potential waves with vayring $\Delta\theta$ values and (b) shows the zoomed-up version of (a) to give a closer look near the singularity.

A.3.2 Full-Scale Voltammograms

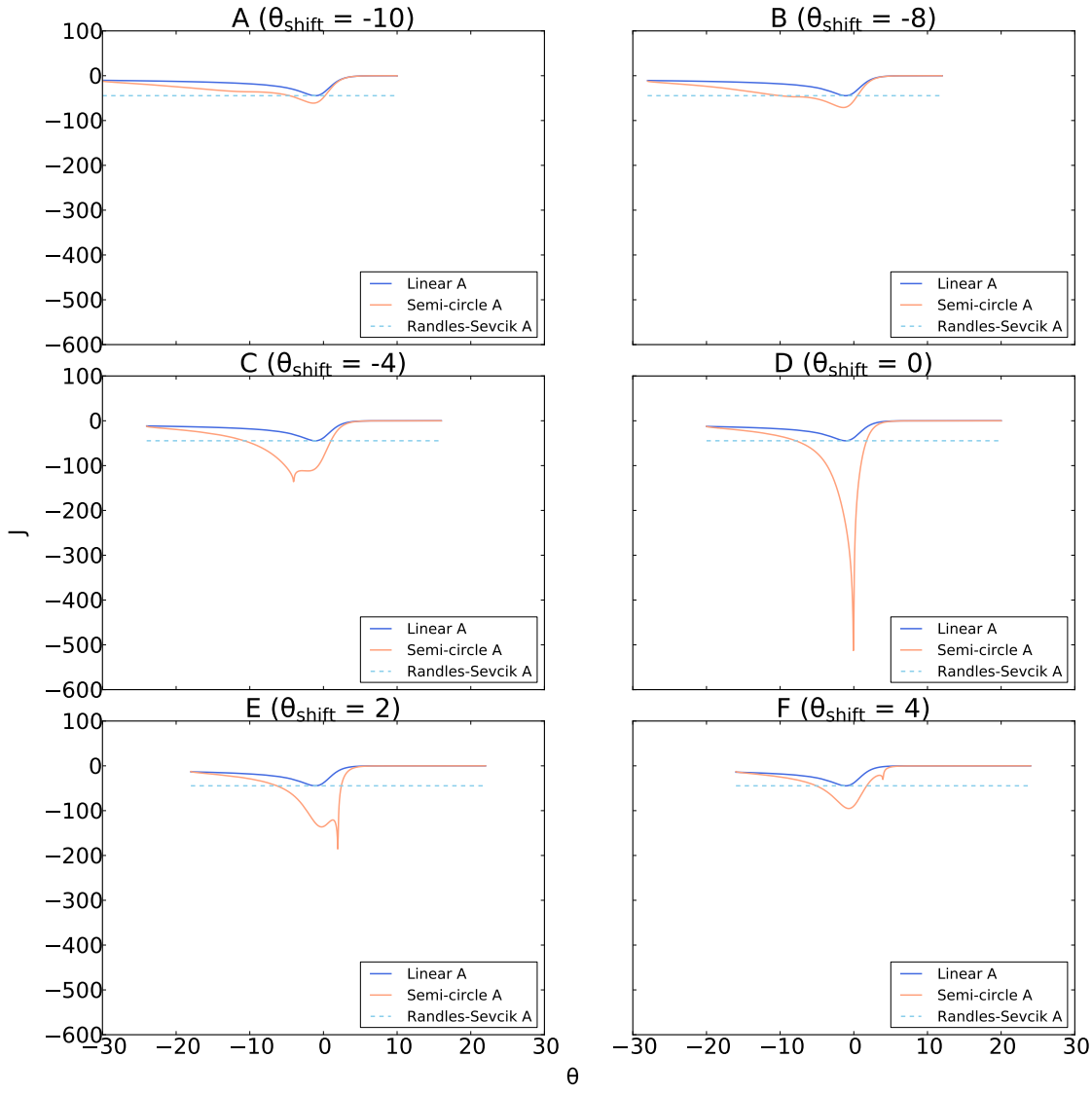


Figure A.8: Full-scale figure of the voltammograms shown in Figure 4.2.

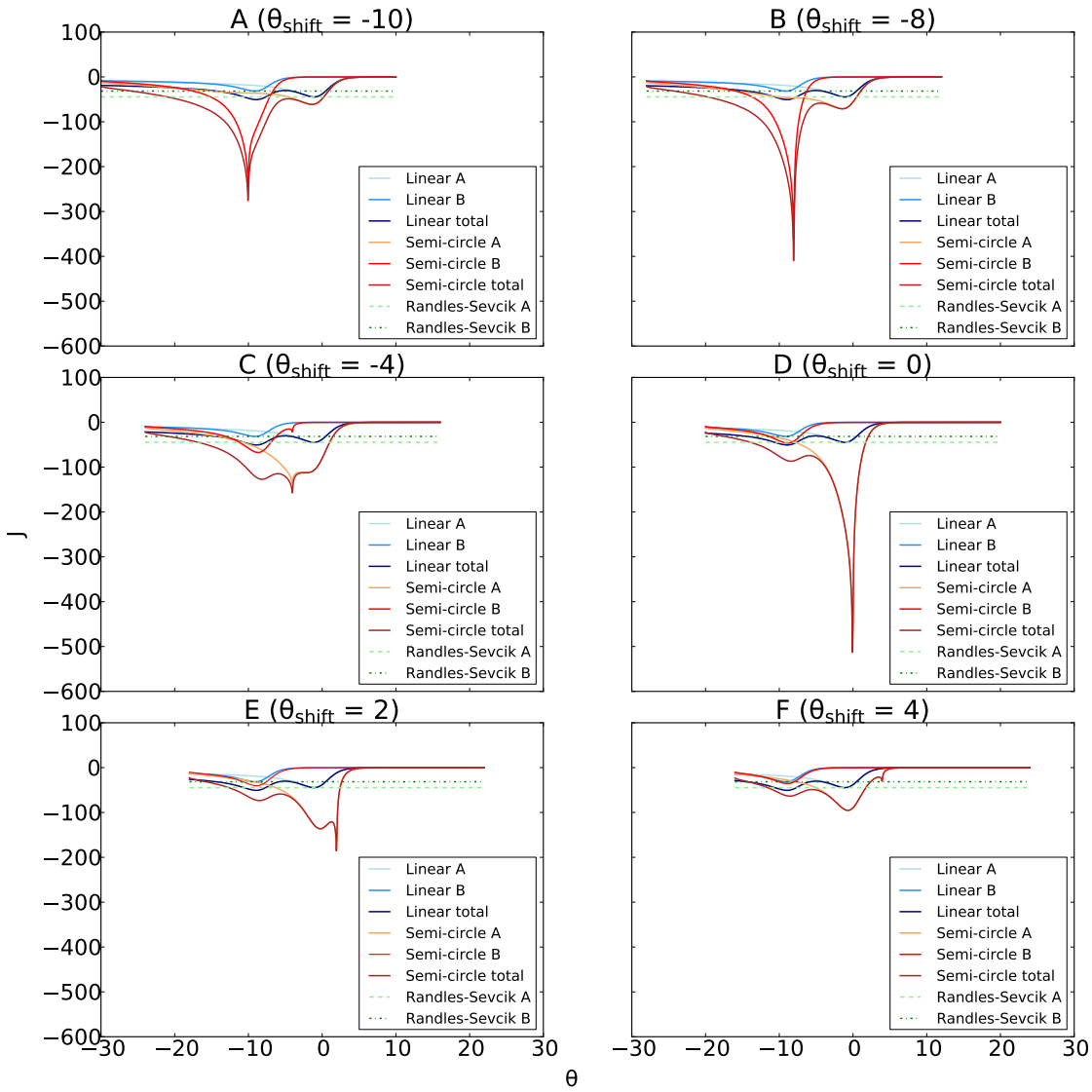


Figure A.9: Full-scale figure of the voltammograms shown in Figure 4.3.

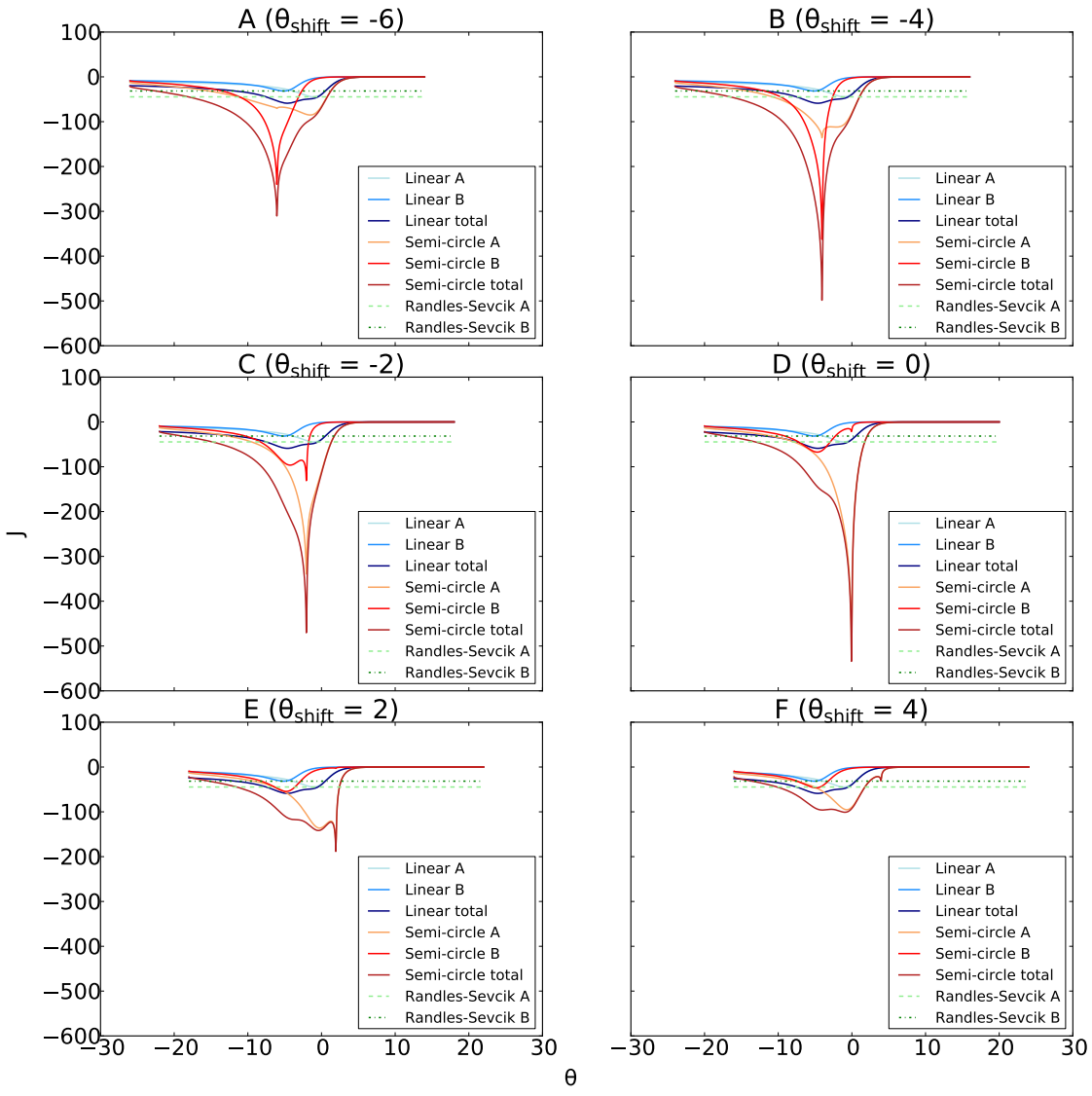


Figure A.10: Full-scale figure of the voltammograms shown in Figure 4.5.

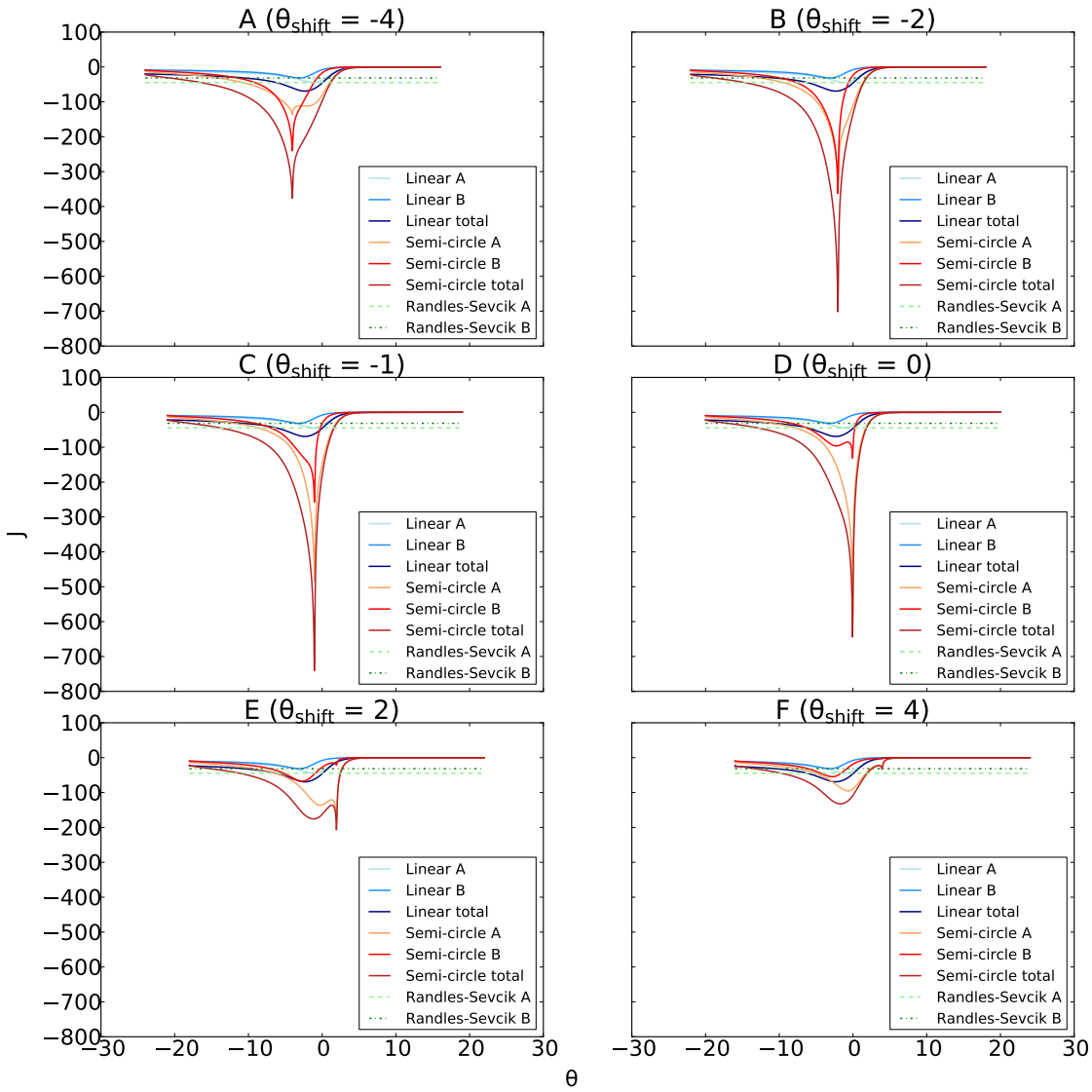


Figure A.11: Full-scale figure of the voltammograms shown in Figure 4.7.

A.4 Chapter 5 Additional Figures

The following section contains the convergence test results to ensure the system investigated in the main text in Chapter 5 is in the reversible limit. For systems that are fully reversible, the Butler-Volmer expression (5.13) converges to the Nernst equation (5.16) and thus beyond a certain minimum large value, increasing the K_0 value should have no effect on the simulated results.

A.4.1 Determination of the appropriate K_0

In the main text a K_0 of 10^{10} was used in order to ensure the full reversibility of the system under study. The use of that value is justified in the following through the peak flux comparison using lower and higher K_0 values with a linear potential wave. Figure A.12 shows the dimensionless peak currents plotted against $\log_{10}$ of the corresponding K_0 values used, and as evident, they do not change with varying K_0's indicating the system is fully reversible in this range. All other parameters used for this analysis are the same as that used in Figure 5.2 of the main text.

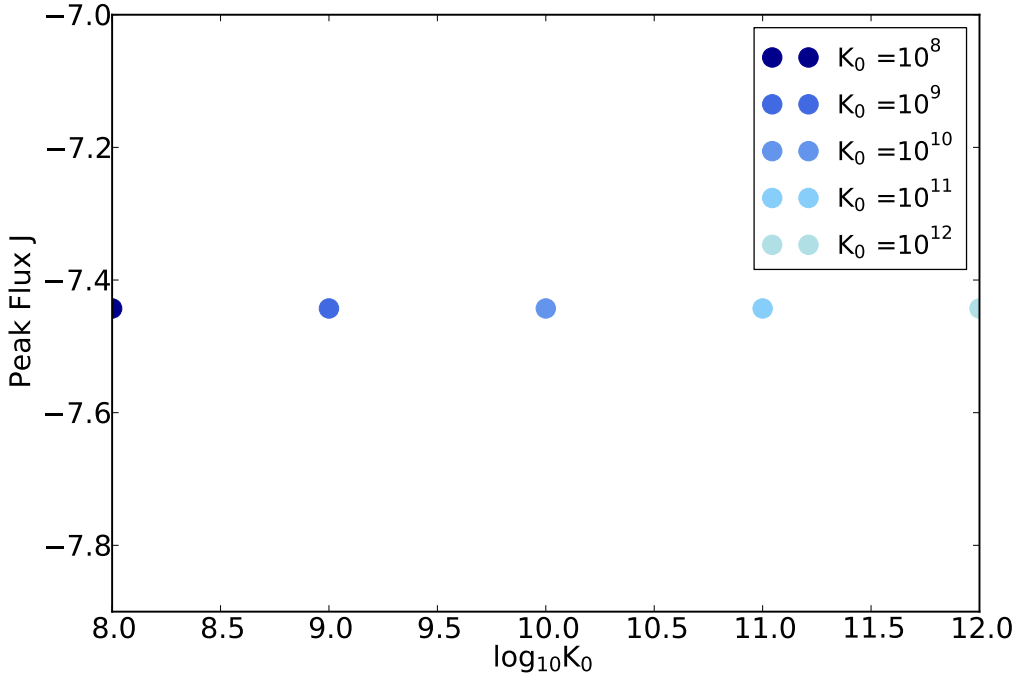


Figure A.12: Peak flux plotted against $\log_{10}$ of the corresponding K_0 values used.

Since the reversibility of a system is affected by the scan rate, a similar investigation was conducted as in Figure A.12 for a semi-circular potential wave, which shows a transiently infinite scan rate at the mid-point of the potential window. Figure A.13 shows the voltammograms obtained using the semi-circular potential wave with varying K_0 values. The shape of the curves and the dimensionless peak currents are almost identical for all five K_0's, as shown through the overlap, and thus indicates that the system is again fully reversible in this range for the semi-circular potential wave as well.

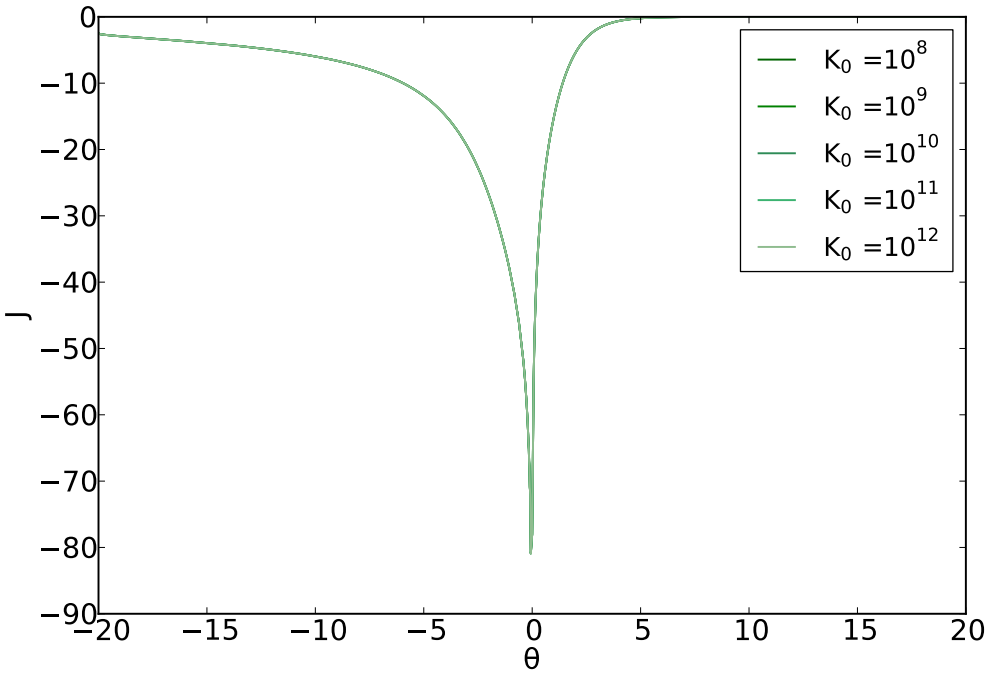


Figure A.13: Voltammograms obtained using the semi-circular potential wave with varying K_0 values.

A.5 Chapter 6 Additional Figures

The following sections contain the convergence test results as mentioned in the main text of Chapter 6.

A.5.1 Convergence Tests

Convergence tests were performed for the parameters $\sigma = 3.89$ and $K_0 = 10^2$. As shown in Figure 6.2 in the main text, this set of parameters lies at the transition from the quasi-reversible to the reversible regime and the peak flux converges to a finite value. Large $K_0 \to \infty$ approach the reversible limit and alongside an infinite peak flux which cannot be convergently modelled by means of finite differences as explained in Section A.3.1.

The numerical parameters considered for the following convergence tests are $\Delta\theta$, h, and ω, and their physical significance is briefly explained along with the corresponding convergence test results. The values used for the figures and analysis reported in the main text are $\Delta\theta = 10^{-4}$, $h = 10^{-6}$, and $\omega = 1.1$, and the justification for using these values are provided below.

The parameter considered first and which has the greatest influence on the peak current is $\Delta\theta$. $\Delta\theta$ is the discretized potential which indicates how much the potential changes between each time step when a linear potential wave is employed. Time is also discretized and $\Delta\theta$ is used to calculate the difference between each time step, defined as $\Delta\tau = \frac{\Delta\theta}{\sigma}$. The discretized semi-circular potential wave equation is:

$$\theta(\tau_k) = \pm\sqrt{\left|\theta_{A_0}^2 - \left[\sigma \cdot (k \cdot \Delta\tau - c\tau_{max})\right]^2\right|} + \theta_{shift} \tag{A.18}$$

Equation (A.18) shows that the potential is dependent on the $\Delta\tau$ value which depends on $\Delta\theta$, and consequently any changes in $\Delta\theta$ will directly be reflected in the sequence of simulated discrete potential values. A smaller $\Delta\tau$ means the difference in potential between corresponding time steps is smaller and will provide a more refined current response, which will be reflected in the peak flux value as shown in Figure A.14.

Figure A.14 shows the peak flux plotted against $\log_{10}$ of the corresponding $\Delta\theta$ values where the blue dots represent results obtained from the linear potential wave and the green diamond shapes represent results obtained from the semi-circular potential wave. The other two parameters, h and ω, were set to 10^{-6} and 1.1, respectively. With increasing $\Delta\theta$ the absolute peak flux value obtained from the semi-circular potential wave decreases indicating the system is not convergent. Meanwhile between $\Delta\theta = 10^{-4}$ and $\Delta\theta = 10^{-5}$ the peak flux does not change and thus shows the results with $\Delta\theta = 10^{-4}$ are convergent when $K_0 = 10^2$.

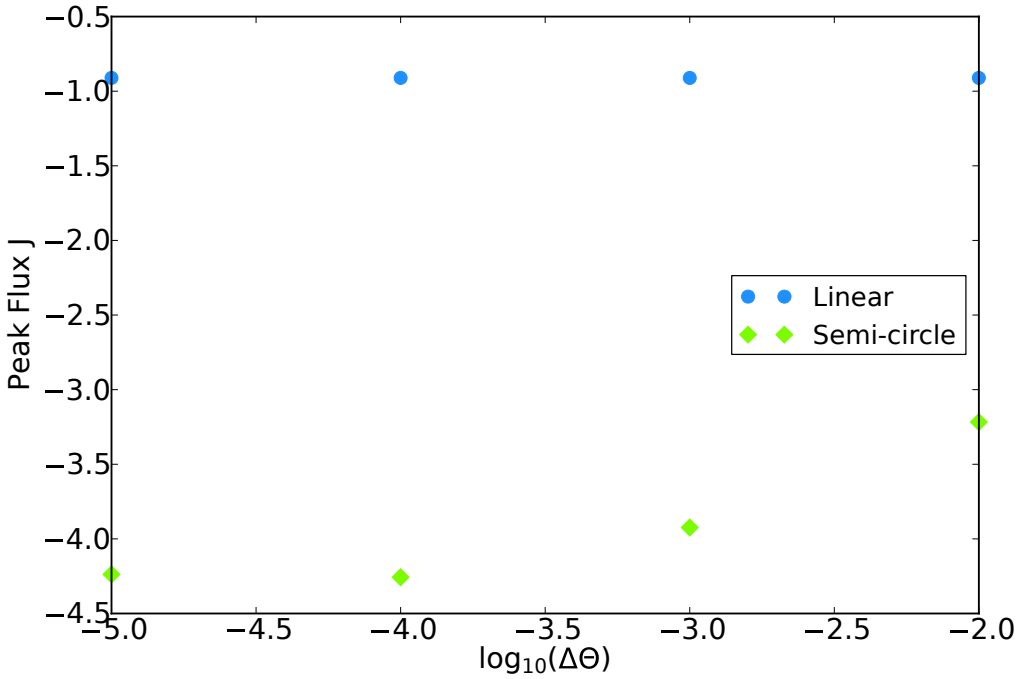


Figure A.14: Peak flux of linear and semi-circular results plotted against $\log_{10}$ of the corresponding $\Delta\theta$ values with $\sigma = 3.89$ and $K_0 = 10^2$. The blue dots represent results obtained using the linear potential wave and the green diamond shapes represent results obtained using the semi-circular potential wave.

Next a convergence test for varying h values was conducted, which is the intial grid space of the expanding spatial grid (further detail provided in Chapter 2). Figure A.15 shows the peak flux plotted against $\log_{10}$ of the h values using the same colors as in Figure A.14. Here, $\Delta\theta = 10^{-4}$ and $\omega = 1.1$. It is clear that the varying h's do not affect the peak flux values for either the linear or the semi-circular

potential wave results and hence the choice of using $h = 10^{-6}$ is justified.

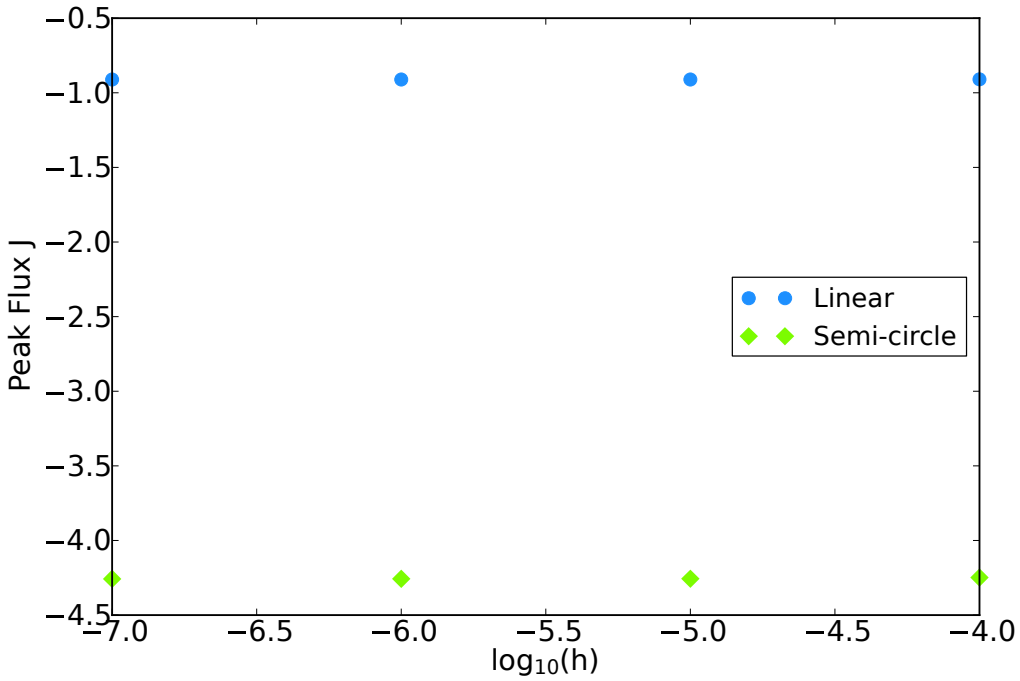


Figure A.15: Peak flux of linear and semi-circular results plotted against $\log_{10}$ of corresponding h values with $\sigma = 3.89$ and $K_0 = 10^2$. The same color scheme as in Figure A.14 is used.

Lastly the convergence test results for varying ω values are shown. ω is the expanding factor of the expanding spatial grid (further detail provided in Chapter 2). Figure A.16 shows the peak flux plotted against the ω values using the same colors as in Figure A.14. $\Delta\theta = 10^{-4}$ and $h = 10^{-6}$. Similar to h values, varying ω's in the range tested shows no effect on the peak flux for both the linear and semi-circular results, indicating the results using $\omega = 1.1$ are convergent.

The three convergence tests show that the results reported in the main text are all convergent up to $K_0 = 10^2$, however, for higher K_0's where the peak approaches infinity, full convergence is not necessarily achieved as, with increasing K_0, the peak flux aproaches an infinite value. When $K_0 \to \infty$, the system establishes a Nernstian equillibrium. The infinite scan rate causes a potential jump, leading to an instantaneous change in the surface concentration which in turn produces

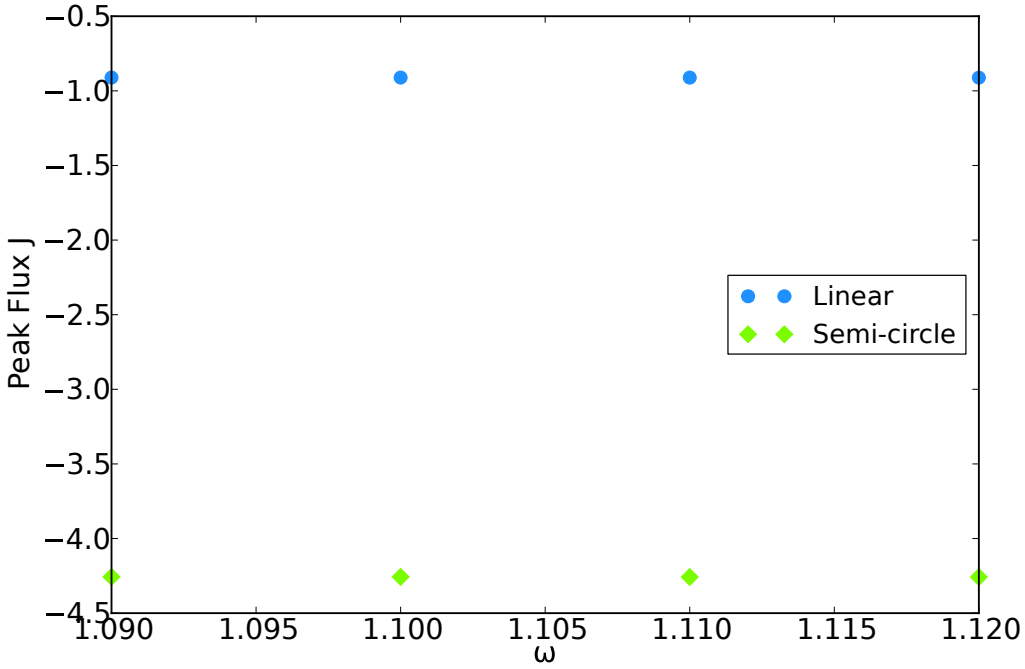


Figure A.16: Peak flux of linear and semi-circular results plotted against corresponding ω values with $\sigma = 3.89$ and $K_0 = 10^2$. The same color scheme as in Figures A.14 and A.15 is used.

an infinite peak current. A more detailed explanation of the infinite peak current convergence is given in Section A.3.1.